

N 70 2970 5
R-8083

NASA CR 102722

THERMODYNAMIC IMPROVEMENTS IN LIQUID HYDROGEN TURBOPUMPS

CASE FILE
COPY



Rocketdyne
North American Rockwell

6633 Canoga Avenue,
Canoga Park, California 91304

THERMODYNAMIC IMPROVEMENTS IN
LIQUID HYDROGEN TURBOPUMPS

Contract No. NAS8-20324

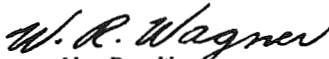
Final Report
December 1969

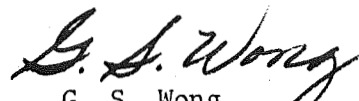
Prepared For


National Aeronautics and Space Administration
Propulsion and Vehicle Engineering Division
George C. Marshall Space Flight Center
Huntsville, Alabama

Prepared by

Advanced Systems and Turbomachinery Departments
Engineering, Liquid Rocket Division
Rocketdyne
A Division of North American Rockwell Corporation
Canoga Park, California


W. R. Wagner
Manager, Heat Transfer


G. S. Wong
Principal Engineer
Manager, Advanced Turbomachinery


E. B. Monteath
Program Manager
Advanced Technology Programs

FOREWORD

Rocketdyne, a division of North American Rockwell Corporation, has prepared this final report, which documents the work performed in fulfillment of the program, "Thermodynamic Improvements in Liquid Hydrogen Turbopumps," during the period from 17 August 1968 to 16 November 1969. This program was sponsored by the National Aeronautics and Space Administration, Marshall Space Flight Center, Huntsville, Alabama, under Contract No. NAS8-20324. The work was performed by the Advanced Turbomachinery unit of the Turbomachinery department; the Materials and Processes unit of the Engineering Department; and the Heat Transfer and Engine Analysis units of the Advanced Systems department. Mr. T. W. Winstead, NASA-MSFC, Huntsville, Alabama, was the Technical Project Manager for the program.

ABSTRACT

This report describes the completed effort in the evaluation of thermal conditioning problems of liquid hydrogen turbopumps to enhance mixed-phase operation and to minimize engine system constraints on starts and restarts. The program consists of the following three interrelated tasks: I: Reduced Gravity Effects on Heat Transfer, II: Coated Feed Systems, and III: Engine System Analyses.

ACKNOWLEDGEMENT

Acknowledgement is made to the following personnel for their contributions to the program: Messrs. M. A. Duffy, T. M. Vahedi, and J. G. Gerstley for heat transfer analyses of turbopumps during chilldown and under zero gravity; Mr. W. R. Bissell for analyses of two-phase flow in hydrogen pumps; Messrs. J. R. Leonard, W. M. Stanley, and E. H. Cross for analyses of engine start and chilldown sequences; Messrs. R. E. Mowers, S. A. Geist, and G. E. Williams for development of thermal insulation coatings for cryogenic applications; Mr. W. S. Brooks and his staff for their cooperation in providing hydrogen turbopump environmental test experience and data; and Mr. R. K. Hoshide for his able assistance in coordinating and directing the technical effort.

Contributions to the program by Messrs. L. Gross, J. Vaniman, and H. F. Beduerftig of NASA-MSFC are also acknowledged.

CONTENTS

Foreword	iii
Abstract	iii
Acknowledgement	v
Introduction	1
Summary	3
Reduced Gravity Effects on Heat Transfer	3
Coated Feed Systems	3
Engine System Analysis	4
Conclusions	5
I: Reduced Gravity Effects on Heat Transfer	11
Pool Boiling	11
Pressure Effects	16
Dimensional Analysis	16
Gravity Effects	22
Forced Convection	24
Effects of Thermal Variables on LH ₂ Pump Chillo down	27
II: Coated Feed Systems	45
Chillo down of Coated Materials	45
Study of Coating Techniques	70
Development of Coating Techniques	71
Coated Pump Tests in LH ₂	91
Analysis of the LH ₂ Pump Coating Tests	98
III: Engine System Analyses	109
Pump Thermodynamic Design Limitations	109
Engine Start Analysis	144
Nomenclature	203
References	209
<u>Appendix A</u>	
Literature Survey	A-1

Appendix B

Engine Start Model Equations B-1

Appendix C

Payload Estimates C-1

Appendix D

Distribution List , D-1

ILLUSTRATIONS

1. Hydrogen Chillo down Flow Reductions Obtainable With Two-Phase Flow Pumping Capability and With Coatings	10
2. Liquid Hydrogen Pool Boiling Data	12
3. Liquid Hydrogen Pool Boiling Film Coefficient	15
4. Effect of Pressure on LH_2 Pool Boiling	17
5. Hydrostatic Force Regimes	19
6. Effect of Gravity on Liquid Hydrogen Nucleate Boiling (Experimental)	23
7. Experimental Gravity Effect on Liquid Nitrogen Pool Boiling	25
8. Theoretical Gravity Effect on Liquid Hydrogen Pool Boiling	26
9. Simple Model of Uncoated Metal Showing Nodal Breakdown for Chillo down Study	29
10. Effect of Gravity and Forced Convection on Liquid Hydrogen Pool Boiling	31
11. Effect of Gravity and Forced Convection on Hydrogen Heat Transfer Coefficients	32
12. Wetted Surface Temperature Vs Chillo down Time Under Pool Boiling Condition Near Zero - g	34
13. Wetted Surface Temperature vs Chillo down Time Under Pool Boiling Condition and Unity Gravity	36
14. Wetted Surface Temperature vs Chillo down Time Under Forced Convection Condition of $G = 2 \text{ lb/in}^2 \text{ sec}$	37
15. Wetted Surface Temperature vs Chillo down Time Under Forced Convection Condition of $G = 5 \text{ lb/in}^2 \text{ sec}$	39
16. Temperature vs Chillo down Time for Titanium Under Forced Convection Condition ($G = 2 \text{ lbs/in}^2 \text{ sec}$)	40
17. Temperature vs Chillo down Time for Coated and Uncoated Aluminum Under Pool Boiling Condition Near Zero Gravity ($\frac{a}{g} = 0.004$)	41
18. \bar{h}/k vs Chillo down Time for Uncoated Metals at Various Surface Temperatures	42

19.	Cooldown of Kel-F Coated K-Monel Plates in Liquid Hydrogen. Initial Plate Temperature: - 24 F	48
20.	Simple Model of Coated Metal Showing Nodal Breakdwn for Chilldown Study	50
21.	Titanium Wetted Surface Temperature vs Chilldown Time for Hydrogen Pool Boiling Condition at Near Zero Gravity	52
22.	Titanium Wetted Surface Temperature vs Chilldown Time for Hydrogen Pool Boiling Condition at Unity Gravity	53
23.	Titanium Wetted Surface Temperature vs Chilldown Time for Forced Convection Condition of $G = 2 \text{ lbs/in}^2 \text{ sec}$	54
24.	Titanium Wetted Surface Temperature vs Chilldown Time for Forced Convection Condition of $\epsilon = 5 \text{ lbs/in}^2 \text{ sec}$	55
25.	Titanium Chilldown Time vs Coating Thickness	58
26.	Temperature vs Chilldown Time for KX 635-Coated Titanium Under Forced Convection Condition ($G = 2 \text{ lbs/in}^2 \text{ second}$) . .	60
27.	Heat Flux vs Mass Flox for Mark - 29 LH_2 - Pump at Saturated Hydrogen Condition	63
28.	Heat Flux vs Mass Flux for Mark - 29 LH_2 Pump at 8.5 Subcooled Hydrogen	64
29.	Heat Flux vs Wetted Surface Temperature for an Uncoated Titanium LH_2 Pump	65
30.	Heat Flux vs Wetted Surface Temperature for a Coated Titanium LH_2 Pump	66
31.	Heat Flux vs Wetted Surface Temperature for an Uncoated Aluminum LH_2 - Pump	67
32.	Thermal Contraction of Various Coatings	74
33.	Tensile Strain Test	87
34.	Tensile Strain Test	87
35.	Tensile Strain Test	87
36.	Tensile Strain Test	87
37.	Tensile Strain Test	88
38.	Tensile Strain Test	88
39.	Tensile Strain Test	88
40.	Tensile Strain Test	88

41.	Tensile Strain Test	89
42.	Tensile Strain Test	89
43.	Tensile Strain Test	89
44.	Tensile Strain Test	89
45.	Inducer Noespice Prior to Application of Coating	93
46.	Inducer Nosepiece After Application of Modified Kel-F Coating	94
47.	Mark 29 LH ₂ Pump With Coated Internal Parts	97
48.	Coated Inducer After 10 Static Thermal Cycles From -320 to 200 F	99
49.	Coated Inducer after 10 Static Thermal Cycles from -320 to 200 F	100
50.	Coated Inducer Nosepiece After 415 Seconds of LH ₂ Pump Testing	102
51.	Coated Inducer Nosepiece After 2586 Seconds of LH ₂ Pump Testing	104
52.	Posttest Condition of Coated Inlet	106
53.	Flow Geometry for Oblique Shock Wave	114
54.	Effect of Vapor Volume Fraction on Constant-Quality, Two-Phase Flow of an Isothermal Gas	115
55.	Inducer Inlet Flow Geometry at Low and High Flow Coefficient Operations	116
56.	Effect of Vapor Volume Fraction on Inducer Inlet Flow Conditions	118
57.	Effect of Variation in Blockage and Design Incidence on Mark 25 Inducer Cavitation Performance in LH ₂	120
58.	Effect of Incidence Angle and Blockage on Vapor Pumping Capacity of LH ₂ Inducers at Design Liquid Flow Coefficient Operation	122
59.	Maximum Vapor Pumping Capabilities of Hydrogen Pumps . . .	123
60.	Mark 15 LH ₂ - Pump Two-Phase Flow Data at a Hydrogen Flowrate of 8200 gpm	126
61.	Mark 15 LH ₂ Pump Two-Phase Flow Data at a Flowrate of 8600 gpm	127

62.	Mark 25 LH ₂ Pump Two-Phase Flow Data With Hydrogen	128
63.	Comparison of Mark 15 LH ₂ Pump Two-Phase Flow Test Results With Theoretical Prediction	130
64.	Comparison of Mark 25 LH ₂ Pump Two-Phase Flow Test Results With Theoretical Prediction	131
65.	Effect of Equilibrium Flow Expansion of Hydrogen From Tank to Pump Inlet	135
66.	Influence of Design Flow Coefficient on Inducer Two-Phase Hydrogen Pumping Capability (Q = 11,300 gpm, N = 30,000 rpm, $\lambda = 0.375$)	136
67.	Influence of Rotational Speed on Inducer Two-Phase Hydrogen Pumping Capability ($\phi r = 0.08$, $dr = 8.00$ inches, $\lambda = 0.375$).	139
68.	Thermal Factor Variation with Vapor Pressure for Different Fluids	140
69.	Vapor Pumping Capacities for MK 15 LH ₂ Pump	142
70.	Estimated Effect of Warm Pump Heat Input on Hydrogen Pump Discharge Pressure	143
71.	Maximum Vapor Pumping Capacity of Hydrogen Pumps	146
72.	Flow Schematic for Engine Start Transient Analysis	149
73.	Typical Basic Tank Head Start Transient	151
74.	Typical J-2S Engine Start Transient	155
75.	J-2S Start and Restart Requirements Based on Various Mission Profiles	156
76.	AEA Engine Idle Stage Operation	158
77.	Typical Chillydown Transients for the J-2 Engine System (Mk 15 LH ₂ Pump)	159
78.	Typical Chillydown Transients for the J-2S Engine System (Mk 29 LH ₂ Pump) From Ambient Condition (Ref. 8)	160
79.	Flow Quality at the Pump Inlet for the J-2 Hydrogen Engine	161
80.	Fuel and Payload Losses for the J-2 Engine Inlet Line Chillydown Transients in Figure 79 for Various Vapor Fraction Pumping Capabilities	162

81.	Flow Quality at the Pump Inlet for the J-2S Engine (Sea-Level Data From Ref. 7 and Conservative Altitude Estimate Based on Temperature Data from Fig. 78)	164
82.	Estimated Typical Propellant Expenditure & Associated Payload Loss for J-2S Engine Chillover Transients in Figs. 78 & 81 for Various Vapor Volume Pumping Capabilities	165
83.	Effect of Pump Heat Input on Engine Start Characteristics	167
84.	Effect of Stepped Main Oxidizer Valve Flow Control on Engine Start Characteristics With a Warm Pump ($Q_i =$ 60 Btu/lb, $t = 5$ seconds)	168
85.	Effect of Prolonged Chillover Period on Engine Start Characteristics With a Warm Pump and With Stepped Main Oxidizer Valve Flow Control ($\bar{A}_{ox_i} = 0.1$)	169
86.	Projected Effects of Pump Coatings on Engine Start Characteristics With A Warm Pump	171
87.	Engine Start Transient with Chillover for a 30,000 lb Thrust Engine (Ref. 7)	172
88.	Fuel Temperature at Pump Discharge During Original Start Showing the Effects of Internally Coating the Pump and/or Ducting	173
89A.	Schematic of Saturn S-IVB Stage Engine Preconditioning And Tank Pressurization Systems	175
89B.	S-IVB LH_2 Preconditioning System	176
90.	Thrust Chamber Chillover for S-IVB Stage	177
91.	Fuel Pump Inlet Pressure for Third Burn of S-IVB Stage for Flight AS-504	177
92.	Mark 15 LH_2 Pump Heat Rejection Rate and Chillover Flowrate for Flight AS-504	179
93.	Expected Mark 15 Fuel Pump Heat Rejection Rate and Chillover Flowrate for Flight AS-505.	180
94.	Expected Mark 15 LH_2 Pump Heat Rejection Rate for Backup AS-505 S-IVB Start Sequence	182
95.	Fuel Flowrate Transient from J-2 System Start Model	183

96.	Fuel Pump Head vs Flow Start Transient From J-2 System	
	Start Model	184
97.	Thrust Chamber Chilldown Transient from J-2 System	
	Start Model	185
98.	Saturn S-IVB Stage Propellant Feed System	186
99.	Fuel Pump Inlet Temperature Transient for Third Burn	
	of S-IVB Stage for Flight AS-504	188
100.	Flushing Time for S-IVB Stage Fuel Pump Inlet Duct	189
101.	Mark 15 Fuel Pump Quality Predictions for AS-504 Flight	
	and Typical AS-505 Flight	190
102.	Effect of Fuel Inlet Duct Temperature on Duct Heat	
	Rejection Rate for a Spin Bottle Start at 8 seconds	191
103.	Effect of Fuel Inlet Duct Temperature on Fuel Pump Inlet	
	Quality for a Spin Bottle Start at 8 Seconds	193
104.	Vapor Pumping Capacities for Mk 15 LH ₂ Pump	194
105.	Effect of Fuel Inlet Duct Temperature on Duct Heat	
	Rejection Rate for a Tank Head Chilldown	195
106.	Effect of Fuel Inlet Duct Temperature on Fuel Pump	
	Inlet Quality for a Tank Head Chilldown	196
107.	Effect of Fuel Inlet Duct Temperature on Fuel Pump Inlet	
	Quality for a Spin Bottle Start at 10 Seconds	198
108.	Effect of Tank Hydrogen Subcooling on Fuel Lead Chilldown	
	Time Required to Reduce Pump Inlet Quality to 25 Percent	
	Vapor	199
109.	Fuel Temperature at Pump Inlet During Recirculation	
	Chilldowns for AS-503 and AS-504 Flights	201

INTRODUCTION

The requirements of minimum chilldown, warm starts, rapid starts, reduced tank pressurization (low tank NPSH), engine flexibility, and engine simplification (reduced cost) are being emphasized for advanced LO_2/LH_2 rocket engines. Various mission applications of cryogenic rocket stages require multiple engine restarts in orbital coast. Present feed system components require low-temperature preconditioning to enable the pump system to develop sufficient head and flow for engine start. A complete understanding of the preconditioning requirement of the LH_2 turbopump is of great importance to the overall engine system start requirements. Simplified methods of preconditioning LH_2 turbopumps in space will significantly affect engine system start time and engine system performance. When accurate hydrogen requirements for preconditioning is known, loss of excessive fuel for prechilling the engine in space can be avoided.

This report describes analytical, experimental, and evaluation studies conducted to investigate engine thermal conditioning problems and to develop thermodynamic improvements of LH_2 turbopumps to minimize, as much as possible, system constraints on engine starts and restarts. Maximum use was made of engine and turbopump data obtained from the J-2S Engine and Saturn V Vehicle programs, from other experimental advanced engine and current engine component programs, and from heat transfer and mixed-phase hydrogen data obtained from associated research study programs.

SUMMARY

The Thermodynamic Improvements in Liquid Hydrogen Turbopumps program was divided into three related tasks: (1) to investigate turbopump chilldown times under reduced gravity, (2) to establish the feasibility and effectiveness of coated feed systems to enhance chilldown, and (3) to establish the effect of improved criteria on engine start capabilities.

REDUCED GRAVITY EFFECTS ON HEAT TRANSFER

The effects of reduced gravity on LH_2 boiling heat transfer were analyzed by using various dimensionless parameters (Re, Nu, Pr, Gr, St, etc.) to determine the predominant forces affecting turbopump chilldown under space conditions. Both dimensional analysis and experimental data were used. The nucleate boiling regime was found to be relatively insensitive to gravity; however, the heat transfer coefficients in the transition and film boiling regime are reduced by as much as a factor of 4 under near-zero gravity.

COATED FEED SYSTEMS

Analytical and experimental studies indicate that a thin layer of low thermal conductivity material applied to a metal surface will produce rapid surface chill. Thus, both quick chilldown time and minimum hydrogen requirements for chilldown will be obtained. Coating material composition, processing, and application techniques were developed for both conventionally applied polymeric materials and plasma-sprayed epoxy resin, and applied to the titanium inlet duct of the J-2S Mark 29 LH_2 -turbopump. Kel-F coating was applied to both the inducer nosepiece fairing and inducer. The Kel-F coating on the inducer nosepiece, operating at 475 ft/sec surface velocity, accumulated a total test time of 2586 seconds in 13 LH_2 turbopump tests, which included hot firing, deep-cavitation starts, over-speed and steady-state operations, and was found to be in excellent condition.

ENGINE SYSTEM ANALYSIS

An analysis of two-phase flow in hydrogen pumps was made to determine design criteria for increasing the allowable vapor capacity of the pump. Performance analyses were correlated with experimental data showing that a maximum vapor volume fraction of 55 percent is obtainable with small head loss.

Engine start analyses using coated feed systems and two-phase flow capability indicate significant potential system gains can be obtained by reducing chilldown flow loss by 35 to 80 percent. This results in reducing engine start time, eliminates ullage and recirculation system weights and complexities, and increases payload for the current S-IVB stage and the proposed Space Shuttle orbiter stage. These analyses were also used to assess the AS-504 third start data, and to develop engine start criteria for possible failure of S-IVB fuel recirculation systems.

CONCLUSIONS

The results of studies conducted indicate that: (1) reduced gravity will not affect nucleate boiling but will reduce the heat transfer coefficients by a factor of 4 (compared with 1 g gravity) in the transition and film boiling regimes of pool boiling in hydrogen; (2) higher vapor pumping capacity LH_2 pumps for zero tank NPSH can be obtained by designing the inducer for higher incidence-to-blade angle ratio, minimum blade blockage, and maximum inlet annulus flow area, and maximum vapor volume fractions from two to three times greater than present pumps are obtainable; (3) a thin thermal insulation coating of optimum thickness will reduce the chilldown time of the pump and reduce the heat rejection rate from the warm pump to the cold hydrogen; (4) initial success was obtained in developing material composition and application technique for bonding polymeric and epoxy resin coatings to aluminum and titanium materials, and a Kel-F-coated, titanium inducer nose-fairing piece has undergone 2586 seconds of LH_2 turbopump testing rotating at 475 ft/sec with complete success. Further development and testing will be required to define the life characteristic of coating, coating thickness, and limitations of complex shapes to which it can be applied.

An engine chilldown and start analysis was made to indicate the potential gains that will be obtained in the overall vehicle and engine system by using the above thermodynamic improvements, such as higher vapor fractions and coatings, that have been developed for hydrogen turbopumps. The J-2 type engines in the Saturn V and Space Shuttle launch vehicles are used for illustrating the potential system gains.

1. Analyses of the S-IVB stage indicate potential reductions in chilldown fuel flow of up to 80 percent, equivalent to approximately 115 pounds of LH_2 per chilldown, and payload increases approaching 2 percent. Elimination of the recirculation system on the S-IVB by using idle mode operation during chilldown eliminates the need for solid-propellant ullage rockets (230 pounds). If a tank head start is used there is no need for auxiliary turbine power such as the start bottle on the J-2 (150 pounds) or

solid-propellant turbine spinners used on the J-2S (which add 115 pounds per engine start). Reduced NPSH requirements allow lower tank pressures and reduced stage weights. The above thermodynamic improvements are most significant on advanced applications, such as the Space Shuttle vehicle, requiring several altitude starts, extended engine life, and reusability. In addition to the lower chilldown flow requirements, other improvements are in stage weight reductions, stage simplifications, and reduced maintenance between flights.

2. Although these studies have centered on LH_2 pumps and feed systems, the technology developed is applicable to oxidizer feed systems as well. The LO_2 system on the S-IVB, for example, is not as critical with regard to chilldown as the LH_2 side because of the higher operating temperatures and the shorter duct length; however, due to the higher LO_2 flowrate and lower specific heat, it is estimated that system improvements could result in chilldown flow reductions similar to those realized on the fuel side.
3. Individual thermal improvement methods are described in Table 1 based on a single start. Up to 10 starts are planned for many engines and would magnify the reduction in chilldown losses. The effect of the vapor pumping capability of the pump on chilldown flow and time requirements has been analyzed for a range of initial feed system temperatures. With a warm feed system (400 R), an increase in allowable vapor fraction from 20 to 45 percent results in a saving of 52 pounds (37 percent) of fuel each time the system is chilled, as shown in Table 1. A further increase to 55 percent saves 64 pounds (45 percent). The chilldown time reductions corresponding to the above weight are 2.5 and 3.5 seconds, respectively. The increase in allowable vapor fraction will also allow reductions in stage weight due to lower tank pressure requirements and elimination of the recirculation system.
4. With inlet duct and pump surfaces coated, a further reduction in chilldown flow to approximately 37 pounds (74 percent) is achieved for an allowable vapor fraction of 55 percent. A potential reduction in start time and less variation in engine mixture ratio

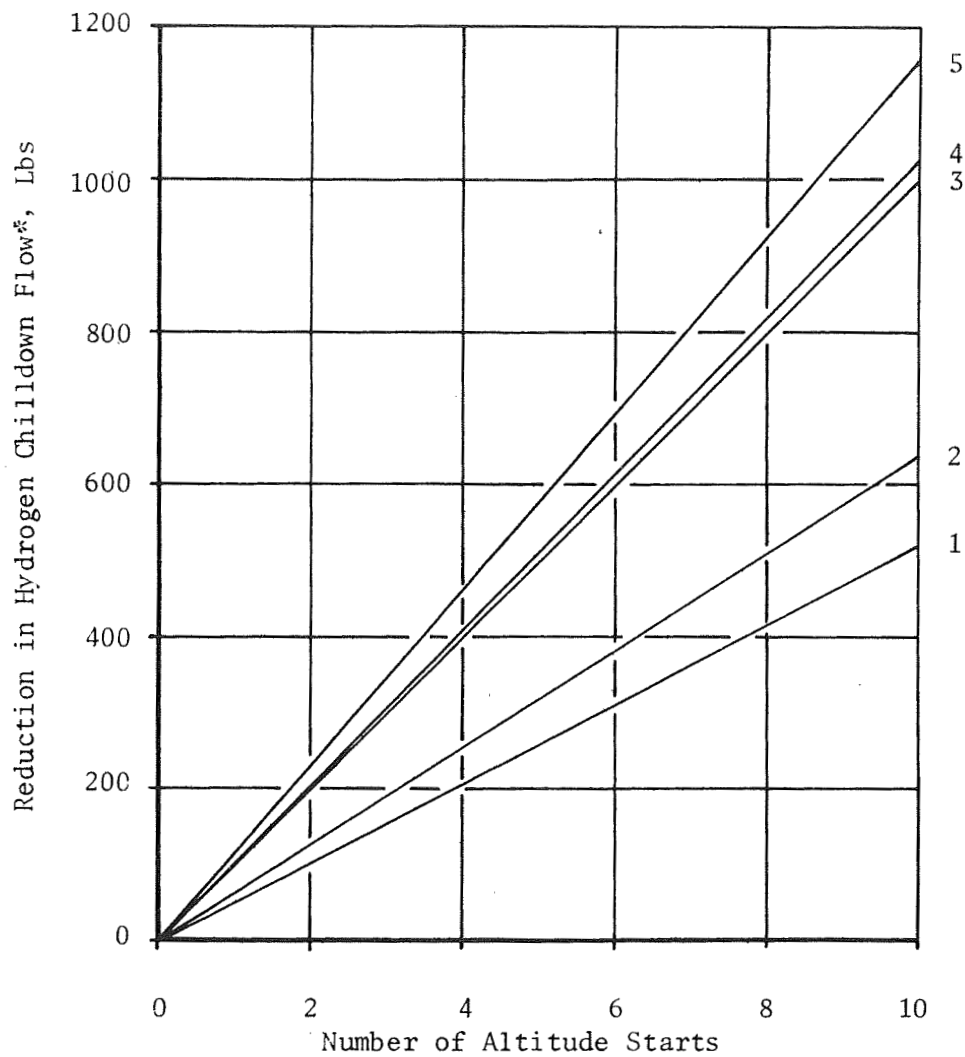
TABLE 1
ENGINE STARTS AT VACUUM

Case	Method Description	Type of Turbine Start	Pump Vapor Fraction	Hydrogen Loss, lb/start	Hardware Weight, pounds	Chilldown Time, seconds	Start Time, seconds	Total Time, seconds
Current Systems (J-2) ($T_i = 400$ R)	1. Recirculation of propellants through pump prior to start	Start Bottle	0.20	0	380	5 minutes	3	-
	2. Propellant dump chill	Start Bottle	0.20	140	150	16.5	3	19.5
Improved Methods ($T_i = 400$ R)	1. Design inducer for improved vapor fraction	Tank Head	0.45	88	0	14	7	21
	2. Coating of inlet lines	Tank Head	0.55	76	0	13	7	20
		Tank Head	0.55	37	0	11	7	18
	3. Coating of pump passages and inlet lines	Tank Head	0.55	37	0	11	6	17
	4. Insulation of feed system ($T = 100$ R)	Tank Head	0.20	67	20	12.8	6	18.8
		Tank Head	0.55	40	20	11	6	17
	5. Idle-mode operation; coatings and improved vapor fraction	Tank Head	0.55	24	0	11	6	17
		SPTS	0.55	24	115 x number of starts	11	3	14

in early phases of the engine start are also obtained. Minimizing the number of system variables will greatly simplify the engine control systems. The analytical results obtained on the relative chilldown rates of titanium, K-monel, and Tens-50 aluminum, were used to estimate the chilldown flow reduction with Kel-F coating applied to the duct and pump wetted surfaces.

5. Some degree of thermal protection will be required on any LH_2 feed system; however, a detailed analysis is necessary to arrive at an optimum configuration for a given application. For purposes of illustration, if the heat input were reduced to limit the feed system temperature to 100 R, the chilldown flow would be 36 pounds less than with a 400 R feed system. The thermal protection would increase the weight of the system slightly. A further reduction in heat input, sufficient to prevent the vapor fraction of the residual propellant from exceeding the vapor pumping capability of the pump, would allow the use of the residual hydrogen and there would be no loss due to chilldown.
6. On advanced engines where weight, complexity, and maintenance requirements are important, the use of auxiliary turbine spinners does not appear applicable for high-flowrate, topping-cycle engines because of the high turbine power requirements. Similarly, the recirculation system used on the S-IVB is not particularly desirable. A meaningful comparison, would be between the propellant dump method of chilldown and idle-mode operation during chilldown. Since the chilldown propellants provide thrust, the loss during idle mode is due to the lower specific impulse. Assuming a 400 R feed system and an allowable vapor fraction of 55 percent, the idle-mode operation has the effect of saving an additional 52 pounds of fuel per start. Additional savings would result from the elimination of the ullage system. (This would amount to some 230 pounds on the S-IVB stage. Also a tapoff cycle engine such as the J-2S, engine start time is reduced by use of a solid-propellant turbine spinner; however, engine weight is increased.)

7. Some of the combined effects of thermodynamic improvement techniques can be seen in the summary of results in Table 1. The effect of missions requiring more than one altitude start is shown in Fig. 1. For selected cases, payload increases were estimated for fuel and oxidizer chilldown flow reductions of 116 pounds (83 percent) per engine start and a mission requiring 10 engine altitude starts each commencing with a warm feed system. Two specific vehicle stages were considered, the current S-IVB and the proposed Space Shuttle orbiter. Estimated payload increases were 1810 and 2290 pounds or 1.7 and 5.7 percent increase, respectively. Hardware weight reduction due to elimination of recirculation systems, ullage systems, and start power system will contribute as much as 610 pounds further increase in payload.
8. Most of the analyses performed have dealt with altitude starts. The enhancement of sea level start characteristics would also prove beneficial by reducing the ground equipment and operations necessary to prepare the vehicle for static testing and for flight takeoff. This would be especially desirable for vehicles designed to fly from multiple land bases, where service operations should be minimized.



1. Inducer design for improved vapor fraction, $\alpha_c = .45$
2. Inducer design for $\alpha_c = .55$
3. Inducer design for $\alpha_c = .55$ and addition of feed system insulation.
4. Inducer design for $\alpha_c = .55$ and KF-635 inlet line coating.
5. Inducer design for $\alpha_c = .55$, coatings, and idle mode operation during chilldown.

*Referenced to S-IVB with fuel-lead propellant chilldown.

Figure 1. Hydrogen Chilldown Flow Reductions Obtainable With Two-Phase Flow Pumping Capability and With Coatings

I: REDUCED GRAVITY EFFECTS ON HEAT TRANSFER

In this task, analytical studies of the reduced gravity effects on heat transfer were performed. To assist in determining the importance of gravity, the heat flux correlations have been reduced to nondimensional form. This was done by analyzing the various dimensionless ratios that were formed from common forces occurring in fluid systems. For pool boiling of saturated LH_2 , the following results were found:

1. For nucleate boiling, both analysis and test indicate that the relation between temperature difference ($T_w - T_{\text{sat}}$) and wall heat flux is insensitive to gravity.
2. The peak nucleate boiling heat flux is predicted to vary as $g^{1/4}$. This agrees with experimental data for LN_2 .
3. The value of $(\Delta T_{\text{sat}})_{\text{max}}$ is found to vary as $g^{1/4}$ based on LN_2 data.
4. The minimum heat flux value where transition boiling changes to film boiling depends on $g^{1/4}$.

The wall heat flux during forced convection saturated boiling, is assumed to be the sum of a constant forced convection term and the appropriate pool boiling function. It should be noted that the above conclusions are applicable to reductions in gravity from standard earth gravity, only.

POOL BOILING

In the determination of reduced gravity effects on heat transfer, the initial step was to define the regions of pool boiling and free and forced convection. Figure 2 illustrates the pool boiling curve for LH_2 at 1 atmosphere and 1 g. The bracketed regions in the nucleate and film boiling regions pertain to the available experimental data, as reported in Ref. 1. A wide variation in heat flux versus ΔT is noted in the nucleate boiling regime. This spread in experimental data is attributed primarily to effects of surface condition, and surface geometry and orientation.

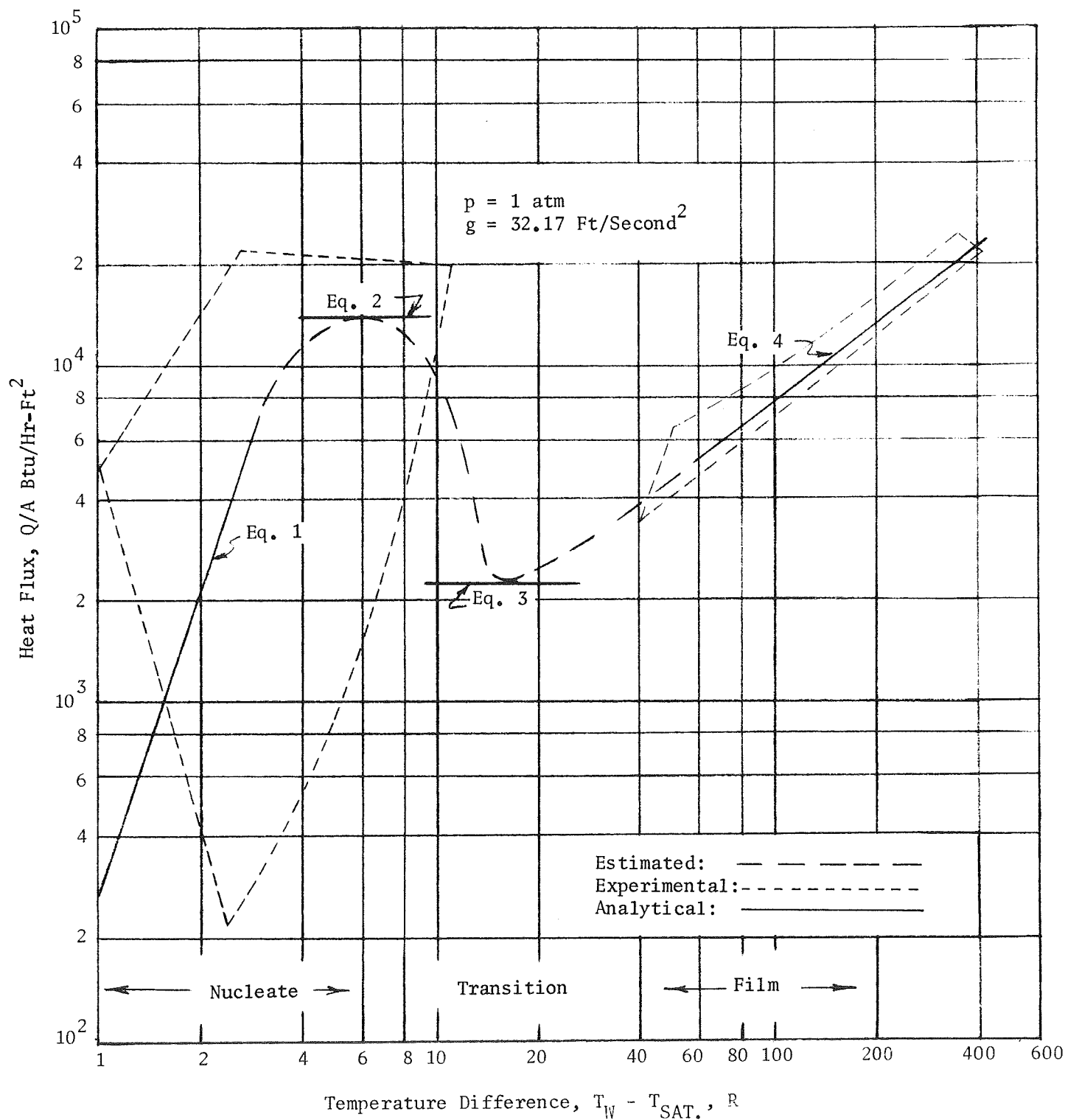


Figure 2. Liquid Hydrogen Pool Boiling Data

The task of choosing an analytical function to correlate the data is clearly difficult, and it is hoped that the predictions will fall within the spread of data. For the present study, a prediction was made utilizing a correlation by Rohsenow (Ref. 2):

$$\frac{C_{p_L} (\Delta T)}{\lambda} = C \left\{ \frac{(Q/A)}{\mu_L \lambda} \left[\frac{g_e \sigma}{g(\rho_L - \rho_v)} \right]^{1/2} \right\}^{0.33} \left(\frac{C_{p_L} \mu_L}{k_L} \right)^{1.7} \quad (1)$$

A value of 0.015 for C was assumed and the properties of hydrogen (at saturated vapor conditions and 1 atmosphere) were taken from Ref. 1. The results obtained with this relationship are shown as a solid line through the nucleate boiling regime.

The peak heat flux as indicated on Fig. 2 has been determined analytically according to:

$$\left(\frac{Q}{A} \right)_{\max} = \frac{\pi}{24} \lambda \rho_v \left\{ \frac{\sigma g g_e (\rho_L - \rho_v)}{\rho_v^2} \right\}^{1/4} \left(\frac{\rho_L + \rho_v}{\rho_L} \right)^{1/2} \quad (2)$$

where all properties are evaluated as for Eq. 1. Although experimental data for LH_2 is scarce, the theoretical prediction is of the right order.

The transition region for pool boiling has been entirely estimated, knowing both the maximum and minimum heat fluxes. Analytical correlations within this boiling regime are not yet available.

The boiling curve passes through a relative minimum in going from the transition region to the film boiling region. Few experimental data points are available for the pool film boiling minimum heat flux. Only nitrogen at atmospheric pressure has been studied to any extent and the results appear to vary widely, depending on surface geometry and orientation.

Nevertheless, an analytical prediction proposed for the present LH_2 case is:

$$\left(\frac{Q}{A}\right)_{\min} = 0.09 \rho_{vf} \lambda \left\{ \frac{\sigma (\rho_L - \rho_v)}{(\rho_L + \rho_v)^2} g g_e \right\}^{1/4} \quad (3)$$

It should be noted that the exact values of ΔT for which both the relative maximum and relative minimum heat fluxes occur are not indicated by the previous relationships. However, a knowledge of the approximate temperature difference at which these phenomena occur allows the appropriate boiling curves to be fitted, although the uncertainty prevalent in these regions is indicated by representing the curves as dashed line segments.

A theoretical prediction of film boiling heat transfer is illustrated, bracketed by a range of experimental data for LH_2 . The heat flux through the vapor film has been shown to be strongly dependent on whether the film is laminar or turbulent (Ref. 2). Only laminar films will be considered here. For a laminar vapor film on a horizontal cylinder of diameter L , the theory predicts:

$$\bar{h} = 0.62 \left\{ \frac{k_{vf}^3 (\rho_L - \rho_{vf}) \lambda_o}{\nu_{vf} L (T_W - T_{sat})} g \right\}^{1/4} \quad (4)$$

where

$$\lambda_o = \lambda \left\{ 1 + \frac{0.4 C_{p_{vf}} (T_W - T_{sat})}{\lambda} \right\}^2$$

Utilizing this film coefficient relationship, the corresponding heat flux profile is shown as a solid line.

Although portions of the curve generated in Fig. 3 are somewhat uncertain, the primary area of interest during chilldown will be the film boiling regime which is fairly well known. Figure 3 depicts the film coefficient profile as a function of temperature difference. During the initial stages

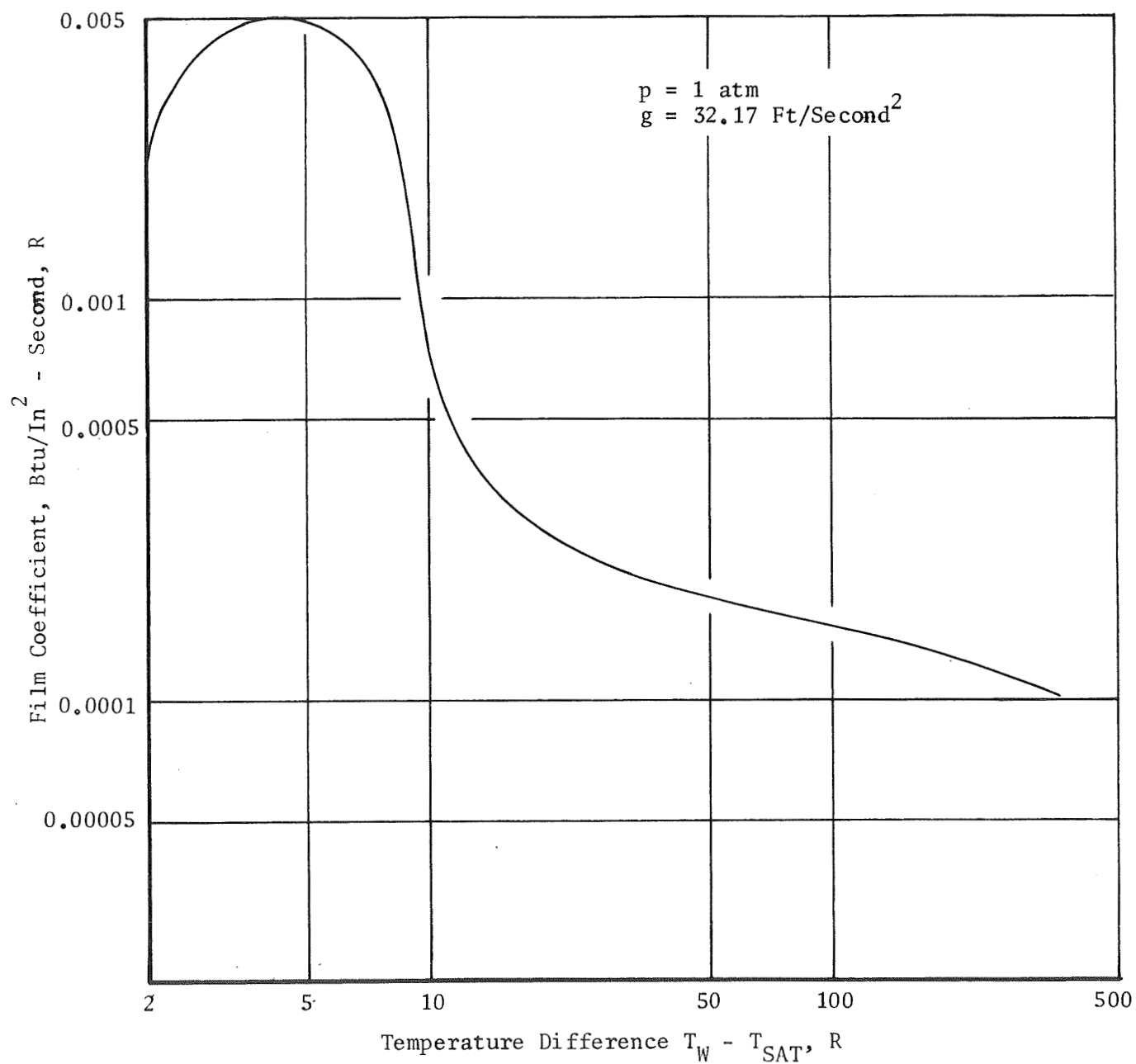


Figure 3. Liquid Hydrogen Pool Boiling Film Coefficient

of pump and line chilldown, the temperature will be at a high enough value to initiate the film boiling (plus forced convection) regime. The values of film coefficient proceed along the curve, from right to left, as time increases.

With these considerations and with a qualitative interpretation of the LH_2 pool boiling curve, the effects of increased pressure and reduced gravity were demonstrated.

PRESSURE EFFECTS

The previously derived analytical pool boiling curve for LH_2 at 1 atmosphere and 1 g is reproduced in Fig. 4. Utilizing this curve as a reference, the effect of increasing the LH_2 to 100 psia is also shown. It should be noted that the hydrogen is still assumed to be at saturated conditions, corresponding to 100 psia. In deriving the curve for an elevated pressure, it has been assumed that the mechanisms of heat transfer are unaffected and that the sole cause of changes in heat flux result from deviations in the thermodynamic properties of hydrogen. The analytical predictions indicate an increase in heat flux over the entire range of pool boiling. However, Ref. 3 has shown experimentally that substantial increases in heat flux occur only during film boiling and at the maximum and minimum heat fluxes. Within the nucleate and transition boiling regimes, the effect of pressure appears minimal, possibly due to the difficulty in obtaining reproducible data in these regimes.

DIMENSIONAL ANALYSIS

To determine the effects of reduced gravity on LH_2 boiling heat transfer, it was necessary to determine the predominant forces acting on the LH_2 fluid system. This was done by analyzing the various dimensionless ratios that can be formed from the common forces occurring in fluid systems (e.g., gravitational, surface tension, inertial, and viscous forces). Table 2 presents the applicable dimensionless force ratios and their critical values. The critical value is that value at which both forces are of equal importance.

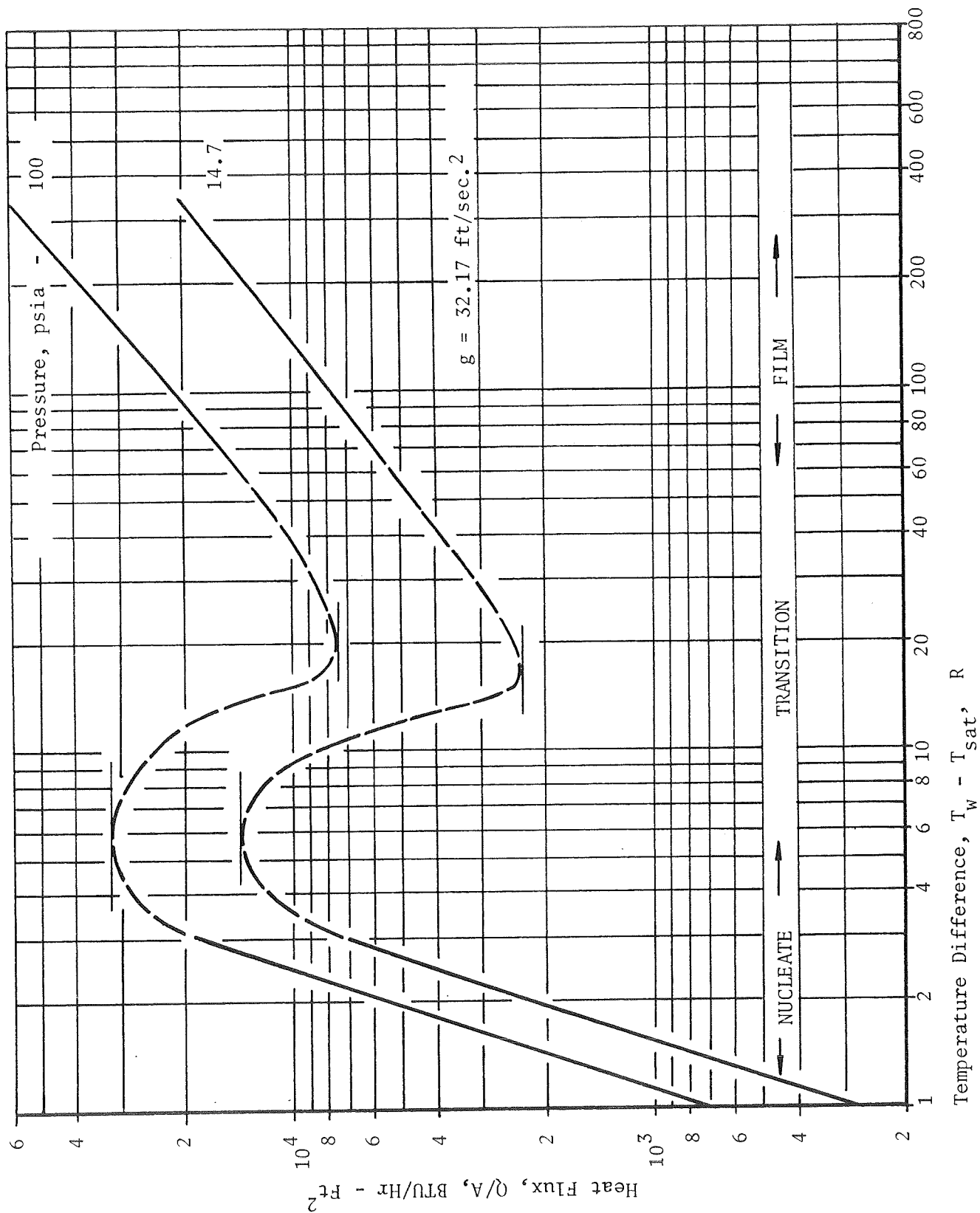


Figure 4. Effect of Pressure on LH₂ Pool Boiling

TABLE 2

APPLICABLE DIMENSIONLESS FORCE RATIOS

<u>Name</u>	<u>Force Ratio</u>	<u>Definition</u>	<u>Critical Value</u>
Bond Number, Bo	$= \frac{\text{Gravitational}}{\text{Surface Tension}}$	$= \frac{g(\rho_L - \rho_V)L^2}{g_c \sigma}$	1
Froude Number, Fr	$= \frac{\text{Inertial}}{\text{Gravitational}}$	$= \frac{\rho V^2}{g(\rho_L - \rho_V)L}$	1
Grashof Number, Gr	$= \frac{\text{Viscous}}{\text{Gravitational}}$	$= \frac{\mu V}{g(\rho_L - \rho_V)L^2}$	10^{-3}
Weber Number, W	$= \frac{\text{Inertial}}{\text{Surface Tension}}$	$= \frac{\rho V^2 L}{g_c \sigma}$	1
Reynolds Number, Re	$= \frac{\text{Inertial}}{\text{Viscous}}$	$= \frac{\rho VL}{\mu}$	10^{-3}

In each of the above terms, L is a characteristic length of the particular surface and V is a characteristic velocity. For instance, within the Froude number, L would be the radius of a representative vapor bubble and V would be the time rate of increase of bubble radius.

For any particular system in which the force ratio deviates greatly from the critical value, one of the forces will become dominant. Figure 5 illustrates this fact for the Bond number. It should be noted that the surface tension may provide the predominant force, even at standard gravity, if the radius is extremely small (capillary action). Similar reasoning can be applied to the remaining force ratios.

The usual dimensionless parameters utilized in heat transfer analysis are presented in Table 3.

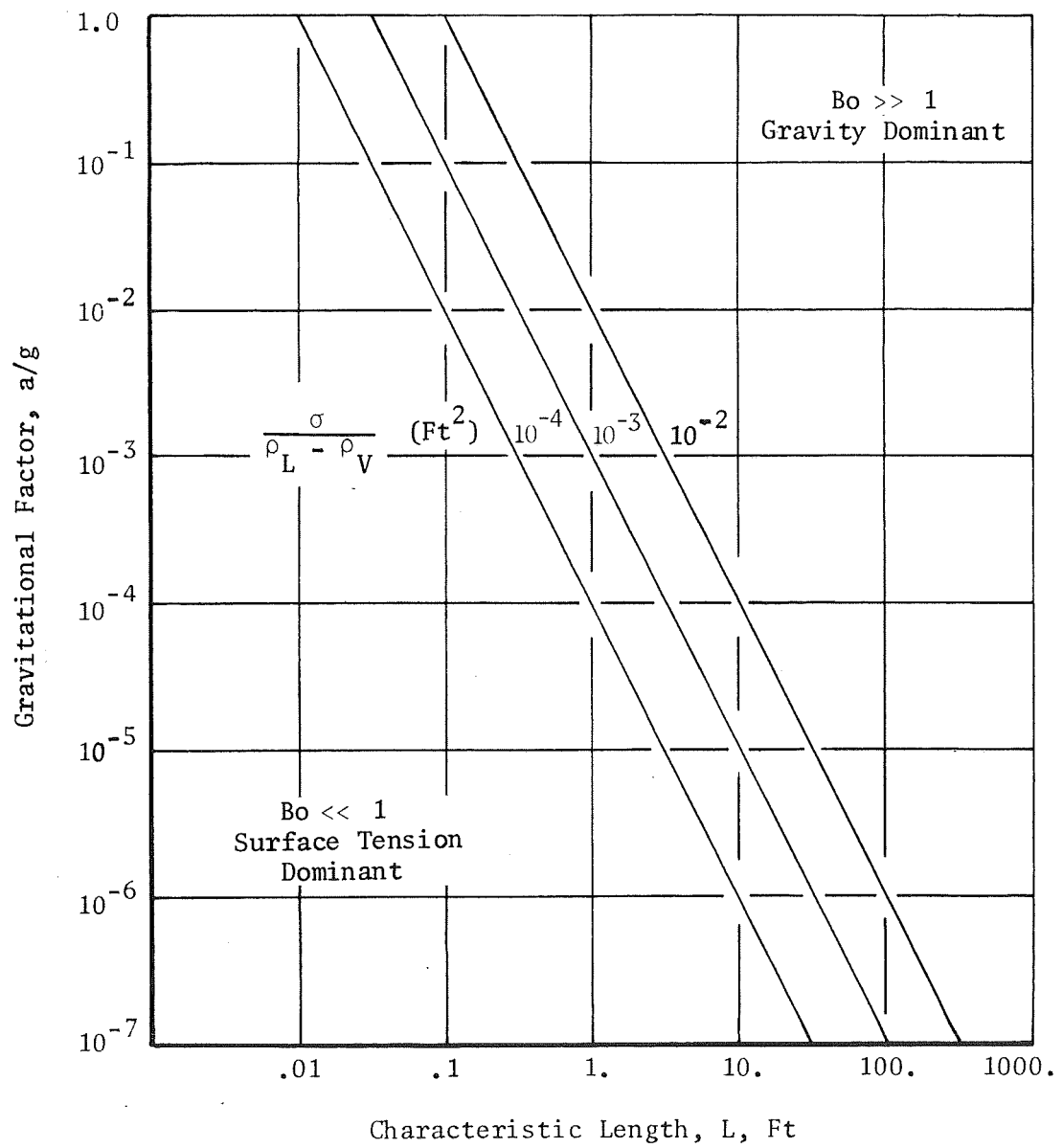


Figure 5. Hydrostatic Force Regimes

TABLE 3

HEAT TRANSFER DIMENSIONLESS PARAMETERS

<u>Name</u>	<u>Ratio</u>	<u>Definition</u>
Nusselt Number	$= \frac{\text{Convective Heat Capacity}}{\text{Conductive Heat Capacity}}$	$= \frac{h D}{k}$
Prandtl Number	$= \frac{\text{Kinematic Viscosity}}{\text{Thermal Diffusivity}}$	$= \frac{C_p \mu}{k}$
Stanton Number	$= \frac{\text{Nusselt No.}}{(\text{Prandtl No.})(\text{Reynolds No.})}$	$= \frac{h}{\rho C_p V}$

Reduction of the previously derived boiling heat transfer equations into nondimensional form will provide a better physical interpretation of the phenomena. Indeed, the rather irregular effect of gravity throughout the pool boiling process may be explained from a knowledge of the force ratios, and it is the magnitudes of all these parameters which govern the heat transfer rates of a particular fluid system. By applying these parameters to Eq. 1 through 4, the following relationships are obtained:

• Nucleate Boiling

$$Nu_L = C_1 \frac{Fr^{-1/2} We^{1/2}}{Pr_L^{4.1}} \left\{ \frac{C_{pL} (T_W - T_{sat})}{\lambda} \right\}^2 \quad (5)$$

• Peak Heat Flux

$$Nu_L = \frac{\pi}{24} Bo^{1/4} Pr_L Re \left\{ \frac{\lambda}{C_{pL} (T_W - T_{sat})} \right\} \left(\frac{\rho_L + \rho_v}{\rho_L} \right)^{1/2} \quad (6)$$

• Minimum Heat Flux

$$Nu_L = 0.09 Bo^{1/4} Pr_L Re_b We^{1/2} \left\{ \frac{\lambda}{C_{pL} (T_W - T_{sat})} \right\} \left(\frac{\rho_{vf}}{\rho_L + \rho_v} \right)^{1/2} \quad (7)$$

where $Re_b = \frac{\sqrt{\rho_v \rho_{vf}} V L}{\mu_L}$

• Film Boiling

$$Nu_{vf} = 0.62 Bo^{1/4} We^{-1/4} Pr_{vf}^{1/4} Re_{vf}^{1/2} \left\{ \frac{\lambda_o}{C_{p_{vf}} (T_W - T_{sat})} \right\}^{1/4} \quad (8)$$

Heat transfer coefficients may be expressed in terms of Stanton number through the relationship:

$$Nu = St \cdot Re \cdot Pr$$

Further simplifications may be made by realizing,

$$We = Fr \cdot Bo$$

however, gravity effects can best be explained with the above forms. The subscripts, L, v, and vf signify, respectively, the liquid, vapor, and vapor-film states.

The basic premise behind dimensional analysis requires each of the parameters in the above equations to be at or near its critical value. Non-uniformities in these relationships is indicative of the fact that they were derived independently by different researchers. Should any parameter differ greatly from its critical value, then the corresponding equation must be rederived. Inspection of Eq. 5 through 8 reveals that the nucleate boiling regime was considered independent of viscous forces and the film

boiling regime independent of surface tension forces. While this may have been justified for the particular system used for the derivation of these forms, care must be taken to evaluate each parameter, and thus determine the predominant forces, when investigating a new situation.

GRAVITY EFFECTS

Referring to Eq. 5 through 8, the heat flux is found to be proportional to $g^{1/2} (Fr^{-1/2})$ for the nucleate boiling regime whereas the maximum and minimum heat fluxes, as well as the film boiling heat flux, are all proportional to $g^{1/4} (Bo^{1/4})$. However, the results of experimental data indicate that the nucleate boiling heat flux (and transition regime) is independent of the local gravitational field, but justifies the remaining analytical predictions.

Experimental data for LH_2 is rather limited; however, Fig. 6 (Ref. 4) illustrates the insensitiveness of heat flux with gravity during nucleate boiling. This can be explained by an investigation of the forces acting on an individual bubble. The ratio of inertial forces to gravitational forces (Froude number) becomes a criterion for the controlling force in bubble growth. When the Froude number is of the order of 1, these two forces have approximately equal value. Should this ratio be greater than unity, then the inertia forces may be expected to predominate. The opposite will be true for Froude numbers less than unity. Reference 5 has indicated that, for cryogenic liquids at 1 atmosphere and 1 g, the Froude number is on the order of 1500. Hence, even at standard earth gravity, the predominant force in nucleate boiling is an inertial force, and buoyant forces are insignificant. This fact would suggest that Eq. 1 and 5 be re-derived for the present problem, independently of gravitational forces, for the boiling process is already operating in an effective zero-gravity atmosphere.

Experimental data for the remaining boiling phenomena are limited to LN_2 . The heat flux dependence on $g^{1/4}$ for both the peak and minimum heat flux values is justified by Lewis et al. (Ref. 3). However, within the film

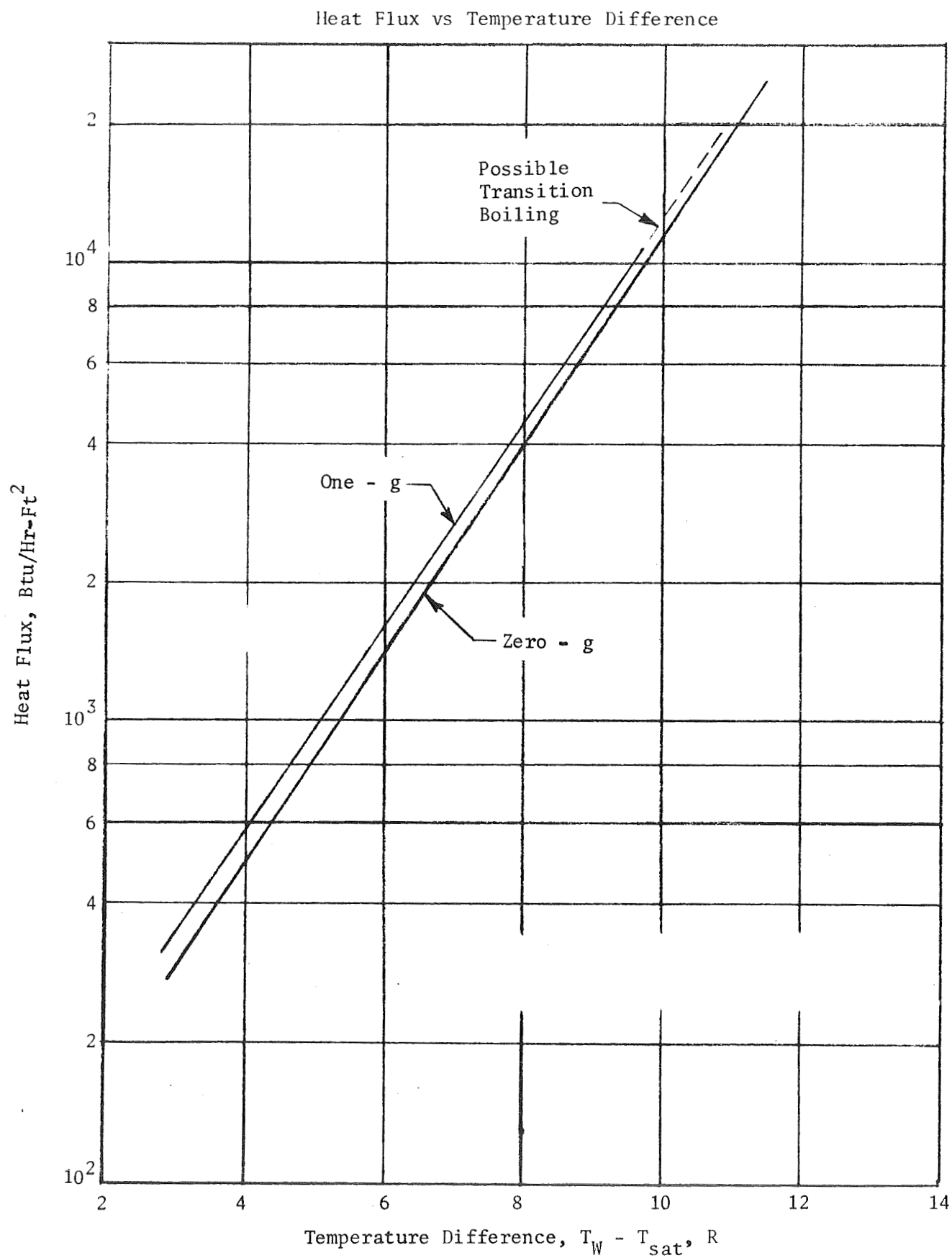


Figure 6. Effect of Gravity on Liquid Hydrogen Nucleate Boiling (Experimental)

boiling regime, they have found Q/A to be proportional to either $g^{1/3}$ or $g^{2/9}$, depending on the geometry. As was noted earlier, the correlation for film boiling was developed for horizontal cylinders with a laminar vapor film. Therefore, for the sake of continuity, the $1/4$ power dependency was retained with consideration that each particular case may have to be investigated separately.

Perhaps the most significant result achieved by Lewis et al. during their experiments was the correlation of $(\Delta T_{\text{sat}})_{\text{max}} \propto (a/g)^{1/4}$ (i.e., the temperature difference at which the peak nucleate boiling heat flux occurs will decrease with a decrease in the local acceleration).

Figure 7 (Ref. 5) represents the entire experimental pool boiling curve for saturated LN_2 at 1 atmosphere and at local accelerations of 1 and 0.02 g. Figure 8 represents the entire analytical pool boiling curve for saturated LH_2 at 1 atmosphere and at local accelerations of 1 and 0.004 g. A qualitative comparison of these two figures indicates that the developed analytical correlations for LH_2 are representative of the actual case.

The value of $(a/g) = 0.004$ was chosen because it will result in a Bond number of 1 at an $L = 1$ inch. This value of L is characteristic of the pump mean hydraulic diameter* for a thrust level of 40,000 pounds as displayed in Ref. 6. Hence, at this value of (a/g) , the surface tension and gravitational forces are of the same order, and further reductions in gravity will have little effect on the heat flux. Variations in the mean hydraulic diameter will result in different critical values of (a/g) .

FORCED CONVECTION

Although general theoretical equations for LH_2 forced convection saturated boiling have not yet been developed, the relatively simple method of superposition can be used:

$$h_{\text{overall}} = h_{\text{forced convection}} + h_{\text{pool boiling}}$$

* Flow through a blade passage area

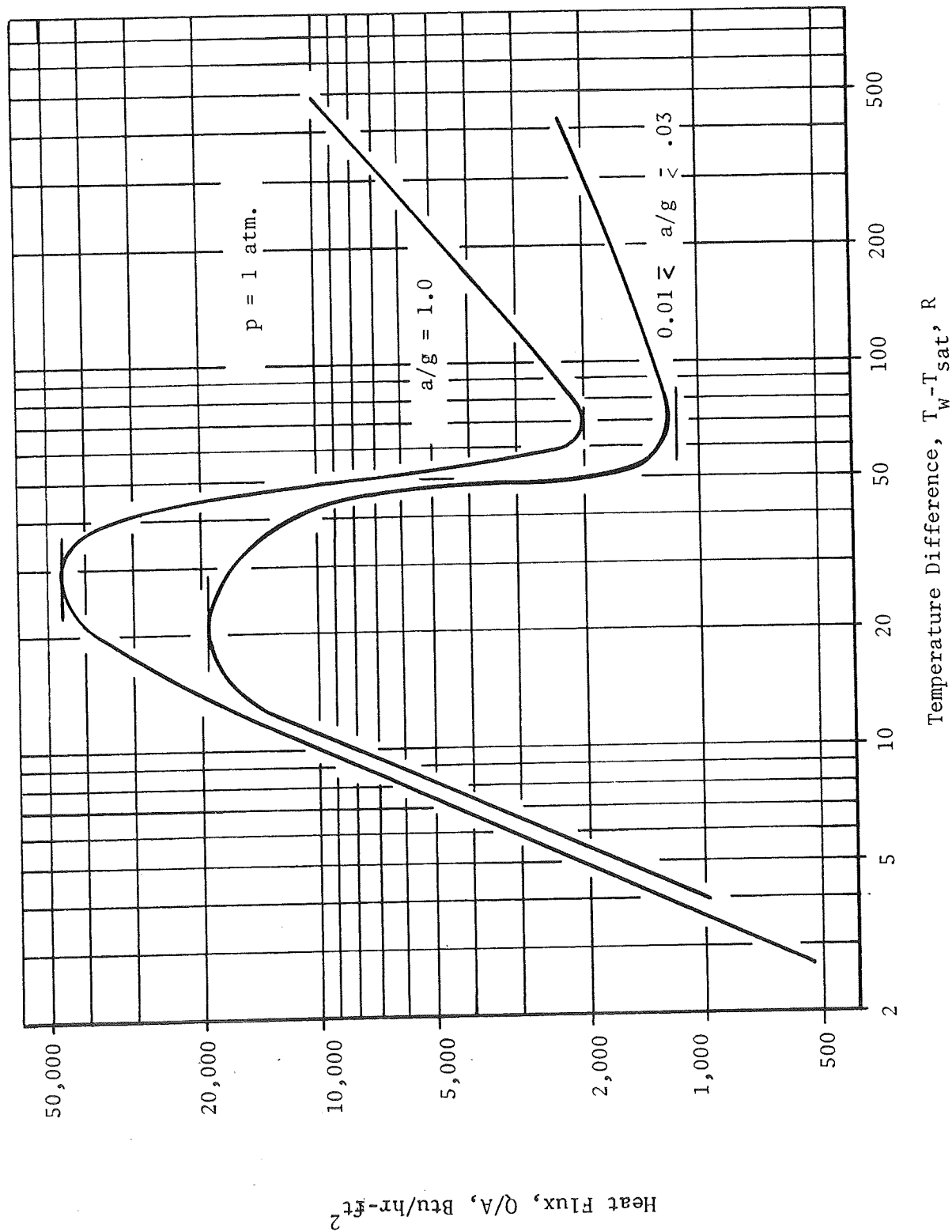


Fig. 7. Experimental Gravity Effect on Liquid Nitrogen Pool Boiling

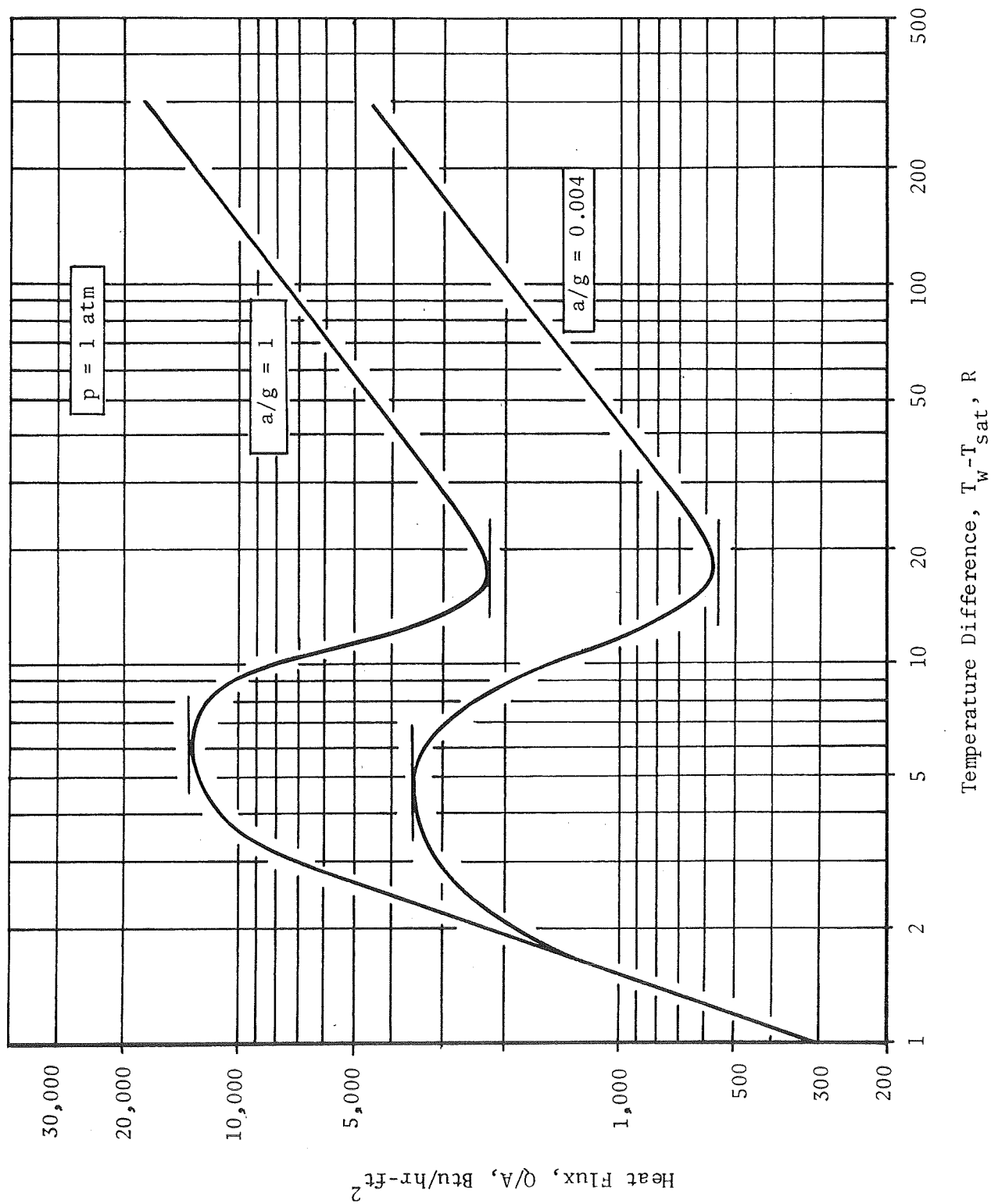


Figure 8. Theoretical Gravity Effect on Liquid Hydrogen Pool Boiling

Therefore, if forced convection heat transfer is independent of variations in the gravity field, the change in heat flux experienced at reduced gravities will be solely attributed to the decrease in heat flux within the pool boiling regime.

$$\Delta(Q/A)_{\text{total}} = \Delta(Q/A)_{\text{pool boiling}}$$

This relationship indicates that even if experimental data cannot be correlated at standard gravity, the resulting heat flux at reduced gravities can be predicted by a knowledge of the pool boiling characteristics alone.

The actual regions of gravity dependence within forced convection heat transfer can be found by considering the Grashof number for any particular case. A representation similar to that of Fig. 5 can be developed and the influence of viscous forces and gravitational forces can be determined. Inherent in assuming a superposition of film coefficients is that the predominant forces of forced convection and the predominant forces of pool boiling are mutually exclusive. For instance, any drag force that might be induced on a vapor bubble by a flowing liquid is neglected. A more accurate representation of forced convection saturated boiling must consider the interrelationship of all forces pertinent to each of the possible flow conditions.

EFFECTS OF THERMAL VARIABLES ON LH₂ PUMP CHILLDOWN

In previous analytical study (Ref. 7), it was shown that a thin layer of very low thermal conductivity material can effectively reduce the chilldown time of a pump. Also, a reduction in total hydrogen requirements for chilldown of the pump was shown. Analytical chilldown analyses were conducted for typical materials used for the fabrication of LH₂ turbopumps. The analyses included metals for heat transfer coefficient boundary conditions of pool boiling under zero and unity gravity and forced convection at LH₂ mass velocities of 2 and 5 lb/in.²-sec.

Analytical chilldown investigations were conducted with coated and uncoated Tens-50 aluminum, titanium, and K-monel materials which represent the Mark 15 and Mark 29 LH₂ pump parts.

The heat transfer coefficient boundary conditions considered in this analytical study were:

1. Pool boiling under zero gravity
2. Pool boiling under a unity gravity
3. Forced convection at LH_2 mass velocities of $2 \text{ lb/in.}^2\text{-sec}$
4. Forced convection at LH_2 mass velocities of $5 \text{ lb/in.}^2\text{-sec}$

The following sections describe the results of the computer study for both coated and uncoated materials.

Chiltdown of Materials (Uncoated)

Analytical chiltdown studies were carried out using three basic metals that are most commonly utilized in the manufacture of LH_2 pumps. These metals were Tens-50 aluminum, titanium, and K-monel. A small model representing a segment of the hydrogen pump was selected and was broken down into smaller nodal pieces. This model and its nodal breakdown is shown on Fig. 9. The model was prepared for an existing thermal analyzer computing program (DEAP). The accuracy of the results depended on the input data; therefore, the specific heat and the thermal conductivity of the metals used in these analyses were input to the program in the form of tables covering the entire range of temperature variations. It was assumed for the study that the metal was initially at 70 F (530 R).

The chiltdown analyses were carried out assuming four different conditions for the coolant hydrogen:

1. Pool boiling under zero-gravity condition
2. Pool boiling under a unity-gravity condition
3. Forced convection at a mass flux of $2 \text{ lb/in.}^2\text{-sec}$
4. Forced convection at a mass flux of $5 \text{ lb/in.}^2\text{-sec}$

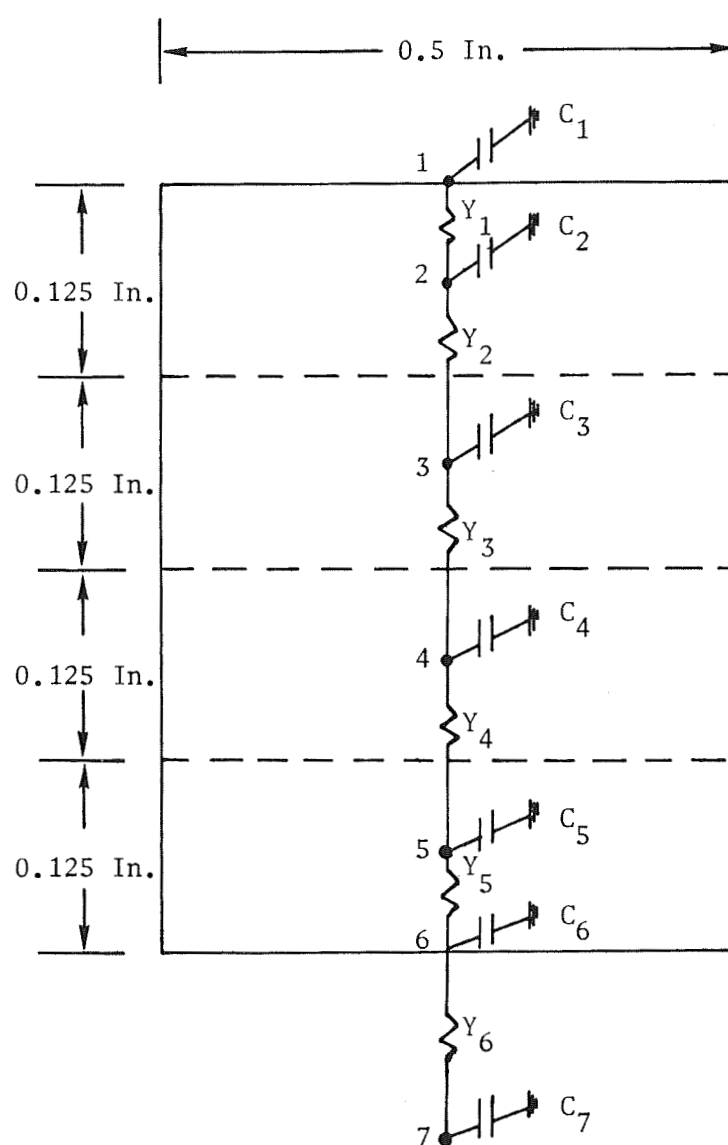


Figure 9. Simple Model of Uncoated Metal Showing Nodal Breakdown for Chilldown Study

The determination of the hydrogen heat transfer coefficients for zero-gravity and unity-gravity conditions was based on the data of Fig. 8. Equation 25 of Ref. 7 (given below) was utilized to compute the hydrogen heat transfer coefficient for the forced flow condition with boiling:

$$h_c = 0.00065 G^{0.5} \quad (9)$$

The results are plotted on Fig. 10 as heat flux versus temperature difference between the wall and the hydrogen-saturation temperatures. Equation 9 is valid for a temperature difference ($T_W - T_{sat}$) of about 20 to 500 R. Below a temperature difference of 20 R, the results of Eq. 9 are lower than the transition and nucleate boiling region. Consequently, below a ΔT of about 20 R, the heat fluxes found through the use of Eq. 9 (dashed section of Fig. 10), which was added to the heat fluxes under the unity gravity condition, was used to determine the heat transfer coefficient. Figure 10 shows the heat flux versus temperature difference for the conditions used in this chilldown analysis. Also, the experimental results of Ref. 8, which are for a mass flux of about 0.586 lb/in.²-sec, are shown on Fig. 10 for comparison purposes. A fair agreement exists between the data of Ref. 8 and the values obtained from Eq. 9. The results of Fig. 10 were transformed into heat transfer coefficients and were inputted into the program in a tabulated form (heat transfer coefficient versus $T_W - T_{sat}$) for all conditions analyzed. Figure 11 shows heat transfer coefficients versus ΔT for various conditions.

The computer program was run long enough so that the wetted surface temperature dropped below -400 F for most of the cases. The temperature of hydrogen was kept constant at -423 F representing all chilldown condition except very low flow conditions. Listed in Table 4 are some of the pertinent data input into the thermal analyzer program.

When the resistance ratios (K/WC_p) of these metals were compared, it was expected that the surface temperature of titanium would drop much faster than that of aluminum and K-monel. However, due to the variation of specific heat and thermal conductivity with temperature, the surface

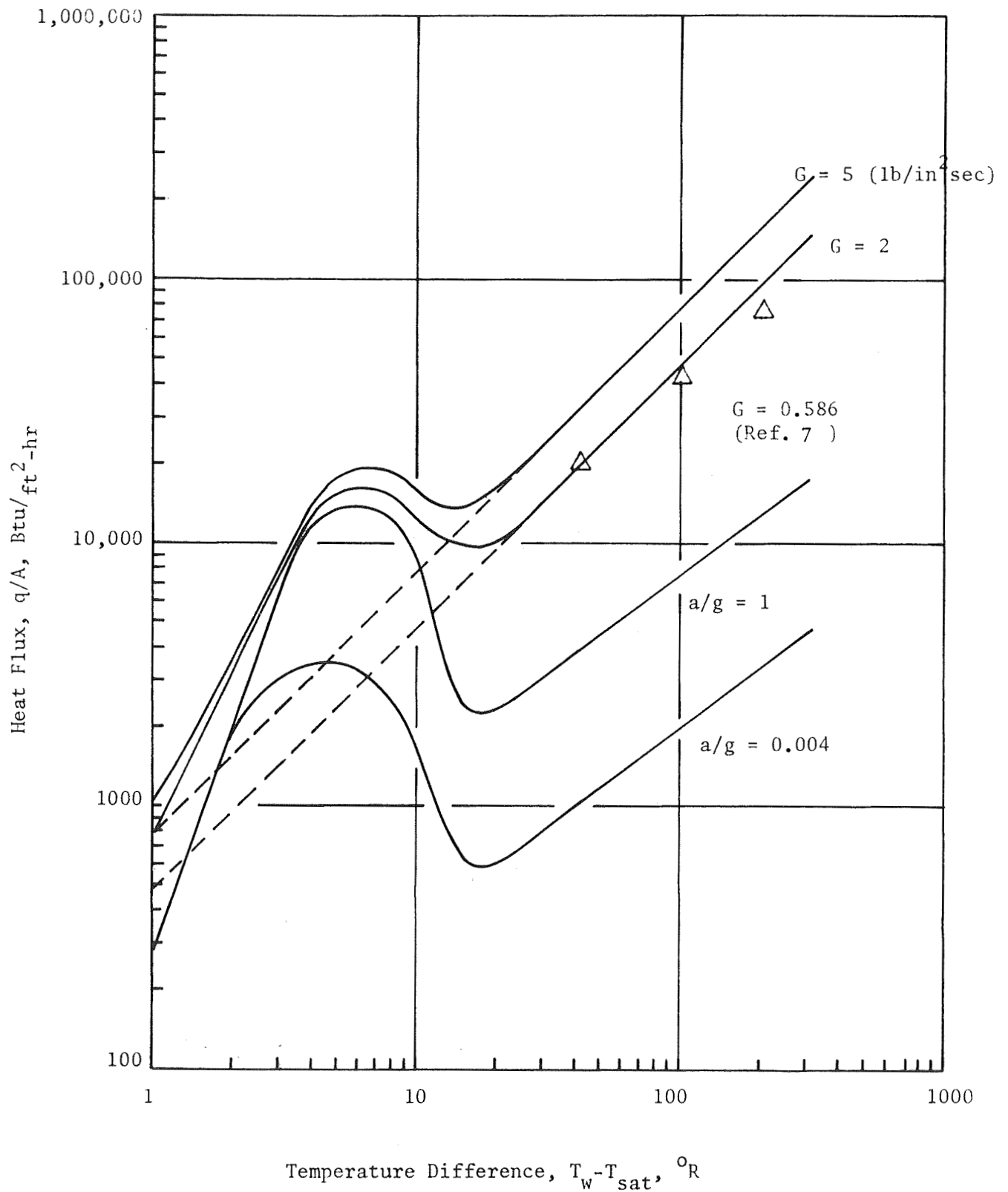


Figure 10. Effect of Gravity and Forced Convection on Liquid Hydrogen Pool Boiling

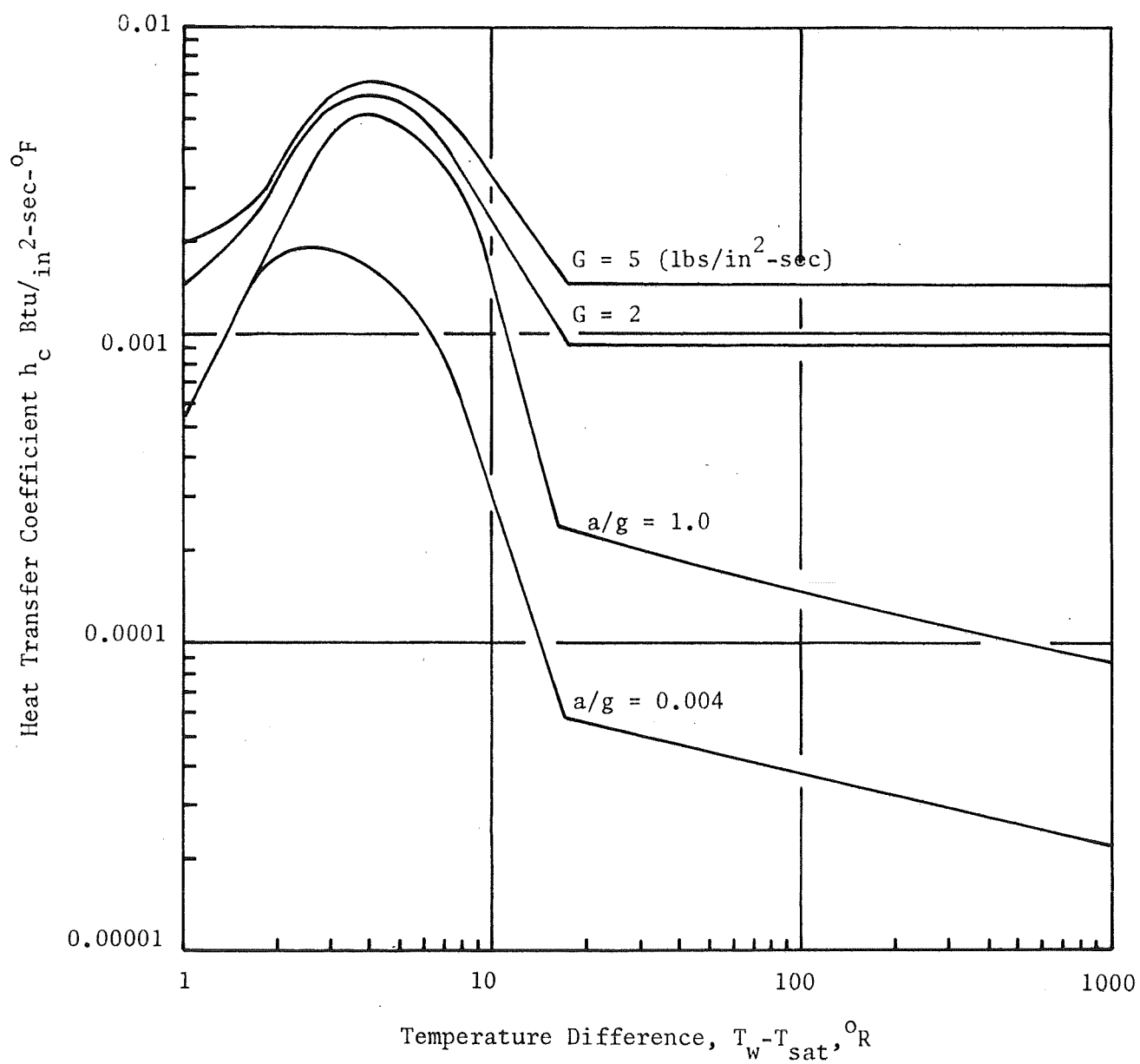


Figure 11. Effect of Gravity and Forced Convection on Hydrogen Heat Transfer Coefficients

TABLE 4

COMPARISON OF AVERAGE CAPACITANCES AND AVERAGE THERMAL
CONDUCTIVITIES OF THE METAL AT -24 F

Metal	WC_p , (Btu/F)	K , (Btu/in.-sec-F)	K/WC_p , (in./sec)
Aluminum	0.00196	0.00102	0.521
Titanium	0.001675	0.0000696	0.0416
K-monel	0.00272	0.000164	0.0602

temperature of Al and Ti remained fairly close together for low values of heat transfer coefficients. At higher values of heat transfer coefficient, the difference in surface temperature became prominent. Again the effect of physical property variation with temperature caused the cooling curves for aluminum and titanium to cross one another for high values of heat transfer coefficients.

Pool Boiling Chillover Under Zero-Gravity Conditions. This condition may exist when a vehicle is in orbit around the earth or during space missions. Before an engine starts, the warm hydrogen pump must be preconditioned to ensure a smooth engine start. If the pump was permitted to be filled with hydrogen without flow (dump case), the heat will be transferred from the warm surfaces of the pump into the nonflowing hydrogen by means of the pool boiling process. The reduced gravity condition caused a reduction in the heat flux. The results of chillover analyses under this condition indicate that to achieve a surface temperature of about -405 F for uncoated Tens-50 aluminum, titanium, and K-monel, chillover times of about 705, 662, and 1100 seconds, respectively, are required. These times are very high and can be reduced if forced convection is applied. Figure 12 depicts the wetted surface temperature versus chillover time for the model cases analyzed.

Pool Boiling Chillover Under a Unity-Gravity Condition. This condition is prevalent during ground hydrogen pump preconditioning when the pump is merely filled with boiling LH_2 . As shown on Fig. 10, the heat fluxes and,

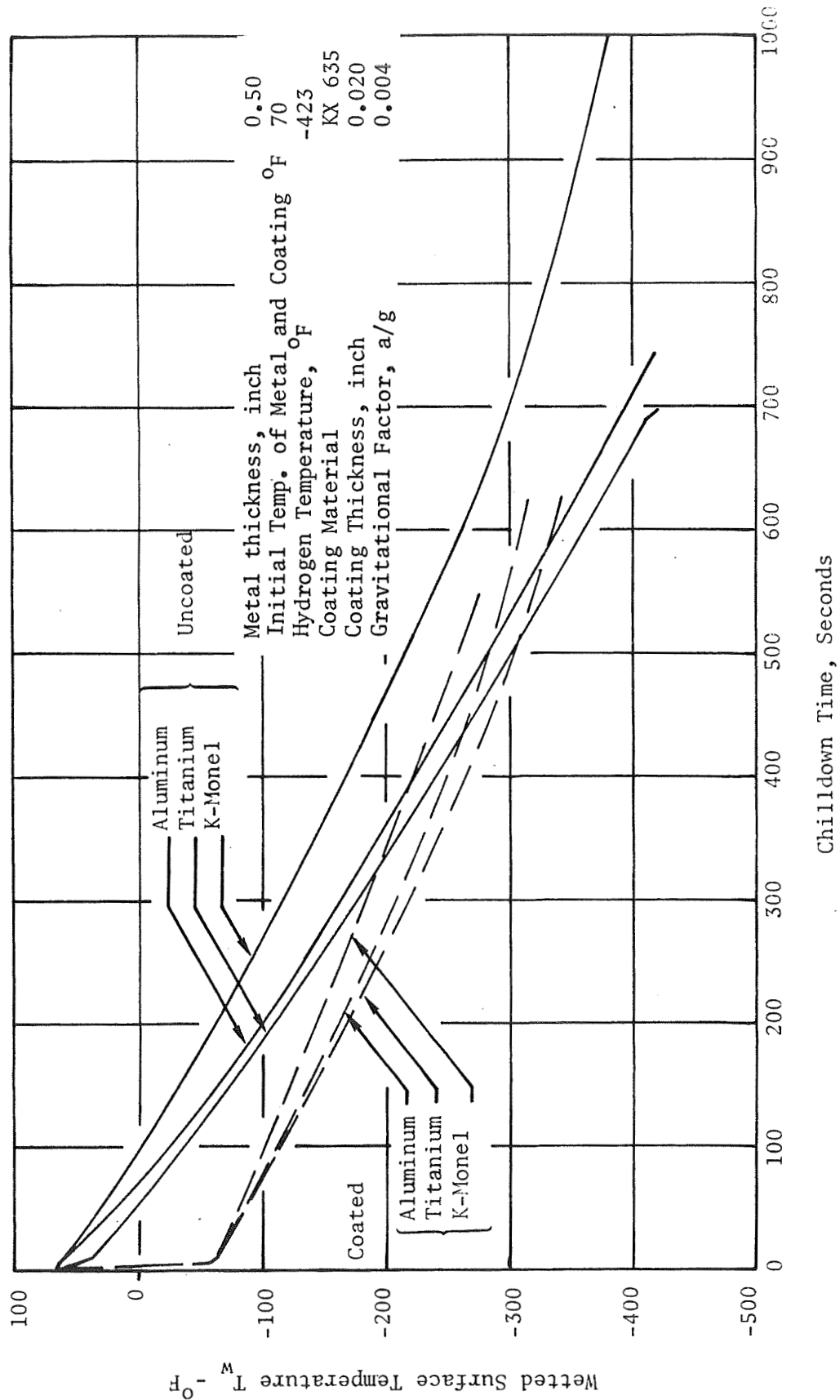


Figure 12. Wetted Surface Temperature vs Chilledown Time under Pool Boiling
Condition Near Zero - g

consequently, the heat transfer coefficients (Fig. 11) under this condition are higher than those of the zero-gravity condition. These heat transfer coefficients were applied to the model and the wetted surface temperature as a function of chilldown time was determined for the three materials under investigation. Figure 13 depicts the results under this condition and shows the required chilldown times for the achievement of a wetted surface temperature of about -405 F. The required chilldown times are about 190, 205, and 315 seconds for uncoated aluminum, titanium, and K-monel, respectively. This is a considerable improvement compared to the pool boiling under zero-gravity conditions. However, the required chilldown time is still high and further reductions are desired.

Forced Convection Chilldown at Mass Flux of 2 lb/in.²-sec. Under forced convection, the resistance of the transfer of heat from the warm surfaces to the hydrogen was much lower than that during the two previous processes. This means that under forced convection, the heat transfer coefficient was much higher. The average heat transfer coefficient between a ΔT of 20 to 1000 R was about 0.000033, 0.000166, and 0.00093 Btu/in.²-sec-F for the zero gravity, unity gravity, and a mass flux of 2 lb/in.²-sec condition, respectively. Therefore, the wetted surface temperature decreased more rapidly under the forced convection than the two previously conditions. The achievement of a surface temperature of about -405 F is accomplished in about 30, 65, and 74 seconds for the uncoated aluminum, titanium, and K-monel, respectively. The results of the chilldown study under this condition are plotted on Fig. 14.

Forced Convection Chilldown at a Mass Flux of 5 lb/in.²-sec. As the hydrogen mass flux was increased, the heat transfer coefficient was also increased, and a reduction in the chilldown time of the metal was obtained. The achievement of a surface temperature of about -405 F was attained in approximately 20, 50, and 60 seconds for uncoated aluminum, titanium, and K-monel, respectively.

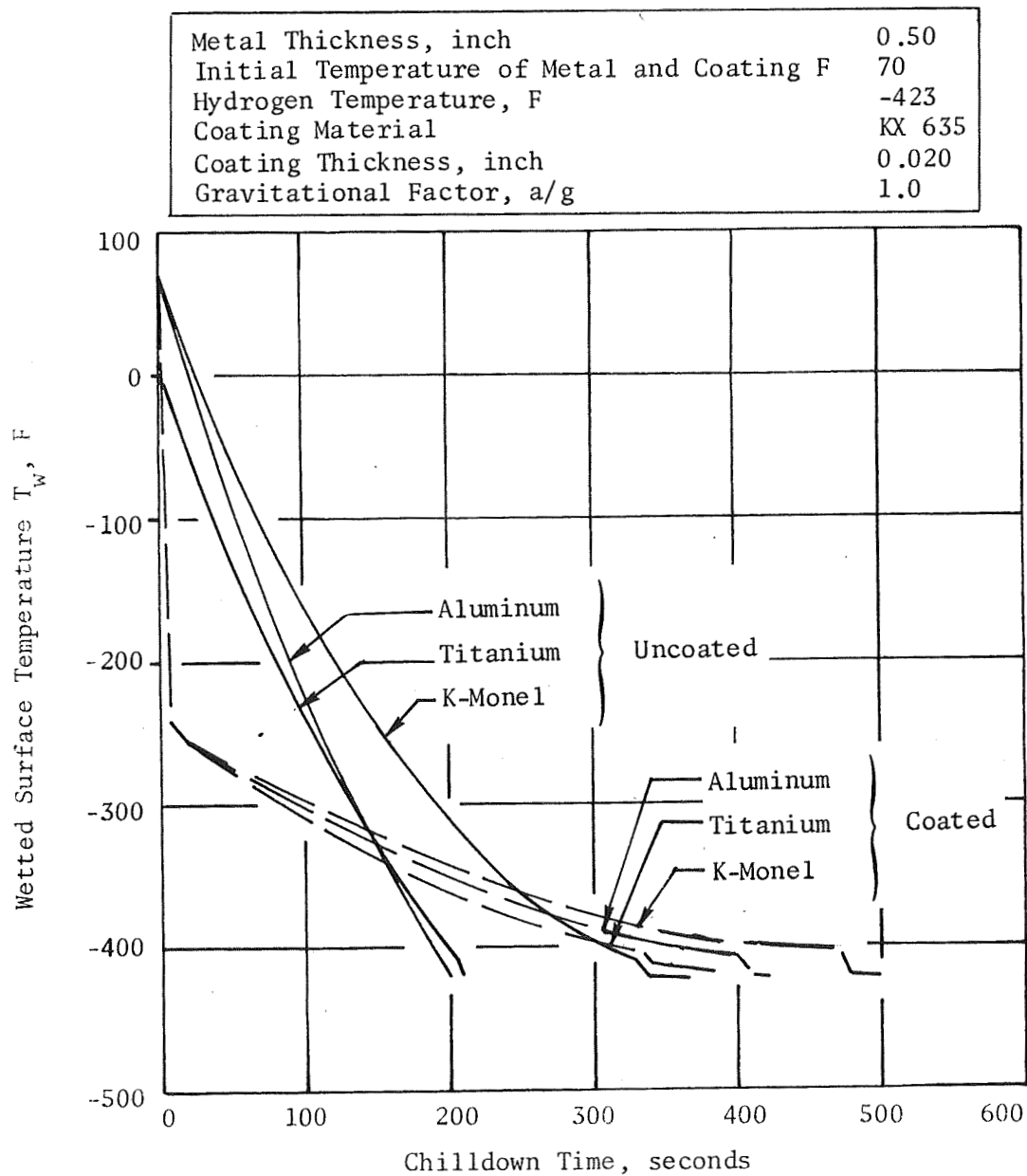


Figure 13. Wetted Surface Temperature vs Chilloid Time Under Pool Boiling Condition and Unity Gravity

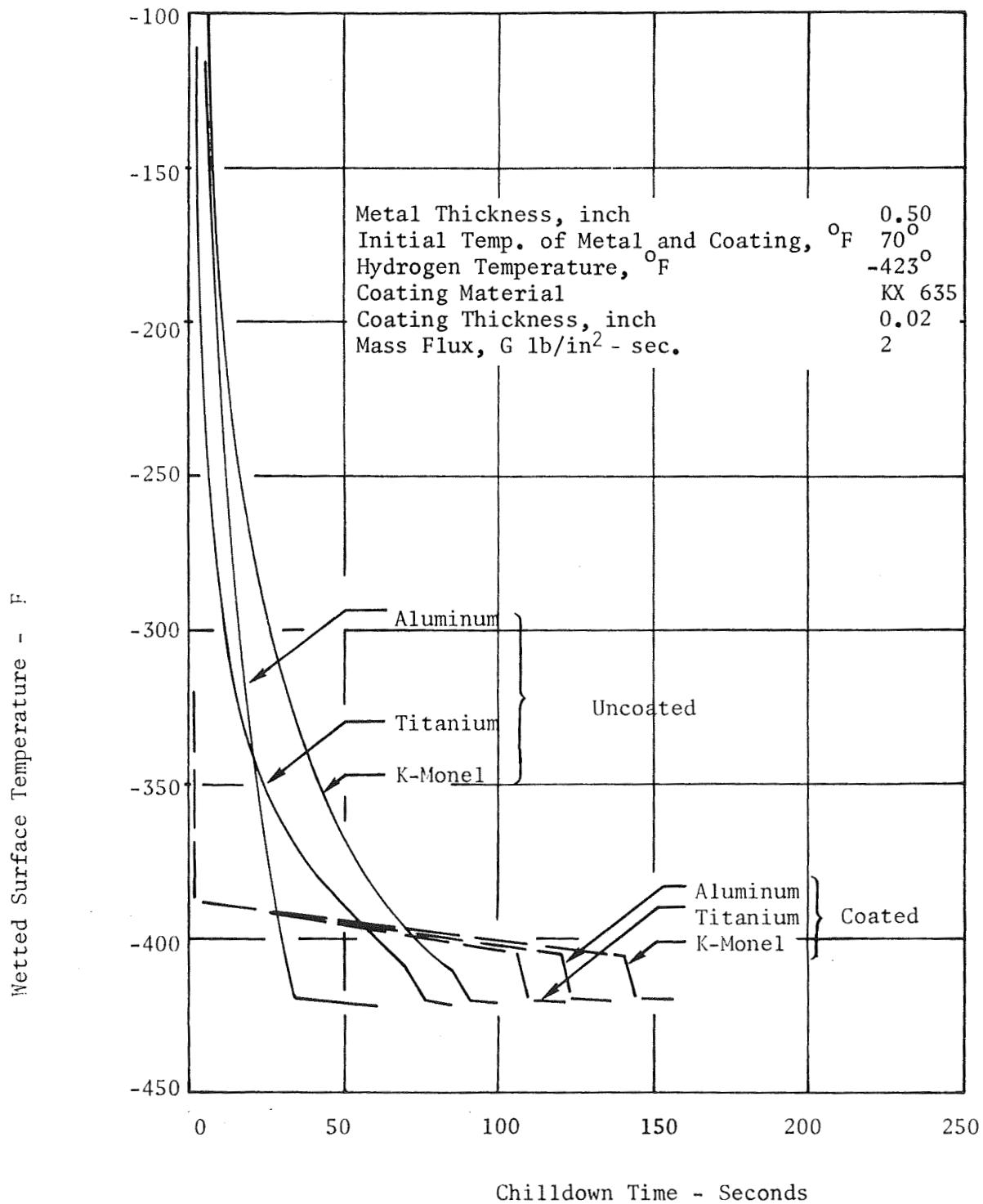


Figure 14. Wetted Surface Temperature vs Chardown Time Under Forced Convection Condition of $G = 2 \text{ lb/in}^2 \text{ Sec.}$

Figure 15 depicts the wetted surface temperature versus chilldown time for this condition. It was noticed (Fig. 12 through 15) that the cooling curves of the uncoated aluminum and titanium cross one another. Based on the average values of WC_p and K/WC_p (given in Table 4), the titanium surface temperature should be lower than that of aluminum at all times. The crossing of the two cooldown curves occurred because the surface temperature of titanium initially decreased very rapidly but because of the low thermal conductivity, the temperature of the main body remained fairly unchanged (Fig. 16). At low surface temperatures, the heat flux and consequently the rate of heat removal was low; therefore, a long chilldown time was required. In the case of aluminum (very high thermal conductivity), the difference between the surface and back side temperatures is small (Fig. 17) and the entire body cooled down at a nearly uniform temperature. Because of the higher surface temperature, the heat flux and the heat removal rate was higher for aluminum. Therefore, a shorter chilldown time was required for Tens-50 aluminum than titanium for very low surface temperatures. For the comparison purposes, a plot of \bar{h}/k versus chilldown time was prepared for the three metals under investigation (Fig. 18). Again average values of \bar{h} and k was used to construct Fig. 18. It is seen that for a given value of \bar{h} the required chilldown time was less for the Tens-50 aluminum to reach the desired surface temperature.

For comparison purposes, Table 4 was prepared to indicate the average values (at -247 F) of WC_p and thermal conductivity. Tables 5 and 6 show the surface and backside temperature of the specimen at various times. At low values of heat transfer coefficient, the chilldown time was much longer and the thermal gradient was much smaller (Table 5) than for the case of high heat transfer coefficient (Table 6).

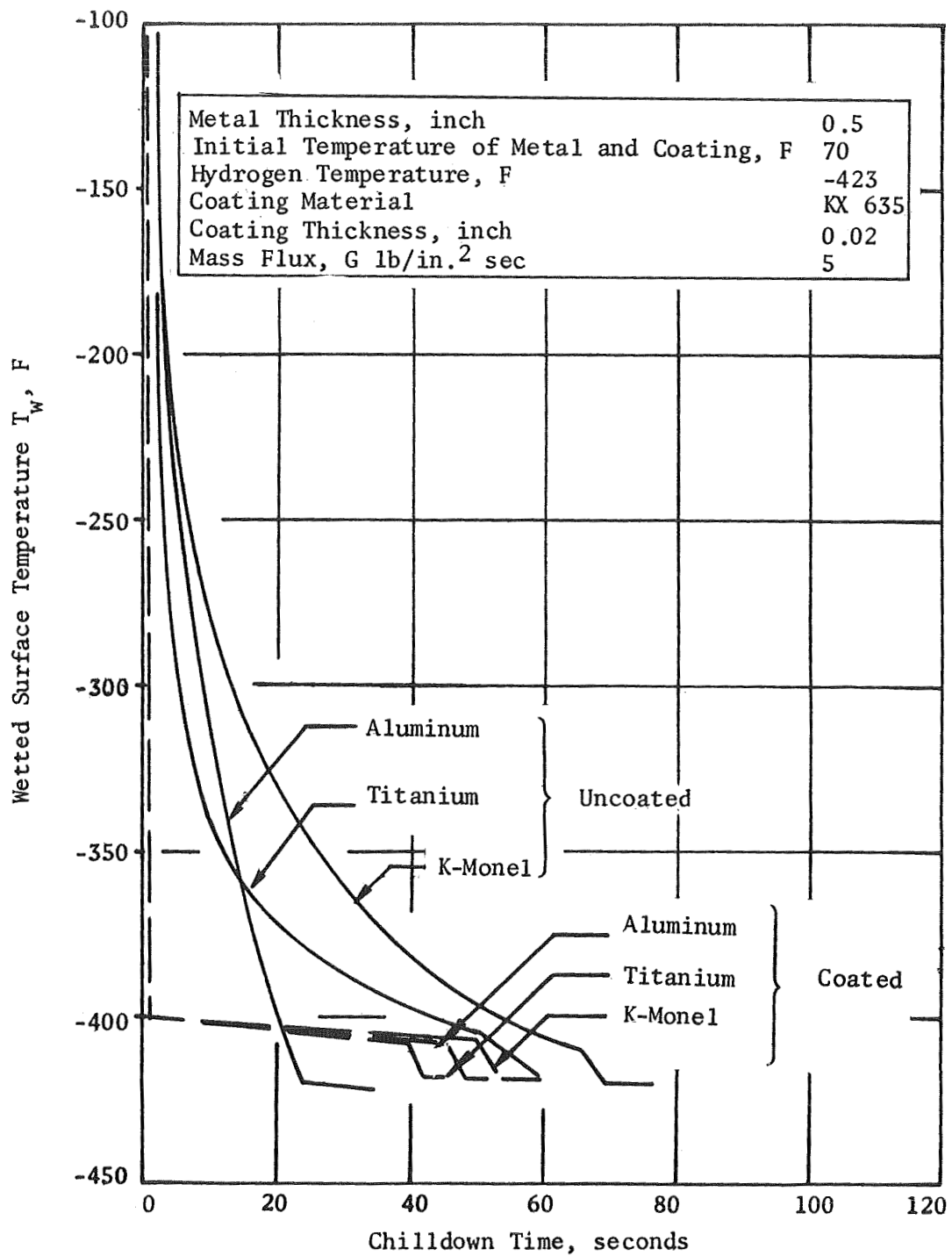


Figure 15. Wetted Surface Temperature vs Chilloid Time Under Forced Convection Condition of $G = 5 \text{ lb/in.}^2 \text{ sec}$

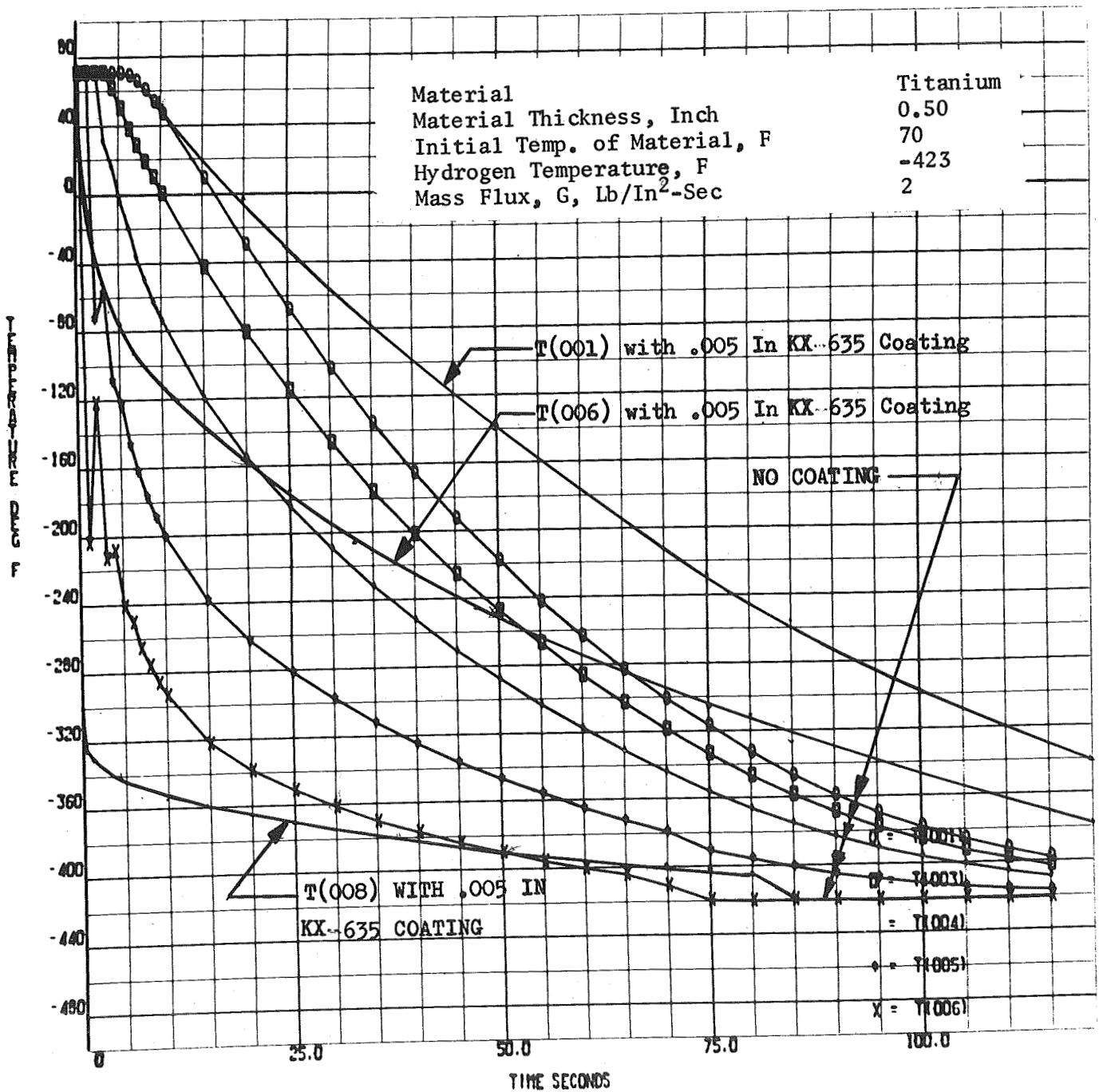


Figure 16. Temperature vs Chillumdown Time for Titanium Under Forced Convection Condition ($G = 2 \text{ Lbs/In.}^2 \text{ Second}$)

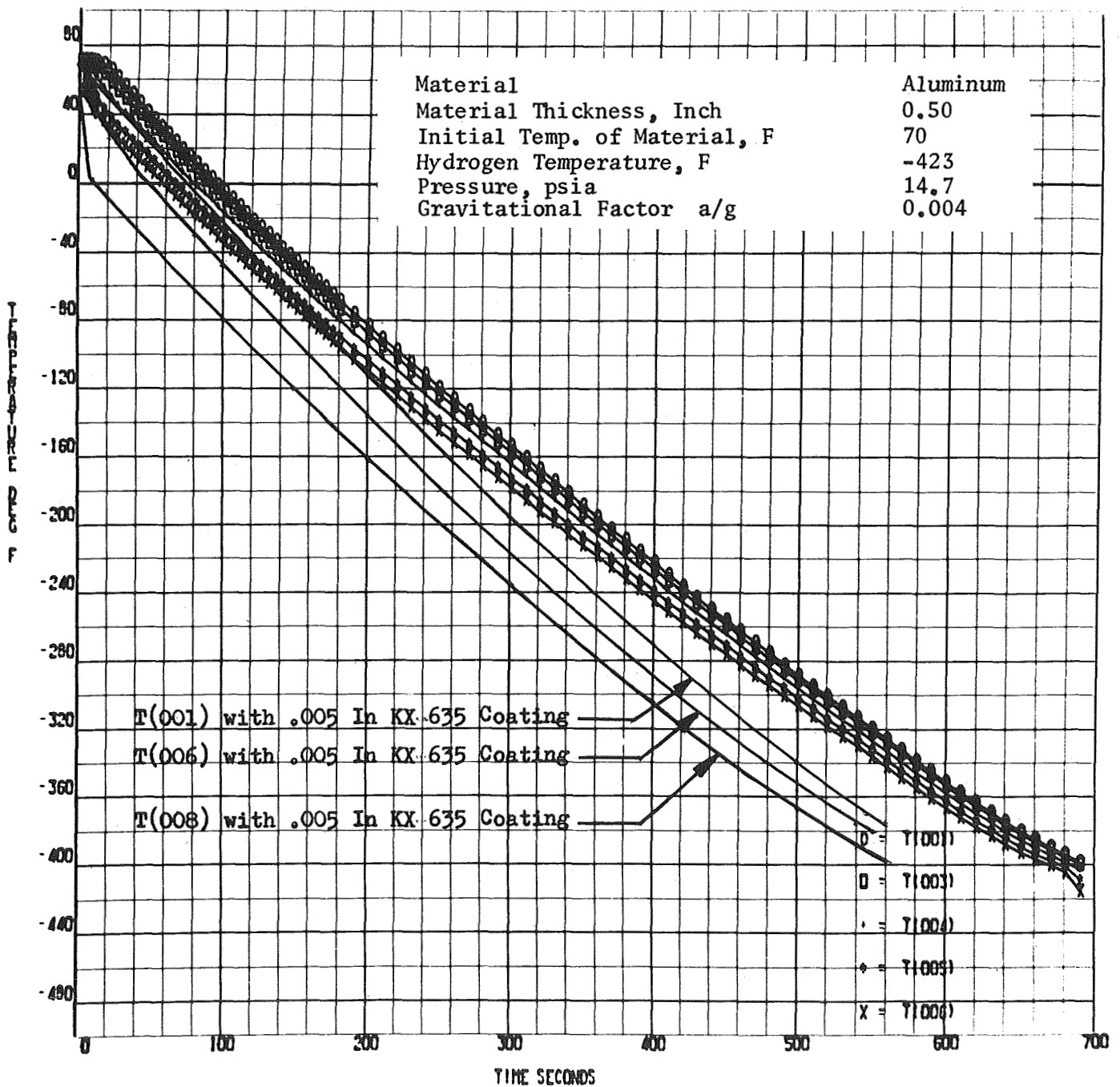


Figure 17. Temperature vs Chillo-down Time for Coated and Uncoated Aluminum Under Pool Boiling Condition Near Zero Gravity ($\frac{a}{g} = 0.004$)

Initial Metal Temperature, °F 70
 Initial Hydrogen Temperature, °F -423

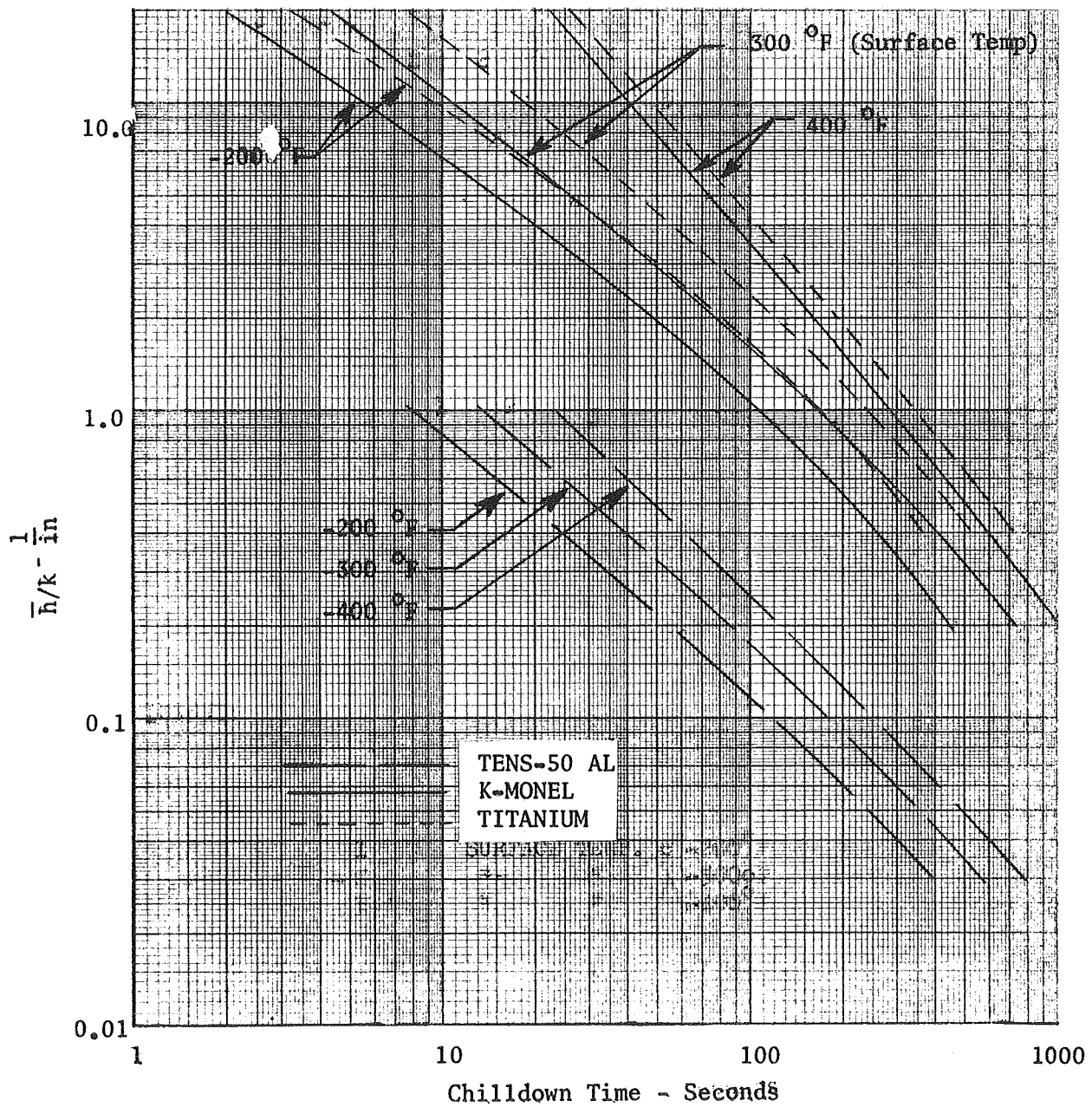


Figure. 18. $\frac{\bar{h}}{k}$ Vs Chillo down Time for Uncoated Metals at Various Surface Temperatures

TABLE 5

COMPARISON OF THE WETTED SURFACE AND THE BACKSIDE TEMPERATURES
OF THE UNCOATED METALS UNDER ZERO-GRAVITY POOL BOILING
($a/g = 0.004$)

Time, seconds	Location	Metal and Temperature, F		
		Tens-50 Aluminum	Titanium	K-monel
60	Backside surface	30	28	43
	Wetted surface	28	-2	35
	ΔT	2	30	18
150	Backside surface	-55	-45	-12
	Wetted surface	-63	-73	-30
	ΔT	5	28	18
600	Backside surface	-335	-351	-240
	Wetted surface	-338	-366	-258
	ΔT	3	15	10

TABLE 6

COMPARISON OF THE WETTED SURFACE AND THE BACKSIDE TEMPERATURES
OF THE UNCOATED METALS UNDER FORCED CONVECTION

($G = 2 \text{ lb/in.}^2\text{-sec}$)

Time, seconds	Location	Metal and Temperature, F		
		Tens-50 Aluminum	Titanium	K-monel
10	Backside surface	-138	46	68
	Wetted surface	-183	-294	-236
	ΔT	45	340	168
20	Backside surface	-282	-30	-50
	Wetted surface	-320	-339	-270
	ΔT	38	309	220
30	Backside surface	-367	-103	-130
	Wetted surface	-400	-361	-270
	ΔT	33	258	140
43	Backside surface	-420	-170	-235
	Wetted surface	-419	-380	-355
	ΔT	1	210	120
75	Backside surface	-422	-317	-356
	Wetted surface	-422	-420	-402
	ΔT	0	103	46

II: COATED FEED SYSTEMS

The effect of coatings on the cooldown time of various materials was investigated in this task, and coating techniques for both conventionally applied polymeric materials and plasma spray coatings were developed. The evaluation and development of these coatings, including thermal and flexural tests, were conducted using coated Tens-5 aluminum and titanium specimens. The most promising coatings were then applied to parts of the Mark 29 LH₂ turbopump, and hot-fire tests were conducted in LH₂. The coated pump parts were reviewed and the results of these tests are included in this section.

CHILLDOWN OF COATED MATERIALS

Thin layers of various coatings have been applied to the surface of metals by numerous investigators and cooldown times of those specimens for both coated and uncoated metals have been experimentally determined in LH₂ and LN₂. These investigators (Ref. 9 through 12) have shown that cooldown times may be appreciably reduced when a thin layer of very low thermal conductivity material is applied to the metal being cooled. This reduction in cooldown time was the result of enhancement of heat transfer coefficient brought about by the coating. The thin layer of coating permits a temperature gradient to be set up between the outer coating surface closer to the critical ΔT of nucleate boiling during the cooldown. Because the heat transfer coefficient is highest during nucleate boiling, the cooldown time of the coated metal was, therefore, lower than the uncoated metal. Reference 9 shows that the cooldown time of a vaseline-coated (~0.10-millimeter thick) cylinder reduced the uncoated cooldown time by 1/4. Reference 9 also shows that the coating thickness is important in reducing the cooldown time, and that there was an optimum coating thickness beyond which the cooldown time was not decreased.*

The heat flux between the coating surface and the fluid adjacent to it is described in the equation below:

$$Q/A = \frac{T_{\text{surface}} - T_b}{(t/k_m) + (t/k)_{\text{coating}} + 1/h} \quad (10)$$

*Also Ref. 22

If one assumes (t/k_m) to be small in comparison to other resistances, then:

$$Q/A = \frac{T_{\text{surface}} - T_b}{(t/k)_{\text{coating}} + 1/h} \quad (11)$$

For the pool boiling condition, $1/h$ is large in the film-boiling region (2.56×10^5 Btu/in.²-sec-F) and small in nucleate boiling region (189 Btu/in.²-sec-F). Therefore, the resistance of a 0.010-inch coating (1×10^4 Btu/in.²-sec) will be controlling when $ht/Kc > 1.0$ (Ref. 13) during nucleate boiling.

The forced convection heat transfer with film boiling can be substantially higher than pool film boiling, but lower than that obtained during pool nucleate boiling. If, throughout the chilldown time, the resistance due to the coating is larger than the fluid-to-wall resistance without the coating, the addition of a coating will result in a slower cooling. A shorter cooldown time can be obtained if:

$$\frac{\bar{h} t c}{Kc} < 1.0 \quad (12)$$

where \bar{h} is the heat transfer coefficient obtained without coatings for a major portion of the cooldown time (Ref. 13). This study, however, is not concerned with the reduced cooldown time of the entire mass of the pump components but, rather, with the reduced cooldown time of the wetted surfaces. That is, the faster (within seconds) the surfaces of the impeller, pump casing, etc., can be chilled, the sooner the pump can be started. Consequently, the surface temperature was of concern in this study, provided that the very rapid chilldown of the metal surface (while thermal stresses caused by it or near the initial temperature) was detrimental, either the surface must be chilled slowly (use of coating will accomplish this) or a different metal chilldown rate, or design, must be selected.

Further experimental study needs to be performed using LN_2 and LH_2 coolants for chilldown with thin insulating coatings (0.010 inch). Typical data, as shown in Fig. 19 from Ref. 13 for plate LH_2 cooldown under unity-g pool boiling conditions, indicate that the presence of the coating can possibly alter the transition point (saturation-to-wall temperature difference) where the onset of nucleate boiling occurs. However, data cannot be derived from the single thermocouple measurement taken in the plate center (not at the coating surface). A recent Russian article (Ref. 14) indicates that, for LN_2 chilldown with coated surfaces, the presence of a Teflon coating can alter the nucleate boiling onset by as much as 130 R (with LN_2) earlier. (However, details of the measurement and data are not provided.) The effect of an earlier transition to nucleate boiling will be to shorten the chilldown times over that shown in the current work in the surface temperature range of -350 to -423 F. For LH_2 cooldown, it is expected that the onset of nucleate boiling should not occur at greater than a $\Delta T = 75$ R wall-to-saturation temperature difference under any surface condition. The effect of an onset of nucleate boiling at this earlier point with a coating, however, should alter the analytical results of this study, particularly in cases where thick-wall sections are used and where reduction of the surface temperature from -350 F appears difficult because of a low film-boiling heat transfer coefficient applied.

It is recommended that further definition of the LN_2 and LH_2 heat transfer coefficient in the range of film to nucleate boiling be provided for Kel-F or Teflon-coated surfaces to verify both the peak nucleate boiling values and temperature-difference (ΔT) range of applicability.

The choice of a coating, in addition to its very low thermal conductivity, depends on the availability, ease of application and, most important, durability. The coating material must be capable of undergoing many chilldown cycles without cracking, peeling, chipping, or becoming damaged.

For the purpose of this analytical study, a KX635 coating applied to the surfaces of Tens-50 Al, titanium, and K-monel was analyzed. A simple model

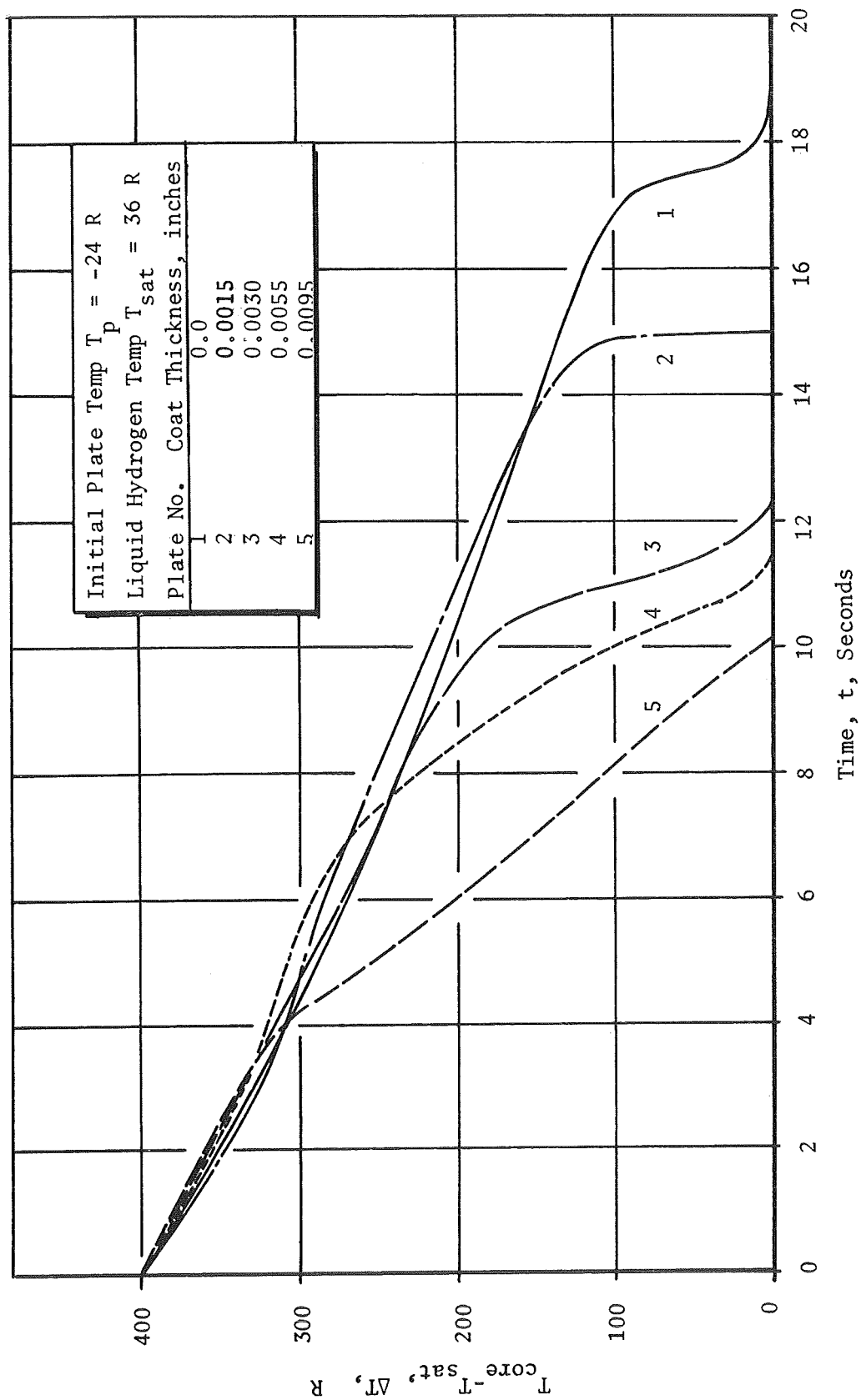


Figure 19 . Cooldown of Kel-F Coated K-Monel Plates in Liquid Hydrogen. Initial Plate Temperature: -24 F

is shown in Fig. 20. The data for this model were made input to the thermal analyzer program. The specific heats and the thermal conductivities of the metals and the coating were given in tabular form as a function of temperature. The hydrogen heat transfer coefficients were assumed to be the same as in the noncoated cases. At first, a coating thickness of 0.020 inch was studied and the results are plotted in Fig. 12 through 15 with the results of the uncoated cases.

Figure 12 shows the surface temperature of the coated and the uncoated metals under a zero-g condition. It can be seen that the surface temperature of the coating decreased very rapidly within the first few seconds. The slope of the cooling curve then changes and the surface temperature decreased at a much slower rate than at the beginning of the chilldown. Eventually, the cooldown curves of the coated metals cross the cooling curves of the uncoated metals. This indicated that, for a 0.020-inch-thick coating, under zero-g conditions, there was a time period where the surface temperature below which coatings are of no value in reducing the chilldown time. For example, the cooling curves of the uncoated and coated titanium crosses at ~500 seconds from the start of the chilldown. The surface temperature corresponding to this time period was ~-307 F. Therefore, from the standpoint of surface chilldown time reduction, the 0.020-inch layer of coating was beneficial for times less than 500 seconds (where the surface temperature is -307 F). A coating can be beneficial regardless of the decrease or increase in chilldown time. A coating was of great help in reducing the thermal gradients in the base metal where large thermal gradients may cause high thermal stresses.

As the heat transfer coefficient was increased, the surface temperature cooldown time of both uncoated and coated metal decreased. This effect can be seen in Fig. 13 for pool boiling under a unity-g condition. This figure shows that the chilldown curves for coated and uncoated titanium cross at a surface temperature of ~-345 F. The time to achieve this temperature was ~155 seconds, which was much lower than that for the zero-g condition (500 seconds) discussed earlier. A further increase of the heat transfer coefficient tended to force the crossing of the surface temperature cooling

curves to occur both at a lower temperature and at a reduced cooldown time for coated and uncoated metals. This phenomenon becomes more prominent under forced convection conditions. For example, Fig. 14 indicates that the two curves for titanium cross at a surface temperature ~ -390 F after a chilldown time of approximately 58 seconds.

Figure 15 shows that the cooling curves for coated and uncoated K-monel and titanium do not cross, indicating that a 0.020-inch-thick coating was beneficial in reducing the surface temperature chilldown time for the entire temperature range. For example, the surface temperature of coated and uncoated K-monel decreased to -410 F in 51 and 66 seconds, respectively. However, the cooling curves for coated and uncoated aluminum still cross at a surface temperature of ~ -430 F in approximately 21 seconds.

To evaluate the effect of coating thickness on the chilldown time, coating thicknesses of ~ 0.005 , 0.010 , and 0.050 inch also were selected, and the analytical cooldowns were studied for titanium only. The results are plotted in Fig. 21 through 24 for zero g, unit g forced convection at a G equal to 2 and $5 \text{ lb/in.}^2\text{-sec}$, respectively. These figures reveal that low heat transfer coefficients (especially under pool boiling conditions) and the cooling curves of various coating thicknesses cross each other. As the coating thickness increased, the surface temperature decreased faster initially, but the time to achieve a final temperature of ~ -410 F increased. The relationship between the coating thickness and the heat transfer coefficient must be satisfied if a coating is to reduce the chilldown time of the entire body of the metal being chilled. Again, this relationship is shown as:

$$\frac{\bar{h} t}{Kc} < 1.0$$

As the coating thickness increased, the inequality above can be reversed to become:

$$\frac{\bar{h} t}{Kc} > 1.0 \tag{13}$$

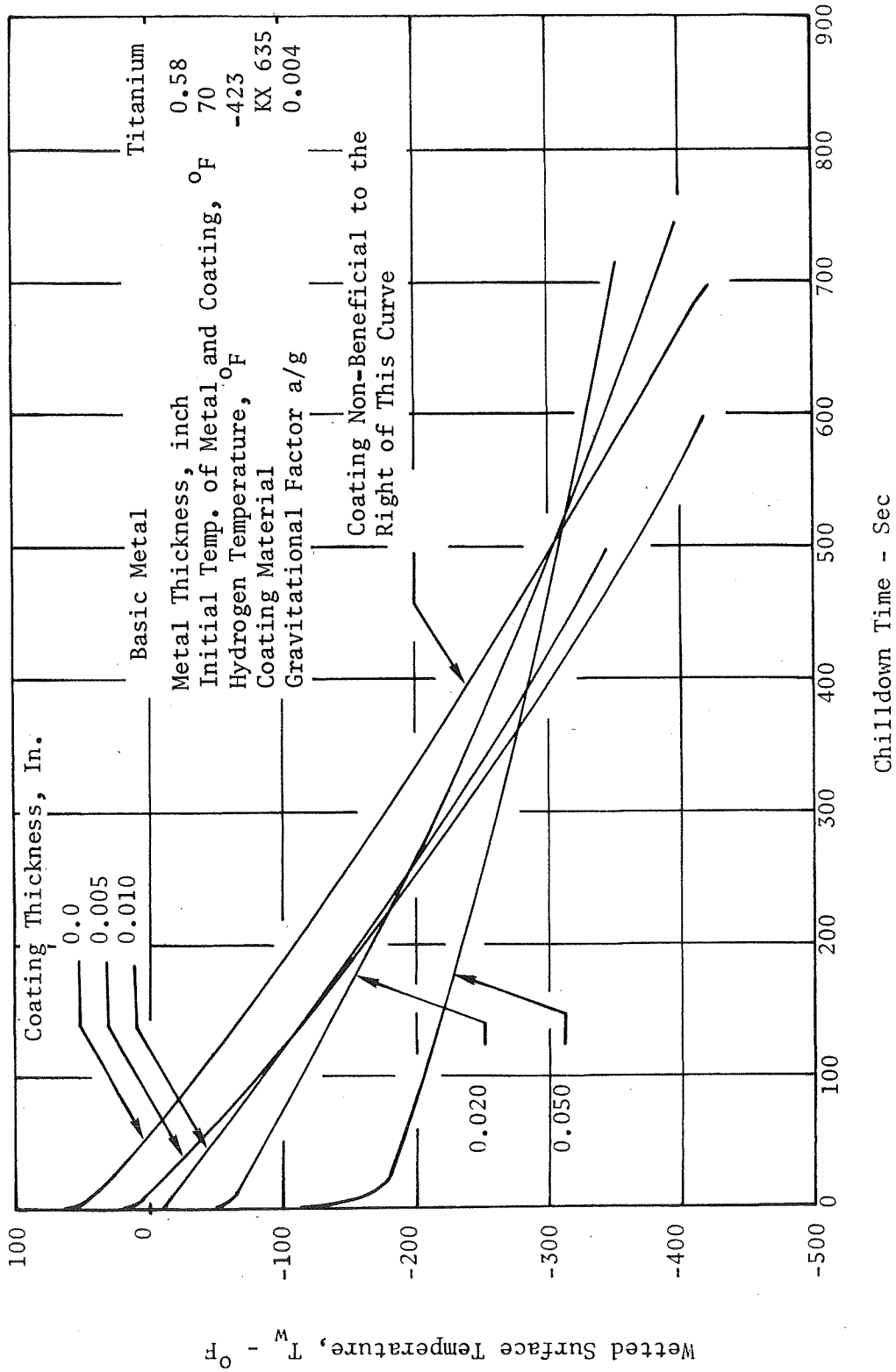


Figure 21. Titanium Wetted Surface Temperature vs Chilldown Time for Hydrogen Pool Boiling Condition at Near Zero Gravity

Basic Metal	Titanium
Metal Thickness, inch	0.50
Initial Temp. of Metal, °F	70
Initial Temp. of Coating, °F	70
Hydrogen Temperature, °F	-423
Coating Material	LX 735
Gravity Factor, a/g	1.0

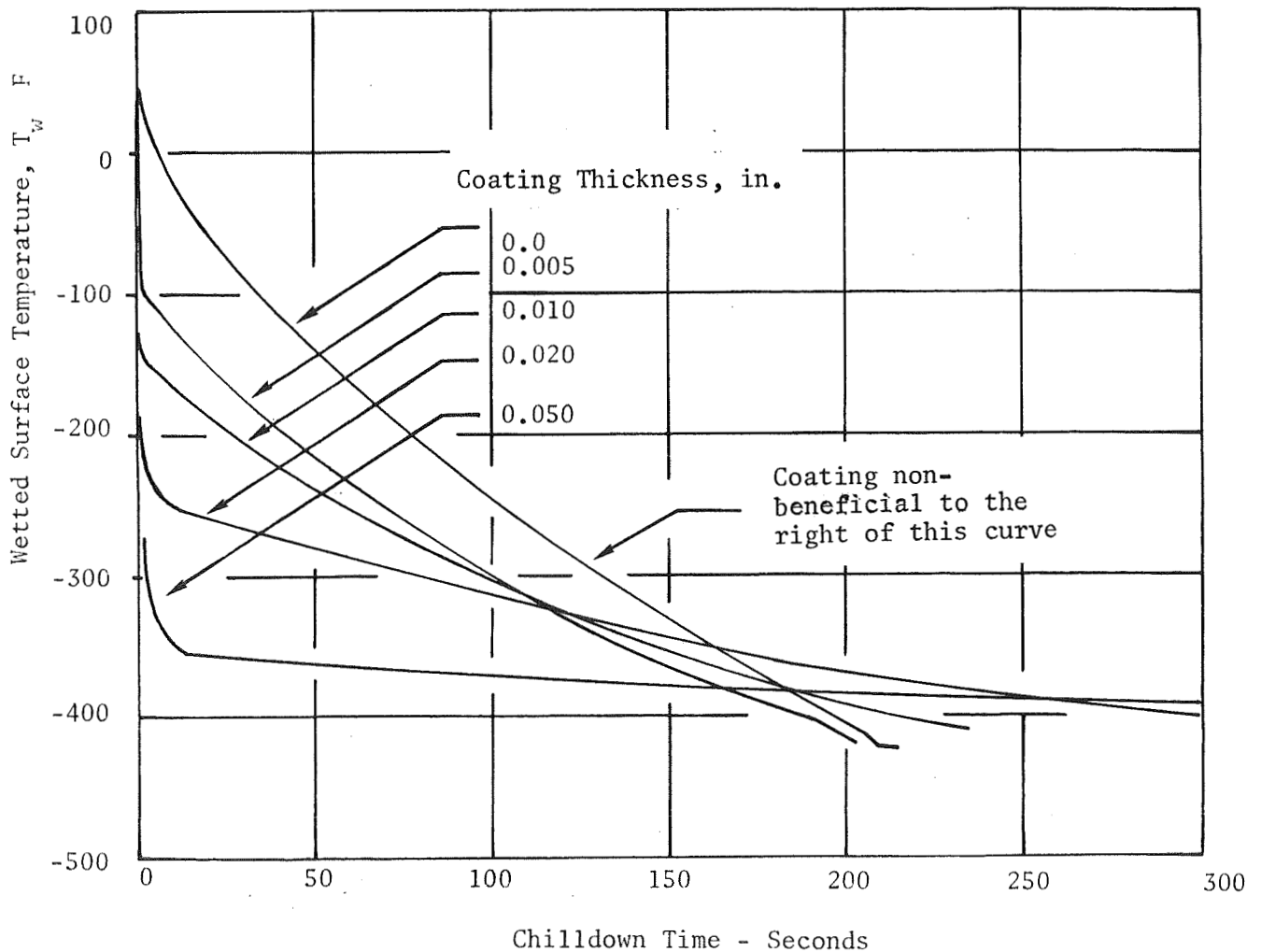


Figure 22. Titanium Wetted Surface Temperature vs Chillydown Time for Hydrogen Pool Boiling Condition at Unity Gravity

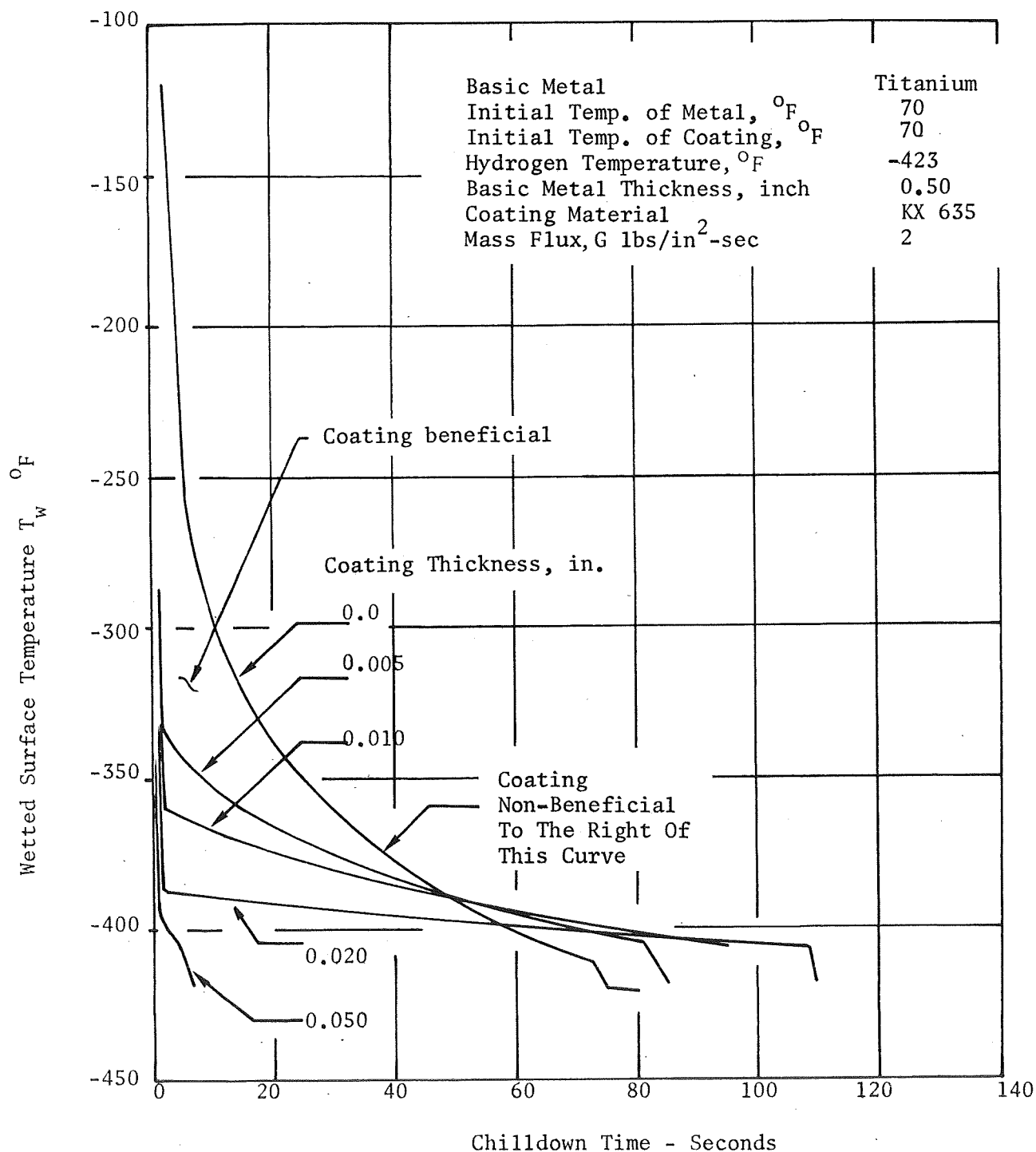


Figure 23. Titanium Wetted Surface Temperature vs Chillumdown Time For Forced Convection Condition of $G = 2 \text{ lbs/in}^2\text{-sec}$

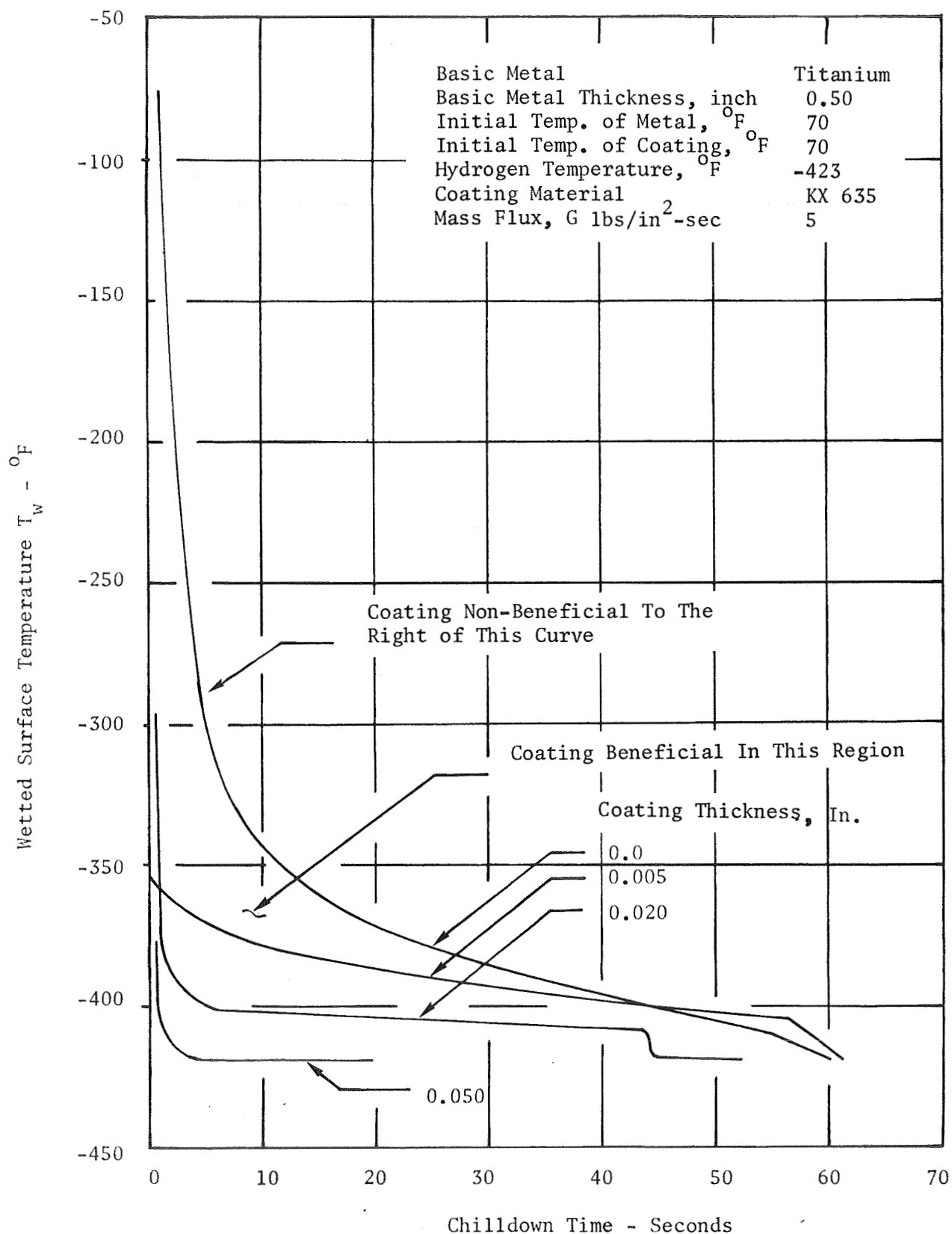


Figure 24. Titanium Wetted Surface Temperature Vs Chillo-down Time For Forced Convection Condition of $G = 5 \text{ lbs/in}^2\text{-sec}$

When this occurs, the resistance due to the coating will be the controlling factor and an increase in cooldown time will take place. If, throughout the cooldown, the resistance due to the coating is larger than the fluid-to-wall resistance without coating, the addition of a coating will result in a slower cooling (Ref. 13). Between a ΔT of 500 and 13 R, the average heat transfer coefficient is $\sim 0.000088 \text{ Btu/in.}^2\text{-sec-F}$ for pool boiling under zero-g condition. Therefore, the resistance of the fluid boundary layer was $\sim 1.135 \times 10^4 \text{ Btu/in.}^2\text{-sec-F}$. The resistances of the coating at an average thermal conductivity of $1.4 \times 10^{-6} \text{ Btu/in.-sec-F}$ for various thicknesses are as follows:

Coating Thickness, inch	Resistance, $\text{Btu/in.}^2\text{-sec-F}$
0.002	0.143×10^4
0.005	0.715×10^4
0.010	1.430×10^4
0.020	2.860×10^4
0.050	7.150×10^4

Therefore, a 0.010-inch coating has higher resistance than the average heat transfer coefficient. Consequently, for coating thicknesses above 0.010 inch, the thickness was definitely the controlling factor. Thus, the cooldown time of the entire body increased as coating thickness was increased. Reference 9 has shown the effect of coating on the cooldown time. The results of the experiments in Ref. 10 indicated that, as the coating thickness increased from zero to optimum thickness, the cooldown time reached a minimum. Any thickness above this optimum thickness raised the cooldown time. A coating thickness of 0.005 inch reduced the cooldown time of the surface temperature and the cooldown time of the entire titanium segment. Figure 21 shows that the cooling curve of the 0.005-inch, coated titanium was (at all times) lower than that of the uncoated case for titanium. This indicates that the entire body of the specimen was chilled faster when 0.005 inch of KX 635 was applied to its surface.

Figure 25 is a plot of the time required to achieve a surface temperature of -400 and -300 F as a function of coating thickness. It can be seen that, for pool boiling condition, an optimum coating thickness (~ 0.005 inch) exists. The minimum chilldown time was obtained at these optimum coating thicknesses. However, at higher heat transfer coefficients, the effect of the coating was a slight increase followed by a sharp decrease in the cooldown time of the surface temperature for a G of 2 and 5 lb/in.²-sec.

Again, as the heat transfer coefficient increased, the chilldown time of the coated and uncoated titanium decreased and the cooling curves crossed at earlier chilldown time. Figure 22 shows, for example, that 0.005- and 0.05-inch coatings have the same cooldown times for a surface temperature of ~ -392 F. This is obvious from Fig. 22 for the pool boiling condition where an optimum coating thickness was indicated. For forced convection conditions with fairly high heat transfer coefficients, the controlling resistance was due to the coating, and the chilldown time of the entire body will increase. Although the surface temperature decreased much faster at the start of the cooling, the final temperature of ~ -410 F cannot be achieved quickly with 0.010- or 0.020-inch coatings. Figure 16 shows the temperature effects of the surface and back-side temperature of the base metal with a 0.005-inch coating. It can be seen that the metal surface and back-side temperatures of the coated metal are higher than that of the uncoated metal. Figure 24 is similar to Fig. 22 except that, because of the higher hydrogen mass velocity, the chilldown times are shorter for both coated and uncoated titanium. Figure 24 indicates that the surface temperature of the coating decreased to ~ -410 F in ~ 3 and 48 seconds for a coating thickness of 0.05 and 0.020 inch, respectively.

Coating Effects

From the results of the coated and uncoated analyses discussed previously, it may be concluded that coatings have a distinct advantage in eliminating the thermal stress problems during a fast chill. An uncoated titanium part being chilled at a mass flux of ~ 2 lb/in.²-sec has a temperature distribution

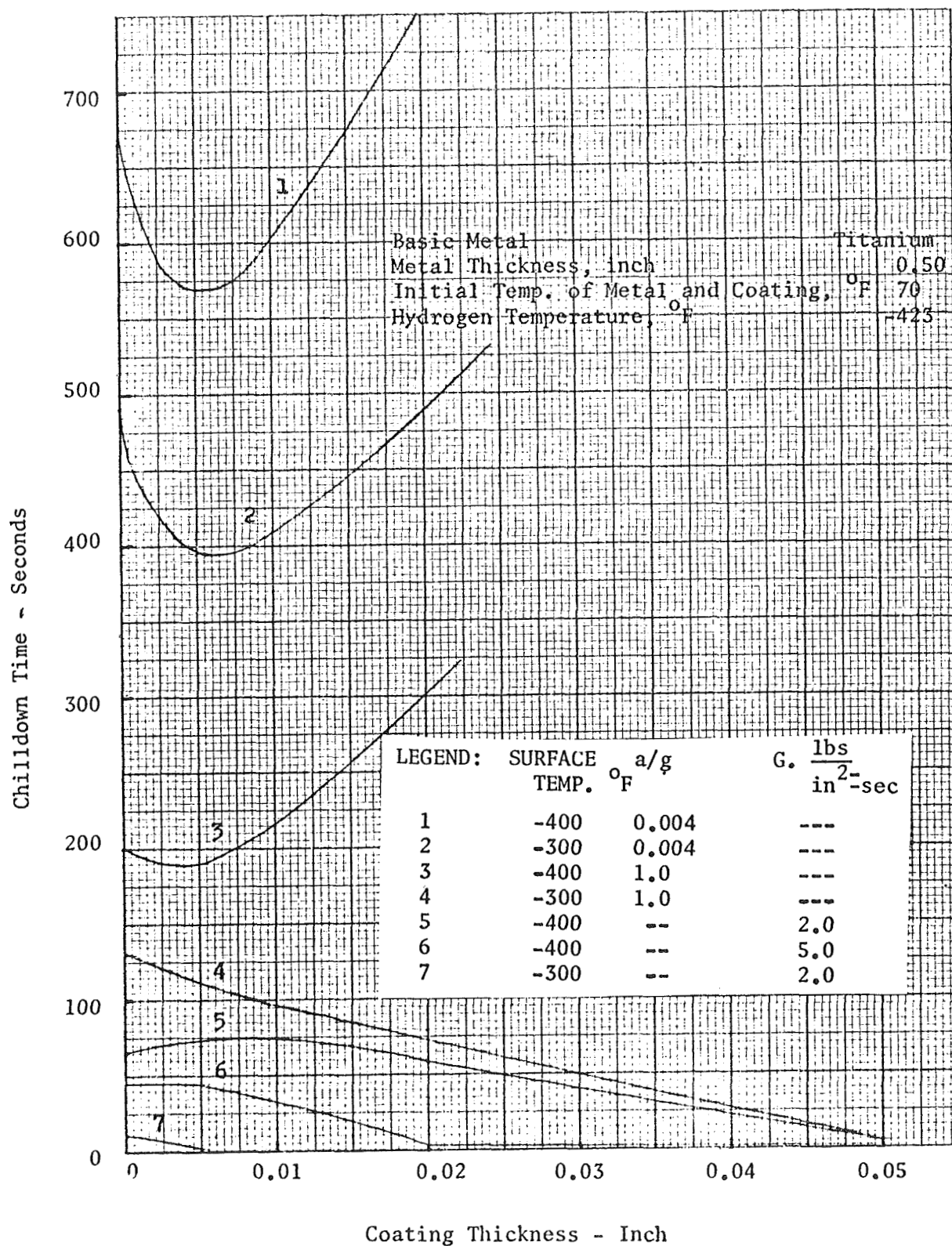


Figure 25. Titanium Chilldown Time vs Coating Thickness

as shown in Fig. 16. The maximum thermal gradient of ~ 320 F occurred at ~ 10 seconds after chilldown, whereas the thermal gradient for a 0.020-inch, KX 635 coated titanium being chilled at mass flux of $2 \text{ lb/in.}^2\text{-sec}$ was ~ 30 F, as shown in Fig. 26. Also, the obvious advantage of coatings was the reduction in chilldown time, particularly under forced convection. The surface temperature of the coating decreased faster than the uncoated case, and results in a lower heat flux and hydrogen propellant vaporization, which may permit earlier pump startup.

Selection of Coating Thickness

The selection of the coating thickness would be relatively simple if it were not for the changes in the chilldown conditions. If the chilldown of the pump takes place either under the worst (pool boiling under zero g) or best chilldown conditions (forced convection at high g value), then one coating thickness could be selected. However, the coating thickness must be selected to meet the predicted system chilldown conditioning requirements. A thin coating (0.005 inch) film was advantageous for zero-g and unit-g pool boiling conditions for surface chill temperatures to ~ -400 F. Thicker coatings (~ 0.030 to 0.050 inch) become more advantageous for chilldown under forced convection. By referring to Fig. 25, it can be seen that a 0.005-inch coating causes a reduction in the chilldown time under zero-g conditions and has no effect under forced convection for the attainment of a surface temperature of ~ -400 F. Under tank-head start, the hydrogen mass flux is low ($\sim 1 \text{ lb/in.}^2\text{-sec}$, Fig. 146 of Ref. 7), and the coating effect on the chilldown time was almost nil. Therefore, it would be beneficial to choose a coating thickness that would be effective in the pool boiling region under zero-g which was ~ 0.005 inch. Therefore, a representative part of Mark 29 LH_2 pump was coated with various thicknesses (from 0.0002 to 0.010 inch) of KX 635 and chilled in LH_2 under zero-g conditions to determine analytically optimum coating thickness and the actual chilldown time reductions obtained. If the chilldown time of a thinly coated pump can be reduced to $1/4$ of its value for the uncoated case (as shown by Ref. 9), the expected chilldown time for a titanium pump can be ~ 167 seconds under the zero-g pool boiling condition.

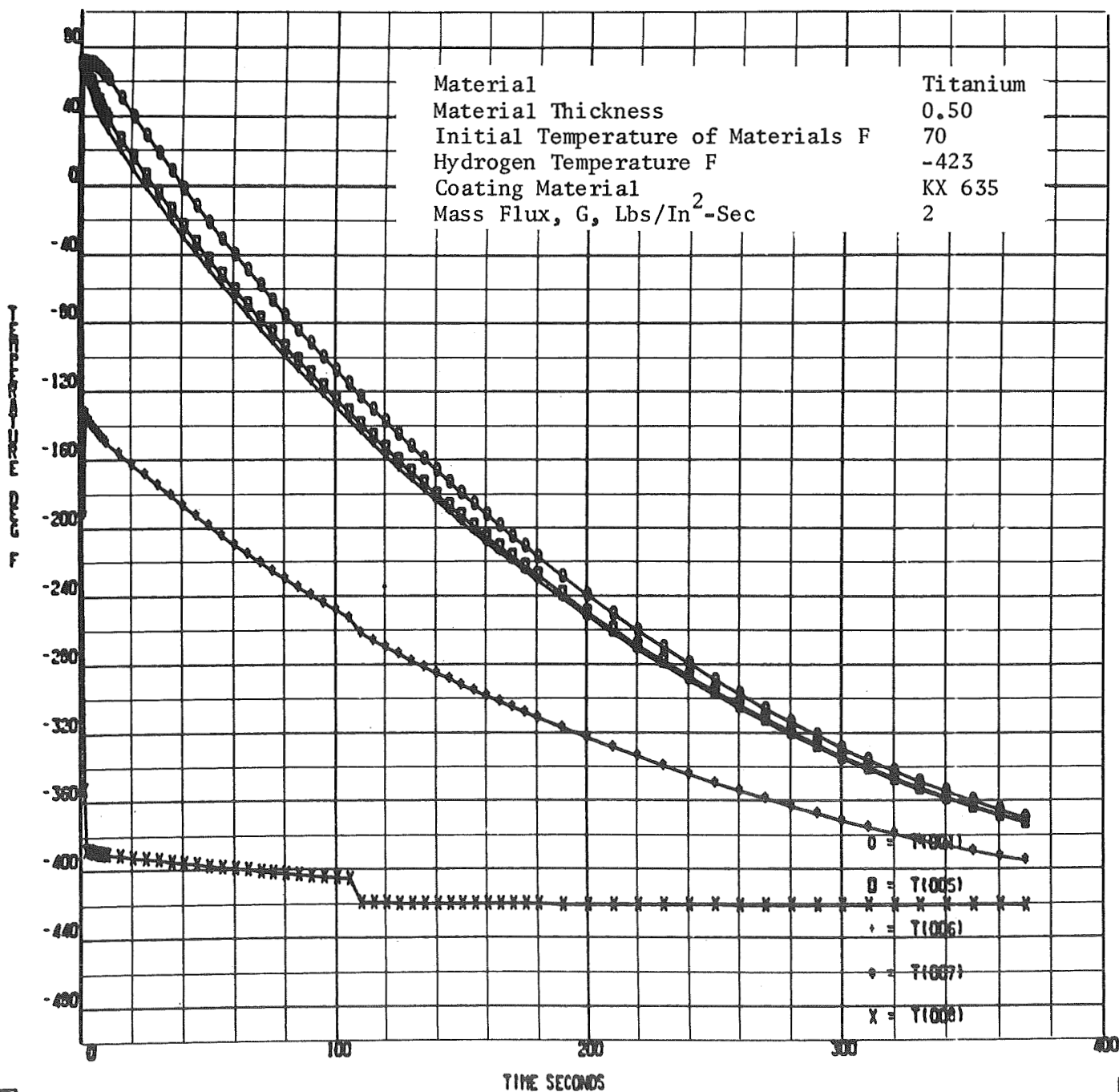


Figure 26. Temperature vs Chillovdown Time for KX 635-Coated Titanium Under Forced Convection Condition ($G = 2 \text{ Lbs/In.}^2 \text{-Second}$)

Reference 15 has shown that a 0.0003-inch, Teflon-coated, stainless-steel plate has a much higher chilldown heat flux than an uncoated plate.

Pumping Capability

During engine start with a warm inlet line and pump, vaporization of the hydrogen may occur because of cavitation on the low-pressure regions of the pump flow passages and heat transfer from the warm inlet duct and the pump itself. However, the major portion of the vaporization was caused by the heat transfer from the warm surfaces to the cold hydrogen. LH₂ pumps similar to the Mark 29 are capable of pumping liquid hydrogen containing vapor of approximately 1 percent by weight (~20 percent by volume), depending on the hydrogen inlet pressure. Therefore, analytical studies were made to investigate the conditions controlling the inlet quality of hydrogen during a warm start. First, the maximum tolerable heat fluxes were computed for 1-, 3-, and 5-percent vapor by weight (approximately 20, 45, and 55 percent vapor by volume at 30 psia) by the following equation:

$$Q = \dot{w} \left[c_p (T_2 - T_1) + X H_v \right] \quad (14)$$

Dividing Eq. 14 by the heat transfer surface:

$$\frac{Q}{A_s} = \frac{\dot{w}}{A_s} \left[c_p (T_2 - T_1) + X H_v \right] \quad (15)$$

where Q/A_s is the heat flux rate. Multiplying and dividing the right-hand side of Eq. 15 by the flow cross-sectional area:

$$\frac{Q}{A_s} = \frac{\dot{w}}{A_c} \left[c_p (T_2 - T_1) + X H_v \right] \frac{A_c}{A_s} \quad (16)$$

but

$$\frac{\dot{w}}{A_c} = G$$

and

$$\frac{A_c}{A_s} = \frac{\text{hydrogen flow area}}{\text{heat transfer surface area}},$$

therefore, the final equation becomes:

$$\frac{Q}{A_s} = G \left[c_p (T_2 - T_1) + X H_v \right] \frac{A_c}{A_s} \quad (17)$$

Equation 17 was solved for subcooled and saturated hydrogen conditions to determine the maximum tolerable heat fluxes. For a saturated LH₂ condition, the term $c_p (T_2 - T_1)$ becomes zero.

The results of Eq.17 were plotted in Fig. 27 and 28 as heat flux versus mass flux for two values of A_c/A_s . One value represents the first row of the inducer blades, and the other simulates the entire pump flow passages. Next, the results of chilldown analysis from the thermal analyzer program were plotted as heat flux versus wetted surface temperature for coated and uncoated Tens-50 aluminum. The chilldown times are cross-plotted in Fig. 29 through 31.

These figures show that the heat flux decreases slowly at first as the wetted surface temperature decreased under pool boiling. This is the region of film boiling where the heat transfer coefficient is low. As the wall temperature dropped, the heat transfer coefficient rose slowly; therefore, the heat flux decreased with a gentle slope. At ΔT of ~ 17.5 R, the heat transfer coefficient began to rise sharply (Fig. 11), which resulted in a faster reduction of the surface temperature. However, the rise in the heat transfer coefficient was so fast that, although the ΔT is very small, the heat flux began to rise at a wetted surface temperature of ~ -404 F). Figure 11 shows that, for a ΔT of 19 R (a wall temperature of -404 F), the heat transfer coefficient was ~ 0.000047 Btu/in.²-sec-F, which results in a heat flux of ~ 0.000894 Btu/in.²-sec. Conversely, at a ΔT of

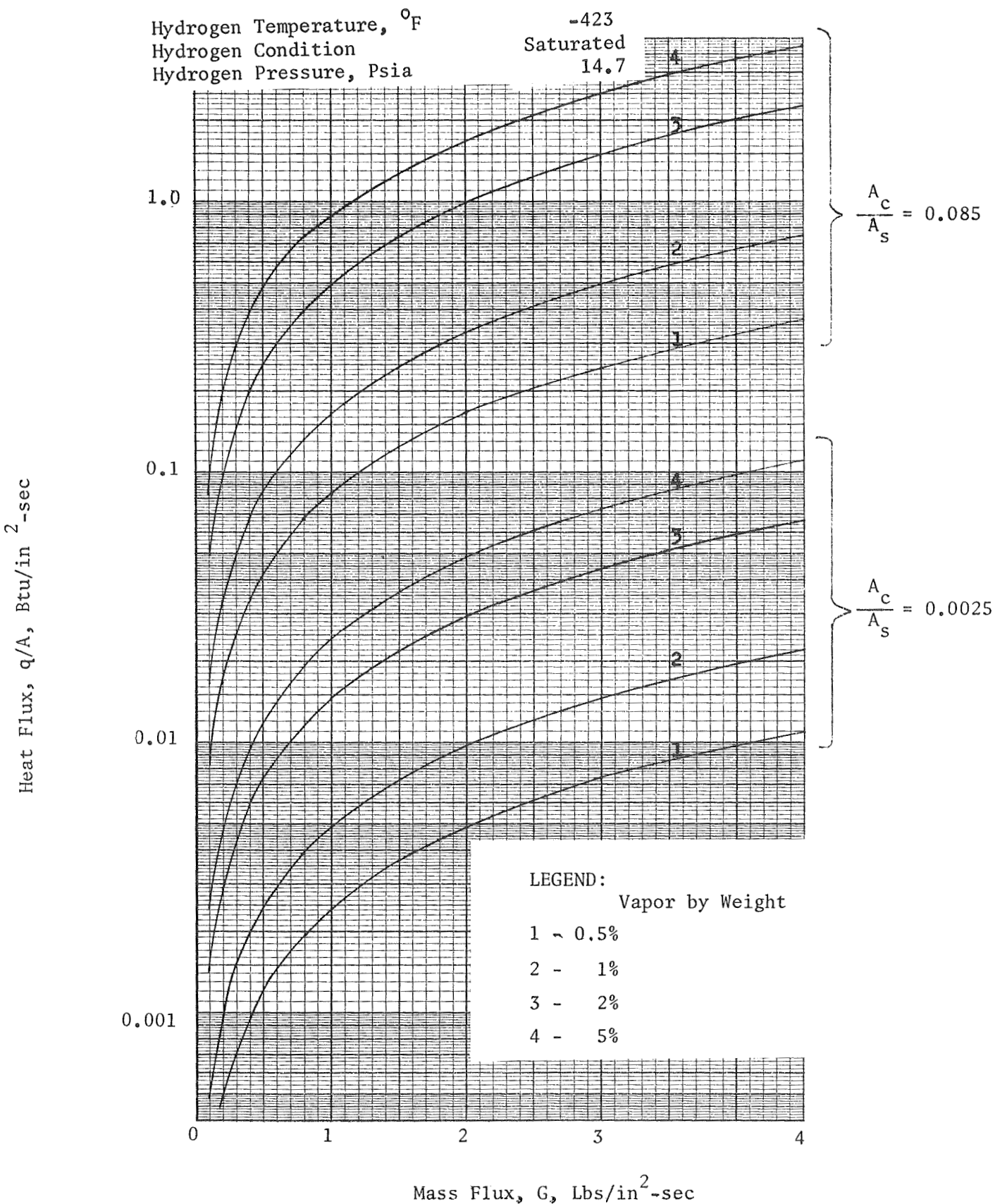


Figure 27. Heat Flux vs Mass Flux for Mark - 29 LH₂ - Pump at Saturated Hydrogen Condition

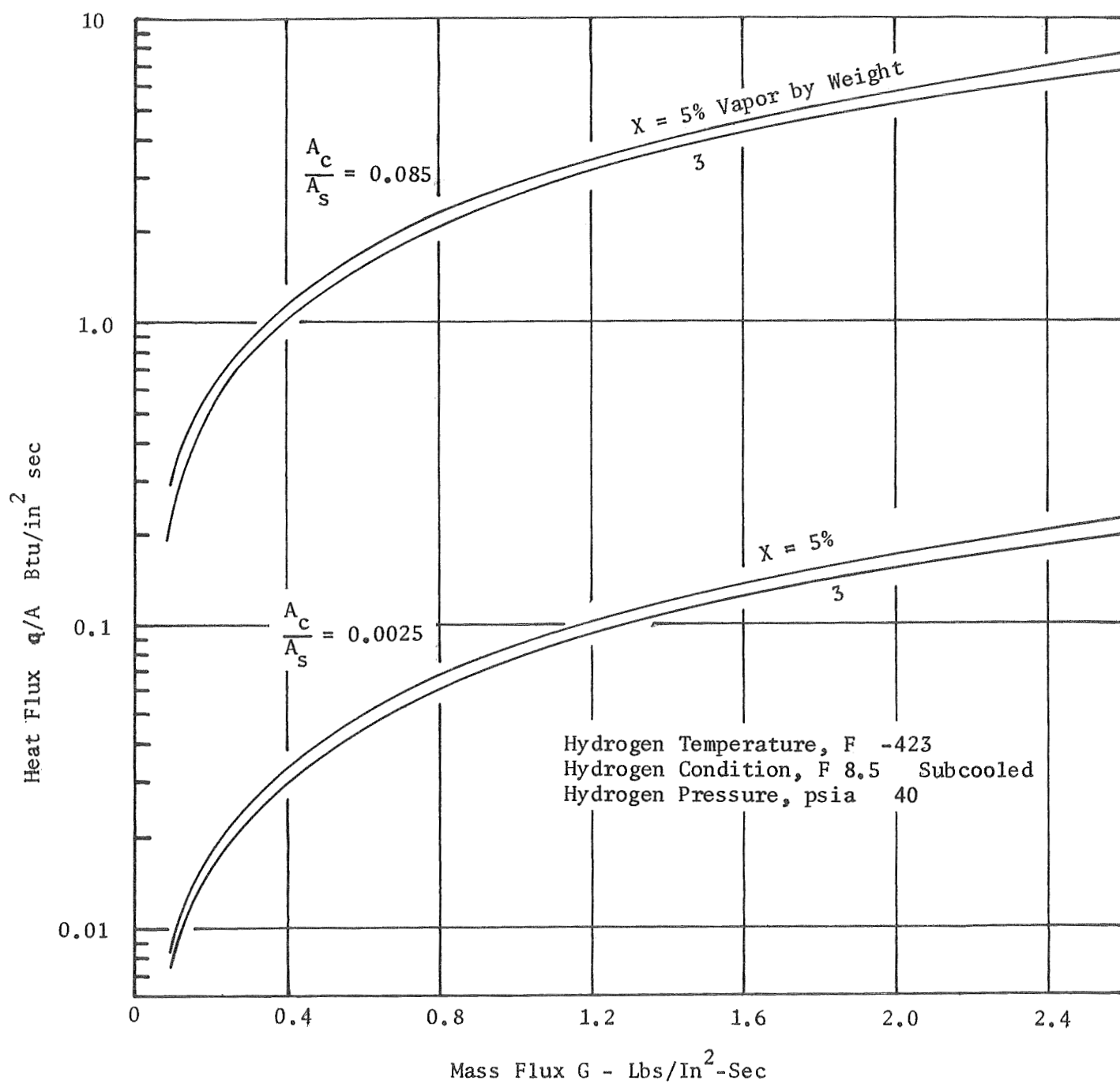


Figure 28. Heat Flux vs Mass Flux for Mark - 29 LH₂ Pump at 8.5 F Subcooled Hydrogen

Basic Metal	Titanium
Metal Thickness, Inch	0.50
Initial Temp. of Metal, °F	70
Hydrogen Temperature, °F	-423

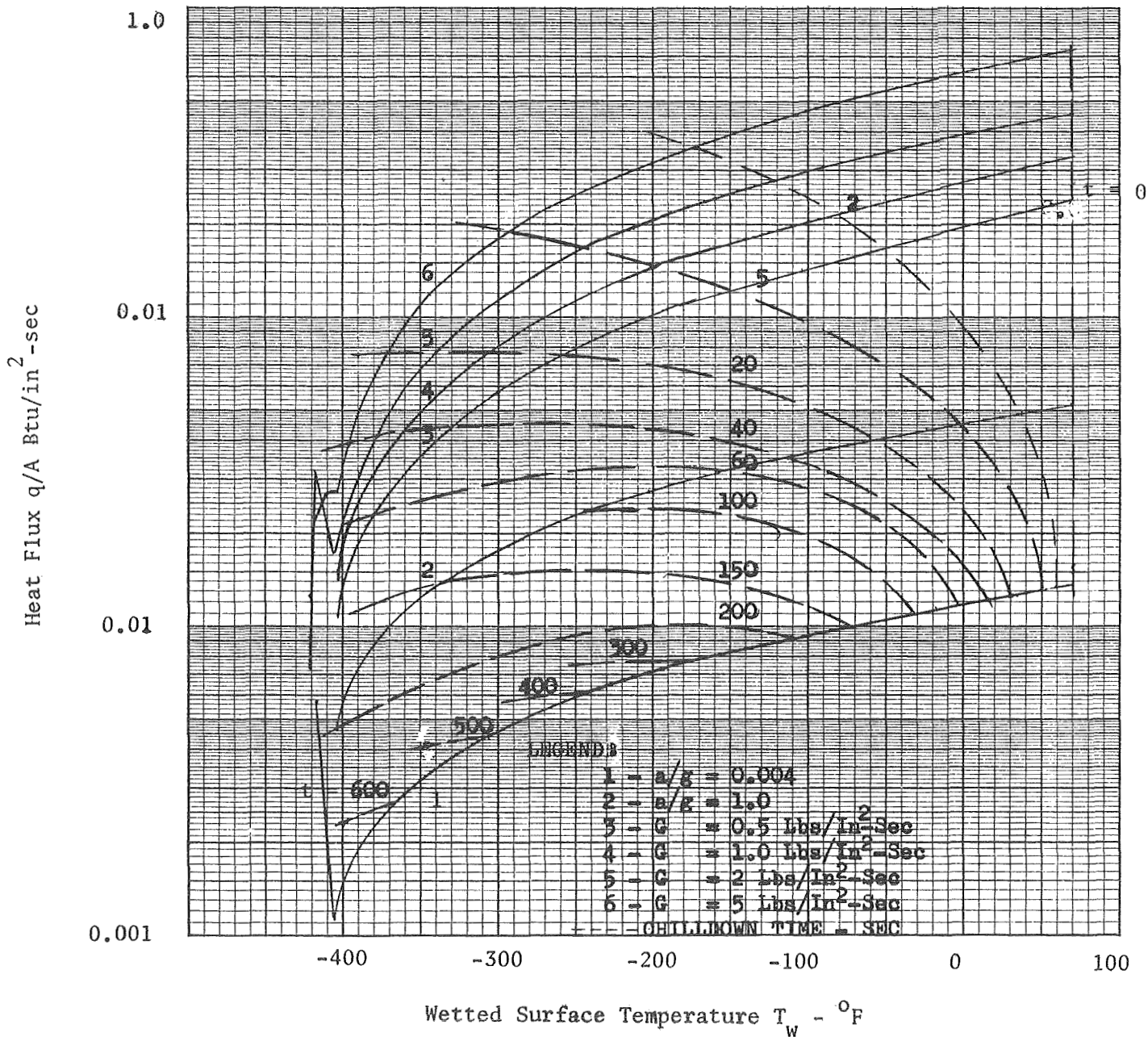


Figure 29, Heat Flux vs Wetted Surface Temperature for an Uncoated Titanium LH₂ Pump

Basic Metal	Titanium
Metal Thickness, inch	0.50
Coating Material	KX 635
Coating Thickness, inch	0.020
Initial Temp. of Metal and Coating	70
Hydrogen Temperature, °F	-423

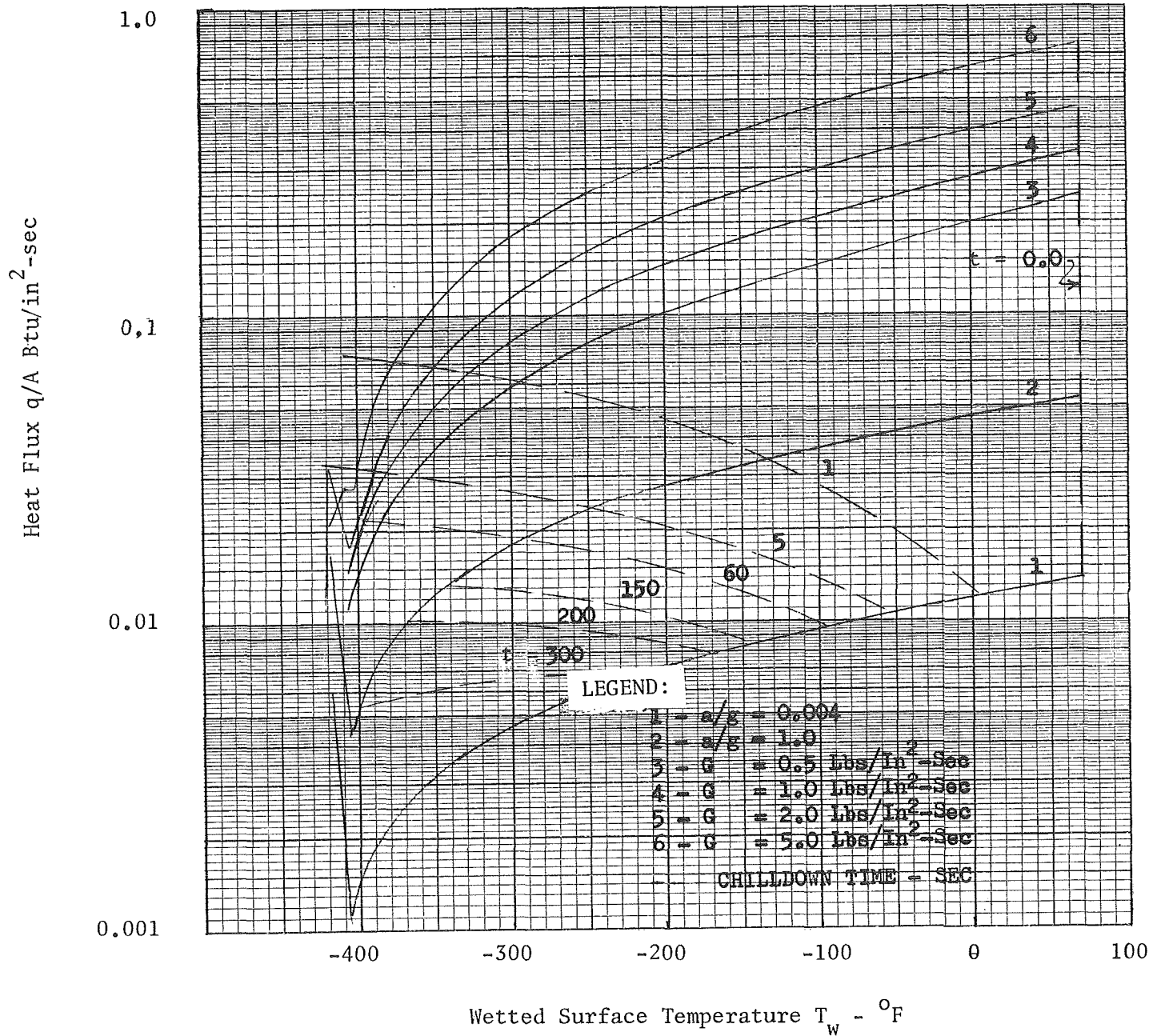


Figure 30. Heat Flux vs Wetted Surface Temperature for a Coated Titanium LH₂ Pump

Basic Metal Aluminum Tens 50
 Metal Thickness, inch 0.50
 Initial Tem. of Metal, °F 70
 Hydrogen Temperature, °F -423

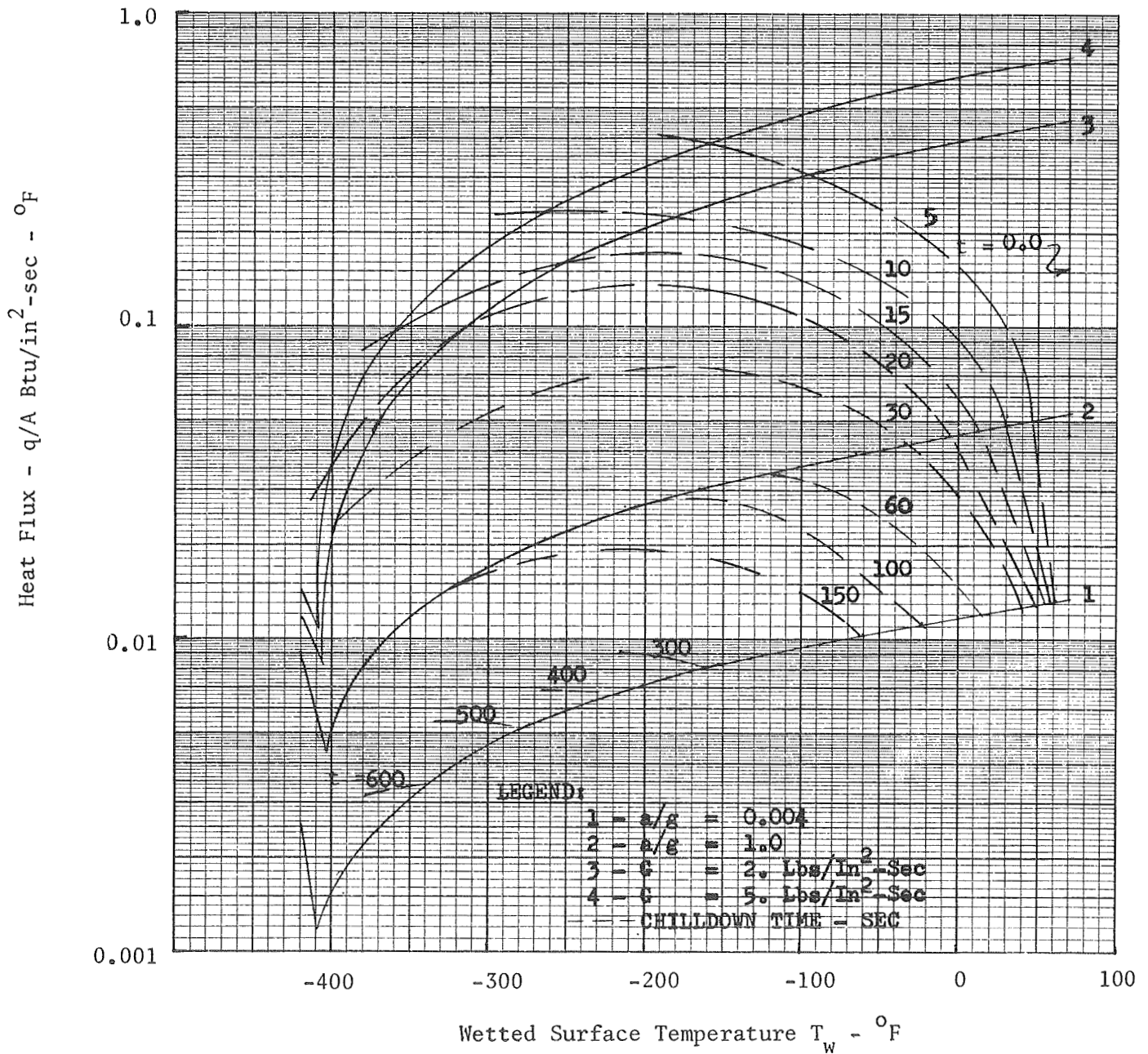


Figure 31. Heat Flux vs Wetted Surface Temperature for an Uncoated Aluminum LH₂ - Pump

3 R (a wall temperature of -420 F), the heat transfer coefficient was $\sim 0.00189 \text{ Btu/in.}^2\text{-sec-F}$, which resulted in a heat flux ($Q/A = h\Delta T$) of $\sim 0.00567 \text{ Btu/in.}^2\text{-sec}$. For this reason, the rapid increases of the heat fluxes occur below a wall temperature of $\sim -40 \text{ F}$ (Fig. 29 through 31). Figures 27 through 31 can be utilized to determine the required surface temperatures of the various parts of the pump prior to pump start.

For example, at a saturated hydrogen mass flux of $2 \text{ lb/in.}^2\text{-sec}$, for a 1 percent by weight vapor condition, Fig. 27 shows that the heat flux was $\sim 0.325 \text{ Btu/in.}^2\text{-sec}$ for $A_c/A_s = 0.085$. Using this heat flux in conjunction with Fig. 29 (for uncoated titanium), the wetted surface temperature of the duct must be -70 F or colder for the pump to start properly. Figure 29 also shows that a cooldown time of ~ 1.5 seconds was required. Because the inducer flow cross-sectional area was $\sim 4.91 \text{ in.}^2$, the minimum hydrogen required was $\sim 14.7 \text{ lb}$ to lower the surface temperature of the inducer to $\sim -70 \text{ F}$. However, the main part of the pump was still warm, and a pump start may not be possible.

Again using subcooled hydrogen at a mass flux of $\sim 0.3 \text{ lb/in.}^2\text{-sec}$, Fig. indicated a heat flux of $\sim 0.0225 \text{ Btu/in.}^2\text{-sec}$ for $A_c/A_s = 0.0025$ (entire pump). Referring to Fig. 29, after some interpolation, one can find an approximate surface temperature of $\sim -370 \text{ F}$. The required cooldown time also was estimated to be 60 seconds; therefore, the minimum required hydrogen is ~ 88.5 pounds. This is in fair agreement with the results of test No. 16 made with engine III (Fig. 147 of Ref. 7), and indicated that in 30 seconds, ~ 100 pounds of hydrogen flowed through the pump. However, at the start of the test, this hydrogen contained a great deal of vapor (Fig. 145 of Ref. 7) that entered the pump. The hydrogen quality dropped in 30 seconds to ~ 25 percent by volume, which was the maximum expected for pump operation. In the present analyses, it was assumed that saturated LH_2 enters the pump and the vaporization takes place in the pump itself. Therefore, it is plausible that the minimum hydrogen requirement should be less than 88.5 pounds, compared to 100 pounds from test III of Ref. 7.

The use of Fig. 27 indicated that, when saturated hydrogen entered the pump at a mass flux of $2 \text{ lb/in.}^2\text{-sec}$ (for 1-percent quality by weight and $\Lambda_c/\Lambda_s = 0.085$), the maximum tolerable heat flux was $0.325 \text{ Btu/in.}^2\text{-sec}$. Figure 27 shows that this heat flux was associated with an approximate coating surface temperature of $\sim 70 \text{ F}$. The cooldown time was less than 1 second and, therefore, the minimum hydrogen requirement was less than 10 pounds based on the inducer cooldown time alone.

It should be noted that the heat flux curves of Fig. 29 through 31 are exactly the same because the heat transfer coefficient is a function of ΔT , and hydrogen temperature was constant, and the heat flux for a given wetted surface temperature was exactly the same for coated and uncoated metal. The difference between Fig. 29, 30, and 31 was due to the cooldown time curves (dashed lines).

To determine the necessary hydrogen requirement to chill the entire pump wetted surfaces to an acceptable temperature level, Fig. 27 through 30 were used. In the preparation of Fig. 28, it was assumed that hydrogen was subcooled (~ 8.5 degrees). The results indicated that, at a mass flux of $2 \text{ lb/in.}^2\text{-sec}$, the wetted surface temperature was $\sim 275 \text{ F}$ and the required cooldown times were ~ 7.5 seconds and less than 1 second for an uncoated and a 0.020-inch KX 635 coated titanium pump, respectively. Therefore, at a mass flux of $2 \text{ lb/in.}^2\text{-sec}$, the minimum hydrogen requirements, based on an inducer area of 4.91 in.^2 , were about 73.5 pounds and 10 pounds for uncoated and a 0.020-inch coated titanium pump, respectively. This clearly points out the advantage of the coating from the standpoint of reducing the cooldown time and hydrogen requirements. Also, as mentioned previously, the use of coatings will reduce the thermal stress problems because of the thermal gradients set up in titanium parts during cooldown was far less with coatings.

At a mass flux of $5 \text{ lb/in.}^2\text{-sec}$, the extrapolation of Fig. 28 for $\Lambda_c/\Lambda_s = 0.0025$ (entire pump) results in the heat flux of $0.385 \text{ Btu/in.}^2\text{-sec}$ for titanium. Figure 29 indicated that this heat flux was associated with a pump start wall temperature of $\sim 152 \text{ F}$. The cooldown time to achieve this temperature was ~ 1.5 seconds, and the minimum total hydrogen required was

~36.8 pounds. The hydrogen requirements for the uncoated titanium pump were ~73.5 and 36.8 pounds at a mass flux of 2 and 5 lb/in.²-sec, respectively. Again, the advantage of high hydrogen flowrates for the purpose of pump chilldown was indicated (as shown in Ref. 7).

When Tens-50 aluminum was examined, Fig. 27 showed that for a mass flux of 2 lb/in.²-sec when saturated LH₂ entered the pump, allowable hydrogen quality was 1 percent by weight. At this heat flux, Fig. 31 indicated a surface temperature of ~-70 F, and the associated chilldown time was ~4.5 seconds.

It should be mentioned that the assumed metal thickness in this study was 0.5 inch, which was slightly thicker than the majority of LH₂ pump parts. Therefore, the chilldown time and the hydrogen requirement for the uncoated Mark 29 LH₂ pump should be less than the values obtained. Also, a mass flux of 2 lb/in.²-sec would be difficult to achieve under a tank-head start with a tank pressure of ~32 to 40 psia. The system pressure drop, as shown in Fig. 117 of Ref. 7, limited the hydrogen flowrate. The best expected flowrate was that shown in Fig. 117 of Ref. 7, which shows that the mass flux was ~1.2 lb/in.²-sec (based on the inducer flow area of 4.912 in.²) after 60 seconds of system chilldown. Therefore, a faster chilldown would require a proportionally higher tank pressure.

STUDY OF COATING TECHNIQUES

The primary purpose of this effort was directed toward the development of insulative coatings for internal surfaces of LH₂ turbopumps. Cryogenic insulation coatings, to be successful, must have low thermal conductivities and coefficients of expansion, must adhere to the metal substrates under vibrating conditions at liquid hydrogen temperatures, and must not erode under the high-flow environments encountered in high-performance LH₂ pumps. Furthermore, the techniques for applying the coatings must not deteriorate the coating or the metal substrates of titanium and Tens-50 cast aluminum.

After extensive investigations of candidate coatings and processing techniques, two generic families of materials were selected for the coating of

prototype hardware. The materials selected were: a conventionally applied, glass-microballoon filled, Kel-F dispersion material (KX 635), and a plasma-sprayed epoxy material.

An extensive literature search was conducted to review the work performed by other investigators in the field of coating techniques and potential coating materials. Emphasis of this search centered on the thermal and physical properties of various materials at ambient and cryogenic temperatures. Coating application techniques, including plasma-spray deposition of organic resins, also were investigated. The feasibility of coating complex geometric shapes, the possibility of material degradation (either substrate or coating) using these processing techniques and the adhesion properties between the coating and metal substrate were investigated.

Literature describing modifications of conventional application techniques of dipping and spraying and subsequent fusing of the applied materials also was studied and is presented in Appendix A.

DEVELOPMENT OF COATING TECHNIQUES

KX 635 Coating

The study of coating techniques revealed that glass-microballoon filled, Kel-F dispersion coatings (KX 635) showed the best potential for internal insulative organic materials for cryogenic temperature applications. One of the largest reported unresolved problem areas was lack of consistent coating adhesion during static and dynamic flow tests at cryogenic temperatures. Further, substrate processing requirements necessary to develop good coating adhesion had to be modified for the individual metal alloys. Initial attempts were to solve these problems on an individual basis although coating adhesion, precoating preparation, and thermal processing problems were related. The following sections present Rocketdyne's approach toward solving the problems relating to coating adhesion and substrate processing during coating application and development.

Adhesion of Coating. Loss of coating adhesion may occur when the material is applied to an improperly prepared substrate or when the thermal strain differential between the substrate and the coating exceeds the strain capability in the coating at the operating temperature of -423 F.

Reduction of Thermal Strains. Modifications were made in the composition of the basic KX 635 material to reduce its thermal contraction further. Basically, fillers were added to the as-supplied KX 635 material to lower the thermal contraction of the composite coating. Additional quantities of glass microballoons were added to the material, and Lithafrax 2121 (a powdered grade of lithium aluminum silicate, which has a negative thermal coefficient of expansion) was evaluated. These fillers were added individually and in combinations to the KX 635 materials.

In addition to the reduction in thermal contraction, two empirical criteria were established for determining the maximum filler loading of the KX 635 dispersion material. First, fillers were added until the material could not be practically applied by conventional spray-coating techniques to metal substrates representative of the geometry of LH₂ turbopump parts that would have to be coated. Also, even if a coating with extremely low thermal contraction values could be successfully sprayed on all of the proposed parts, the cured coating had to have enough resin to be reasonably tough, have sufficient low-temperature ductility, be smooth or capable of being smoothed, and be resistant to erosion caused by contact with high-velocity cryogenic fluid flow.

High solvent contents were evaluated to reduce the viscosity and make it easier to spray the heavier filled materials. However, the higher solvent content resulted in greater coating shrinkage during cure of the coating. These prestressed coatings tended to separate more easily from the primed substrate during cryogenic thermal cycling than did the material without solvent addition. Filler loadings greater than 16.5 parts per hundred (pph) glass and 16.0 pph Lithafrax would have reduced the contraction of cured coatings further. However, they resulted in materials so viscous that they could not be applied using normal spray-coating techniques. Quantitative contraction measurements were not obtained for these heavily loaded materials.

Figure 32 shows the total contraction from ambient temperatures down to -423 F of several of the most promising materials based upon KX 635, along with comparative data for titanium and aluminum. These preliminary data for the modified materials were obtained using replicate determinations and nonstandard dilatometric samples. Therefore, the values may be slightly in error. For comparative purposes, however, the effect of adding fillers to Kel-F resins is clearly shown. For example, the total contraction from 70 to -423 F for Kel-F 81 resin is approximately 0.0105 in./in., while the standard KX 635 (with about 11.5-percent glass microballoons and a total solids content of 60 percent) has a total contraction over the same temperature range of 0.0066 in./in. The addition of 5 pph glass microballons further decreases the contraction to 0.0047 in./in., while the addition of 16 pph Lithafrax reduces the contraction to 0.0044 in./in. The combination of 5 pph glass plus 16 pph Lithafrax added to the standard KX 635 resulted in essentially an additive effect, with the total contraction reduced to 0.0033 in./in. from 70 to -423 F. The contraction for this material may be seen to be less than that of the Tens-50 aluminum casting alloy frequently used for cryogenic turbomachinery applications. Table 7 summarizes the data obtained for the KX 635 based coating materials regarding their total solids content, quantity of low contraction fillers added, percentage of solids composed of low contraction fillers, and the total contraction from 70 down to -423 F for each of these materials.

Substrate Preparation and Processing. The importance of preparing substrates for subsequent coating application cannot be over emphasized. In general, this preparation includes cleaning, chemical etching or abrasive blasting, and priming. The coating is then applied and cured to the previously prepared substrate. Because of potential strains resulting from the low-temperature operating environment and the inherent brittleness of the coatings at cryogenic temperatures, these preparatory processing steps must be meticulously followed if the coatings are to be successfully utilized.

Two metal substrates, a titanium alloy (Ti-5Al-2.5Sn), and an aluminum casting alloy (Tens-50), commonly used in the fabrication of LH₂ turbopumps,

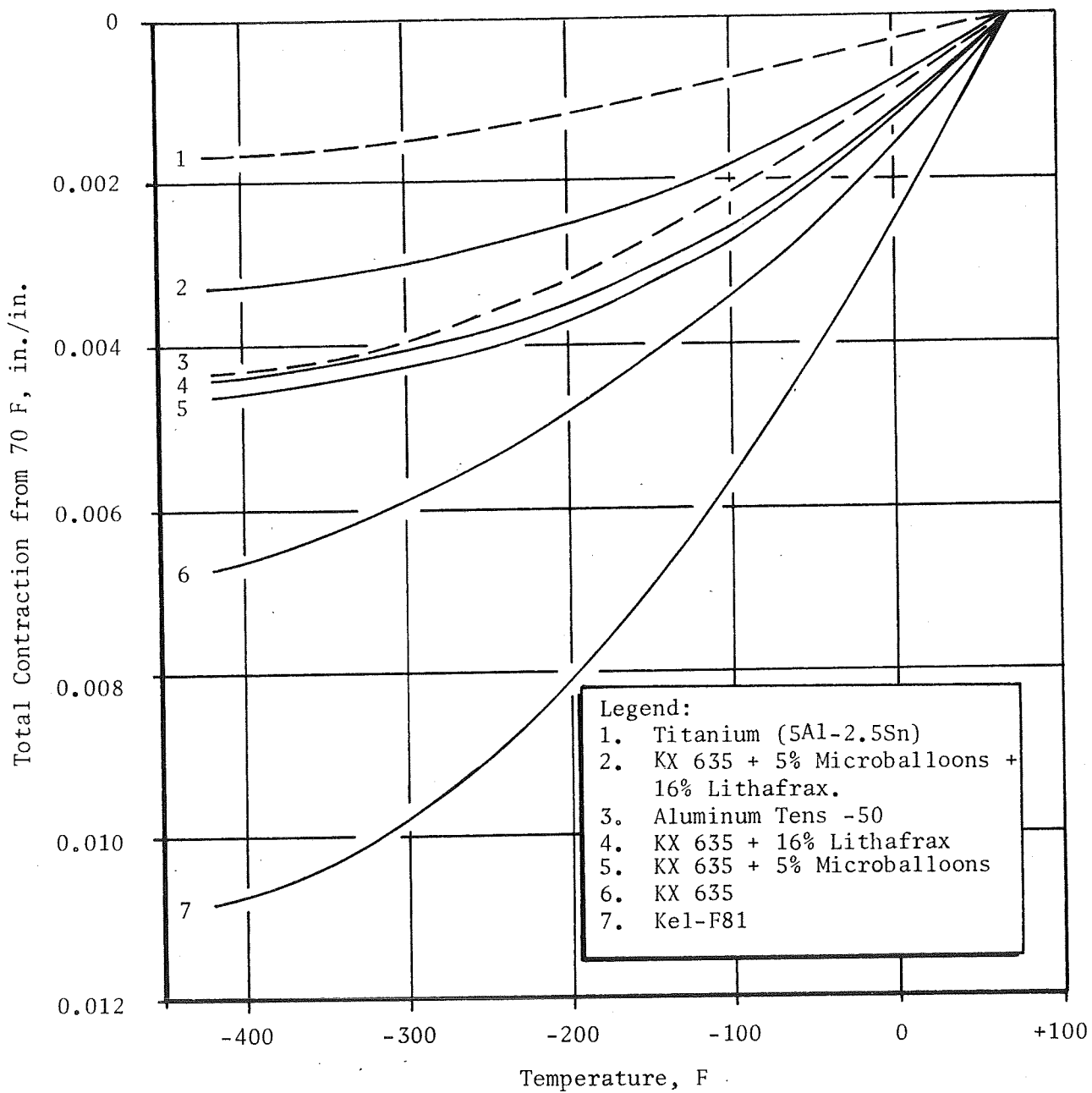


Figure 32. Thermal Contraction of Various Coatings

TABLE 7

COMPARISON OF KX 635-BASED MATERIALS
TO KEL-F RESIN

Description	Total Solids, Percent by weight	Quantity of Fillers Added, pph	Amount of Low Contract Fillers In Total Solids, percent	Total Contraction 70 to -423 F, in./in.
Kel-F 81	100	0	0	0.0107
KX 635 (standard)	60	11.5 glass microballoons	19	0.0066
KX 635 + Microballoons	62	16.5 glass microballoons	26.5	0.0047
KX 635 + Lithafrax	65.5	11.5 glass microballoons 16.0 Lithafrax	42	0.0044
KX 635 + Microballoons + Lithafrax	67	16.5 glass microballoons 16.0 Lithafrax	48.5	0.0033

were utilized during this phase of the coating evaluation program. Each of the materials had unique problems that had to be solved before organic coatings for cryogenic service could be applied to them. A discussion describing the processing techniques developed for each of the materials is presented below.

Titanium. It is much more difficult to prepare the surface of titanium for bonding or coating than it is for aluminum. Because this was basically an experimental program, the usual prebonding, nitric-phosphoric acid etch of titanium was not used for completed components. Therefore, the surface was solvent wiped with a thermally degreased Ketone at 675 ± 25 F and grit blasted with new 100-grit garnet.

For normal coating applications, KF 7 640 dispersion primer would be applied and cured to this freshly prepared titanium surface. However, it was found

through simple cryogenic tensile tests of coated titanium samples (described below), that additional processing steps were required to prepare the titanium for the KX 635-based coating systems.

The following sequence was used to develop a reliable bond at cryogenic temperatures between the coating and the prepared titanium surface. By definition, this joint had to have sufficient cryogenic strain capability to remain bonded to the metal surface up to the yield strain point of the titanium.

First, titanium tensile samples were prepared with the primer applied directly to the clean, grit-blasted surface and cured at 500 F. Subsequently, the samples were coated and fused using the KX 635-based materials. Tensile tests at -320 F indicated that the primer tended to separate from the titanium before its yield point was reached. A complete adhesive separation occurred between the grit-blasted titanium surface and the coating primer, regardless of which filler combination was utilized. This indicated that the thin primer layer with a contraction rate similar to Kel-F 81 resins could not absorb the total cryogenic differential strain between itself and the titanium substrate.

An inorganic, bonded, aluminum coating on the titanium was then evaluated to reduce the thermal strain at cryogenic temperatures between the metal substrate and the insulative coating system. Coated tensile samples were made and tested at ambient and cryogenic temperatures with this aluminum coating on the titanium substrate. Results indicated that there was still an adhesive separation between the aluminum coating and the KF 640 primer. However, it was observed that there was an extremely thin aluminum film on the bottom of the primer layer. Visual examination of the inorganic bonded aluminum surface under 15X magnification indicated that there seemed to be a somewhat nonadherent film on the aluminum surface. Subsequently, it was found that this film could be removed by pneumatically peening the surface with fine glass beads.

The final, successfully used treatment of titanium for this insulation program, therefore, included these steps. The titanium was solvent cleansed, thermally degreased, and grit blasted as previously described. A single layer of inorganic, bonded aluminum coating was then applied and cured at 650 F. Finally, the nonadherent surface film was removed by glass-bead peening.

Titanium tensile samples made using these precoating procedures were successful in meeting the ambient and cryogenic temperature strain capability of the total metal-coating system.

Aluminum Preparation. Tens-50 aluminum specimens were prepared for subsequent coating using standard adhesive bonding preparation techniques. The surface was solvent cleaned and grit blasted similarly to the titanium samples. However, the thermal degreasing cycle was omitted because it would anneal the heat-treated aluminum. After grit blasting, residues were removed from the surface using GN_2 . The KF 640 primer was then applied and cured similarly to the titanium, except that the temperature was reduced from 500 to 470 F to minimize the deterioration of the heat treat condition.

The sensitivity of heat-treated aluminum to the temperatures required to fuse the various organic coating systems was a limiting factor in the selection of coatings for aluminum alloys. Earlier work (Appendix A) using KX 635 required cure schedules that annealed the aluminum alloys. During a previous coating program at Rocketdyne, a cure schedule for KX 635 was developed that permitted a coating deposition of approximately 1/8-inch thick while maintaining a T-710 heat treat condition on Tens-50 aluminum. By controlling cure temperature, cure time, and solvent evaporation schedules, coating thickness per cycle was increased from the 0.020 inch (recommended by the supplier of the material) to approximately 0.060 inch.

Plasma Coating Systems

Material Selection. The following materials were selected for study based on their availability as plasma-spray powders and physical and mechanical

properties:

Resins

Polyamide, Zytel 101

Epoxy, 800 F

Chlorinated Polyether, 803 F (Penton)

Polyethylene, 807 F

Kel-F 6061

Pigments and Fillers

Titanium Dioxide, R-900

Zinc Oxide, SP-500

Lithafrax 2121

Processing Technique. In the plasma-spray process, powders of the desired coating materials are fed via a carrier gas (argon) into a plasma-arc flame where they are then propelled in the molten state onto the substrate. The molten particles are quenched on contact with the cooler substrate, and a solid film results. The molten particles conform to the contour of the surface, providing intimate contact and correspondingly good adhesion. Generally, more surface contact area is obtained by blasting the surface with a coarse grit (20 mesh) prior to spraying.

The optimum molten state of the particles is determined by trial and error. The flame temperature is controlled over a wide range by varying the power input (voltage and/or amperage). Generally, the lower the melting point of the material being sprayed, the lower the power requirements. The molten stage also can be controlled to some extent by varying the torch-to-specimen distance, i.e., the farther away, the cooler the particles will be on impact. A third method of controlling the molten state to some degree is the location of powder feed into the plasma stream. For lower melting materials, particularly plastics, the front electrode is designed to feed the powder into the stream well ahead of the gun where the flame is relatively cool. Higher melting materials are fed into the stream either at the nozzle exit or even

through a port on the inside of the nozzle. For example, better Kel-F coatings have been reported when using a high-velocity electrode, which has an attachment for feeding the powder at the exit of the electrode, rather than when using the standard plastic electrode. Other methods of controlling the molten condition of the particles are by varying the arc-gas flowrate, the powder-gas flowrate (whether the particles are fed into the center or edge of the plasma flame), and the type of arc gas (for its heat capacity, ionization properties, etc.).

Frequently, the best coatings may not be obtained with the optimum control of the above variables because of oxidation of the particles by the surrounding air. Also, rapid quenching of the particles on impact results in the deterioration of physical and mechanical properties of the coating (thermal cracking and spalling). Other controls such as spraying in an inert atmosphere and preheating the substrate at a higher temperature are used to reduce or eliminate these effects. Most plastics require some degree of substrate preheating for proper coating properties.

Fabrication and Test of Coated Samples. A Plasmatron SG-1 plasma gun was used throughout the program. Most coatings were deposited with standard plastic-spray electrodes; however, Kel-F and pigmented (or filled) Kel-F coatings were sprayed using high-velocity electrodes. A venturi-type feeder-hopper and a Plasmatron Roto-Feed hopper was used for applying the epoxy coatings to the test specimens.

All substrates sprayed were first grit blasted with 20-mesh aluminum. Thermocouples were attached to the back side of thermal cycle test panels so that some control of substrate temperature could be maintained during processing. Pure powders, as were some mixed powders, were fed into the plasma flame through the feeder hopper without any previous processing. Later in the program, pigmented (or filled) powders were ball-milled for 12 hours and then sieved to various size ranges. The type of feeder system and parameters used for each powder are shown in Table 8.

TABLE 8

PLASMA-SPRAY PARAMETERS AND THERMAL CYCLE RESULTS FOR PURE POWDERS

Test No.	Material	Arc Gas	Substrate	Substrate Temperature, F	Hopper Type	Coating Thickness, inch	Remarks
1	Polyamid (Zytel 101)	Argon + Helium	6061-T6	250	Venturi	-	Familiarization tests; coating discolored and sagged
2	Polyamid (Zytel 101)	Argon + Helium	6061-T6	250	Venturi	-	Same as above
3	Epoxy (800-F)	Argon	6Al-4V Ti	185	Venturi	-	Fine mud cracks on first thermal cycle; no chipping when impacted after tenth cycle
4	Penton (803-F)	Argon	6Al-4V Ti	300	Venturi	-	Cracked open to substrate on second thermal cycle
5	Polyethylene (807-F)	Argon + Helium	6Al-4V Ti	300	Venturi	-	Cracked open to substrate on third thermal cycle
6	Epoxy (800-F)	Argon	Tens-50	185	Venturi	0.014	Fine mud cracks on first thermal cycle; good adhesion when impacted after tenth cycle
7	Penton (803-F)	Argon	Tens-50	300	Venturi	0.020	Fine cracks after first cycle; chipped at corners when impacted after tenth cycle
14	Epoxy (800-F)	Argon	Tens-50	225	Roto-Feed	0.016	Fine cracks after one cycle, increasing in size through 10 cycles; passed impact test
20	Kel-F-6061	Argon	Tens-50	400	Roto-Feed	0.007	Fine cracks after three cycles; passed impact test
21	Kel-F-6061	Argon	5Al-2.5Sn Ti	400	Roto-Feed	0.007	Fine cracks after three cycles; chipped when impacted after tenth cycle

NOTE: Torch-to-specimen distance was 3 to 4 inches

Thermal shock tests were run on 1 by 6 inch panels as part of fabrication process development. The objective was to establish the optimum spraying parameters to produce coatings which could survive 10 cycles of heating to 200 F and quenching in LN_2 followed by impacting the specimen while still at approximately LN_2 temperature after the tenth cycle. The results of the thermal cycle study also are shown in Table 8.

Familiarization tests were conducted with nylon (Zytel 101 polyamide) powder (tests No. 1 and 2 of Table 7) to check out the equipment and the operator. Only this powder and the 6061-T6 aluminum alloy panels were available at the initiation of the program. The results were encouraging in that the coating did not flake or spall during application, but there was some evidence of particle deterioration. Sagging was caused by inadequate control of other variables.

The second series of tests (No. 3 through 7, Table 7) were conducted on an epoxy (800 F), a chlorinated polyether (Penton, 803 F), and polyethylene (807 F), all locally available from the Plasmadyne Corporation. The spraying parameters were those recommended by Plasmadyne, except that a Roto-Feed hopper was not available at the time. A substrate temperature of 300 instead of 500 F also was used for polyethylene because the substrate was Tens-50 aluminum alloy. As indicated in Table 7, the epoxy performed best, even though fine cracks formed during temperature cycling.

A review of available linear expansion data showed that thermal expansion coefficients for organic resins and plastics are some 10 to 20 times those of Tens-50 aluminum alloy and 5Al-2.5Sn titanium alloy (Table 9).

Differential expansion was, therefore, expected to be a problem because coatings were applied on preheated substrates. The fine cracks observed during the thermal shock tests on the pure resin coatings were attributed, in part, to differential expansion.

The effects of differential expansion could be lessened by mixing the resins with pigments or fillers having lower coefficients of expansion than the metal substrates. Therefore, titanium dioxide, zinc oxide, and

TABLE 9

APPROXIMATE THERMAL EXPANSION COEFFICIENTS

<u>Materials</u>	<u>Coefficient of Expansion, 10⁻⁷ in./in./F</u>
Resins and Plastics	
Epoxy	330
Polyester	450
Polyamide (Nylon)	480
Chlorinated Polyether (Penton)	660
Polyethylene	1050
Metal Substrates	
Titanium Alloy	53
Tens-50 Aluminum Alloy	120
Pigments and Fillers	
Lithium Aluminum Silicate (Lithafrax)	-5
Zinc Oxide	18
Titanium Dioxide	42

lithium aluminum silicate (Lithafrax) powders were mixed 1 to 4 parts resin by volume, and the thermal shock tests repeated. Information obtained from Janowiecke and Willson indicated that this ratio and special powder preparation (ball milling and sieving) produced promising coatings by the plasma-spray process.

The spraying parameters and thermal shock test results on the mixed-powder coatings are shown in Table 10. As expected, the addition of pigment or filler reduced the amount of cracking. The coatings selected from Tables 9 and 10 for further study were the pure epoxy and epoxy filled with Lithafrax 2121. The epoxy not only produced better looking coatings with fewer cracks, but could be deposited on cooler substrates, a factor of importance when considering the size and configuration of actual turbopump components to be coated.

TABLE 10

PLASMA-SPRAY PARAMETERS AND THERMAL CYCLE RESULTS FOR PIGMENTED POWDERS

Test No.	Material	Arc Gas	Substrate	Substrate Temperature, F	Hopper Type	Coating Thickness, inch	Remarks
8	4 Parts Epoxy (800-F)/ 1 Part TiO ₂ by Volume	Argon	Tens-50	185	Venturi	0.017	Fine cracks but better than in test No. 6; good adhesion when impacted after tenth cycle
9	4 Parts Penton (803-F)/ 1 Part TiO ₂ by Volume	Argon	Tens-50	300	Venturi	0.021	Fine cracks but improved over test No. 7; good adhesion when impacted after tenth cycle
10	4 Parts Epoxy (800-F)/ 1 Part TiO ₂ by Volume	Argon	Tens-50	185	Venturi	0.014	Few fine cracks at seventh cycle; no change when impacted after tenth cycle
11	4 Parts Penton (803-F)/ 1 Part TiO ₂ by Volume	Argon + Helium	Tens-50	185	Venturi	-	Fine cracks after three cycle; edges chipped when impacted after tenth cycle
12	4 Parts Epoxy (800-F)/ 1 Part TiO ₂ by Volume (Ball Milled)	Argon	Tens-50	225	Roto-Feed Gear 13 Setting 100	0.015	Few small cracks after seven cycles; passed impact test on tenth cycle
13	4 Parts Epoxy (800-F)/ 1 Part ZrO by Volume (Ball Milled)	Argon	Tens-50	225	Roto-Feed Gear 13 Setting 100	0.015	Fine cracks after one cycle; passed impact test on tenth cycle
15	4 Parts Epoxy (800-F)/ 1 Part Lithafrax 2121	Argon	Tens-50	225	Roto-Feed Gear B Setting 100	0.015	Very few cracks after one cycle and no increase through ten cycles; passed impact test; coating looked good
16	4 Parts Kel-F-6061/ 1 Part TiO ₂ by Volume (Ball Milled)	Argon	Tens-50	400	Roto-Feed Gear B Setting 60	0.004	Fine cracks after five cycles; passed impact test
17	4 Parts Kel-F-6061/ 1 Part TiO ₂ by Volume (Ball Milled)	Argon	5Al-2.5Sn Ti	400	Roto-Feed Gear B Setting 60	0.004	Fine cracks after five cycles; passed impact test
18	4 Parts Kel-F-6061/ 1 Part Lithafrax by Volume (Ball Milled)	Argon	Tens-50	400	Roto-Feed Gear B Setting 60	0.006	Some cracks after three cycles; passed impact test
19	4 Parts Kel-F-6061/ 1 Part Lithafrax (Ball Milled)	Argon	5Al-2.5Sn Ti	400	Roto-Feed Gear B Setting 60	0.010	Fine cracks after first cycle; chipped when impacted after tenth cycle

Epoxy pigmented with TiO_2 performed equally well as epoxy filled with Lithafrax 2121; however, the latter was chosen because of its negative expansion coefficient. It was considered that a closer match in thermal expansion (or contraction) between the coating system and the substrate would be beneficial on actual components under dynamic conditions.

Tensile and flexure test specimens were subsequently coated with epoxy and Lithafrax-filled epoxy, and the latter was plasma sprayed onto a section of a Mark 29 LH_2 turbopump inlet for testing.

COATING EVALUATION

Physical and Thermal Property Testing of Coatings

Modified Kel-F and Plasma-spray deposition coated, standard test samples using both Tens-50 aluminum and Ti-5Al-2.5Sn titanium unnotched test bars in accordance with ASTM D-671 were thermally and physically tested using cryogenic cycling, flexural fatigue, and tensile strain tests. In addition, contraction tests on modified Kel-F dispersion samples were conducted.

Cryogenic Cycling Tests

Cryogen cycling consisted of cycling representative standard test samples from -320 to 200 F for 10 cycles and visually observing any crazing or any separation of the coating from the metal substrate. The -320 F temperature was achieved by placing the test samples in a dewar flask filled with LN_2 . After attaining the required -320 F temperature, each sample was examined for surface irregularities. Each sample was then placed in a 200 F, thermostatically controlled, forced-convection oven. After reaching this maximum temperature, each sample was again examined for any coating irregularities that may have occurred during the thermal cycling process. Cycling continued until crazing or loss of adhesion of the coating was noticed, or until the maximum of 10 cycles was completed.

All standard test samples with a modified Kel-F coating that were successfully completed in the cycling process are listed in Table 11. Several types of plasma-spray deposition samples crazed during cycling and were eliminated from further testing. Only two different epoxy coatings that exceeded the cycling test requirements were retained for further testing on both aluminum and titanium test bar specimens (Table 11).

Tensile Strain Tests

Tensile tests using the Instron Universal test machine at a crosshead speed of 0.05 in./min were performed at 77 and -320 F on the coated specimens that had previously passed the cryogenic cycling test. Three test bars with each coating were tested at -320 F, and two bars were tested at 77 F. Each coated metal bar was visually examined after testing for any crazing of the coating or any separation of the coating from the metal substrate as the strain was applied. No coating irregularities were exhibited until the yield point of the metal substrate was reached and when the metal substrate began necking down. On most specimens, the metal substrate had failed and, on some specimens, crazing, cracking, or lifting of the coating was due to the failure or yielding of the metal itself (Fig. 33 and 34).

The four different, modified Kel-F coatings on the aluminum substrate successfully met tensile strain test criteria (Table 11 and Fig. 34). In general, the modified Kel-F coatings on titanium exhibited few irregularities. The modified Kel-F coatings (consisting of the KF 640 primer, the KX 635, and microballons and/or Lithafrax) tended to separate between the primer and the titanium metal (Fig. 35 and 36). Addition of the inorganic, bonded aluminum coating to the titanium before the primer seemed to alleviate the adhesion problem in some samples (Fig. 37) while, in other samples, it did not help (Fig. 38 and 39). However, samples having the peened, inorganic, bonded aluminum coating had no adhesion problem (Fig. 40 and 41) between the titanium surface and the coating itself. Comparison of Fig. 39 and 41 shows identical coatings, Fig. 41 having the peened, aluminum coating and Fig. 39 having no aluminum coating. No adhesion loss occurred between the coating and the titanium metal in Fig. 41,

TABLE 11
TEST SAMPLES CYCLING PROCESS

Coating Type	Metal Substrate	Thermal Cycling Performance*	Tensile Strain Performance*		Flexural Fatigue Performance*	
			77 F	-320 F	77 F	-320 F
KX 635-A	Tens-50-Al	+	+	+	+	+
KX 635-B		+	+	+	+	+
KX 635-C		+	+	+	+	+
KX 635-D		+	+	+	+	+
KX 635-A	Ti-5Al-2.5Sn	+	+	Loss of Adhesion (Fig. 35)	+	+
KX 635-E		+	Loss of Adhesion (Fig. 98)	Loss of Adhesion	+	+
KX 635-E1		+	+	+	+	+
KX 635-E2		+	+	+	+	+
KX 635-B		+	+	+	+	+
KX 635-F		+	+	Loss of Adhesion (Fig. 37)	+	+
KX 635-G		+	+	Loss of Adhesion	+	+
KX 635-C		+	+	Loss of Adhesion (Fig. 39)	+	+
KX 635-H		+	+	+	+	+
KX 635-J		+	+	Loss of Adhesion (Fig. 39)	+	+
KX 635-K		+	+	Loss of Adhesion	+	+
Epoxy-A		+	+	Loss of Adhesion (Fig. 41)	+	+
Epoxy-B	Tens 50-Al	+	+	Loss of Adhesion (Fig. 42)	+	+
Epoxy-A	Tens 50-Al	+	+	+	+	+
Epoxy-B	Ti-5Al-2.5Sn	+	+	+	+	+
Epoxy-B	Ti-5Al-2.5Sn	+	+	Loss of Adhesion (Fig. 33)	+	+

* +acceptable performance
-unacceptable performance

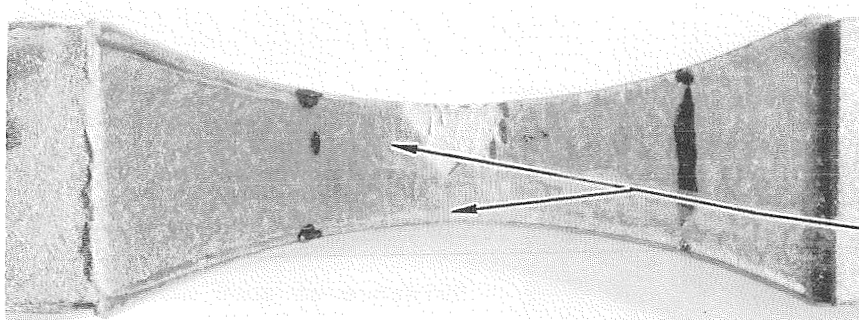


Figure 33

Test Temperature: -320 F
Base Metal: Ti-5Al-2.5 Sn
Coating Type: Epoxy - B

"Crazing" due to metal
substrate failure.

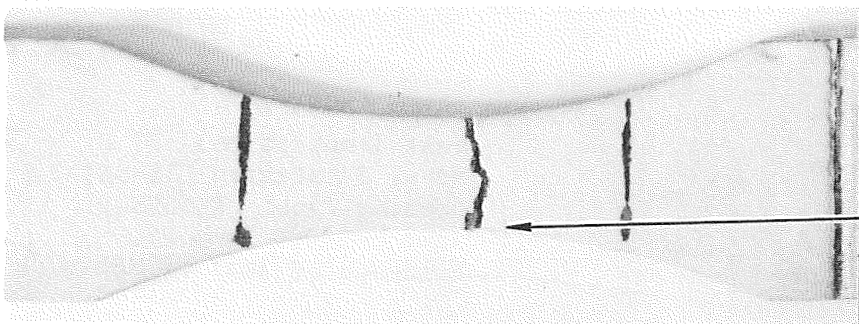


Figure 34

Test Temperature: -320 F
Metal Substrate: Tens-50 Al
Coating Type: KX 635-A

Cracking due to metal
substrate failure.

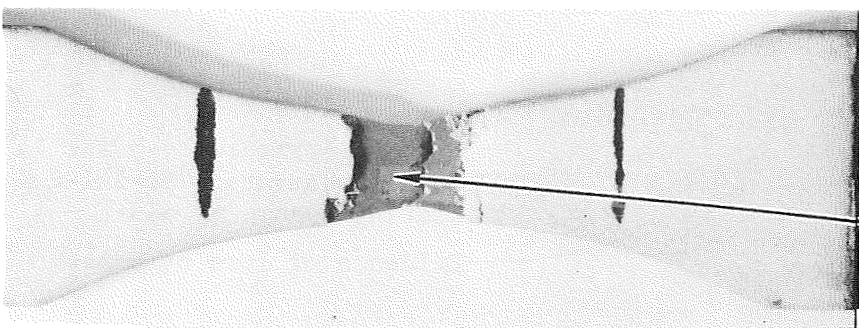


Figure 35

Test Temperature: -320 F
Metal Substrate: Ti-5Al-2.5Sn
Coating Type: KX 635-A

Evidence of loss of adhesion.

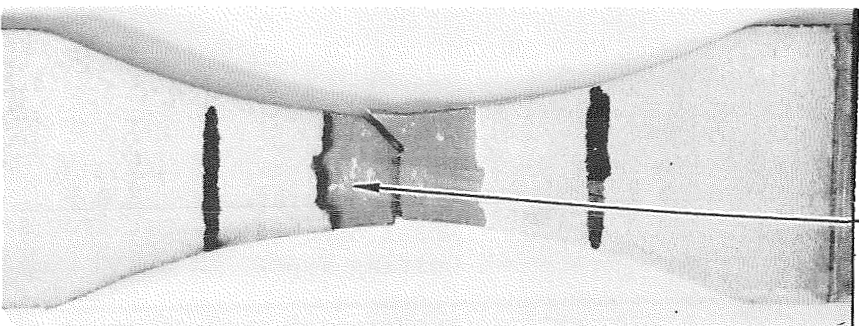


Figure 36

Test Temperature: -320 F
Metal Substrate: Ti-5Al-2.5Sn
Coating Type: KX 635-F

Evidence of loss of adhesion.

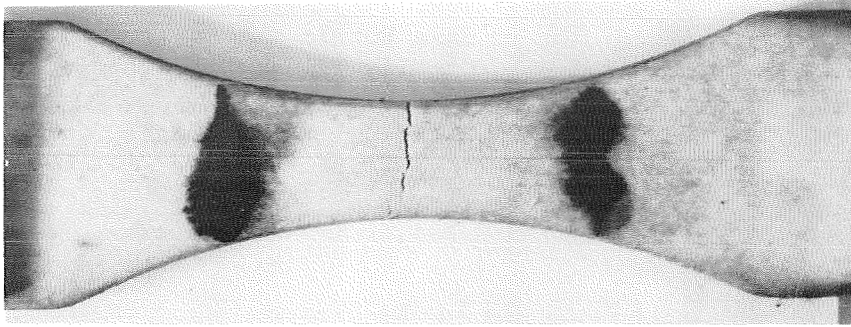


Figure 37

Test Temperature: -320 F
Metal Substrate: Ti-5Al-2.5 Sn
Coating Type: KX 635-E2

Evidence of good adhesion.

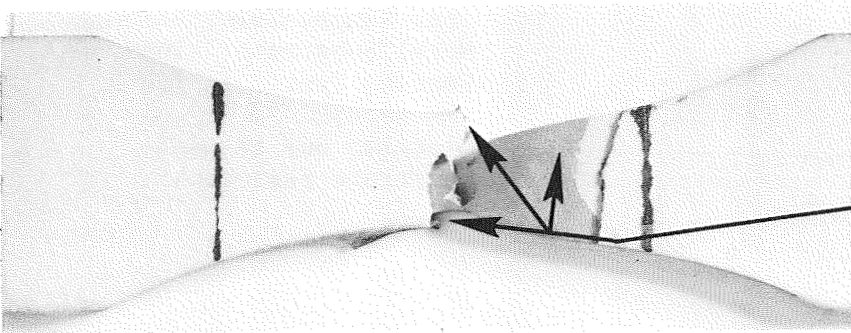


Figure 38

Test Temperature: 77 F
Metal Substrate: Ti-5Al-2.5 Sn
Coating Type: KX 635-E

Evidence of loss of adhesion

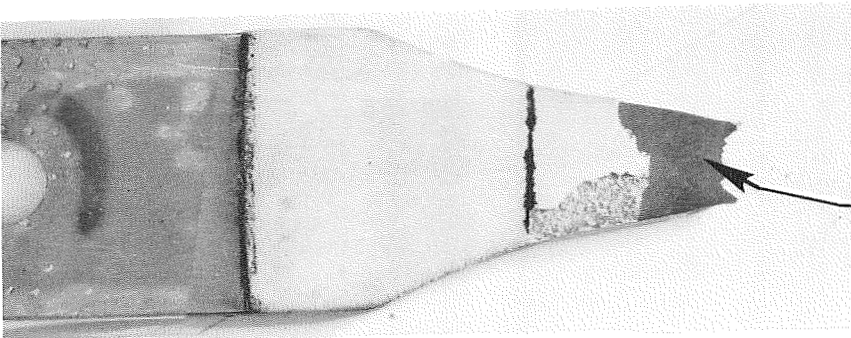


Figure 39

Test Temperature: -320 F
Metal Substrate: Ti-5Al-2.5 Sn
Coating Type: KX 635-H

Evidence of loss of adhesion.

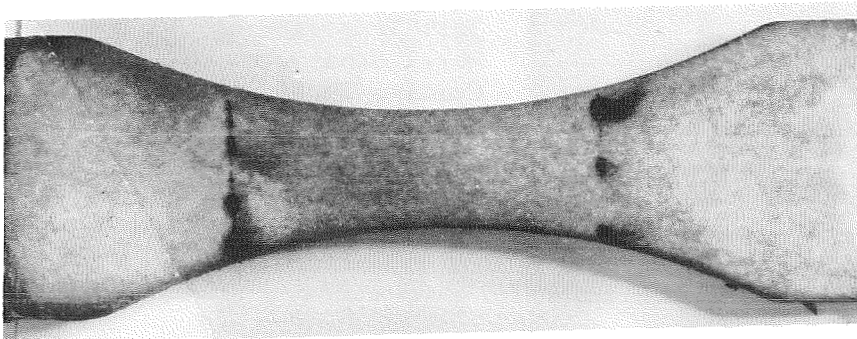


Figure 40

Test Temperature: -320 F
Metal Substrate: Ti-5Al-2.5 Sn
Coating Type: KX 635-G

Evidence of good adhesion.

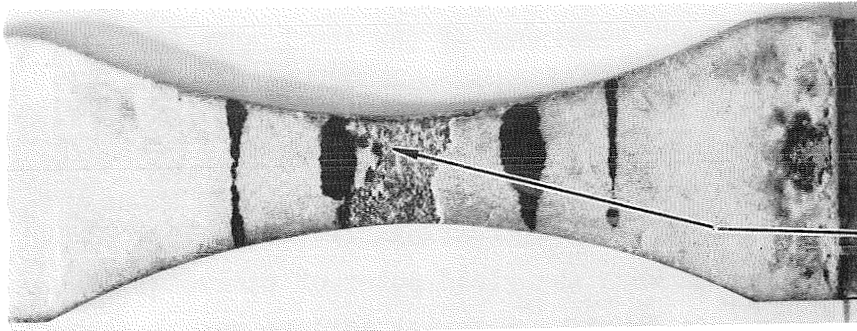


Figure 41

Test Temperature: -320 F
Metal Substrate: Ti-5Al-2.5 Sn
Coating Type: KX 635-K

Evidence of cohesive failure.

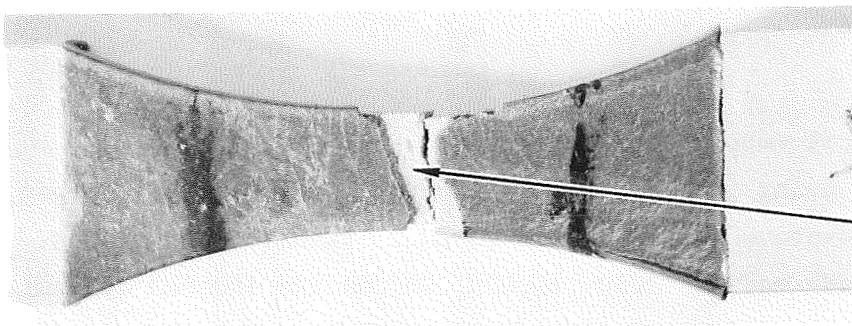


Figure 42

Test Temperature: -320 F
Metal Substrate: Tens-50 Al
Coating Type: Epoxy - A

Evidence of cohesive failure.



Figure 43

Test Temperature: -320 F
Coating Type: KX 635-C

Typical flexural fatigue test sample showing no irregularities after 100,000 cycles.

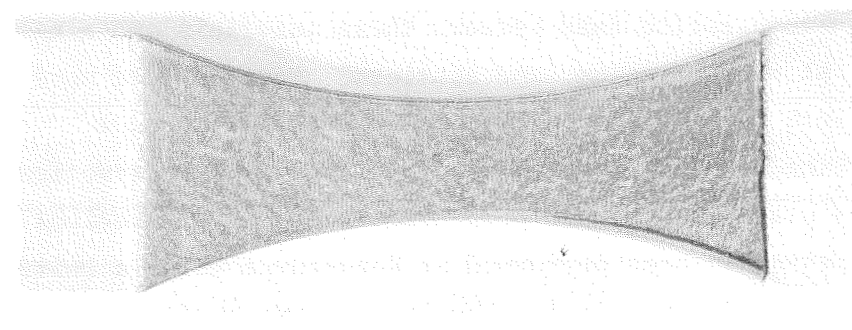


Figure 44

Test Temperature: -320 F
Coating Type: Epoxy-A

Typical flexural fatigue test sample showing no irregularities after 100,000 cycles.

as compared to Fig. 39. Loss of the remainder of the coating in Fig. 41 was similarly due to a cohesive material failure rather than an adhesive failure as described above.

During examination of the epoxy plasma-spray coatings listed in Table 11, it was found that crazing occurred when the yield point of the metal substrate was reached, resulting in a cohesive material failure rather than an adhesive failure on both the titanium and aluminum test bars (Fig. 42 and 33).

Flexural Fatigue Tests

Flexural fatigue specimens were tested at 77 F and -320 F with a total deflection of 0.10 inch using a Krause constant deflection flexural fatigue machine modified with adapters for immersion in LN_2 . Visual examinations of the test specimens were made at 2000, 10,000, 50,000 and 100,000 cycles. All of the coatings submitted for tensile strain tests listed in Table 11 showed no material failures. Therefore, three test bars of each of the coatings were submitted to fatigue testing at -320 F and two at 77 F testing. No posttest irregularities were noted on any of the samples. Figures 43 and 44 show the appearance of a typical modified Kel-F and a typical plasma-spray applied, epoxy-coated flexural test bar after 100,000 cycles at -320 F.

Contraction Tests

Contraction tests to -320 F were performed on three modified Kel-F dispersion materials using nonstandard dilatometric samples. These limited tests were performed to obtain comparative data between these materials and similar data for Kel-F 81, KX 635, titanium, and aluminum. Samples used were approximately 2 by 3/4 inch by 1/8 inch thick. Measurements were made using a dial indicator immediately after removal from LN_2 . The contraction test data with the above plate samples are presented in Fig. 32. Previous standard contraction testing has been performed at Rocketdyne using a Leitz-Wetzlar dilatometer with cylindrical samples immersed in the cryogen.

COATED PUMP TESTS IN LH_2

Those coating materials found most promising during the coating evaluation tests were selected for coating of hardware of a prototype J-2S turbopump. The coated parts were then evaluated in LH_2 turbopump hot-fire tests. Three parts from a J-2S LH_2 turbopump (S/N R006-0 and R002-2) were coated with organic coatings and tested under actual operating conditions. The three parts included the inducer fairing, inlet, and inducer which were all fabricated from 5 Al-2.5Sn titanium alloy. These parts were selected to evaluate coating material and processing problem areas that would have to be solved before coatings could be considered for production parts. Although no aluminum turbopump parts were coated, no coating problems are anticipated because: (1) thermal cycles for application and fusion of both conventional and plasma-spray coatings have been developed that do not deteriorate the heat treat condition of aluminum alloys; (2) aluminum contracts more than titanium between ambient and cryogenic temperatures, and, therefore, less thermal strain is applied on the coating; and (3) because there were fewer adhesion problems with the coated aluminum samples tested than with titanium.

The inducer nosepiece fairing presented an opportunity to evaluate an insulative coating on the outside diameter of a high-speed rotating part with simple contours. The inlet was selected for evaluating organic materials as insulative coatings of an ID cylindrical static member. Coating the external surfaces of the inducer, however, presented a much more difficult problem. The geometry of the part was more complex and resulted in severe coating application problems. In addition to the coating problems, the thermal strain requirements of the coating at cryogenic temperatures were more difficult for complex geometries. Finally, the coating has to withstand both the high-velocity fluid as well as the dynamic rotating forces including hydrodynamic blade loading, vibration, and centrifugal forces.

Inducer Nosepiece

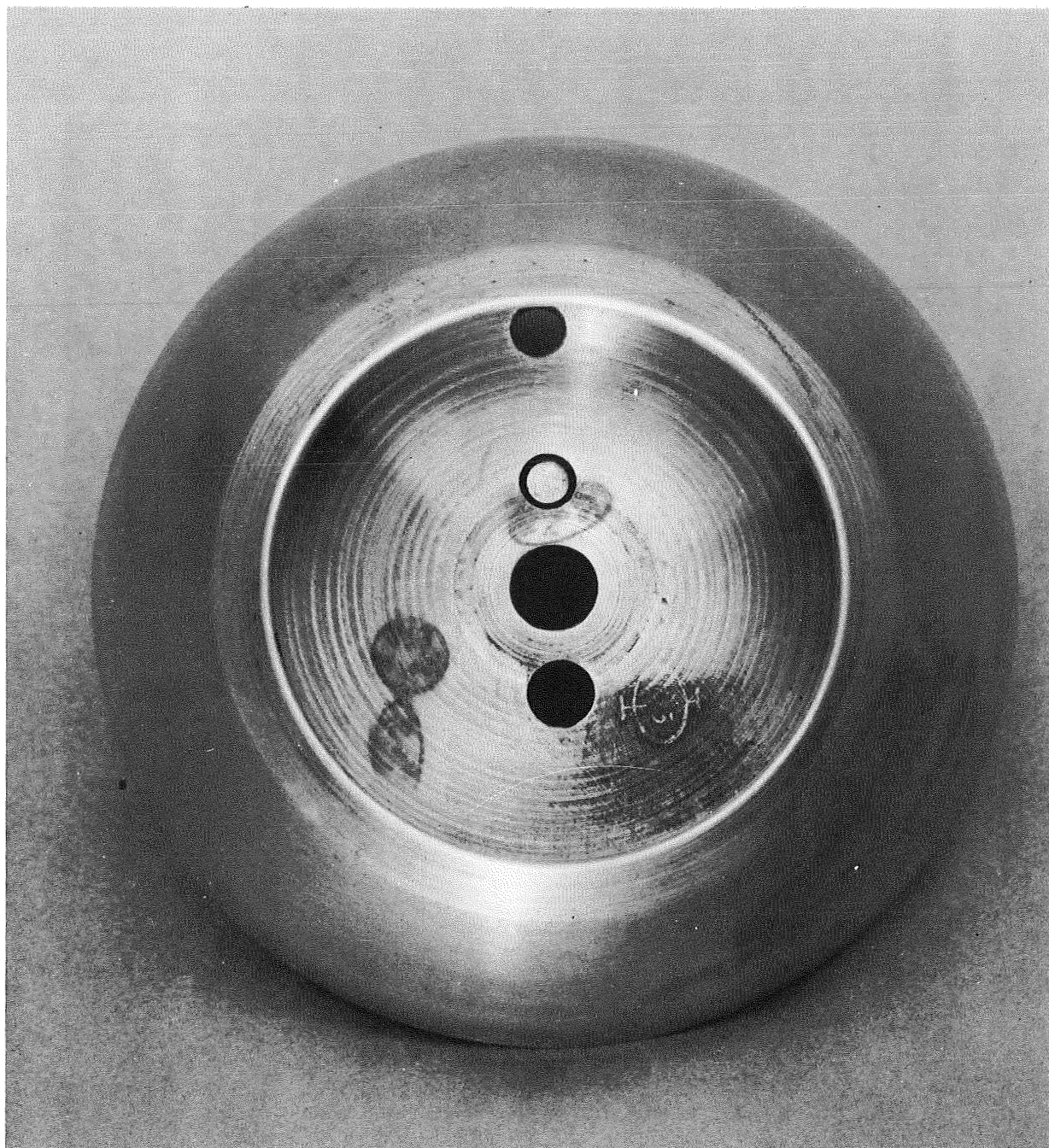
The titanium inducer nosepiece from the Mark 29 LH₂ turbopump was the first prototype hardware coated and tested. Figures 45 and 46 show the part prior to and after coating. The nosepiece was coated with the 5-percent glass-microballoon, KX 635-modified coating in accordance with previously established techniques. The coating thickness was a nominal 0.020 inch.

The coated inducer nosepiece was installed in a high-performance Mark 29 turbopump (S/NR006-0) and subjected to five hot-fire tests at CTL-3, cell 45B, Santa Susana Field Laboratories. Total time accumulated on the coated hardware was 1365 seconds; the test summary is presented in Table 12. The first test was conducted at a turbopump maximum speed of 31,750 rpm and 415 seconds duration. Four subsequent tests at maximum speeds in excess of 34,400 rpm were conducted for an additional 950 seconds duration. This speed corresponds to a maximum surface speed of ~475 ft/sec for the coated inducer nosepiece. The inducer nosepiece was removed from the turbopump and installed along with two other coated parts (inlet and inducer) in the Mark 29 LH₂ turbopump S/N R002-2 for additional LH₂ hot-fire testing. Eight tests, accumulating an additional 1221 seconds duration (Table 12), were compiled, which brought the total test time to 2586 seconds (43 minutes). These eight tests were comprised of various turbopump operation test conditions including steady-state, low NPSH, seal evaluation, and SPTS starts.

Inducer Inlet

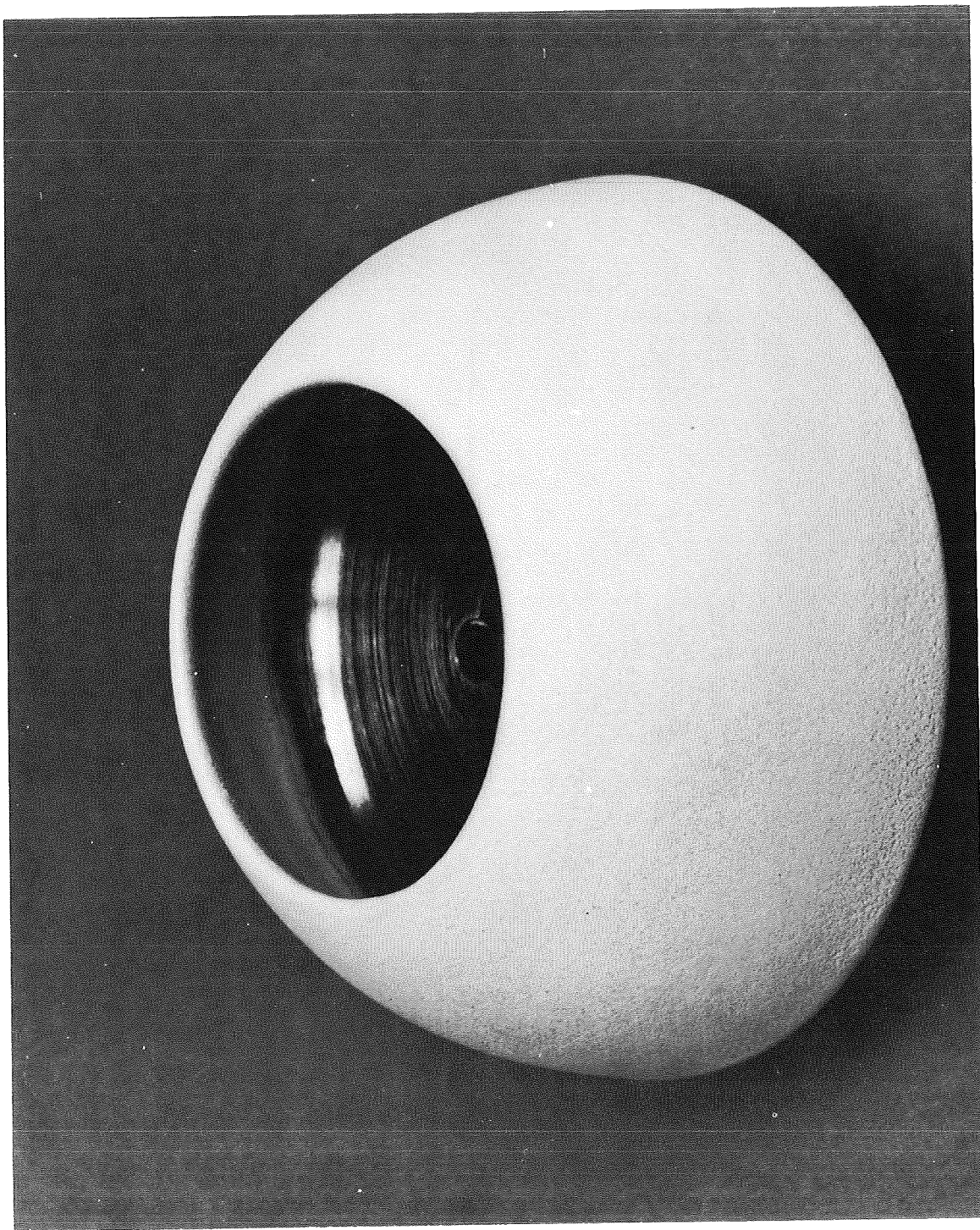
The titanium inlet ID of the Mark 29 LH₂ pump was coated with three different organic materials. Each material was coated in a complete cylinder to obtain the effects of the differential coefficients of contraction between the organic materials and the metallic substrate.

The first material on the upstream side of the inducer was plasma-coated with an epoxy resin filled with 20 percent by volume Lithafrax. Limitations governing spraying angle, as established during the processing



1YW53-7/14/69-C1A

Figure 45 Inducer Nosepiece Prior to Application of Coating



1YW52-7/18/69-C1A

Figure 46 Inducer Nosepiece After Application of Modified Kel-F Coating

TABLE 12

J-2S LH₂ TURBOPUMP HOT-FIRE TEST SUMMARY

Mark 29 LH ₂ Turbopump R006-0, CTL-3, Cell 45B, SSFL										
Test No.	Date, 1969	Duration, seconds	Maximum Speed, rpm	Type of Test	Time Slice, seconds	Speed, rpm	Pump Discharge Pressure, psig	Pump Inlet Pressure, psig	Suction Flow, gpm	Turbine Inlet Temperature, F
041	7-22	415	31,750	Steady State	350	31,744	2038	51.3	10,348	1249
043	8-7	304	34,400	Steady State	170	34,362	2408	51.5	11,161	1221
044	8-11	176	34,600	Steady State	83	34,453	2498	52.4	11,174	1130
045	8-11	195	34,600	Steady State	125	34,455	2456	50.3	11,198	1144
046	8-13	275	34,500	Steady State	268	34,463	2420	51.2	11,319	1229
5 Tests		1365								
Mark 29 LH ₂ Turbopump R002-2, CTL-3, Cell 45B, SSFL										
052	10-14	15	27,100	Steady State	8	26,921	1578	53.5	8091	913
053	10-16	357	27,800	Low NPSH	285	27,635	1469	32.0	8060	894
054	10-17	87	27,865	Low NPSH	84	27,865	1611	22.2	8179	897
055	10-21	223	27,930	Low NPSH	160	27,764	1536	19.2	8022	903
056	10-23	2.4	17,200	SPTS Start	-	-	-	-	-	-
057	10-24	389	30,465	Seal Evaluation	341	30,000	1750	50.7	9556	1172
058	10-27	2.4	17,600	SPTS Start	-	-	-	-	-	-
059	10-28	145	30,020	Steady State	140	30,000	1798	52.6	9566	1192
8 Tests		1221								

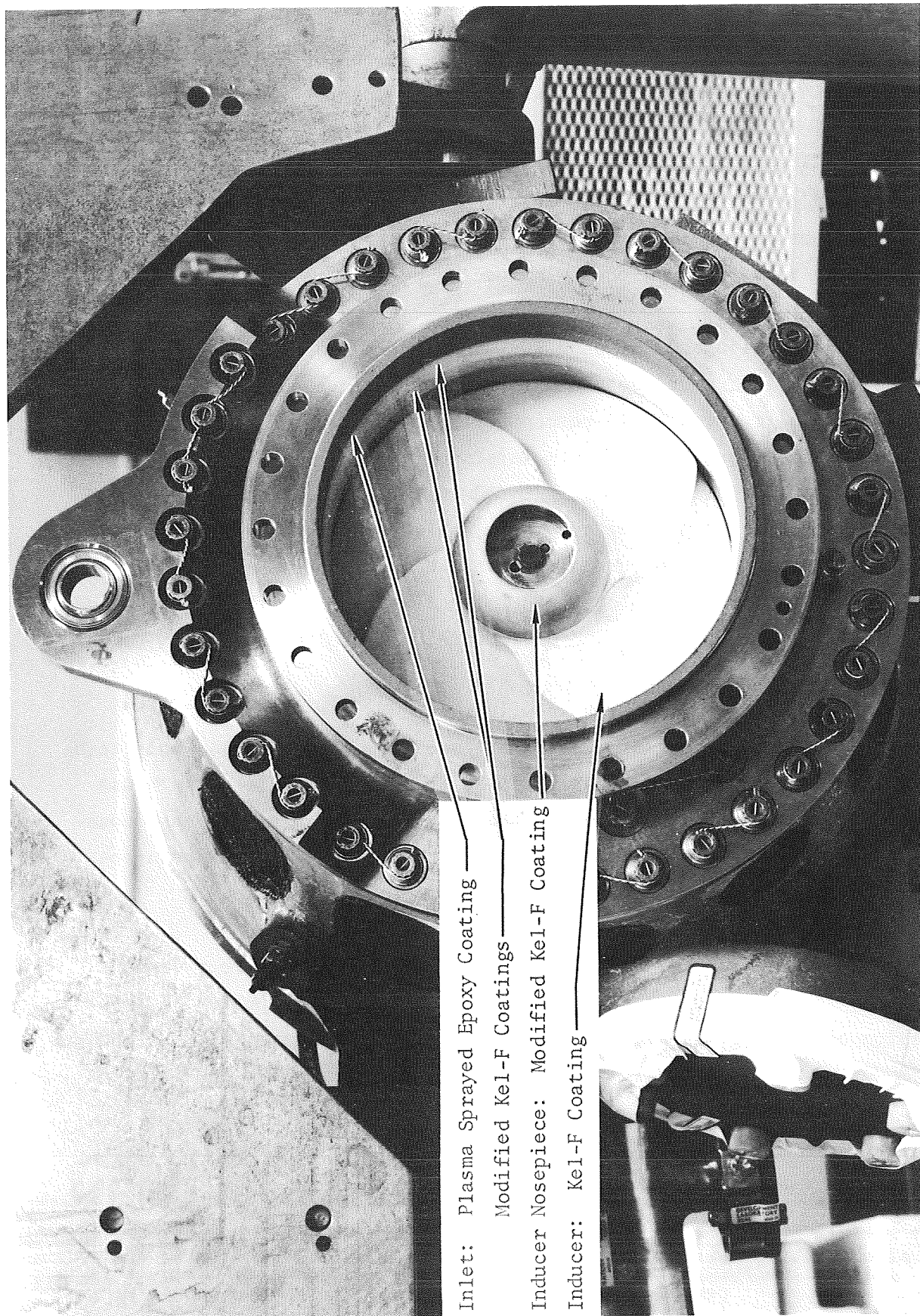
development portion of this program, made it easier to plasma spray the upstream portion of the inlet. The land area directly preceeding the ID of the inlet also was plasma sprayed with the filled epoxy material in an attempt to prevent the coating leading edge from being lifted by the flow of fluid.

The two other materials applied to the inlet were the modified Kel-F materials. The second material applied adjacent to the epoxy coating was a KX 635 Kel-F dispersion coating with a nominal 5-percent microballoon filler. The titanium surface was prepared in accordance with processing techniques acquired under the development of coating techniques effort. The leading edge of the coating was faired to eliminate the step in the flow path of the fluid.

A third material was a Kel-F coating applied to the inlet. The material was a KX 635 dispersion coating with nominal 5-percent glass microballoon and 16-percent Lithafrax fillers. The material was butted against the preceeding Kel-F material. The thickness of all coatings was a nominal 0.025 inch. The coated inlet was subjected to 10 static thermal cycles (-320 to 77 F) without loss of adhesion between the organic coatings and the metallic substrate. This part was then installed in the Mark 29 LH₂ turbopump S/N R002-2 (Fig. 47) and tested as discussed above (Inducer Nosepiece section).

Inducer Rotor

The final and most difficult piece of hardware to coat was the titanium inducer. Because of the excellent results from the coated inducer fairing tests, the same coating system was selected for the inducer. Application difficulties were encountered during the first processing attempts when the coating was sprayed onto the hub area. The particles rebounded from the target area due to the small spray angle of incidence used for applying the heavily filled material into this confined space. Some of the solid particles bounced off the hub and adhered to the blade surfaces adjacent to the hub, which resulted in a cobweb finish. Furthermore, the material tended to build up in thicknesses greater than the nominal values established.



Inlet: Plasma Sprayed Epoxy Coating

Modified Kel-F Coatings

Inducer Nosepiece: Modified Kel-F Coating

Inducer: Kel-F Coating

Figure 47 Mark 29 LH₂ Pump With Coated Internal Parts

1XY52-9/23/69-C1

The primary cause of this difficulty may be attributed to the sprayed material being too heavily filled with the low contraction fillers. There were insufficient Kel-F resin in the total mixture to produce a uniform, cured coating with good cohesive strength. To minimize the particles from bouncing and producing the cobweb finish, the spraying pressure was reduced. This caused an inadequate impact force of the sprayed particles and the target which resulted in a poorly compacted coating in the cured state.

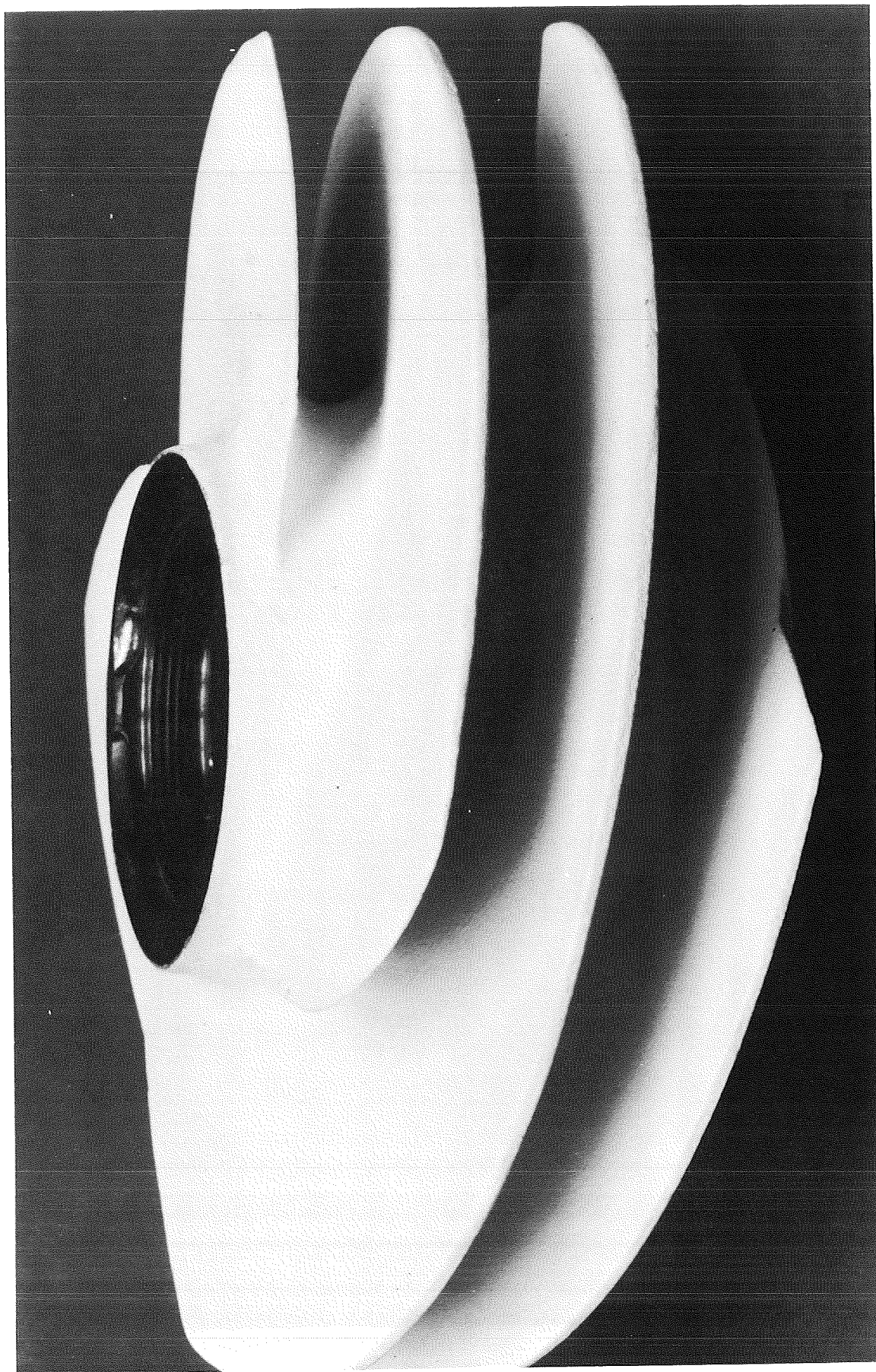
Because the initial material used contained approximately 20-percent glass-microballoon filler added to the base resin, the second inducer was coated with a material reduced to 14-percent filler. By reducing the filler percentages, thinner and more uniform layers of the Kel-F material were applied to the surface. This slight reduction in solid content also allowed an increase in spraying pressures, which resulted in a more dense and uniform coating. Good cohesive strength and proper thickness limits previously established were obtained. The final coating thickness was a nominal 0.05 inch on the hub and 0.010 inch on the blades.

Alternative coating application solutions were examined to reduce the viscosity of the sprayed material by the addition of solvents. This technique would decrease the percentage solid content and allow an increase in spraying pressures, which would produce a more uniform and dense coating. Samples were sprayed and examined, but because of the evaporation of the additional solvents, a spongy coating finish resulted.

The second coated inducer was subjected to 10 low-temperature thermal cycles in LN_2 from -320 to 77 F without cracking or any apparent loss of adhesion of the organic material to the metallic substrate (Fig. 48 and 49). The inducer was installed in the Mark 29 LH_2 turbopump (S/N R002-2) and hot-fire tested (Table 12).

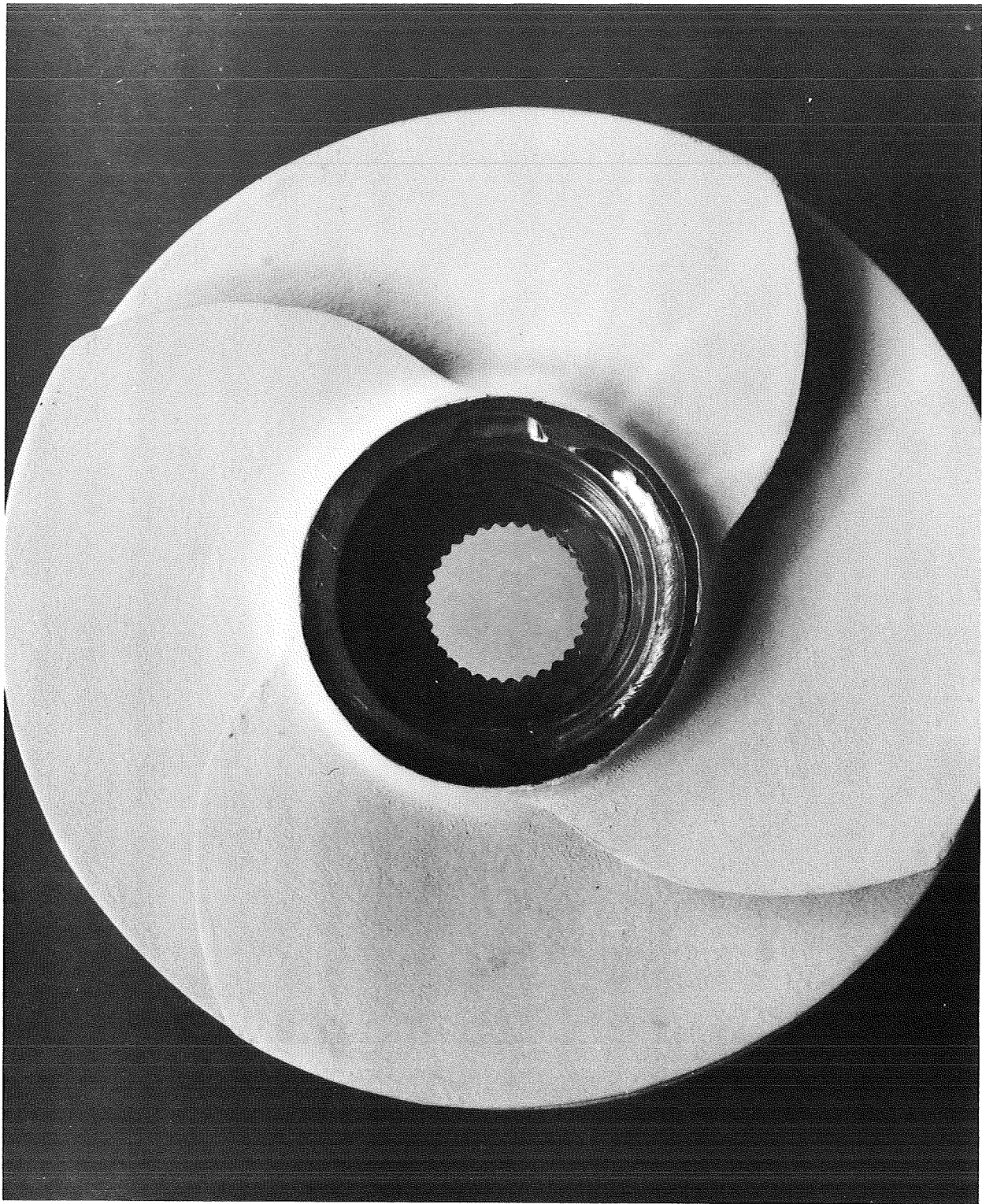
ANALYSIS OF THE LH_2 PUMP COATING TESTS

Visual examinations were conducted for analyzing each of the three coated titanium component parts. These observations were conducted when time was permitted between the turbopump hot-fire tests.



IYW52-9/10/69-C1C

Figure 48 Coated Inducer After 10 Static Thermal Cycles From -320 to 200 F



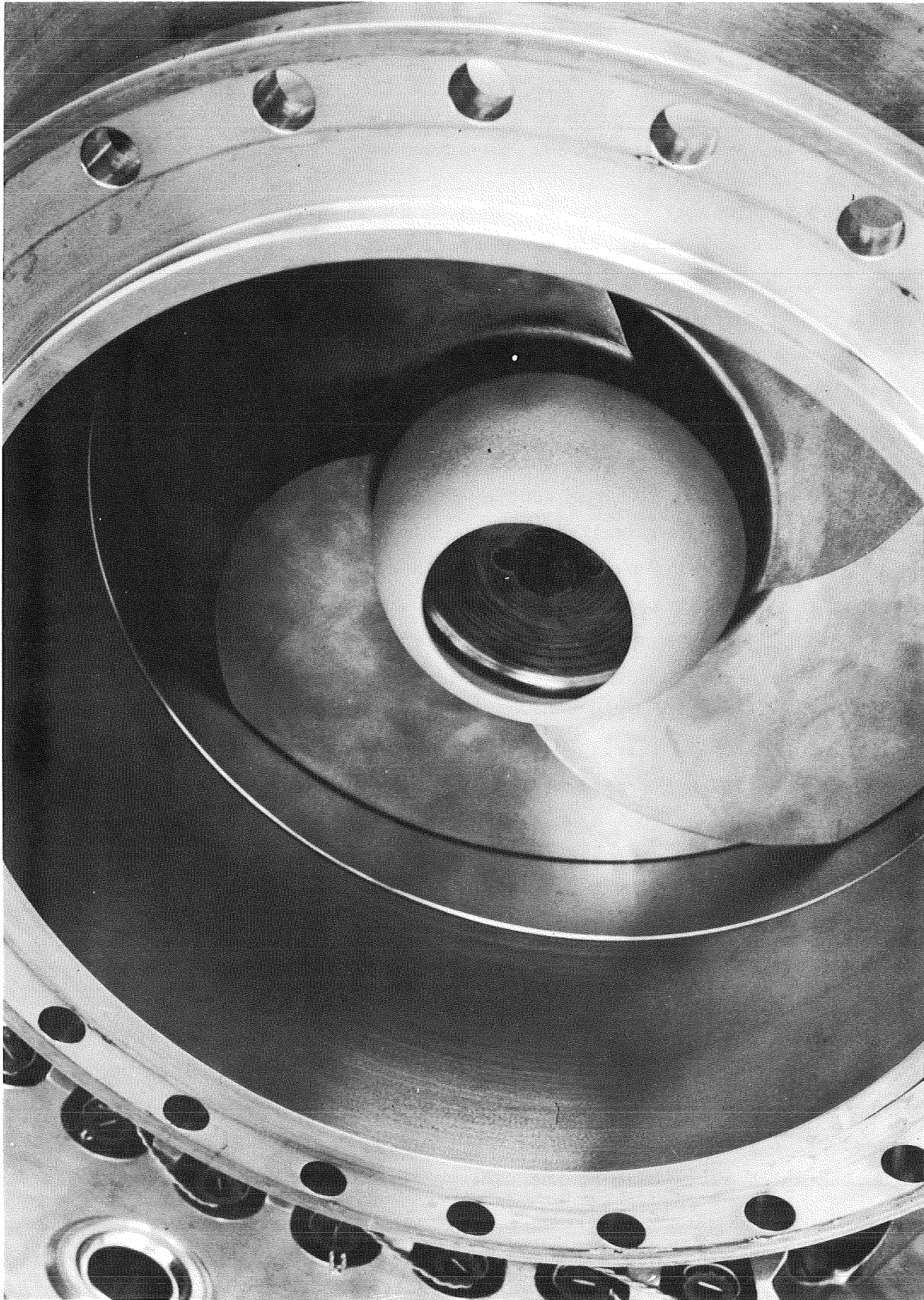
1TW52-9/10/69-C1B
Figure 49 Coated Inducer After 10 Static Thermal Cycles From -320 to 200 F

The examinations for each of the coated parts are discussed separately in the following sections.

Inducer Nosepiece

The coated (conventionally applied KX 635 with 5-percent microballoon filler) inducer nosepiece (Fig. 46) was first installed and tested in J-2S Mark 29 LH₂ turbopump (S/N R006-0). The first visual examination was performed after completing test No. 41 (Table 12). The duration for this test was 415 seconds, and the maximum speed was 31,750 rpm. The coating was in excellent condition, and is shown in Fig. 50 . Four additional high-speed, hot-fire tests were conducted at speeds up to 34,600 rpm to complete the test program for this turbopump build. This maximum test speed corresponds to an equivalent coating tip speed of 475 ft/sec. This second examination revealed that the nosepiece remained in excellent condition after the five tests which accumulated a total test duration of 1365 seconds (22.75 minutes). No loss of adhesion of the coating to the substrate, cracking, spalling, or any other anomalies in the coating was noted from the posttest condition. This nosepiece is shown posttest in Fig. 47 in the Mark 29 LH₂ (S/N R002-2). The turbopump was later reassembled utilizing the coated inlet, inducer, and the inducer nosepiece. This turbopump build was then hot-fire tested at the various test conditions listed in Table 12. A visual examination was conducted after three LH₂ turbopump hot-fire tests were completed with this build. The additional duration for these tests was 459 seconds, and the maximum rotating speed was 27,865 rpm. The coating was in excellent condition except for numerous small nicks that were sustained from impact of foreign material.

Five additional tests which included low NPSH, SPTS start, seal evaluation, and a steady state were conducted to complete the test program. The accumulated total tests and test time were 13 runs and 2586 seconds (43.1 minutes), respectively. On completion of the testing, a visual examination was conducted which revealed that the coating appeared in the same good



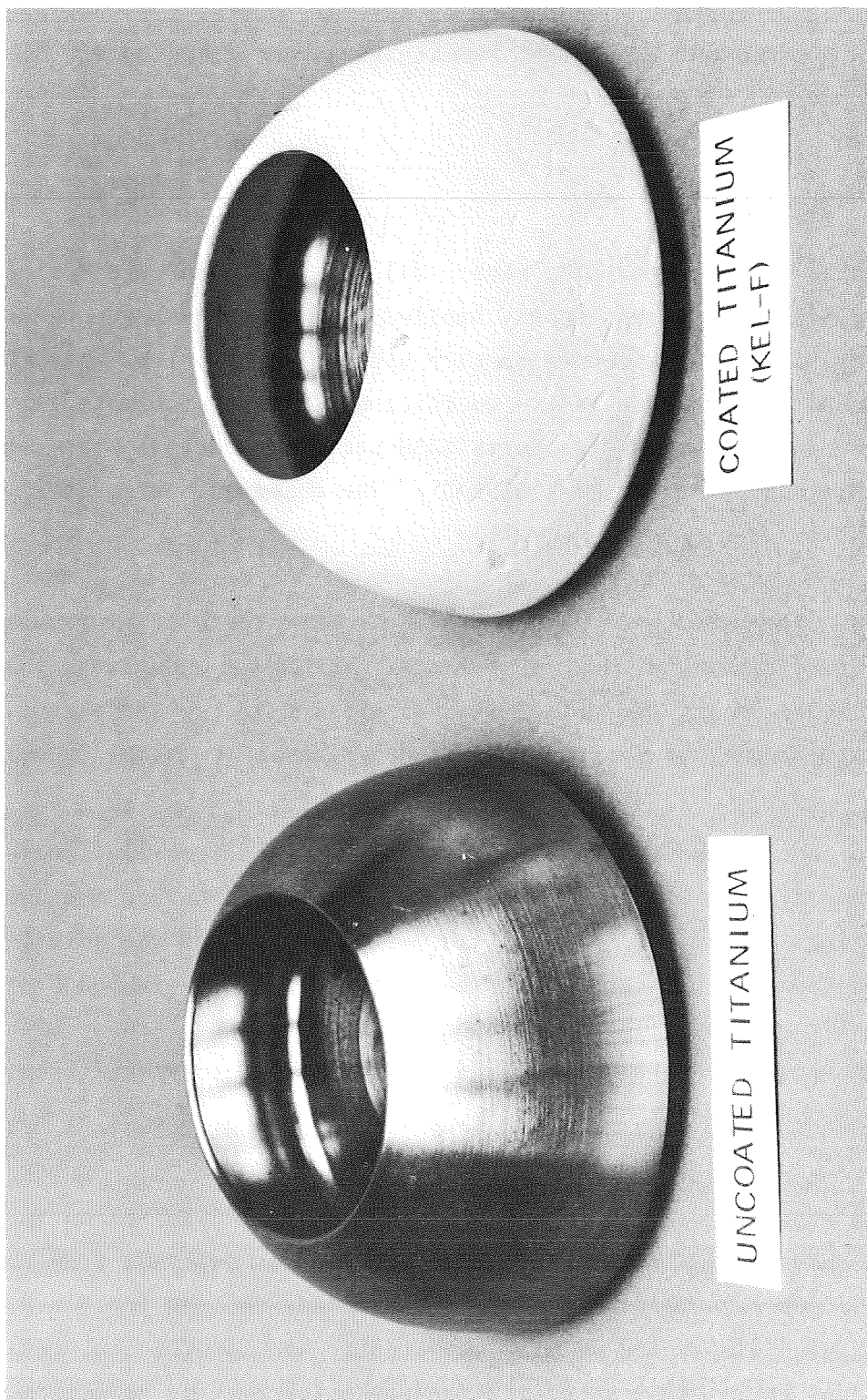
ICS35-7/25/69-S1
Figure 50. Coated Inducer Nosepiece After 415 Seconds of LH_2 Pump Testing

condition as the preceding inspection. Figure 51 shows the posttest condition of the coating. Note the small nicks that were attributed to the impact of foreign material. Other than these small nicks, the coating material was in excellent condition, showing excellent adhesion and cohesion of the coating.

Inducer Inlet

The inlet coated circumferentially with: (1) the plasma-spray deposited epoxy coating, (2) the conventionally applied KX 635 with 5-percent microballoon filler, and (3) the conventionally applied KX 635 with 5-percent microballoon and 16-percent negative coefficient of expansion material was examined after the three hot-fire tests (459 seconds duration) were completed with Mark 29 turbopump S/N R002-2. The observations obtained are as follows:

1. Plasma Spray-Deposited Epoxy Coating. No material failure was observed after the three pump tests. The small mud cracks that developed during the initial thermal cycling did not propagate, and there was no apparent loss of adhesion to the metal substrate.
2. Conventionally Applied KX 635 Plus 5-Percent Microballoon Filler. This coating was essentially intact. A slight removal of material was noticed at the joint between the epoxy coating and the above coating. The Kel-F material was feathered down at the joint, and this apparent chipping of the coating was probably caused by the erosive action of the high-speed fluid and is not a cause of concern because the actual coating was in satisfactory condition.
3. Conventionally Applied KX 635, Plus 5-Percent Microballoon, Plus 16-Percent Negative Coefficient of Expansion Material. A cohesive separation between the clear top coat and filled Kel-F coatings was observed. The material, however, did not separate from the metal substrate and maintained a continuous coating for 360 F. The Kel-F dispersion material apparently had insufficient resin content to maintain a satisfactory cohesive coating condition.



1YW52-12/23/69-CLB

Figure 51 Coated Inducer Nosepiece After 2586 Seconds of LH_2 Pump Testing

The remaining five tests were completed and the accumulated total tests and test time were eight runs and 1221 seconds (20.35 minutes), respectively. The condition of the coatings did not deteriorate from that observed after the 459 seconds of turbopump testing except for the plasma-sprayed epoxy coating. A 2-inch piece about one-half the coating width was missing. Figure 52 shows the coated inlet in the posttest condition.

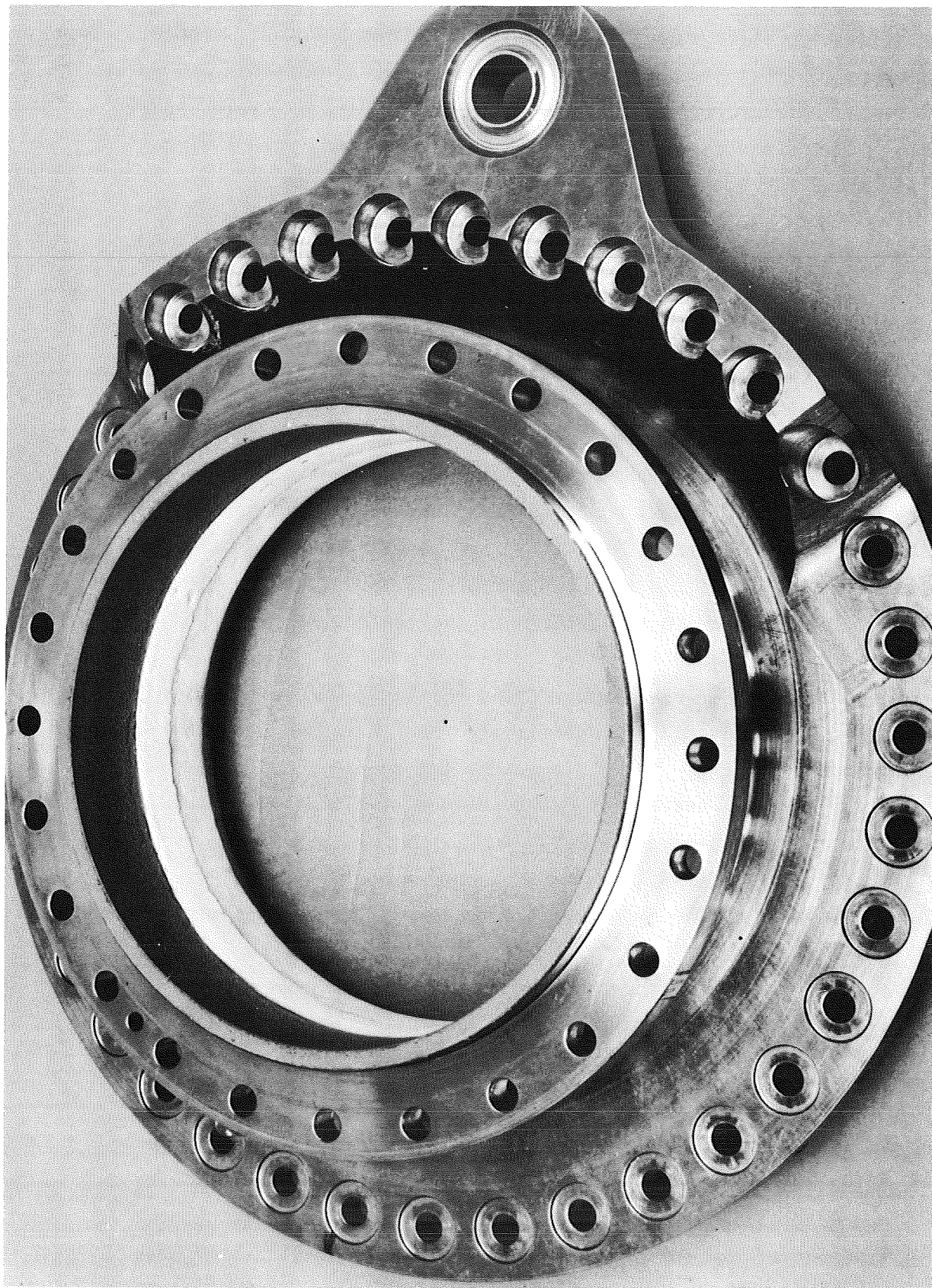
Inducer Rotor

Visual examination of the coated (KX 635 plus 5-percent microballoon filler) inducer, after the completion of the initial three hot-fire tests (459 seconds duration) with the Mark 29 turbopump (S/N R002-2), revealed that approximately 80 percent of this coating was removed from the upstream side of the inducer blades. The coating material failed adhesively, between the inorganic, bonded, aluminized coating (sermetel) and the metal substrate. The examination of the metallic substrate and residual coating material found in the system indicated that the surface of the substrate was not adequately prepared prior to application of the coating system.

The remaining five tests were completed and the inducer re-examined. The condition of the coating did not deteriorate from that observed after 459 seconds turbopump testing. The observations and conclusions discussed after the initial three tests on the condition of the coating material, therefore, remains the same.

From the examination of the hardware, the following conclusions were made:

1. The preparation of the substrate should be improved prior to application of the coating system. The surface seemed smooth when compared to the relatively rough surface necessary for good bonding of the aluminized intermediate coating to the titanium.
2. The thickness of the coating on the inducer hub was two to three times that desired. This may have led to large thermal stains and the initiation of cracks because of increased thermal contraction of the thick materials. The coating failure may have been initiated from these cracks.



1YW55-11/19/69-C1D

Figure 52 Posttest Condition of Coated Inlet

3. The LH_2 testing of the thermally coated, full-scale Mark 29 fuel turbopump, operating under severe conditions, has been a relative success. (The Mark 29 fuel inducer has encountered problems of blade vibration and fatigue.) The results of static and flexural tests on titanium and aluminum laboratory samples and actual hardware have demonstrated the feasibility of bonding Kel-F and plasma-sprayed epoxy thermal coatings successfully; however, further refinement of the application process and technique will be required.

III: ENGINE SYSTEM ANALYSES

In this task analyses to investigate engine start for various engine preconditioning and restart requirements were conducted. System preconditioning, two-phase pumping capabilities, coating effects, and the analysis of Saturn S-IVB stage fuel-lead chilldown were areas emphasized. A mathematical model of the engine was formulated and used in the study of engine operation during start and restart. Transients predicted with the model and results of the system study to evaluate liquid hydrogen pump improvements are presented. A start sequence with fuel-lead thermal conditioning of the J-2 engine system was analyzed to provide a backup start sequence in the event the normal pump recirculation preconditioning system became inoperative.

PUMP THERMODYNAMIC DESIGN LIMITATIONS

Various two-phase and inducer flow phenomena were studied and theoretically analyzed. The theoretical predictions were compared with four sets of test data. Blade blockage fraction and inducer leading edge incidence-to-blade angle ratio are two factors that can limit two-phase pumping capability and their influence on allowable inlet vapor volume fraction was determined. Other factors that can limit two-phase pumping capability are: inducer stator cavitation, choking in the annulus at the inducer blade leading edges, and vapor recirculation. These limitations can be avoided by: using thin stator blades with positive incidence at design and uncambered leading edges; using an inducer inlet annulus large enough to pass the flow during an equilibrium flow process through the pump inlet area contraction upstream of the inducer blade leading edges, and avoiding recirculation of any vapor through the inducer.

The above limits to two-phase pumping capability were used to determine the best approach to design an inducer for operation with zero tank NPSH. To minimize the required tank saturation pressure during design operation,

inducers should have large inlet diameters (low design flow coefficients) and large blade leading incidence angles. However, the latter involves a compromise with the range of two-phase pumping capability at low flow coefficients. For a given design inlet flow coefficient, decreasing the design rotational speed also reduces the required tank saturation pressure. Thus, a low-speed inducer can be used to obtain zero tank-NPSH performance.

The limits to two-phase pumping capability were also used to estimate the two-phase pumping performance of the Mark 15 liquid hydrogen pump and to predict the effects of heat rejection from a warm pump on hydrogen pump discharge pressure over a range of cold pump discharge pressures. The results were used to analyze the feed system conditions that would be encountered during restart for the Saturn S-IVB stage during flights AS-504 and AS-505 (page 174).

Two-Phase Compressible Flow

Because the constant quality, two-phase flow process Mach numbers relative to the inducer leading edge RMS diameters ranged between 0.5 and 2.0 for the inducer test data analyzed, an analysis of two-phase compressible flow was conducted to determine the conditions under which choking would occur in the inducer flow passages. A constant-quality flow process was assumed because, within an inducer, the flow velocities are high and the area changes are relatively sudden. In addition, an isothermal gas (Eq. 18) was assumed

$$\frac{\rho_v}{P} = \text{constant} \quad (18)$$

rather than an isentropic gas (Eq. 19). This was done to simplify the flow equations.

$$\frac{\rho_v}{P^\gamma} \quad (19)$$

An acoustic velocity check indicated that this is a reasonable approximation. In reality, some degree of vaporization and/or condensation will occur and, therefore, the more compressible isothermal gas assumption could approximate the real situation more closely than the isentropic gas assumption. It is felt this is justified within the existing knowledge of single-component, two-phase flow.

Equations 20, 21, and 22 are the basic flow equations used for the analysis constant quality flow process with an isothermal gaseous phase.

$$M_2^2 = \frac{M_1^2 - 2\alpha_1^2 \left[\left(\frac{1 - \alpha_1}{\alpha_1} \right) \left(\frac{P_2}{P_1} \right) - 1 + \ln \left(\frac{P_2}{P_1} \right) \right]}{\left[\alpha_1 + \frac{P_2}{P_1} (1 - \alpha_1) \right]^2} \quad (20)$$

$$\frac{A_2}{A_1} = \frac{P_1}{P_2} \frac{M_1}{M_2} \quad (21)$$

$$\alpha_2 = \frac{1}{1 + \frac{P_2}{P_1} \left(\frac{1 - \alpha_1}{\alpha_1} \right)} \quad (22)$$

For subsonic flow, M_2 in Eq. 20 and 21 was set equal to 1 and the resulting equations (Eq. 23 and 24) were solved simultaneously to obtain the choking area ratio as a function of entrance values of Mach number and vapor volume fraction.

$$M_1^2 = \alpha_1^2 \left\{ \left[1 + \frac{P^*}{P_1} \left(\frac{1 - \alpha_1}{\alpha_1} \right) \right]^2 + 2 \left[\left(\frac{1 - \alpha_1}{\alpha_1} \right) \left(\frac{P^*}{P_1} - 1 \right) + \ln \left(\frac{P^*}{P_1} \right) \right] \right\} \quad (23)$$

$$\frac{A^*}{A_1} = \frac{P_1}{P^*} M_1 \quad (24)$$

For two-phase mixtures of liquid water and gaseous nitrogen (which, of necessity, follow a constant quality flow process), R. B. Eddington (Ref. 16) proved experimentally that normal and oblique shock waves

occur in constant quality two-phase flow. In addition, he obtained excellent agreement with theoretical constant quality predictions in which the gaseous phase was assumed to be isothermal.

Because most of the two-phase hydrogen pump test data were taken at inducer inlet relative Mach numbers between 1 and 2 and because an inducer blade may be considered as a wedge with an angle of approximately 2 degrees, the normal and oblique shock wave relationships were developed to predict the choking area ratio downstream of the inducer inlet.

The normal shock flow equations (Eq. 25, 26, and 27) for this type of flow process are quite simple.

$$M_2 = 1/M_1 \quad (25)$$

$$P_2/P_1 = M_1^2 \quad (26)$$

$$\alpha_2 = \frac{1}{M_1^2 \left(\frac{1 - \alpha_1}{\alpha_1} \right) + 1} \quad (27)$$

The choking area ratios are obtained by applying Eq. 23 and 24 to the downstream conditions.

Equations 28 through 31 predict the flow characteristics across oblique shocks in this type of flow process.

$$M_1 = \frac{1}{\sin \sigma \sqrt{1 - \frac{1}{\alpha_1} \left[1 - \frac{\tan(\sigma - \delta)}{\tan \sigma} \right]}} \quad (28)$$

$$M_2 = \frac{1}{M_1 \sin \sigma \sin(\sigma - \delta)} \quad (29)$$

$$\frac{P_2}{P_1} = M_1^2 \sin^2 \sigma \quad (30)$$

$$\alpha_2 = \frac{1}{1 + \left(\frac{1 - \alpha_1}{\alpha_1} \right) M_1^2 \sin^2 \sigma} \quad (31)$$

The geometry of an oblique shock wave is shown in Fig. 53. The corresponding choking area ratios are obtained by, as with the normal shocks, applying Eq. 23 and 24 to the downstream conditions.

Figure 54, which was generated from Eq. 23 through 31, illustrates the flow characteristics across both normal and oblique shocks and the choking area ratios between Mach numbers of 0.3 and 3.0. For the oblique shocks, a typical inducer blade leading edge wedge angle of 2 degrees was assumed. Note that there are two oblique shock wave solutions for each upstream condition at which an oblique shock exists. One solution is a weak shock in which the shock angle σ is small and the downstream Mach number can be greater than 1.0. The other solution is a strong shock in which the shock angle σ is large and the downstream Mach number is always both less than 1 and less than the weak shock value. As discussed in Ref. 17, the proper solution is a function of the downstream flow conditions.

The important conclusion to be drawn from Fig. 54 is that, between upstream Mach numbers of 0.6 and 1.8 and for upstream vapor volume fractions up to 50 percent, 10-percent area contraction will cause downstream choking to occur, this corresponds to A^*_2 being 90 percent of the entrance flow area A_1 .

Inducer Blade Blockage

The flow model that best predicts the limit to two-phase pumping capability is the inducer blade blockage model. Referring to Fig. 55, the minimum static pressure is upstream of the inducer leading edge as long as the inlet flow coefficient [which is the ratio of the inlet axial velocity (C_m) to the blade tangential velocity (U) and is the tangent of the entrance flow angle ($\beta - i$)] is low enough to permit the flow area within the inducer to be greater than the entrance flow area (Fig. 55a). However, when the combined effects of high flow coefficient and blade blockage cause the

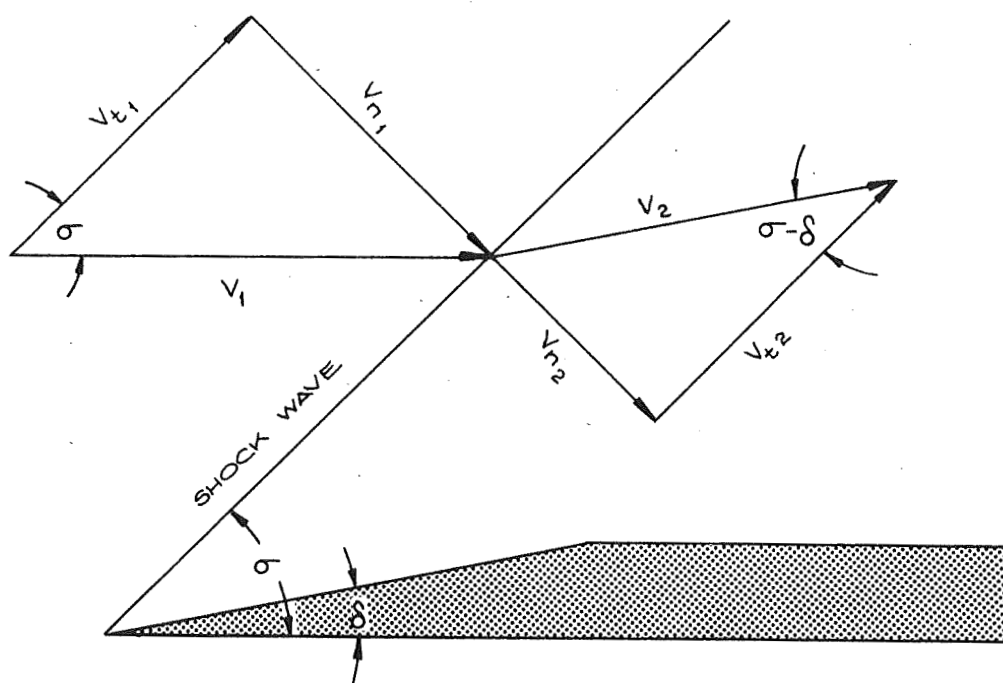


Figure 53. Flow Geometry for Oblique Shock Wave

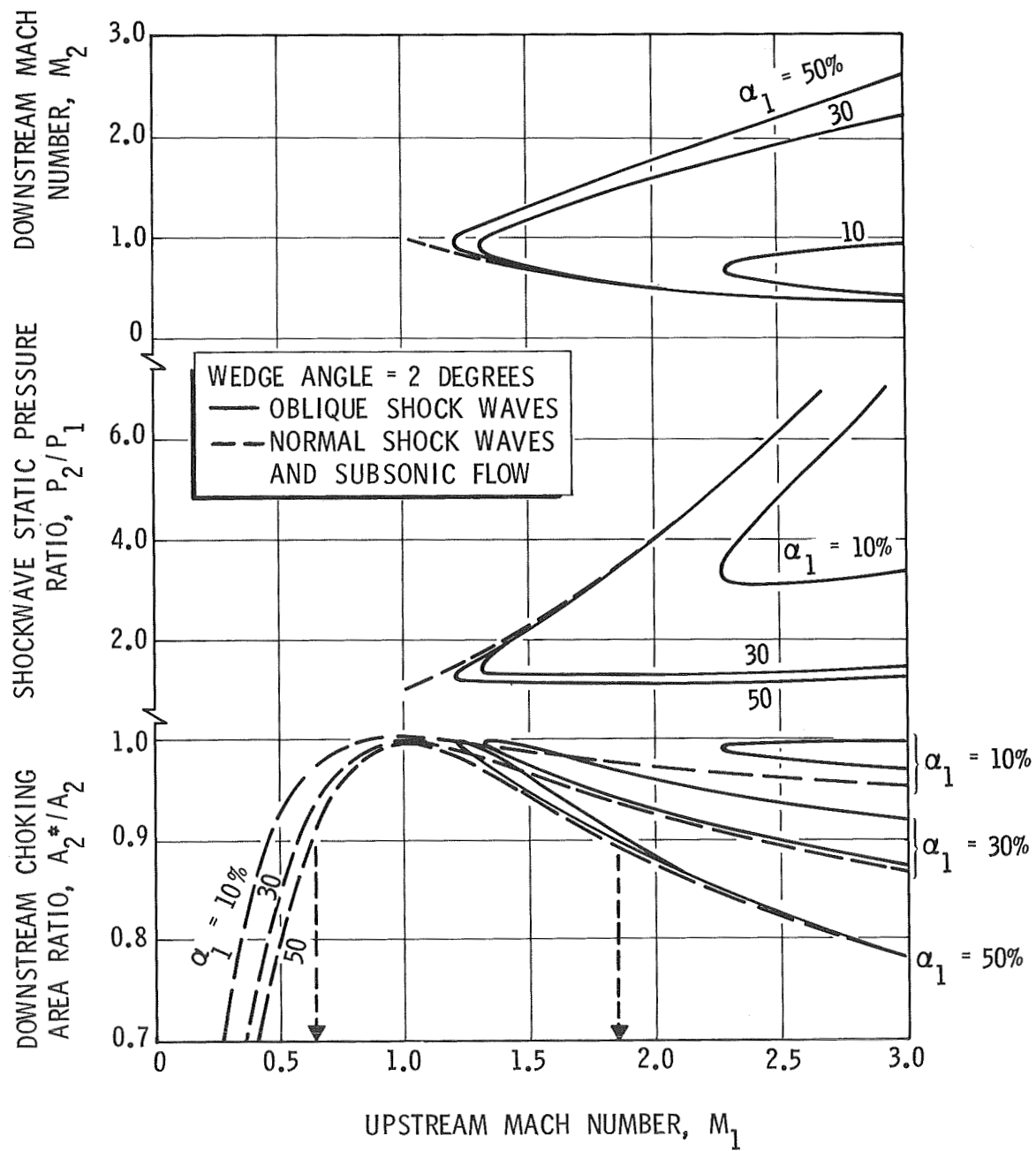
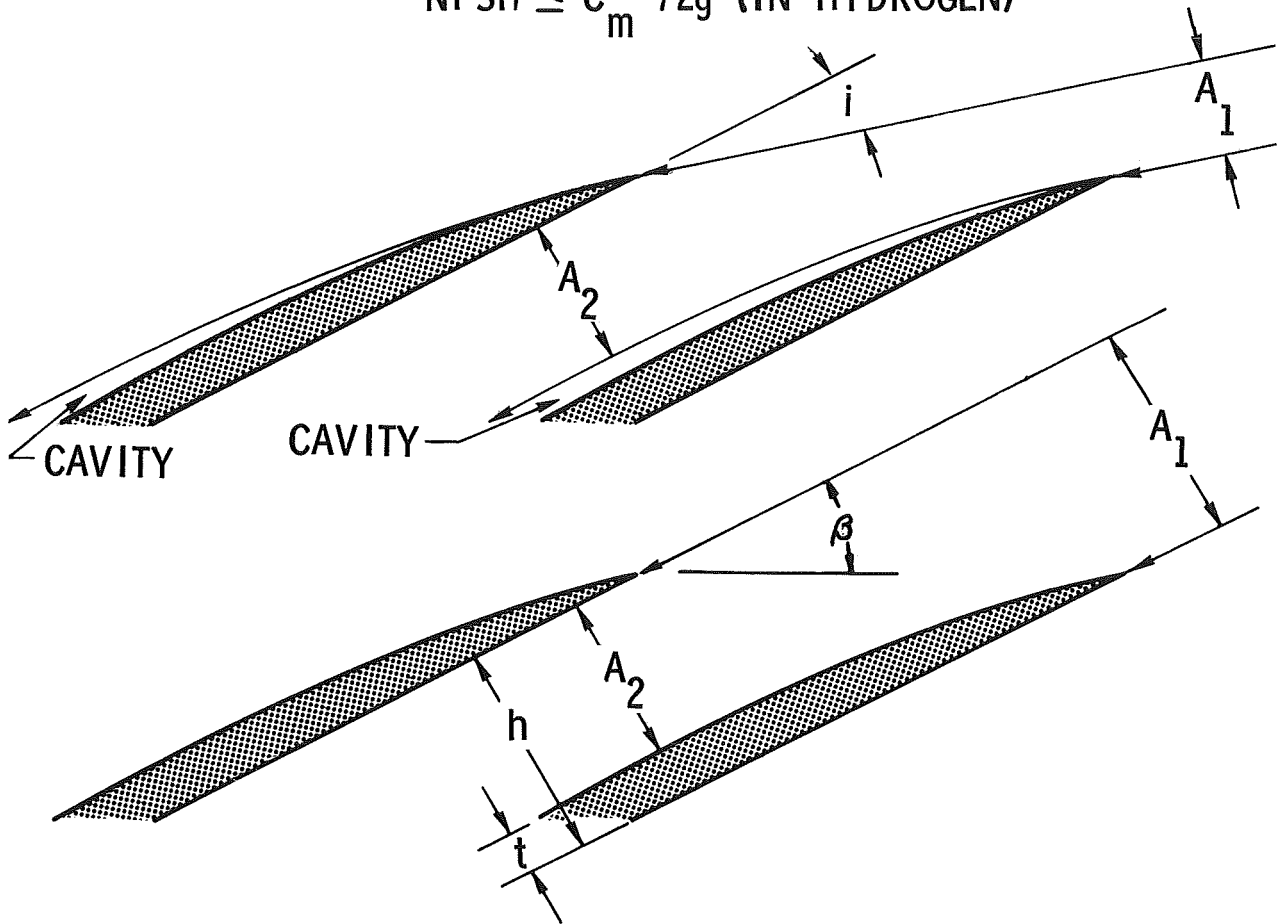


Figure 54 Effect of Vapor Volume Fraction on Constant-Quality, Two-Phase Flow of an Isothermal Gas

a) LOW FLOW COEFFICIENT OPERATION

$$A_2 > A_1, P_2 > P_1$$

$$\text{NPSH} \leq C_m^2 / 2g \text{ (IN HYDROGEN)}$$



b) HIGH FLOW COEFFICIENT OPERATION

$$A_2 < A_1, P_2 < P_1$$

$$\text{NPSH} \gg C_m^2 / 2g$$

Figure 55 Inducer Inlet Flow Geometry at Low and High Flow Coefficient Operations

minimum flow area to be within the inducer blade passages (Fig. 55b), the minimum static pressure occurs within the blade passages and, consequently, the inlet pressure must be great enough to force the flow through the blades.

This blade blockage limit is actually a choking limit. For example, assuming an inlet pressure of 15 psia, an inlet velocity of 600 ft/sec, and liquid flow at the inlet, an area contraction of only 4 percent ($A_2/A_1=0.96$) would reduce the pressure to 0 psia if the flow remained liquid. This would almost certainly cause a portion of the liquid to flash into vapor. Assuming a constant quality flow process downstream of the flashing point and a relative Mach number range of 0.6 to 1.8 (the two-phase pump test data range), the corresponding values of choking area ratio (A_2^*/A_1) are greater than 0.9 (Fig. 54, the normal shock curves approximate the A_2^*/A_1 for this case) and, therefore, a subsequent area contraction of less than 10 percent would cause choking.

In the event that this type of flow follows an equilibrium flow process, choking would occur as soon as the liquid saturation line was reached because, for an isentropic expansion that crosses the liquid saturation line and for inducer blade relative velocities that are currently used ($U > 200$ ft/sec), the maximum flow per unit area occurs at the saturation line.

If the flow entering the blade row is two-phase, less than 10-percent area contraction will also cause choking if the inlet relative Mach numbers are between 0.6 and 1.8 (Fig. 54). An interesting feature of the two-phase flow entrance condition is the resulting shock wave patterns. Assuming operation at the design liquid flow coefficient, the effect of inlet vapor volume fraction on two-phase flow coefficient, inlet relative Mach number, pressure and suction surface wedge angles, and downstream-to-inlet area ratio (A_2/A_1) are shown in Fig. 56 for a typical inducer operating condition. For vapor fractions over about 29 percent, a normal shock attached to the pressure surface was found to occur between 5 and 20 percent vapor volume fraction, an oblique shock attached to the pressure surface was found to occur between 20 and 43 percent vapor volume fraction, and an oblique shock was found attached to the suction surface.

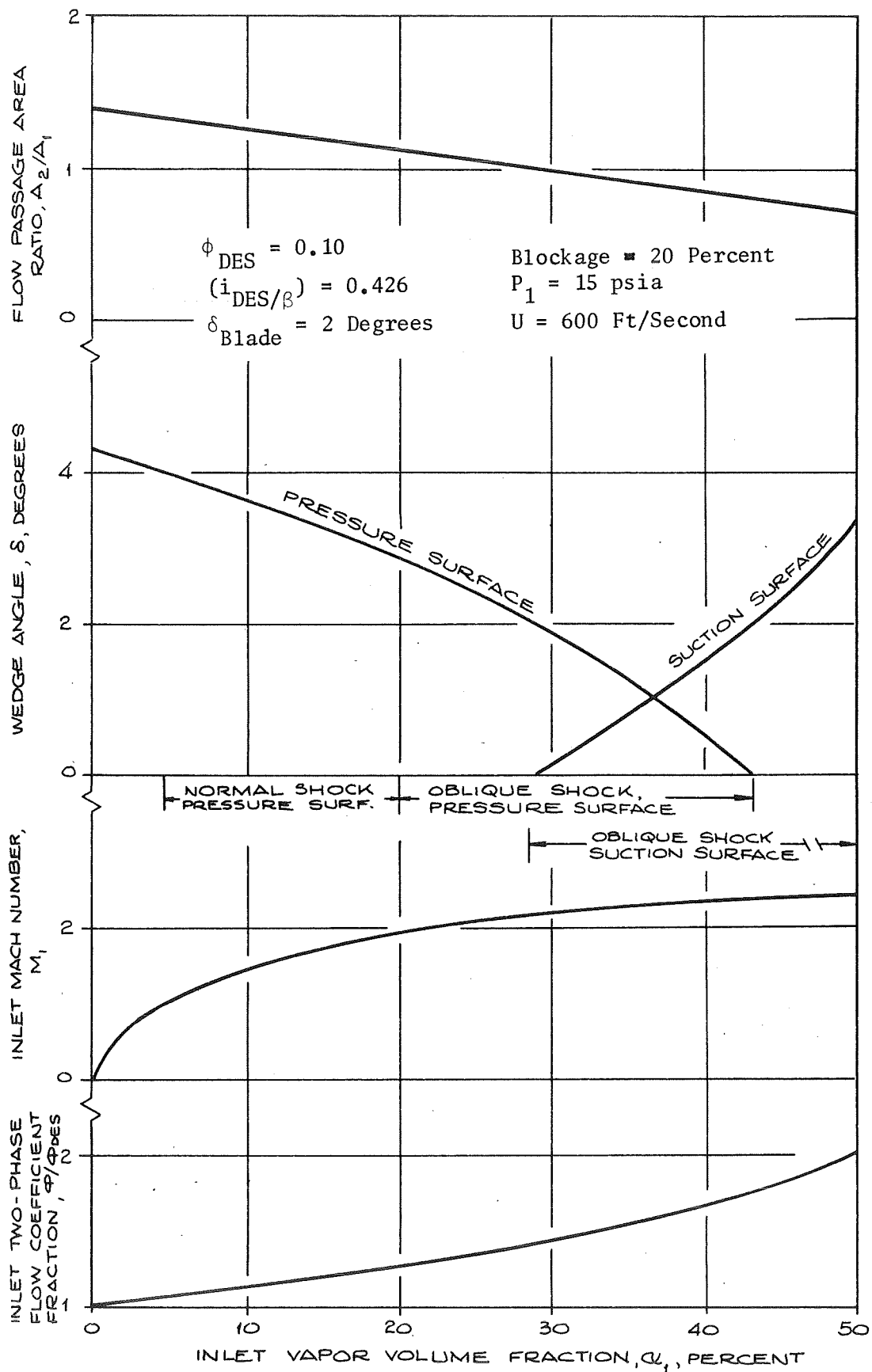


Figure 56. Effect of Vapor Volume Fraction on Inducer Inlet Flow Conditions

Because the allowable 10-percent effective area contraction could be caused by boundary layer growth, it may be concluded that, when the inlet flow is saturated, choking is likely whenever the inducer inlet flow coefficient is high enough such that the inlet flow area is equal to the geometrical flow area within the inducer blades ($A_2/A_1 = 1$). This is true regardless of whether the inlet flow is two phase or a saturated liquid. If A_2/A_1 is less than 1, the pump inlet must be increased to avoid having the flow reach its vapor pressure before it reaches the minimum flow area. Under these circumstances, the pump inlet flow must be a pure liquid. By using Bernoulli's equation and continuity and setting the internal blade pressure P_2 equal to the vapor pressure, the amount of NPSH required to avoid choking becomes:

$$\tau = \frac{2g \text{ NPSH}}{U^2} = \phi^2 + (1 + \phi^2) \left[\left(\frac{A_1}{A_2} \right)^2 - 1 \right] \quad (32)$$

where

$$\frac{A_1}{A_2} = \frac{\sin(\beta - i)}{(1 - B) \sin \beta} \quad (33)$$

$$\phi = \tan(\beta - i) \quad (34)$$

Using the Mark 25 inducer geometry and determining the cavitation parameter (τ) at the inlet RMS diameter, the influences of blade blockage (B) (Fig. 55b) and design incidence-to-blade angle ratio $(i/\beta)_{\text{des}}$ on Mark 25 inducer performance were determined (Fig. 57). It is apparent that reducing B and increasing i/β will increase the flow coefficient at which the blockage limit occurs.

As discussed before, two-phase flow will also choke when A_2/A_1 equals 1 and, therefore, the blockage limits on Fig. 57 also apply to the two-phase flow coefficient. The volume flowrate of vapor that can be pumped is equal to the difference between the volume flowrate at the limit and the liquid volume flowrate. Writing this in terms of flow coefficient ratios by treating the vapor as a void fraction,

$$\alpha_1^* = 1 - \frac{\phi_{L/\phi_{\text{des}}}}{\phi^*/\phi_{\text{des}}} \quad (35)$$

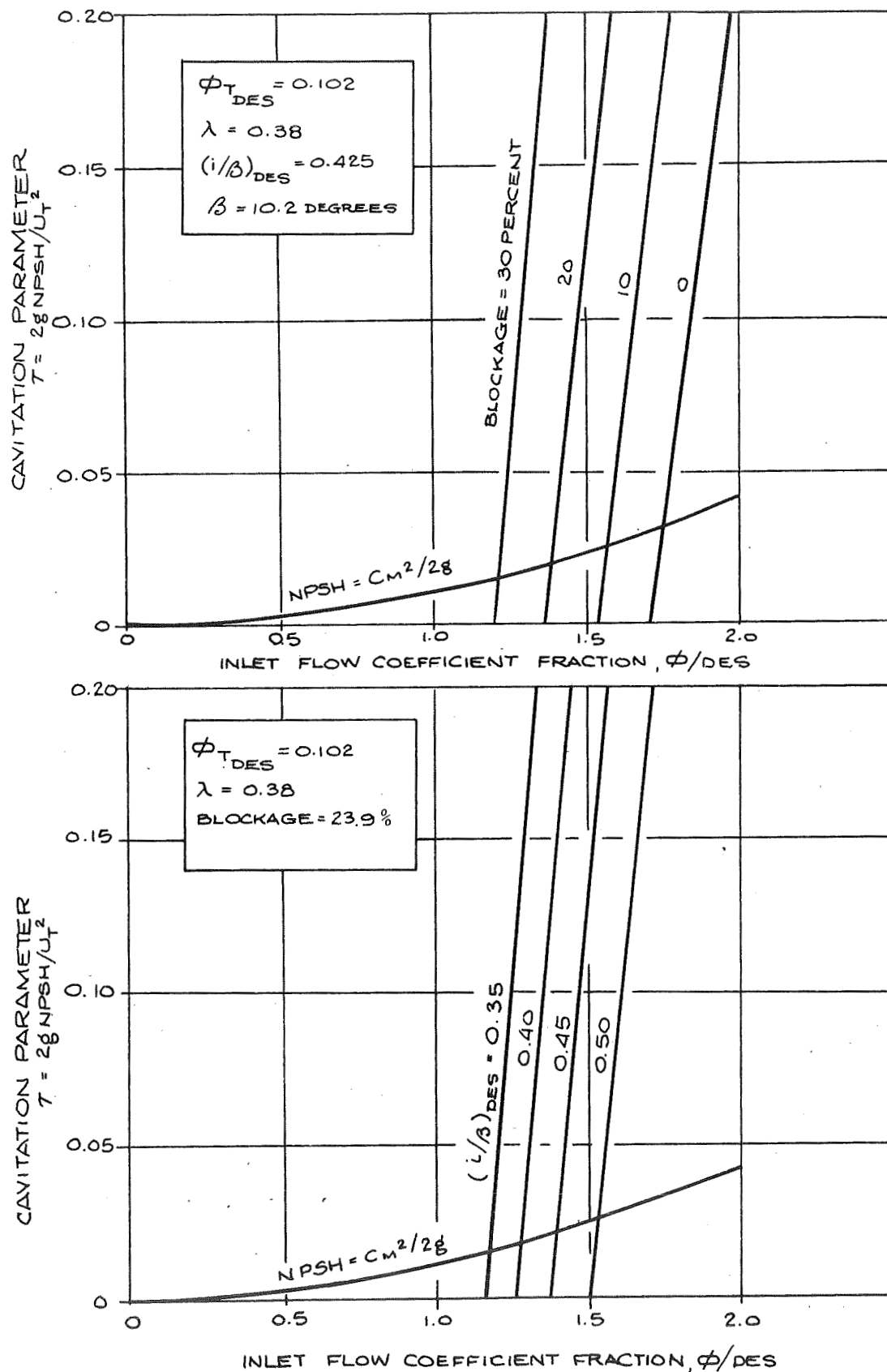


Figure 57. Effect of Variation in Blockage and Design Incidence on Mark 25 Inducer Cavitation Performance in LH₂

Therefore, the allowable vapor volume fraction decreases linearly from 100 percent at $\phi_L = 0$ to 0 percent when $\phi_L = \phi^*$. Equation 35 can be reduced to much more basic terms by making a few simple approximations. Because A_1/A_2 equals 1 at the blockage limit and because the flow angles are small, Eq. 33 reduces to:

$$\frac{A_1}{A_2} = \frac{\sin(\beta - i^*)}{(1 - B) \sin \beta} \frac{1 - (i/\beta)^*}{1 - B} = 1 \quad (36)$$

solving for $(i/\beta)^*$,

$$(i/\beta)^* = B \quad (37)$$

Therefore,

$$\frac{\phi^*}{\phi_{des}} = \frac{\tan \{ \beta [1 - (i/\beta)^*] \}}{\tan \{ \beta [1 - (i/\beta)_{des}] \}} \approx \frac{1 - B}{1 - (i/\beta)_{des}} \quad (38)$$

Finally, substituting this into Eq. 35, the allowable vapor volume fraction becomes the following function of liquid to design flow coefficient fraction, design incidence-to-blade angle ratio, and blockage fraction:

$$\alpha_1^* \approx 1 - \left(\frac{\frac{\phi_L}{\phi_{des}} [1 - (i/\beta)_{des}]}{1 - B} \right) \quad (39)$$

Using this equation and assuming operation at the design liquid flow coefficient (based on liquid volume flowrate), the influences of blockage fraction and inducer leading edge incidence-to-blade angle ratio on allowable inlet vapor volume fraction were determined (Fig. 58). As shown, the allowable vapor fractions for existing high tip speed inducers could be increased from 20 percent to 45 percent by redesigning at the maximum leading edge incidence angle that will permit two-phase pumping. By using a low speed inducer to minimize blade thickness, a further increase to 55 percent should be possible. The operating regions for such a design are shown in Fig. 59.

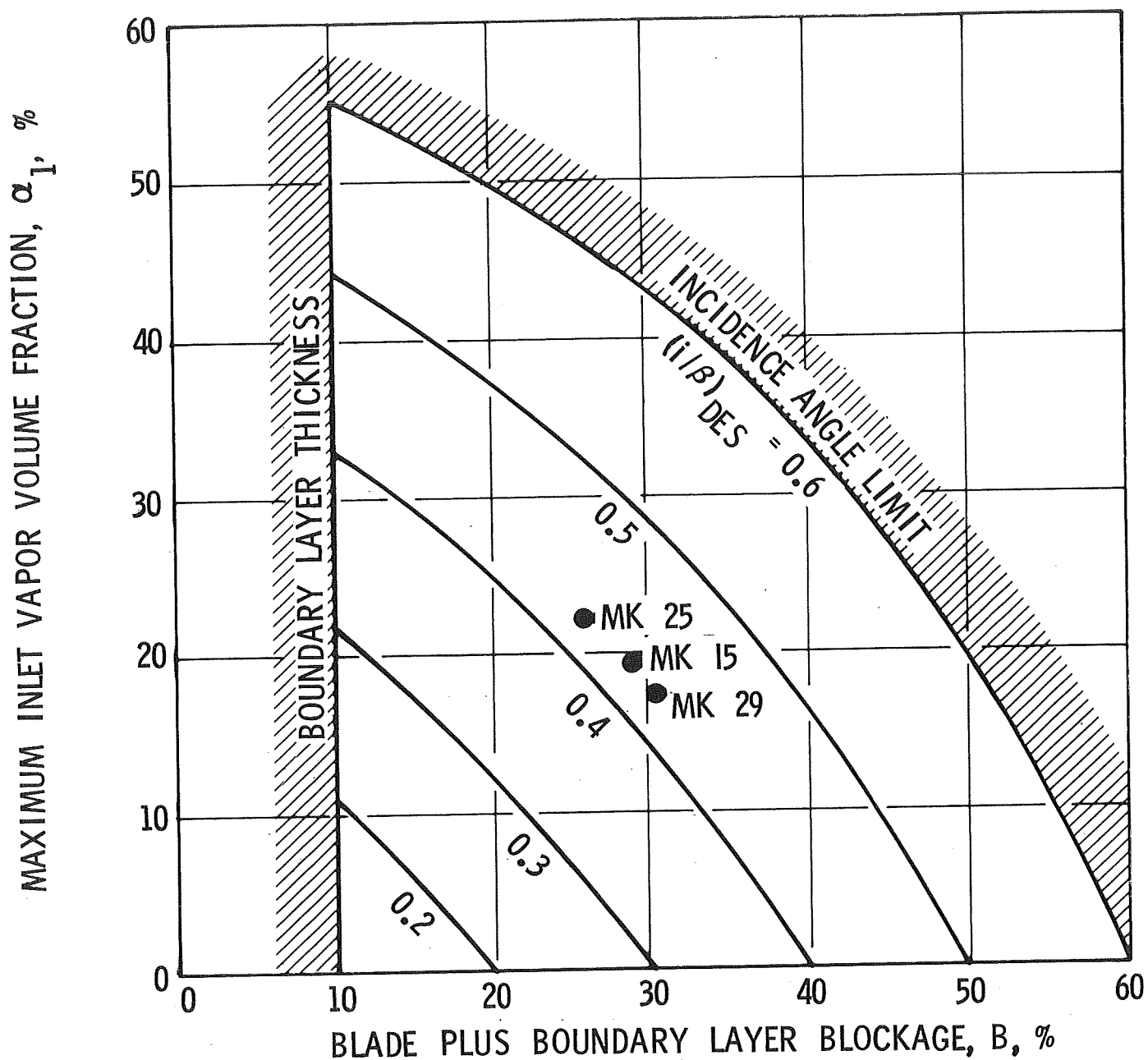


Figure 58 Effect of Incidence Angle and Blockage on Vapor Pumping Capacity of LH_2 Inducers at Design Liquid Flow Coefficient Operation

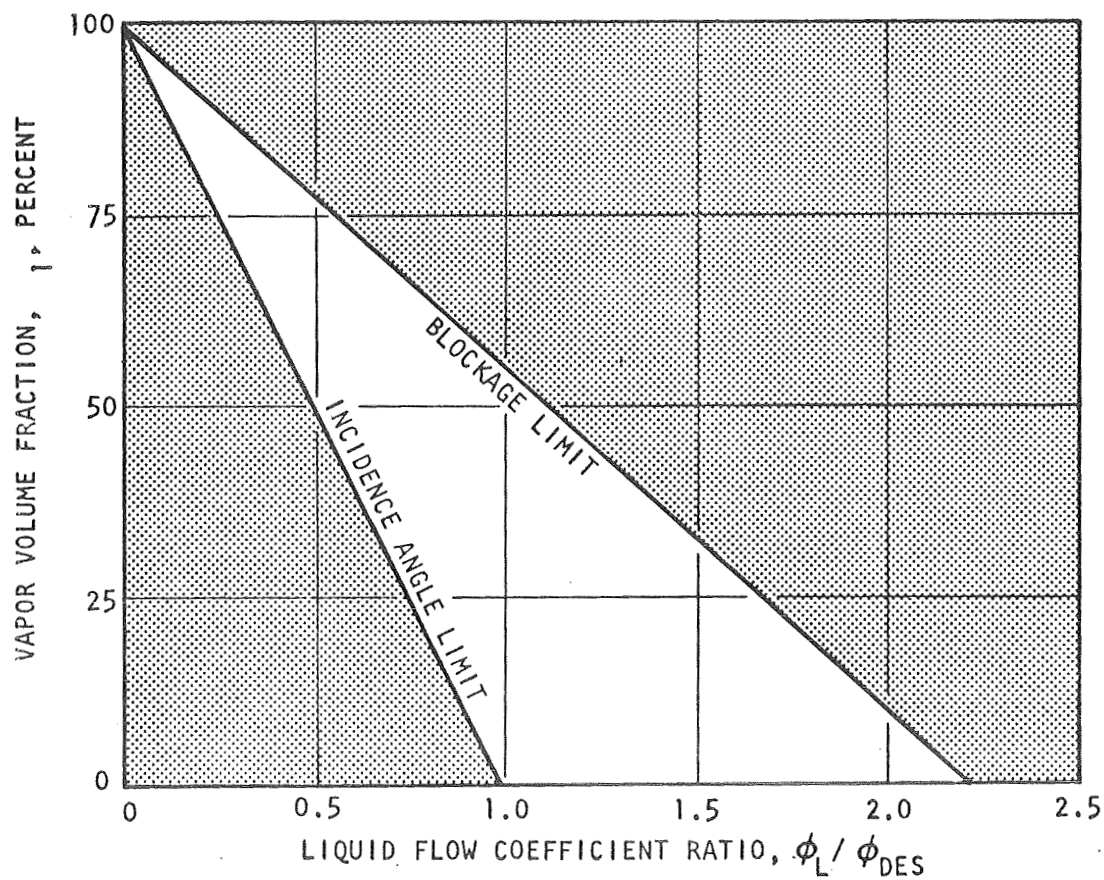
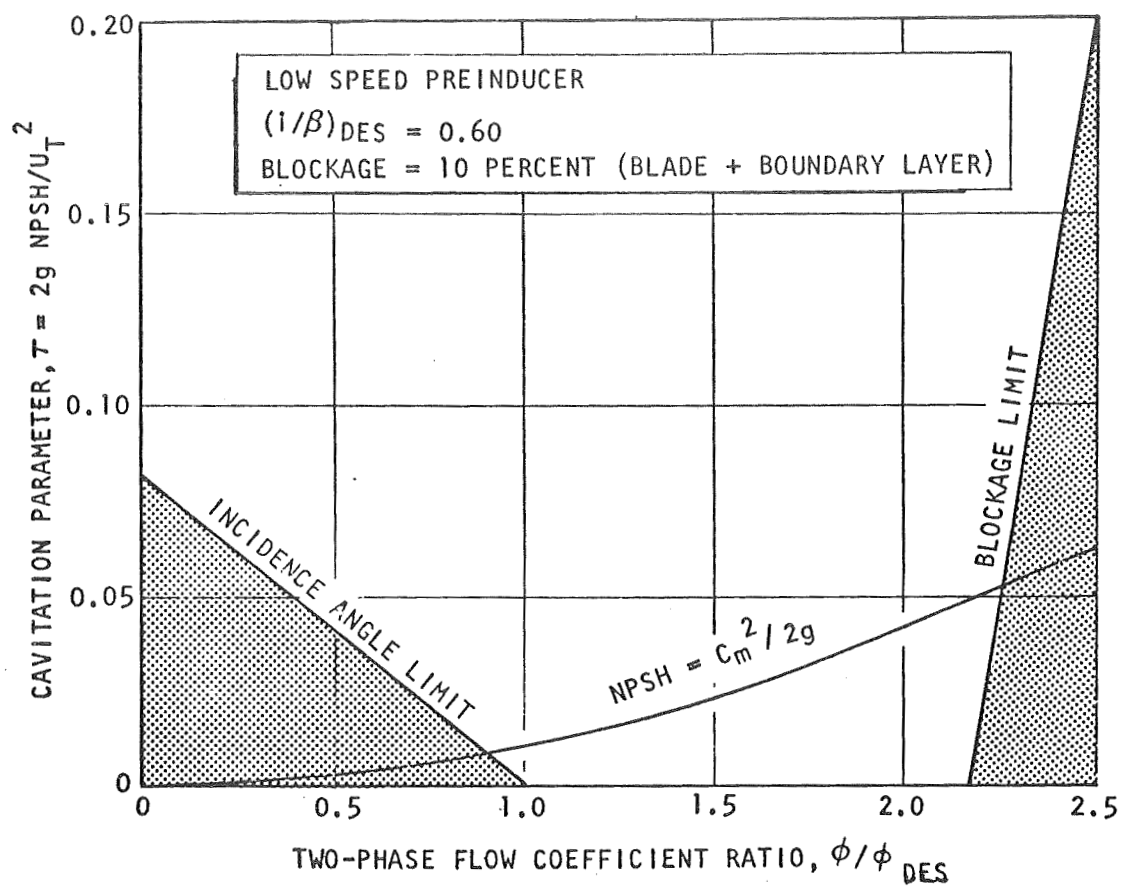


Figure 59 Maximum Vapor Pumping Capabilities of Hydrogen Pumps

Test Data Analysis

The theoretical predictions obtained from two-phase flow analysis were compared with four sets of experimental test data for LH_2 pumps and inducers. Pertinent design and test data for three of these pumps and inducers are listed in Table 13 in the order of increasing design flow coefficient.

The Mark 15 LH_2 pump was tested in two-phase hydrogen at Rocketdyne under the J-2X engine program. Two-phase hydrogen was generated by a Frantz screen that was installed upstream of the pump inlet. The vapor fractions were determined from measurements of pressure and temperature in the pure liquid upstream of the screen and in the two-phase fluid downstream of the screen. The test pump pressure-rise fractions are shown in Fig. 60 and 61 as a function of inlet line vapor volume fraction and inlet line hydrogen temperature.

The model Mark 29 LH_2 inducer was tested in water at Rocketdyne under the J-2S engine program. No pump inlet vapor fractions were obtained because these were cavitation tests and the test fluid was water. However, the wide range of flow coefficients over which this inducer was tested provided an excellent illustration of the effects of blade blockage.

Rocketdyne's Mark 25 hydrogen pump was tested in two-phase hydrogen by the Nuclear Rocket Development Station in Nevada (under the University of California Contract No. CTZ 39600-4). The method used to generate and measure vapor at the pump inlet was similar to that used in the previously discussed Mark 15 LH_2 pump two-phase hydrogen testing. The resulting pump pressure-rise fractions are shown in Fig. 62 as a function of inlet vapor volume fraction, inlet saturation pressure, inlet liquid volume flowrate, and pump rotational speed.

A NASA inducer (Ref. 18) was also tested in both LH_2 and two-phase hydrogen at NASA Lewis Research Center. For the two-phase tests, vapor was generated upstream of the pump inlet by heating the inlet duct. The vapor volume fractions and NPSH at the pump inlet were then obtained from the various pump inlet measurements of pressure, temperature, and heating rate.

TABLE 13

SUMMARY OF INDUCER DESIGN DATA AND TEST RESULTS AT 10-PERCENT
LOSS IN PRESSURE RISE ($\Delta P/\Delta P_L = 90$ percent)

Inducer	Mark 15 LH ₂	Model Mark 29	Mark 25
$\phi_{T_{des}}$ ($i_{des}/\beta = 0.425$)	0.0735	0.075	0.102
β_T , degrees	7.35	7.5	10.2
D_T , inches	7.80	6.56	7.85
Blade Blockage, percent	21	22	18
Blade Blockage (with 10-Percent Boundary Layer), percent	29	30	26
Test Fluid	LH ₂	Water	LH ₂
T_{line} , R	37.7 to 46.2	Ambient	40.1 to 41.6
Q_L , gpm	8470 to 9310	800 to 1700	7290 to 10,530
N , rpm	27,270	6322	18,100 to 24,200
ϕ_L/ϕ_{des}	0.966 to 1.064	0.66 to 1.39	0.812 to 0.993
α_{line} , percent	0 to 24.4	0	14.2 to 38.3
α_{line} (with 0.5 lb/sec Recirculation), %	6.1 to 30.4	DNA	DNA

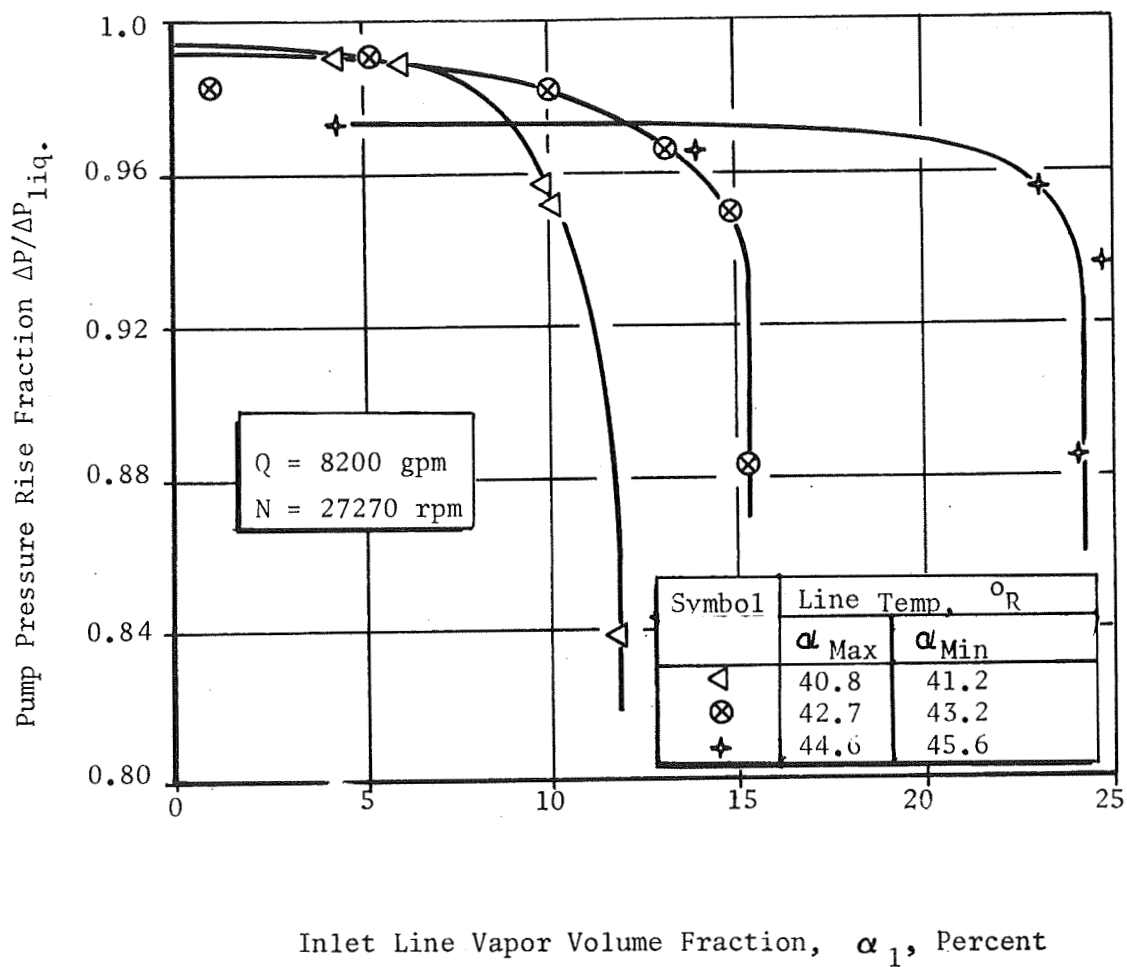


Figure 60. Mark 15 LH_2 - Pump Two-Phase Flow Data at a Hydrogen Flowrate of 8200 gpm

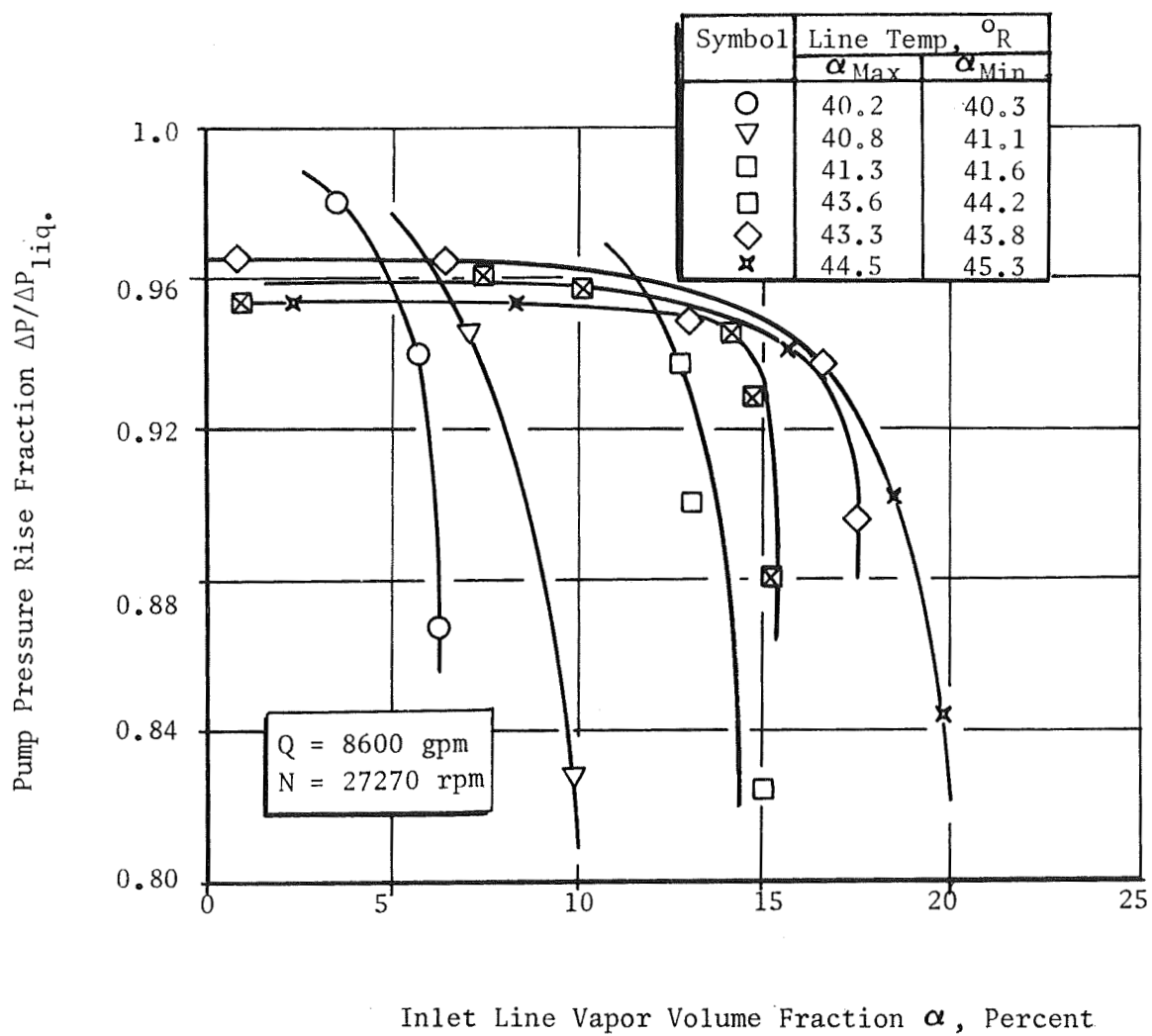


Figure 61. Mark 15 LH₂ Pump Two-Phase Flow Data at a Flowrate of 8600 gpm

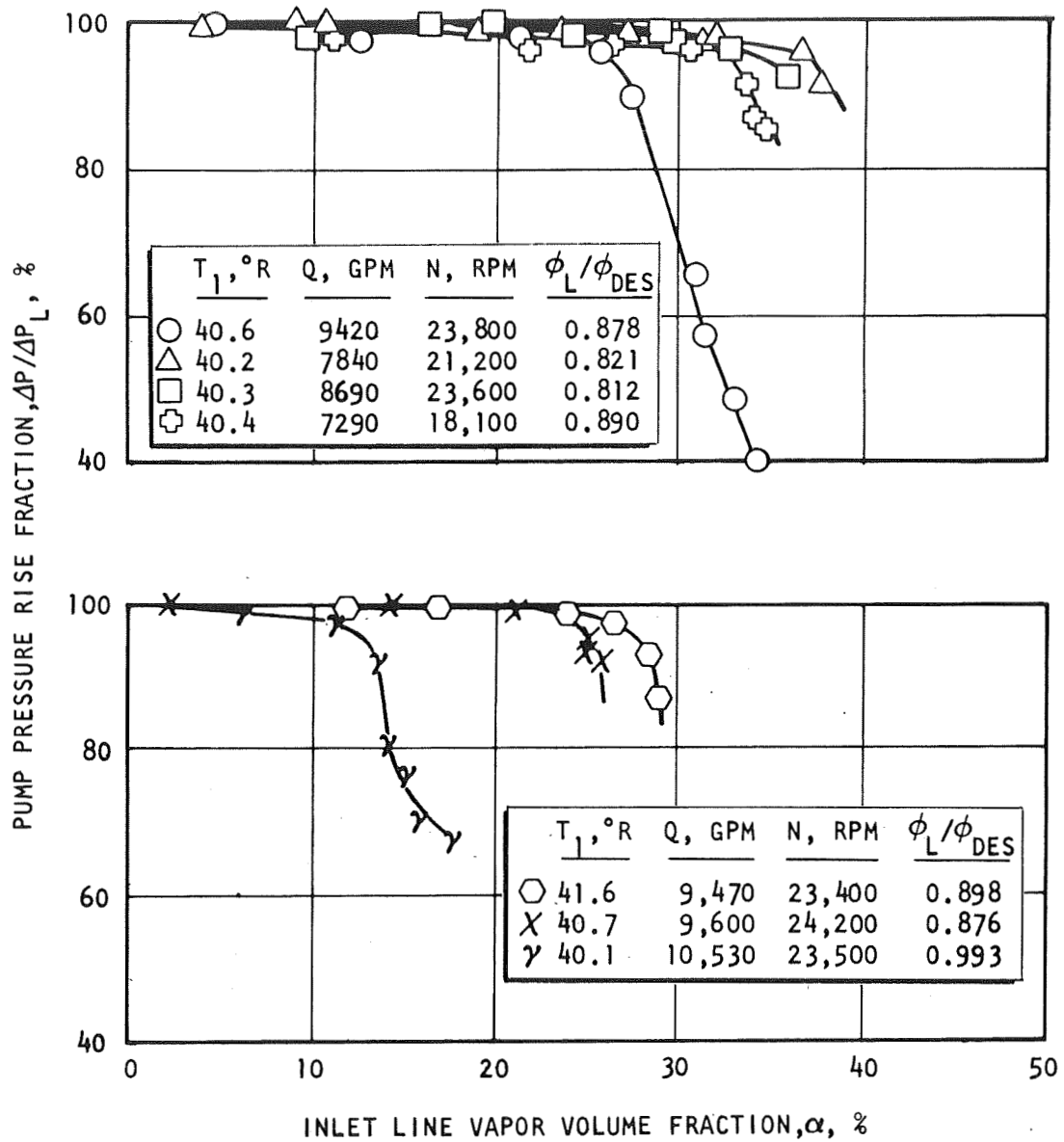


Figure 62 Mark 25 LH₂ Pump Two-Phase Flow Data With Hydrogen

Inducer Blade Blockage

For the NASA inducer, correcting the liquid flow coefficient to account for the inlet vapor fraction (Eq. 40) caused the two-phase data to fall on top of the liquid data (Ref. 18).

$$\phi = \frac{\phi_L}{1 - \alpha} \quad (40)$$

This supports the theory that the blockage limit is a function of flow coefficient for either two-phase or liquid flow. The data crossed the $NPSH = C_m^2/2g$ line at a flow coefficient of 116 percent of design, thereby indicating that pump inlet pressurization above saturation is necessary to operate at high flow coefficients and, therefore, this is the two-phase pumping limit. These results support the blade blockage theory because the 33-percent predicted value of blockage at the crossing point agrees with the actual value (with 10-percent boundary layer). At high flow coefficients, the data paralleled the 25-percent blockage predictions. This, in turn, agrees with the zero boundary layer blockage estimate. This variation in blockage is probably the result of less flow distortion at high flow coefficients because the flow is entering the blade row more directly (Fig. 55).

At high flow coefficients, the model Mark 29 LH_2 inducer data parallel the 27- to 31-percent blockage prediction curves. This agrees with the actual blade blockage with 10-percent boundary layer rather than (as with the NASA inducer) the zero boundary layer blockage value. Possible reasons for this difference may be the thermodynamic suppression head effect in hydrogen and the tapered hub effect on A_2 for the Mark 29 LH_2 inducer.

For the Mark 15 and the Mark 25 LH_2 pumps, the 10-percent loss in pump pressure rise data points from Fig. 60, 61, and 62 are shown in Fig. 63 and 64, respectively. With the exception of the high flow coefficient data points, most of the data fall between the zero and the 10-percent boundary layer predictions.

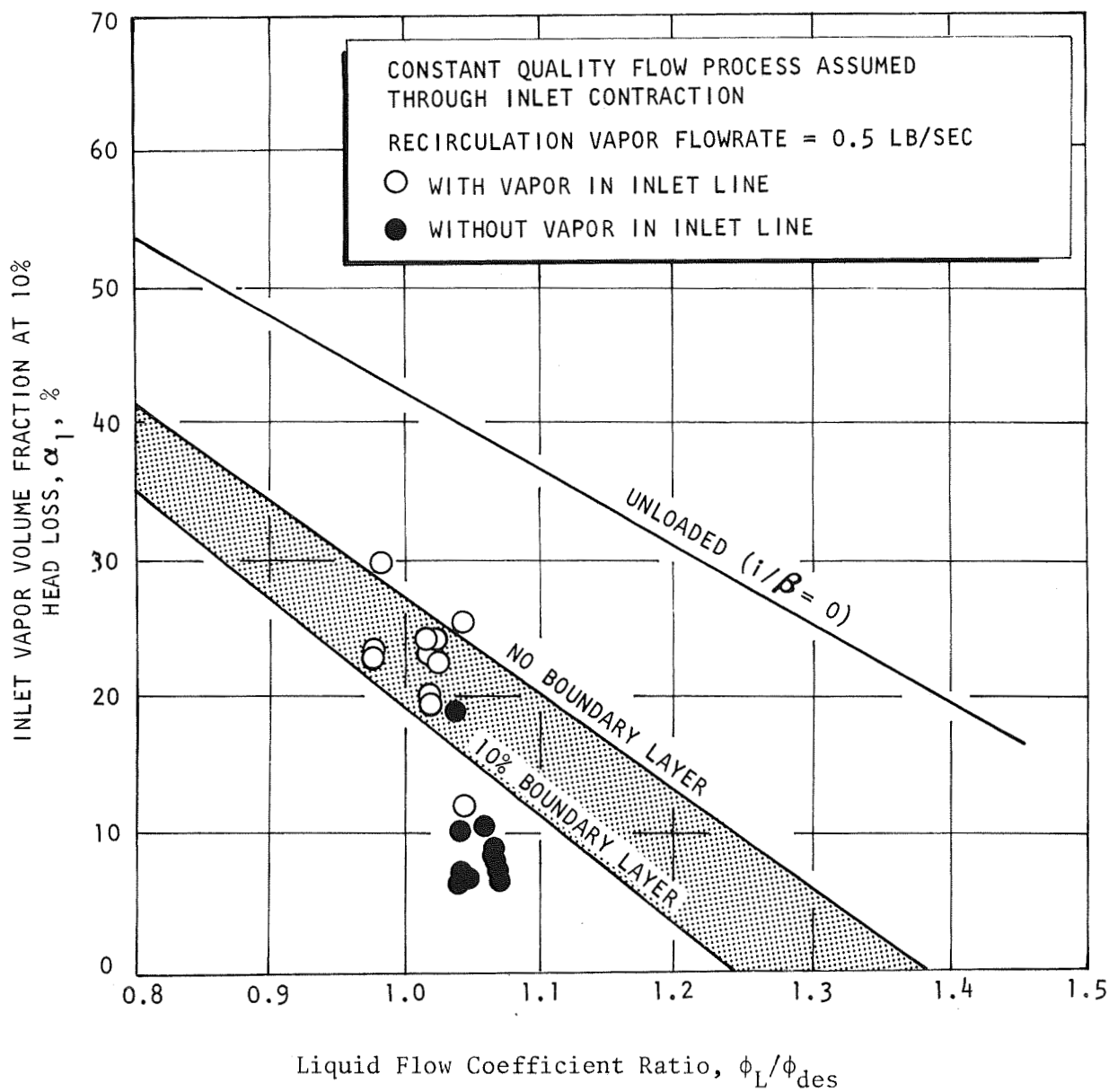


Figure 64. Comparison of Mark 15 LH_2 Pump Two-Phase Flow Test Results With Theoretical Prediction

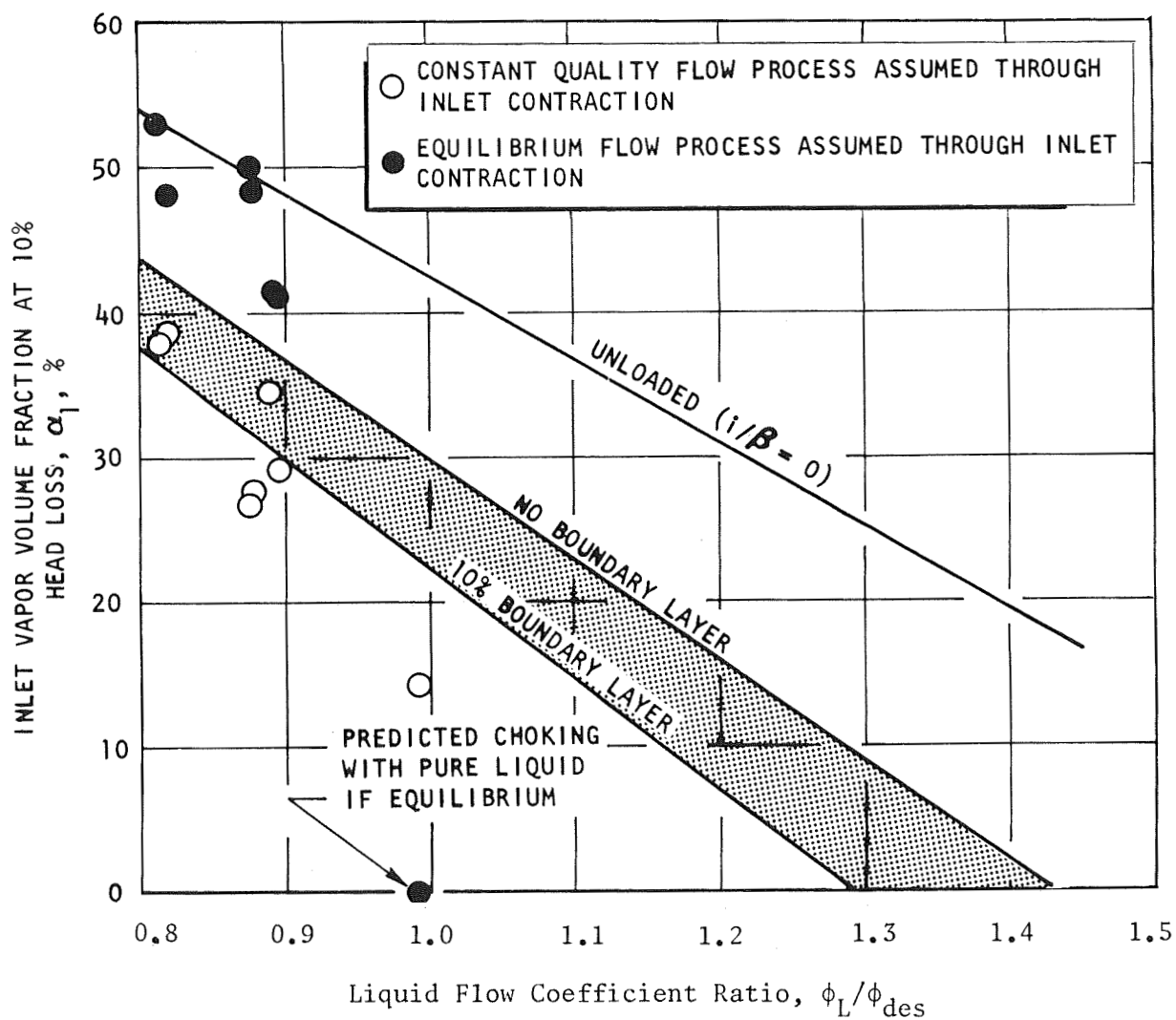


Figure 63. Comparison of Mark 25 LH_2 Pump Two-Phase Flow Test Results With Theoretical Prediction

It may be concluded that, with the exception of the data points at the high flow coefficients for the Mark 25 and Mark 15 LH_2 pumps, the upper limit to two-phase pumping capability is choking caused by blade blockage limit (Eq. 39). As shown in Fig. 60, 61, and 62, the pump pressure rises are dropping rapidly with increasing vapor fractions at 90-percent pump pressure-rise fraction and, therefore, drop suddenly when choking occurs. The data points that are exceptions in Fig. 63 and 64 are caused by stator cavitation and inlet choking, respectively, that will be discussed below.

Stator Cavitation. For liquid flow coefficients greater than 103 percent of design, the vapor fractions for the Mark 15 LH_2 pump were found to be much less than the predicted values (Fig. 63). Earlier high flow coefficient cavitation data for the Mark 15 LH_2 pump indicate that the inducer pressure-rise fraction is unaffected by NPSH whereas the pressure-rise fraction across both the inducer and its stator is strongly affected by NPSH. Therefore, the deviation shown in Fig. 63 was probably caused by stator cavitation.

For the Mark 25 LH_2 pump, stator cavitation was not apparent in either the two-phase testing or earlier cavitation tests in which testing was conducted up to 130 percent of design flow coefficient. In the two-phase testing, the inducer plus stator pressure-rise fraction followed closely the inducer pressure-rise fraction.

It may be concluded that stator cavitation is an important consideration when designing a hydrogen pump for two-phase flow and that the problem can be alleviated through proper design. Rules for this stator design are similar to those for an inducer, i.e., use thin blades with a positive incidence at design flow coefficient and with little or no camber on the forward portion of the blade.

Inlet Choking. The vapor volume fraction for the highest flow coefficient data point for the Mark 25 LH_2 pump (Fig. 64) is 14.5 percent rather than the predicted value of 23 percent. As discussed previously, this

was not the result of stator cavitation but was probably caused by choking at the inducer inlet annulus. Assuming a constant quality flow process through the pump inlet contraction, the choking limit would occur in the inlet line upstream of the contraction. However, the inlet line equilibrium Mach number was only 0.73, a value that, although higher than for any of the other test points on either Fig. 63 or 64, is not enough to indicate choking. Assuming an equilibrium flow process through the inlet annulus, the choking limit would occur in the inducer inlet annulus. However, for such a flow process, choking would have occurred with zero inlet line vapor fraction, to say nothing of the 14.5 percent indicated in Fig. 64 .

It may be concluded that some vaporization occurred as the flow passed through the inlet contraction and that the deviation from theory of the high flow coefficient data point on Fig. 64 was caused by choking at the inducer inlet annulus downstream of the contraction. It may also be concluded that, although the flow process through the contraction is probably closer to constant quality than to equilibrium, equilibrium should be assumed during design to ensure sufficient flow area.

Vapor Recirculation. Approximately 0.5 lb/sec of bearing coolant was recirculated through the inducer of the Mark 15 LH₂ pump during the two-phase tests. Because this recirculated flow was close to 100-percent vapor and because the vapor at the pump inlet is the sum of this vapor and the inlet line vapor, the allowable vapor fraction in the inlet line was severely limited (Table 13), particularly at low inlet pressures where the recirculated vapor occupies a large volume.

To avoid this limitation, all recirculated flows should be returned to the main stream downstream of the inducer. The Mark 25 LH₂ pump test data were unaffected by this problem because the recirculated flow was ducted overboard.

Design for Zero Tank NPSH

The limits to two-phase pumping capability were used to determine the best inducer design approaches for operation with zero tank NPSH. The three basic limits to two-phase pumping capability are choking caused by inducer blade blockage, incidence angle on the inducer blade leading edge, and choking in the annulus just upstream of the inducer blade leading edges. Choking caused by blade blockage (Eq. 41) provides the upper limit to the vapor volume fraction that can be pumped.

$$\alpha_{\max} = 1 - \left[\frac{\frac{\phi_L}{\phi_{\text{des}}} \left(1 - (i/\beta)_{\text{des}} \right)}{1 - B} \right] \quad (41)$$

When the incidence angle on the inducer blade leading edge exceeds approximately 60 percent of the blade angle, the required inlet static pressure exceeds the vapor pressure and, therefore, the inlet flow must be a pure liquid. This effect provides the lower limit to the vapor fraction than can be pumped and is expressed by Eq. 42.

$$\alpha_{\min} = 1 - \frac{\phi_L}{\phi_{\text{des}}} \left[\frac{1 - (i/\beta)_{\text{des}}}{0.4} \right] \quad (42)$$

For zero tank NPSH operation (saturated liquid hydrogen in the tank), choking will occur in the annulus just upstream of the inducer inlet if the vapor volume fraction exceeds approximately 50 percent (Fig. 65). This provides an additional upper limit to the vapor pumping capacity for systems in which the tank NPSH is zero. As shown in Ref. 7, the choking vapor fraction is less than 50 percent if the tank NPSH is greater than zero and, if vapor is added by a warm inlet line, is greater than 50 percent.

For a design volume flowrate of 11,300 gpm and a design rotational speed of 30,000 rpm, the effects of design inlet flow coefficient on vapor pumping capacity are illustrated in Fig. 66 for design incidence to blade angle ratios of 0.425 and 0.600. As shown, the solid envelopes surround

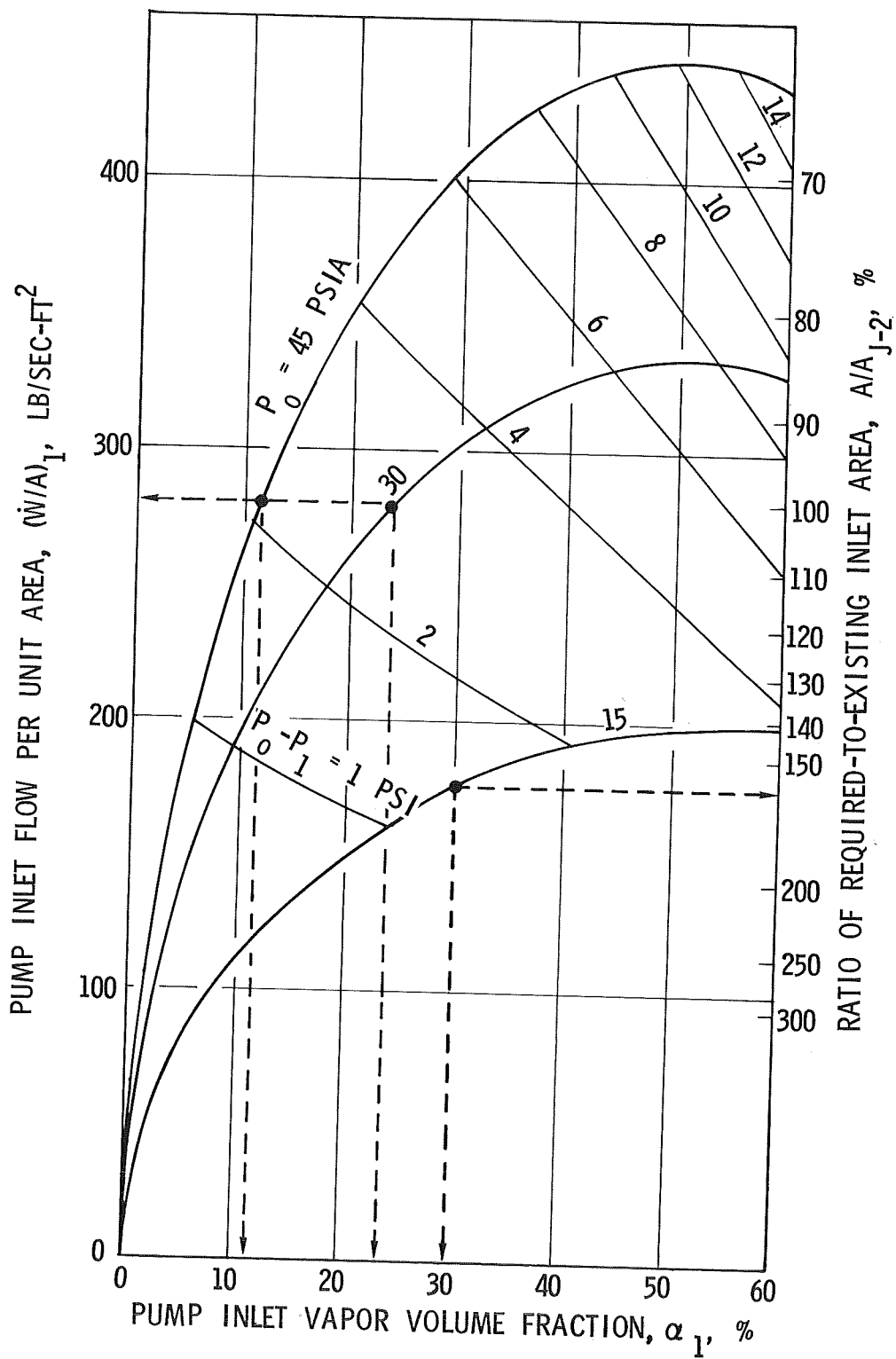


Figure 65 Effect of Equilibrium Flow Expansion of Hydrogen From Tank to Pump Inlet

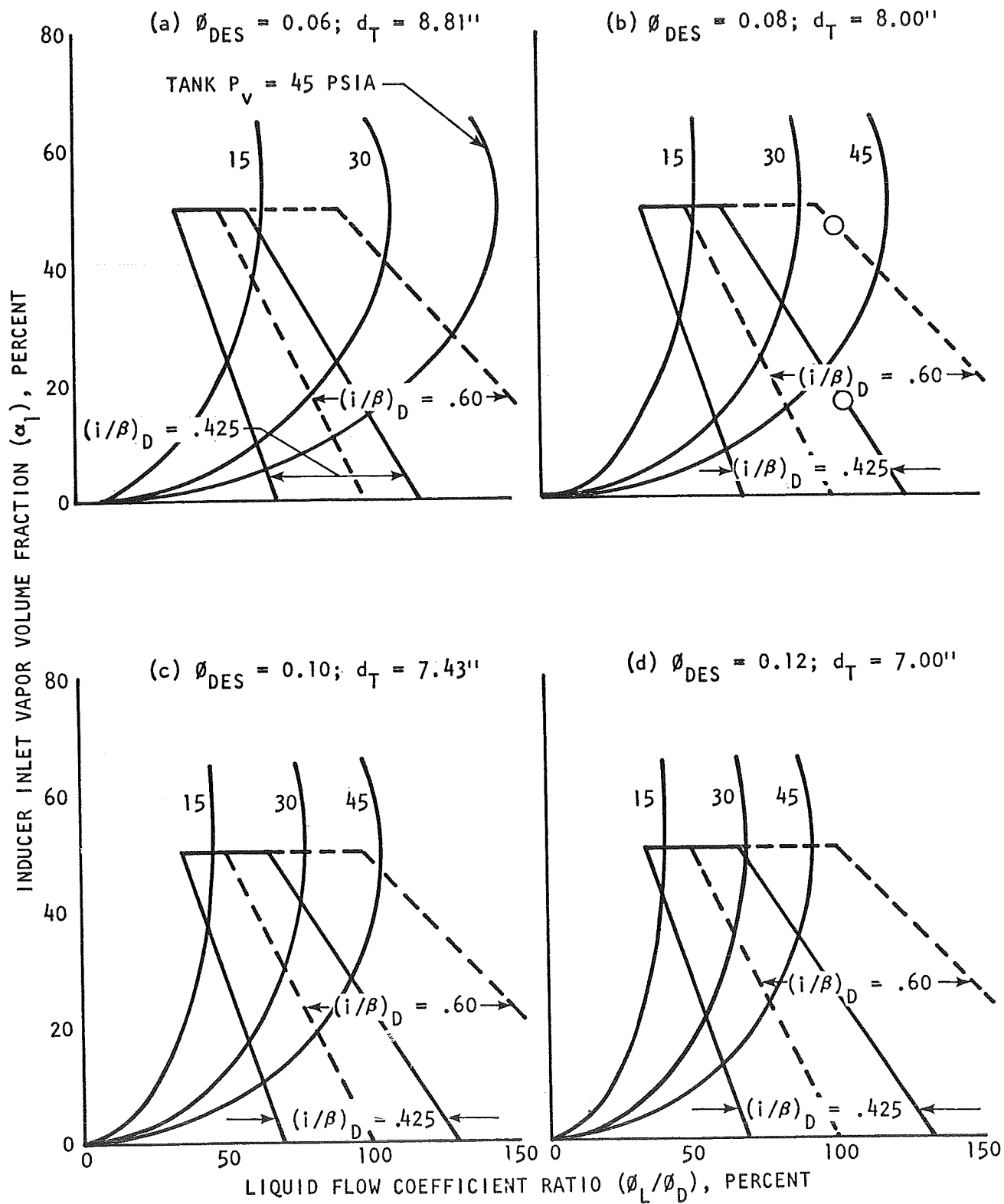


Figure 66 Influence of Design Flow Coefficient on Inducer Two-Phase Hydrogen Pumping Capability ($Q = 11,300$ gpm, $N = 30,000$ rpm, $\lambda = 0.375$)

the operating regions for $(i/\beta)_{des} = 0.425$ and the dashed envelopes surround the regions for $(i/\beta)_{des} = 0.600$. The choking due to blade blockage, incidence, and choking in the inlet annulus limits are used in generating these parametric curves. The average blade thickness was held constant. The constant tank pressure lines are for equilibrium isentropic expansions from the tank to the pump inlet annulus.

As shown, increasing the design incidence-to-blade angle ratio increases the maximum vapor volume fraction that can be pumped and, consequently, decreases the minimum tank pressure required for zero tank NPSH operation. For example, at a design inlet flow coefficient of 0.08 and at design point operation (Fig. 66d), the maximum vapor volume fraction and minimum tank pressure are 20 percent and 50 psia, respectively, for an $(i/\beta)_{des} = 0.425$ and 47 percent and 35 psia for an $(i/\beta)_{des} = 0.600$. However, for a tank pressure of 30 psia, the minimum flow coefficient at which a two-phase pumping capability exists increases from 60 percent of design at an $(i/\beta)_{des} = 0.425$ to 75 percent of design at an $(i/\beta)_{des} = 0.600$. Therefore, it is apparent that selection of the proper design value of incidence-to-blade angle ratio requires a compromise between maximizing the vapor pumping capacity (minimizing the tank pressure) and maximizing the operating range at below design flow coefficients.

As also shown in Fig. 66, decreasing the inducer inlet tip diameter increases the maximum vapor volume fraction that can be pumped. This is because (for constant values of flowrate and rotational speed) smaller diameter inducers have higher blade angles and, therefore, less blade blockage. However, decreasing the diameter also increases the minimum tank pressure at which the zero NPSH operation can be obtained, thereby penalizing rather than improving the vehicle pressurization requirement. For example, at an $(i/\beta)_{des} = 0.425$, decreasing the inlet diameter from 8.81 inches (Fig. 66a) to 7.00 inches (Fig. 66d) increases the minimum allowable tank pressure from 40 psia to approximately 60 psia. For an $(i/\beta)_{des} = 0.60$, the same diameter decrease raises the tank pressure

requirement from 20 psia to 50 psia. This effect is caused by the fact that small diameter inducers have high flow per unit area requirements and therefore require a high tank pressure before a given vapor fraction can be pumped (Fig. 65 and 66). It may be concluded that large inlet diameters should be used for zero tank NPSH applications.

During part speed operation at the same flow coefficient (i.e., $Q \propto N$), the blade blockage and the incidence limits are the same function of design flow coefficient as at high rotational speed. However, the inducer inlet flow per unit areas will be lower, thereby reducing the inducer inlet vapor volume fraction (Fig. 65) and permitting the inducer to operate at zero NPSH at a lower tank saturation pressure. This effect is shown in Fig. 67. For example, at design flow coefficient, decreasing the rotational speed from 30,000 to 10,000 rpm reduces the tank pressure requirement for an inducer with an $(i/\beta)_{\text{des}} = 0.425$ from 45 to approximately 10 psia. At an $(i/\beta)_{\text{des}} = 0.600$, the corresponding tank pressure reduction is from 35 to less than 10 psia. It must be noted that for these low pressures to be valid, the thermodynamic suppression head must be sufficient to allow two-phase inducer operation. As shown in Fig. 68, the thermal factor (which is proportional to thermodynamic suppression head) decreases with vapor pressure, thereby reducing the capability of the inducer to pump two-phase hydrogen at low vapor pressures.

Figure 67 also approximates the vapor pumping capacities of low-speed inducers. For example, a 0.08 flow coefficient, 5780-rpm inducer designed for the full flowrate of 11,300 gpm would have a tank saturation pressure capability similar to that shown in Fig. 67c. In fact, such an inducer would have a larger diameter because the tip speed and, consequently, the blade thickness would be less. In addition, due to thermodynamic suppression head effects, the lower tip speed would drop the minimum vapor pressure at which two-phase pumping is possible.

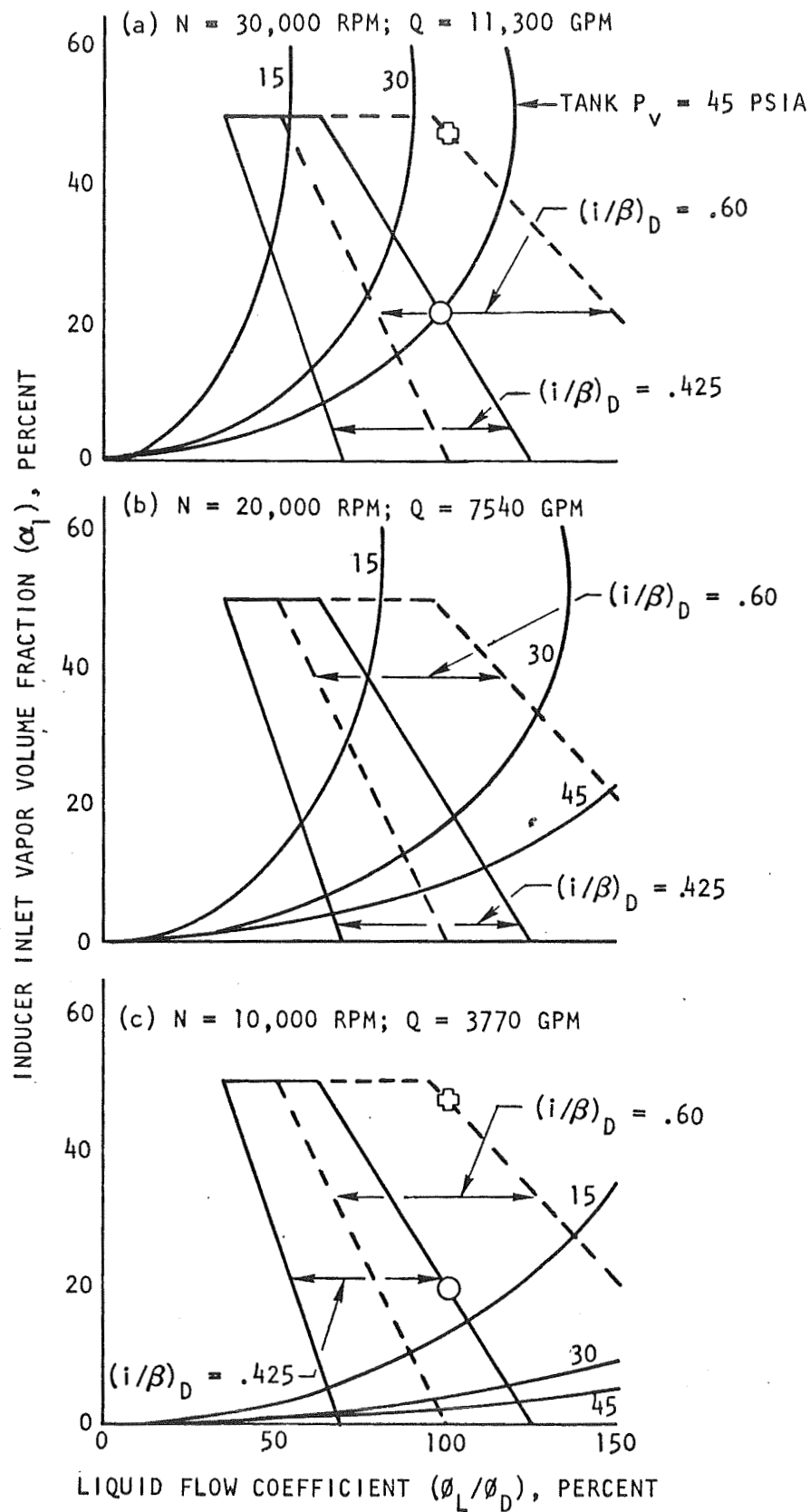


Figure 67 Influence of Rotational Speed on Inducer Two-Phase Hydrogen Pumping Capability ($\phi r = 0.08$, $d_r = 8.00$ inches, $\lambda = 0.375$)

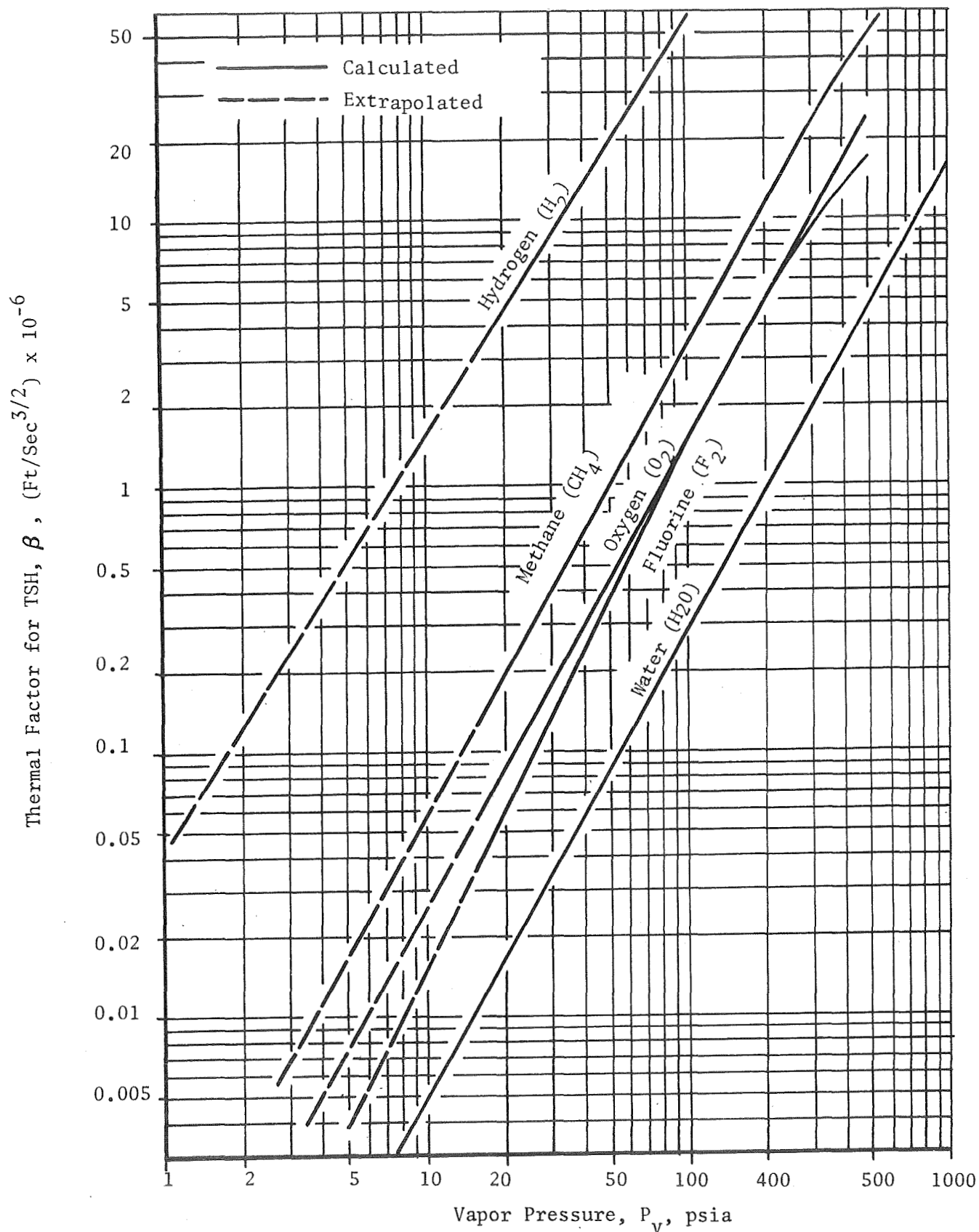


Figure 68. Thermal Factor Variation with Vapor Pressure for Different Fluids

Prediction of Mark 15 LH_2 Pump Vapor Capacity

The vapor pumping capacity of the Mark 15 LH_2 pump was estimated by using the results of the two-phase flow analysis (Eq. 41) to facilitate the analysis of the S-IVB stage restart for Saturn flights AS-504 and AS-505. The resulting allowable inlet line vapor-volume fraction is shown in Fig. 69 and will vary with inlet static pressure because the bearing coolant flow is recirculated through the inducer at a constant flowrate of 0.5 lb/sec and will be a pure vapor when it reaches the pump inlet. The inability of the Mark 15 LH_2 pump to pump two-phase flow at inlet pressures below 22.5 psia is attributed to either insufficient thermodynamic suppression head (TSH) or choking in the inlet annulus.

Prediction of Warm Pump Heating Effects

To provide warm pump performance characteristics for the engine start analysis and also to facilitate the analysis of the S-IVB stage restart for Saturn flight AS-504 and AS-505, the effects of warm pump heating on hydrogen pump discharge pressure were estimated over a range of design (cold pump) discharge pressures (Fig. 70). As shown, adding heat to the propellant as it passes through the pump will reduce the pump discharge pressure. This occurs for two reasons: (1) heating reduces the propellant density and, therefore, reduces the amount of pressure rise obtained for a given energy input, and (2) heating increases the propellant volume flowrate and, therefore, reduces the energy input because the slopes of pump H-Q curves are generally negative. Also shown is that the effects of heating are more severe if the propellant becomes two phase within the pump. The reason for this is that vapor generation greatly increases the volume flowrate and, therefore, greatly reduces both the pressure rise per unit energy input and the energy input. As indicated in Fig. 70, the slope of the pump characteristic curve ($\Delta H / \Delta H_{\text{des}}$) versus (Q / Q_{des}) is -2. Pumps with a more steeply negative characteristic will have less range than indicated and pumps with a flatter characteristic will have more.

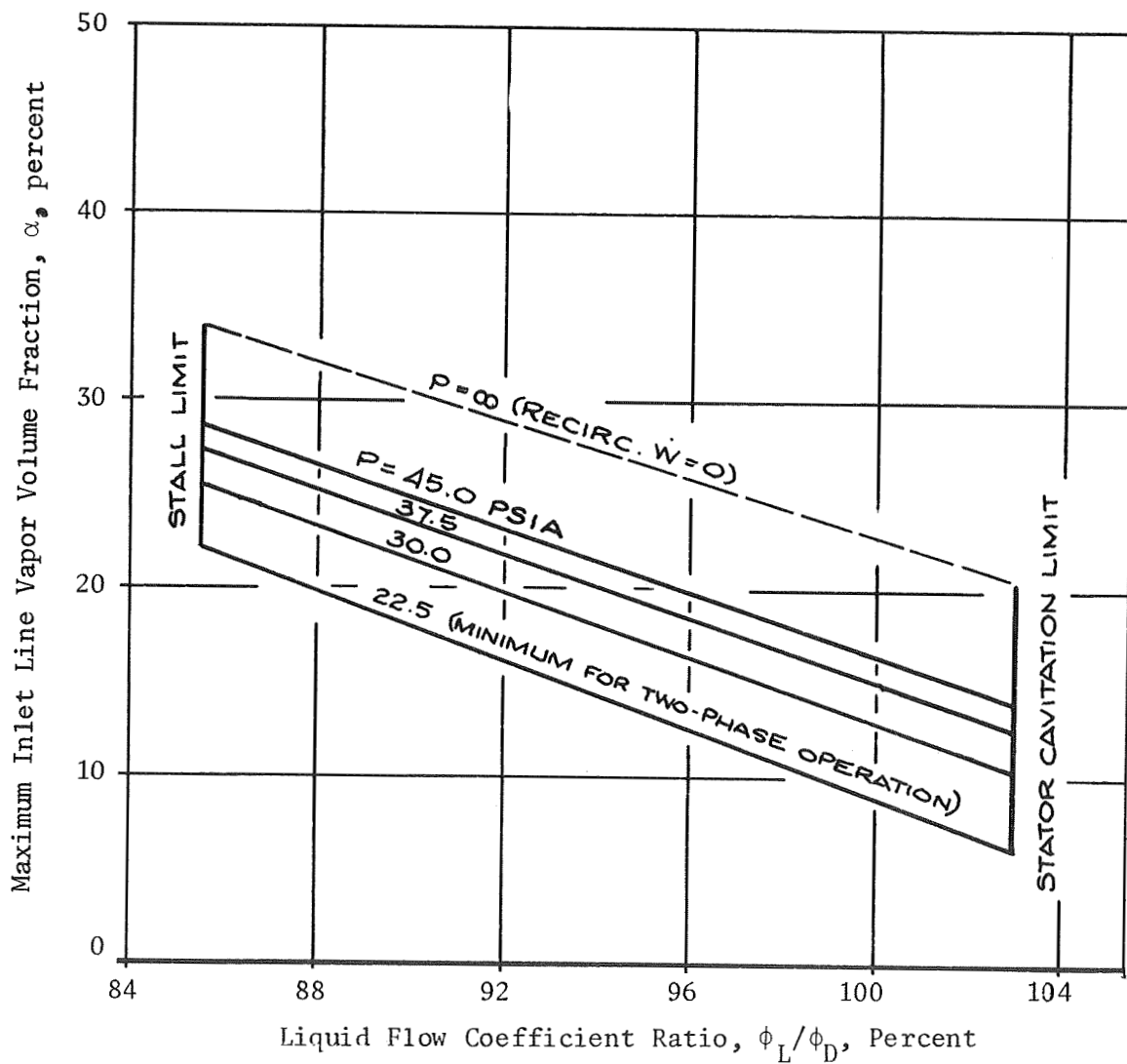


Figure 69. Vapor Pumping Capacities for MK 15 LH_2 Pump

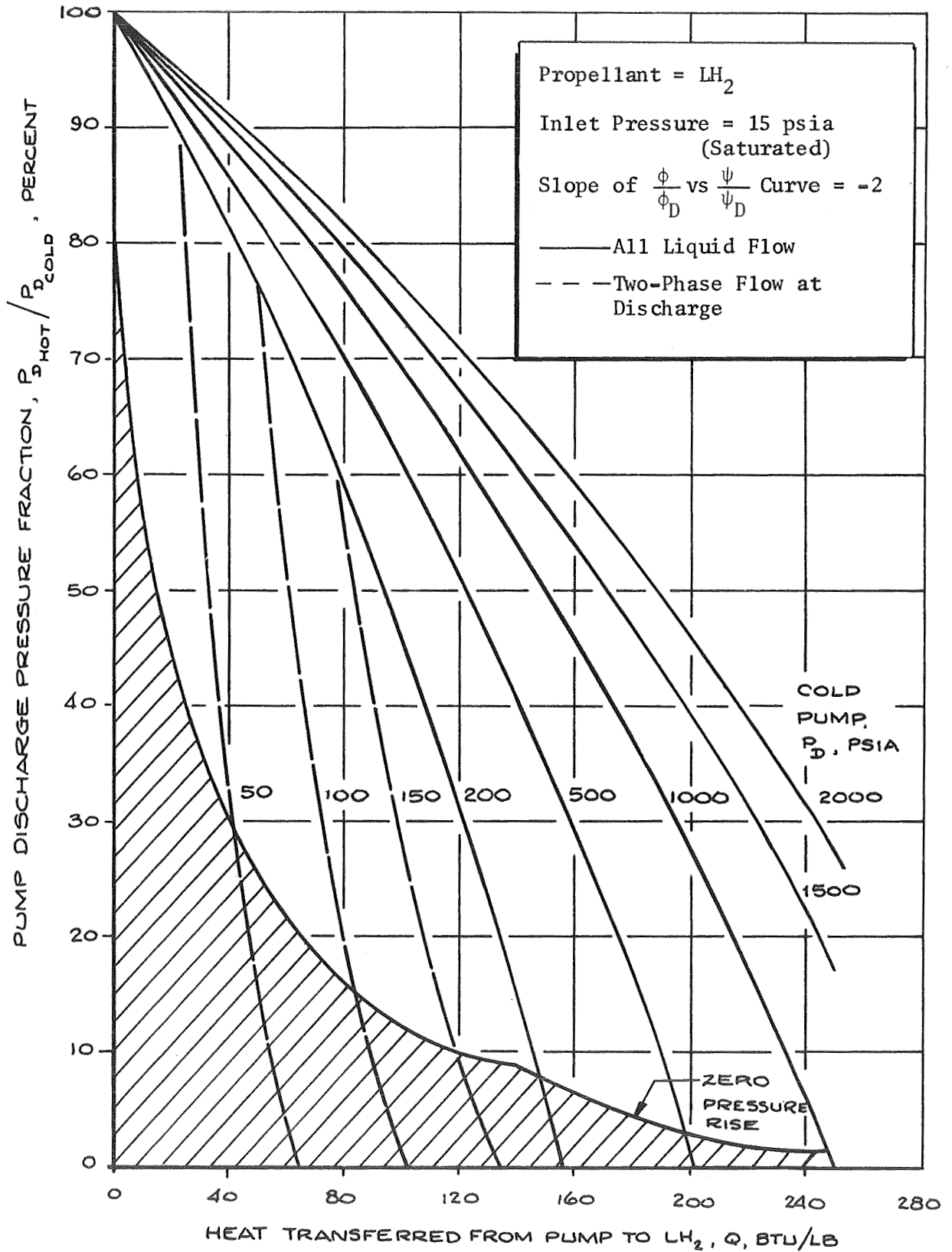


Figure 70. Estimated Effect of Warm Pump Heat Input on Hydrogen Pump Discharge Pressure

ENGINE START ANALYSIS

The object of this study is to determine the significance of thermodynamic improvements in LH_2 pumps in terms of overall engine system simplification benefits. System preconditioning and two-phase hydrogen pumping capabilities are areas emphasized. To aid in the evaluation of the influence of pump improvements on system off-design operating characteristics, a simplified mathematical model of the engine system was formulated and used to study engine operating during start. The model is qualitative in the sense that it does not represent a specific configuration, but it does reflect most of the component operating characteristics prevalent in a typical modern LH_2/LO_2 engine. The engine system analysis effort study includes a description of the start model.

By first reviewing the analytical description of hydrogen turbomachinery with two-phase flow and heat transfer, the equations and logic employed in the start model are described. Typical transients predicted with the model and results of a systems study to evaluate LH_2 pump improvements are presented. This includes aspects of pump modifications to improve operation with an initially cold feed system and also with an initially warm feed system considering inlet line and pump chilldown along with pump insulations. Several areas require further work, which includes formulation of analytical representation of a thrust chamber bypass line, auxiliary turbine power sources, and thrust chamber tube chilldown effects in the start model; start transient analysis of the effects of these additions; and additional analysis of pump operation during start with heat transfer.

Hydrogen Turbomachinery Aspects

Two general turbopump operating regimes have been investigated. The first considers hydrogen flow through the system is initially two phase but no heat transfer occurs from the system to the fluid; and the second regime

considers the fluid being pumped is two phase and is initially heated by a warm feed system. The case without heat transfer is encountered primarily when engine restart is attempted with a chilled system but with some residual two-phase propellant remaining in the inlet line from the previous burn, or when the engine is operated with very low NPSH such that the static pressure of the flow in the inlet line drops below its vapor pressure causing partial vaporization at the pump inlet. The second case (with heat transfer) is encountered when engine restart is attempted without preconditioning after a long coast when the system can reach equilibrium temperatures ranging between -100 to 300 F.

Cold Feed System (No Heat Transfer). Studies reported in Ref. 19 theoretically describes flow characteristics and pumping capability with two-phase hydrogen at the inlet of a cold pump and matching these predictions with available experimental data. The conclusions of this study were that two-phase hydrogen can be pumped by means of proper pump designs that avoid inlet stator cavitation, inducer blade blockage, choking in the inlet annulus, and vapor recirculation through the inducer. This allows very low NPSH operation and/or mixed-phase starts. It was found that the basic limit to pumping two-phase hydrogen occurs when the combined effects of high flow coefficient operation and blade blockage cause the minimum flow area to occur within the inducer blade passage. When this occurs, the flow will choke, and the pump head will drop drastically.

At design liquid flow coefficient, allowable pump inlet vapor-volume fractions of approximately 20 percent have been obtained experimentally for blade blockages in the order of 30 percent. It is indicated in Ref. 19 that inlet vapor-volume fractions nearly three times this value can be pumped at high speeds by means of proper inducer design which, among other things, minimizes blade blockage. The manner in which the allowable vapor-volume fraction due to inducer blade blockage varies with flow coefficient from Ref. 19 is shown in Fig. 71. Pump pressure rise is equal to that obtained with pure liquid flow up to this limit. The capabilities of

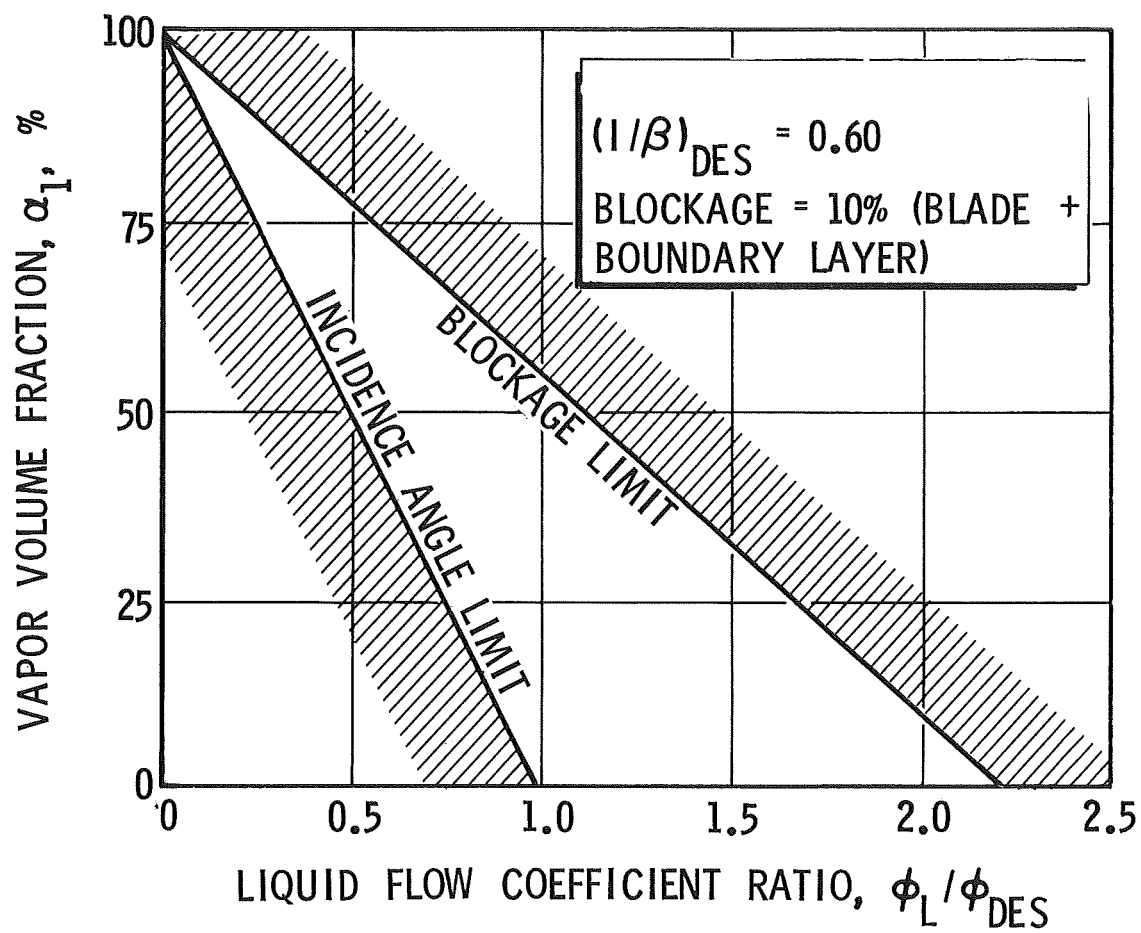


Figure 71. Maximum Vapor Pumping Capacity of Hydrogen Pumps

current designs are included for purposes of comparison. Below design flow coefficient, a stall limit also occurs for axial pumps and a stability limit exists for centrifugal pumps. Above design flow coefficient, a zero-head limit (i.e., ψ goes to zero in the $\phi - \psi$ curve) exists for both designs, but ϕ is greater for centrifugal pumps. In general, reducing the design incidence angle reduces the allowable vapor-volume fraction limit due to blade blockage, such that the upper curve in Fig. 71 has a steeper slope and intersects the abscissa at a lower flow coefficient.

Warm Feed System. The analytical description of pump operation when heat is transferred from the pump surfaces to the fluid is accomplished by assuming that the heat input to the flow results in a decrease in average flow density, which effectively increases the pump flow coefficient. This results in a reduction in pump pressure rise in accordance with the characteristics of the $\phi - \psi$ curve for a given pump. The flow density within the pump is determined by averaging the inlet and outlet flow densities. The inlet flow and flow within the pump may be two phase as long as choking or cavitation does not occur, as discussed earlier.

Typical results of a parametric analysis to determine warm pump operating characteristics obtained are shown in Fig. 70. The slope of the $\phi - \psi$ curve indicated in the figure represents an axial flow pump. For a centrifugal pump, the slope of this curve is less negative and, hence, the reduction in discharge pressure will be less with equivalent heat input. Increasing the inlet pressure has a negligible effect on the results in Fig. 70 if the design discharge pressure is high and the heat input is low. However, if the reverse is true (i.e., operation is such that the heat input is sufficient to vaporize a portion of the fluid), then the inlet pressure can have a strong influence on the amount of vapor generated within the pump and on the associated reduction in discharge pressure.

Engine Start Model

Development of a simple analytical model of a representative engine system was completed to aid in the analysis of the effects of two-phase flow on engine system operation during the start transient. A number of simplifying

assumptions has been made to enable efficient computer solutions for parametric studies and, therefore, the model cannot be applied directly to specific systems. Nevertheless, the salient operating characteristics of a current engine cycle (tapoff) are represented, and the trends predicted are expected to be valid for a wide range of applications. Geometry and components are characteristic of the J-2S engine which is shown schematically in Fig. 72. The analytical description of this system is outlined in the following paragraphs. Most of the equations used in this analysis are normalized with respect to steady-state operating conditions. A normalized quantity is indicated by an overbar.

Controls. Simultaneous solution of the above equations at each instant completely defines off-design engine operation during the start transient. This solution has been programmed for the digital computer with the aid of an existing program called MIDAS, which permits digital simulation of analog programming techniques. Operation of the model on the computer begins by selecting and inputting a set of initial conditions such as tank pressure, flowrates, pressures, valve areas, etc., along with known transients such as valve areas and heat inputs. Engine operating corresponding to these conditions is then computed throughout bootstrap operation to steady state. Desirable initial and controlled conditions are determined by evaluating various transients on a trial and error basis, similar to experimental evaluation of the system.

An investigation was conducted to determine valve sequences for the basic system in the model that prevent undesirable operational characteristics during start, such as turbopump stall, excessive mixture ratio and chamber pressure overshoots, long starts, etc. In this evaluation, it was established that rapid starts could be simulated by initially providing high tank pressures and higher than nominal tapoff valve areas. An upper

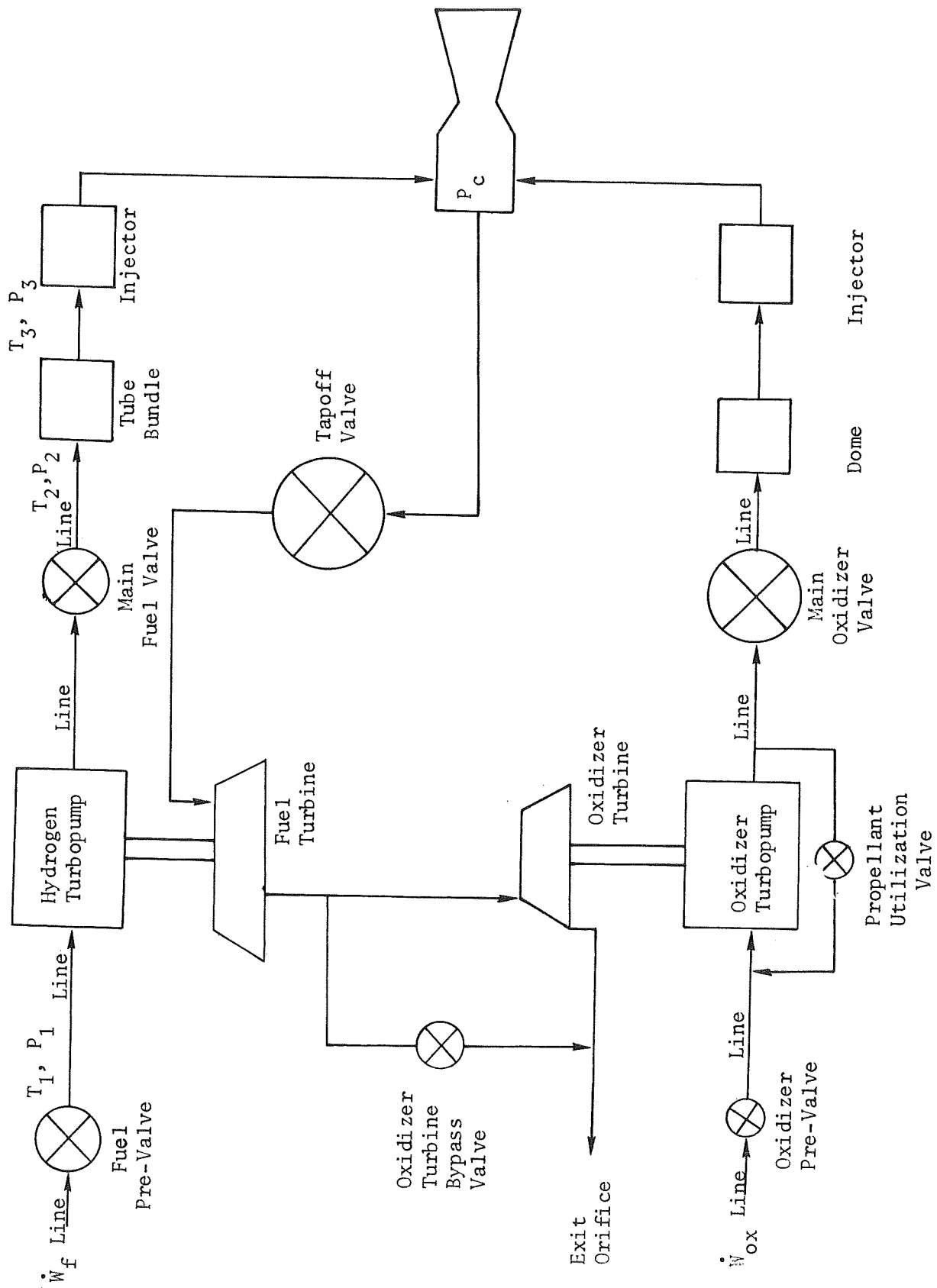


Figure 72. Flow Schematic for Engine Start Transient Analysis

limit for the tapoff valve area was found to be fixed by pump instability line considerations. Because of the relatively low turbine bypass flow utilized in this case, it was found necessary to control mixture ratio by means of a two-position main oxidizer valve downstream of the oxidizer pump. In the model, positioning of this valve is determined on the basis of computed mixture ratio. This control was also found to result in higher flow coefficient operation for the fuel pump, thereby providing a more favorable stability margin for this pump. Typical start characteristics predicted by the model are illustrated in Fig. 73. In this particular case, a single-position oxidizer valve was found to be adequate for mixture ratio control.

Simulated effects of two-phase pump flow and system chilldown have also been investigated with the model using preliminary two-phase pump performance maps presented in Ref. 7. Results of this study are reported in Ref. 7.

System Analysis

This analysis was divided into two general categories to determine the facets of engine operation which benefit most from turbopump improvements. The first concerns cases in which the engine system is thermally conditioned and is depicted as a cold feed system. The second category concerns cases in which engine start is attempted when feed system is warm. As indicated earlier, two-phase flow can exist at the pump inlet in the first case because of low tank NPSH or due to engine start with mixed-phase residual propellants in the inlet lines. Therefore, two-phase pumping capability should be beneficial to these facets of engine operation, but because the conditions are strongly dependent on specific mission requirements and characteristics, analysis in this area was conducted primarily by examining the benefits of pump and cycle improvements for existing systems.

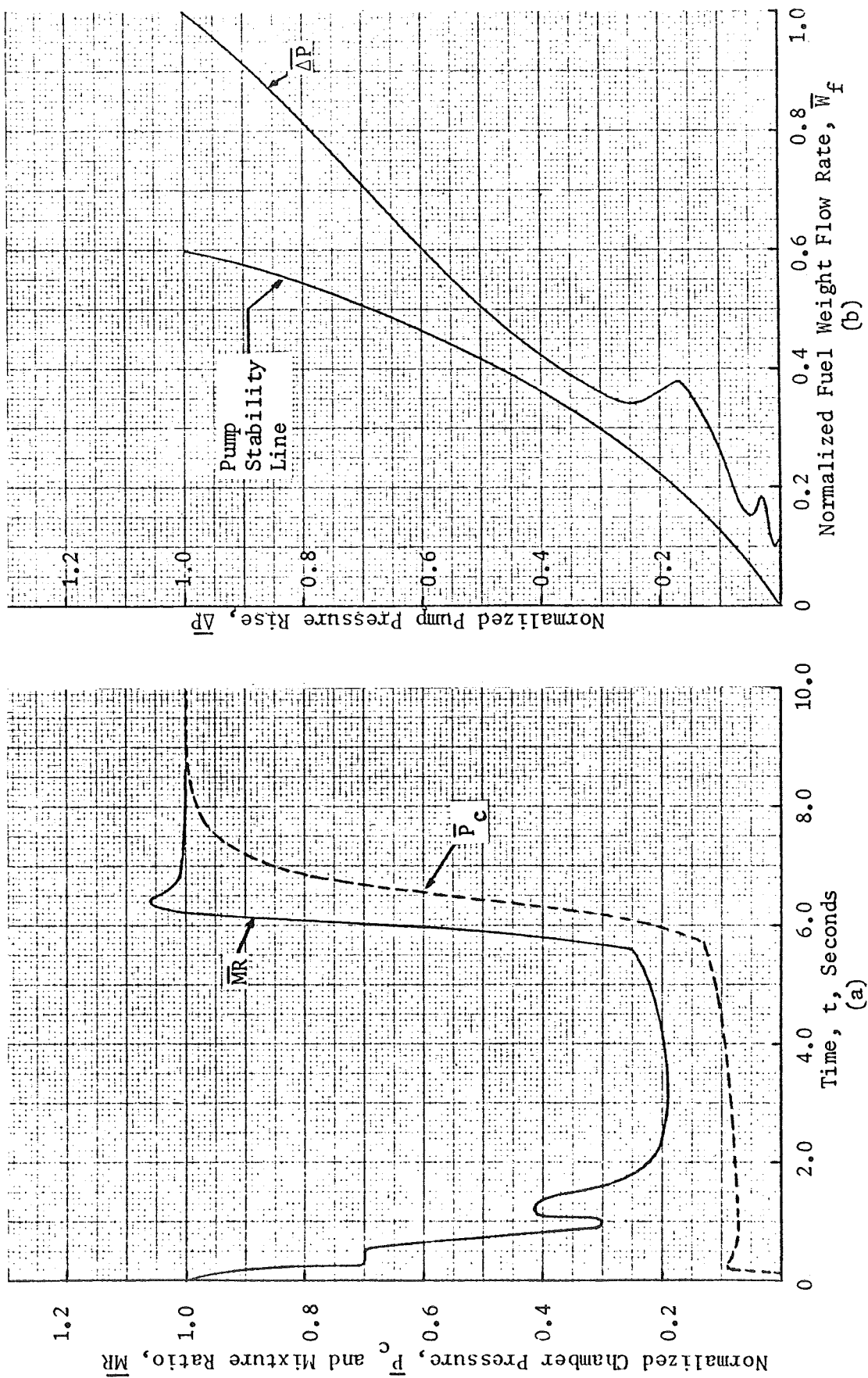


Figure 73. Typical Basic Tank Head Start Transient

Of primary interest in the second category are the effects of inlet line and pump chilldown. In the area of inlet line chilldown, pump improvements (to allow ingestion of increased amounts of mixed-phase flow) were evaluated. The chilldown flow required to lower the inlet quality to permit pumping was converted into payload losses for a typical mission. Representative chilldown transients were obtained for this purpose from a review of existing J-2 and J-2S data. Pump chilldown effects and the benefits of insulation coatings were studied by superimposing the performance curves in Fig. 70 on the $\phi - \psi$ curves in the start model, and determining the resulting engine start characteristics for various heat inputs. Results of these studies are discussed in the following paragraphs.

Cold Feed System

Zero NPSH. In a preconditioned system, reductions in required tank NPSH made possible by means of two-phase pumping capability are always beneficial to the operation of a rocket engine system, but the magnitude of these benefits depends strongly on the requirements and design of each system. Most boost vehicles require some pressurization in addition to pump NPSH requirements for structural reasons. This often prohibits complete elimination of the pressurization system. However, reductions in NPSH requirements do allow simplifications and reductions in the size and weight of conventional systems, and in the length of required operating time.

In some instances, a reduction in pump NPSH requirements in conjunction with certain other features provides more significant improvements and simplifications compared to existing systems. This is the case with the J-2S system as discussed in Ref.21 . In this design, heated hydrogen is tapped from the cooling jacket and used to pressurize the fuel tank, thereby eliminating numerous existing complex components such as heat exchangers, helium bottles, associated plumbing, etc. The weight savings associated with the improved system for the S-IVB has been estimated to

be approximately 2130 pounds (Ref. 21). Of course, further reductions in NPSH requirements via increased two-phase pumping capability will result in a reduction in the amount of hydrogen pressurant required with some increase in cycle efficiency, even for this advanced system. For these reasons, low NPSH operation is currently a design goal for all known LO_2/LH_2 boost vehicles. The analysis presented in Ref. 19 indicates that this can be easily achieved by means of improved inducer designs which permit ingestion of two-phase hydrogen at the pump inlet.

Two-Phase Starts. Current studies seem to indicate that improved two-phase pumping capability will improve mixed-phase start operation with a cold feed system in most typical near-term applications. The current Saturn vehicle uses a recirculation system to duct poor quality propellants in the pump and inlet line back into the tank prior to engine start.

A simpler but less efficient backup technique as used in this application consists simply of using sufficient fuel lead under tank pressure to flush the system of poor quality fuel. Flight test data indicate that about 10 seconds of fuel lead is needed with a relatively cold system to fill the inlet duct with tank quality fuel. If the duct were initially nearly full of residual liquid, this would amount to a maximum of about 30 pounds of propellant lost per engine inlet duct per restart. Unfortunately, the quality of residual propellants in the duct prior to restart is unknown in this application. If the duct is initially warm, some additional propellant vapor is generated as it passes through the duct, thereby making the time required for the fuel lead a function of initial duct temperature or coast time.

Two-phase pumping capability may not significantly decrease the fuel lead propellant loss because a higher quality inlet condition can be tolerated. Of course, the pump will produce head once the inlet quality falls below the limiting value which may occur before the 10 seconds has elapsed. This only represents a limiting condition so spinning the pump and initiating the start sequence once head rise is detected will decrease required fuel lead time and propellant losses.

In this regard, improved two-phase pumping capability will be beneficial, for an application with a cold feed system (based on the maximum propellant loss per engine duct of 30 pounds).

Another consideration that arises is that the vapor volume limits established in Ref. 19 are valid only for upstream relative Mach numbers in the range from 0.6 to 1.8 (these are representative of high-speed operation), thus corresponding more closely to the design point than to the low speeds encountered during the start transient. According to the curves presented in Ref. 19, choking does not necessarily occur for small area contractions at lower Mach numbers and, consequently, higher vapor pumping capability than shown in Fig. 71 can be expected for any system at start, although the head rise and flow are much less than at design due to the lower speed.

This characteristic is used to advantage in the J-2S engine system. A solid-propellant turbine spin (SPTS) cartridge is utilized in conjunction with a brief idle-mode operation (approximately 1 second) to flush the inlet ducts of mixed-phase propellants. Idle mode is used for propellant settling, and its results are similar to those obtained with the present S-IVB system with a fuel lead during ullage motor operation, except that the mixed-phase residual propellants are consumed with relatively high specific impulse (~ 280 seconds) rather than being dumped directly overboard. The SPTS duration is such that all of the residual fuel and most of the oxidizer in the ducts are replaced prior to burnout. Also, its starting characteristics are such that pump cavitation is avoided at all times. These features enable elimination of the recirculation system for J-2S applications with an estimated weight savings of 1600 pounds for the Saturn vehicle (Ref. 6). Engine operation during start is illustrated in Fig. 74. At altitude, tank head starts with this system are possible with longer idle-mode durations (20 to 100 seconds) to provide system conditioning. Typical mission sequences are shown in Fig. 75.

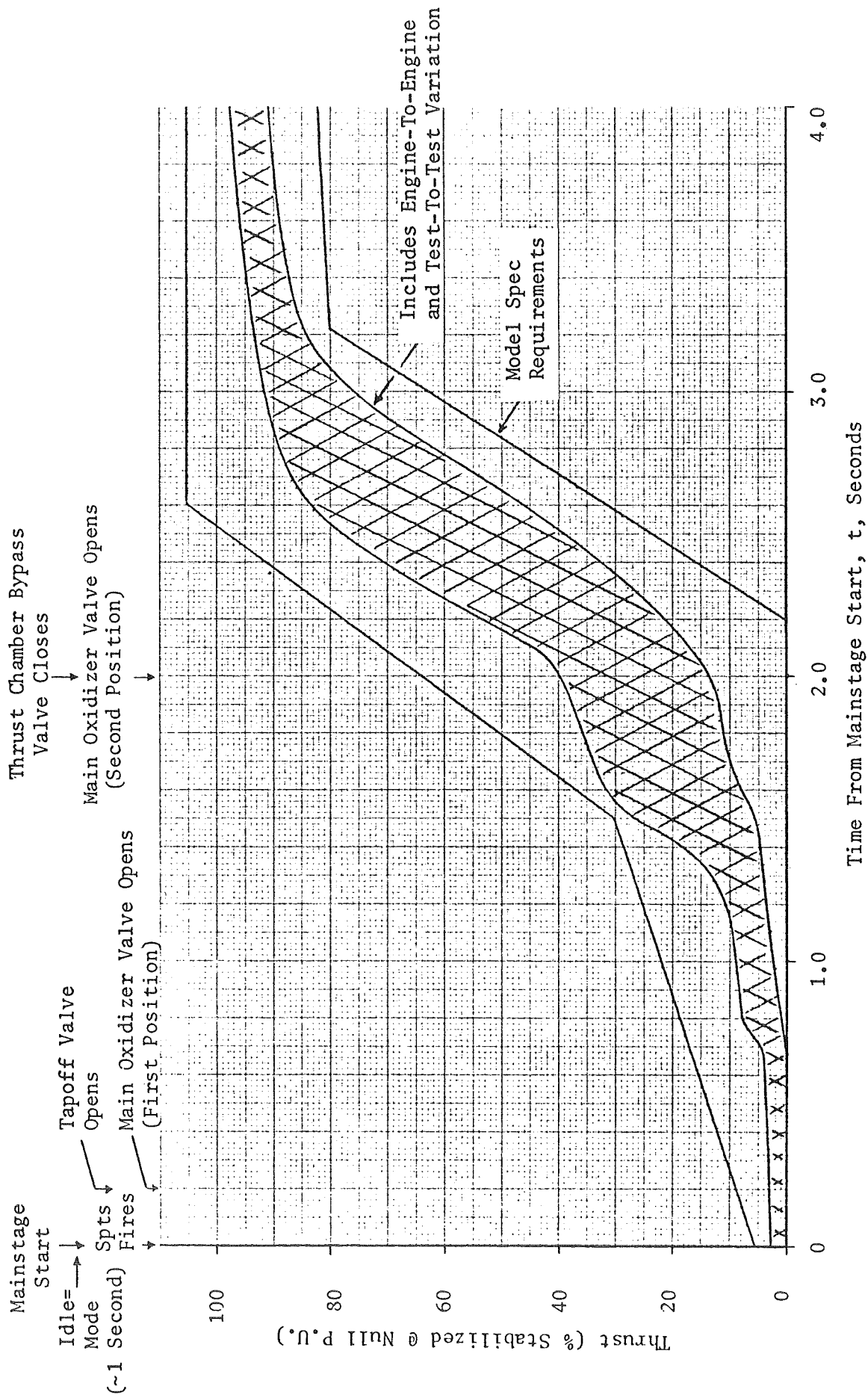


Figure 74. Typical J-2S Engine Start Transient

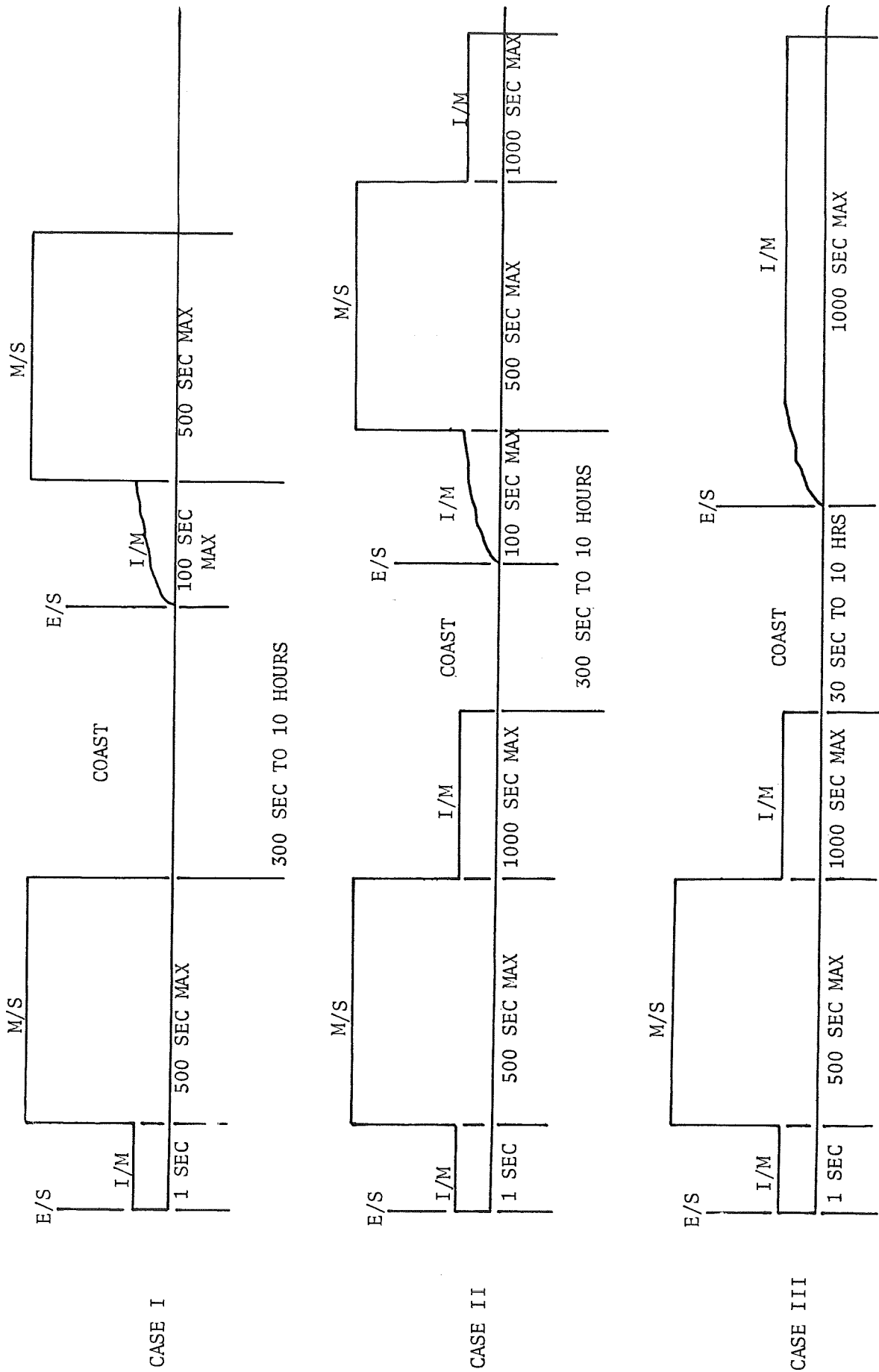


Figure 75. J-2S Start and Restart Requirements Based on Various Mission Profiles

More advanced LO_2/LH_2 systems are expected to be configured on the basis of J-2 and J-2S experience. With the relatively low tank pressures and advanced cycles currently envisioned for these applications, studies indicate that some form of auxiliary turbine power similar to that used in the J-2 system may be used to enable a rapid and efficient start. Current designs feature an idle-stage combustor operating initially under tank head pressure in conjunction with a low-resistance feed system downstream of the pump, as shown in Fig. 76. If this is the case, further improvements in two-phase pumping capability for low inlet Mach numbers may be desired.

Warm Feed System. Attempting engine start and/or restart with initially warm hardware places stringent requirements on the system, and has received considerable attention during development of the J-2, J-2X, and J-2S engines. A good analysis of available data generated during sea level tests of these engines is presented in Ref. 7. The analysis indicated that chilldown time and propellant usage are a strong function of flowrate. This is illustrated by the chilldown data for the Mark 15 LH_2 pump shown in Fig. 77. It is readily seen that the higher flowrates achievable with tankhead blowdown through the injector at high altitude result in much shorter pump chilldown periods.

Additional test results have been obtained with the J-2S engine, which uses its idle mode capability to provide system preconditioning prior to mainstage. Sea level idle mode chilldown data for a case where the entire J-2S engine is initially at ambient temperature is presented in Ref. 7 and is reproduced in Fig. 78. Simulated flight testing has also been conducted in an altitude chamber at Arnold Engine Development Center and these results are included in Fig. 78. For the sea level tests good quality fuel is seen to exist at the pump outlet (Fig. 81b) once the fuel temperature (Fig. 78A) drops below the saturation level.

Inlet Line Chilldown. Analytical inlet quality data that corresponds to the flight data in Fig. 77 indicate that once the inlet duct is flushed, pump inlet quality drops very rapidly for the fuel lead flowrate utilized with the S-IVB system, regardless of the initial line temperature. These results are shown in Fig. 79. Total propellant losses corresponding to these conditions are shown in Fig. 80a as a function of the limiting vapor

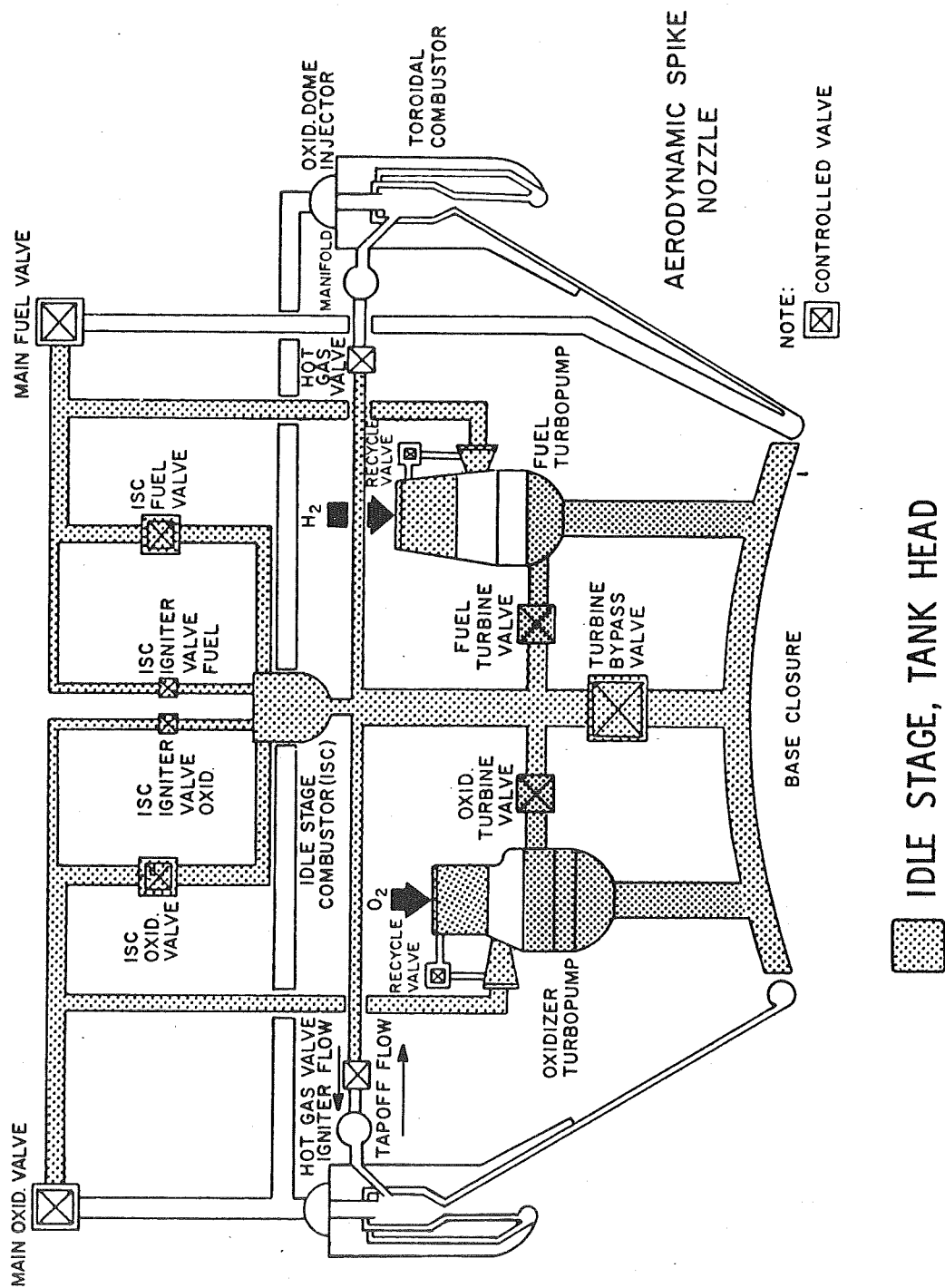


Figure 76. AEA Engine Idle Stage Operation

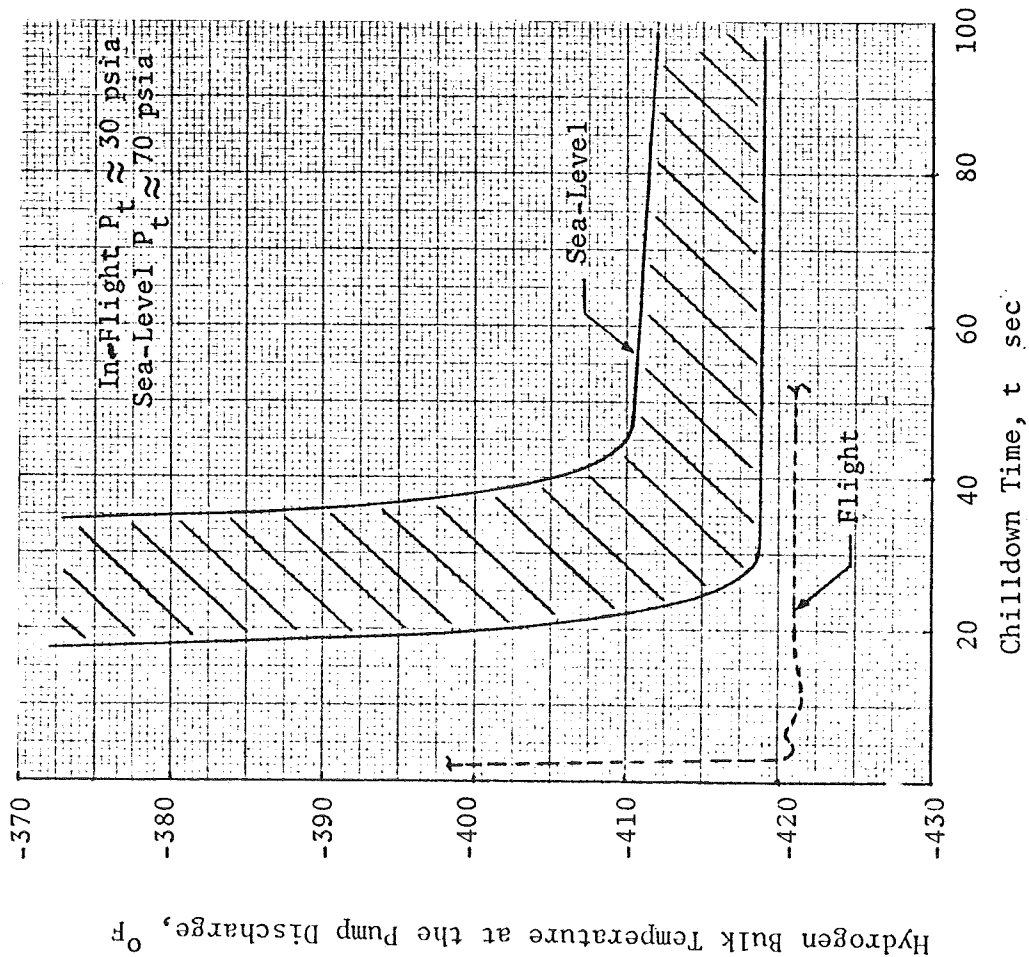
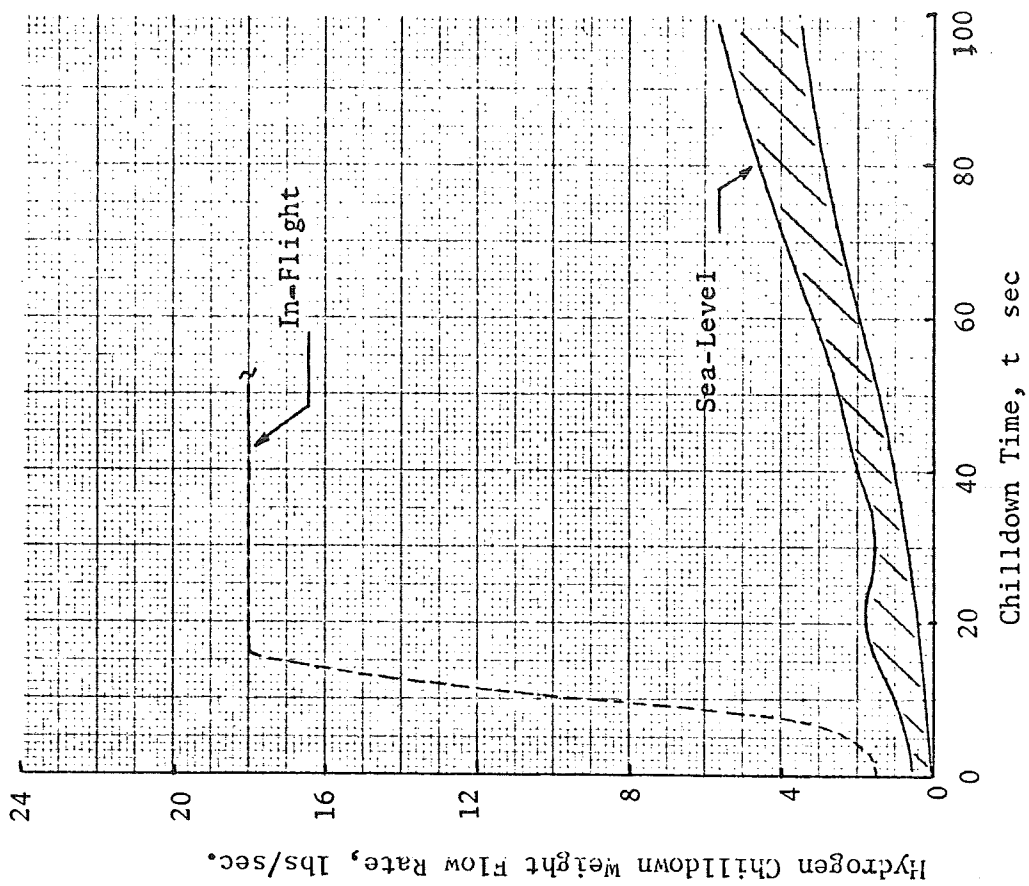


Figure 77. Typical Chilldown Transients for the J-2 Engine System (Mk 15 LH₂ Pump)

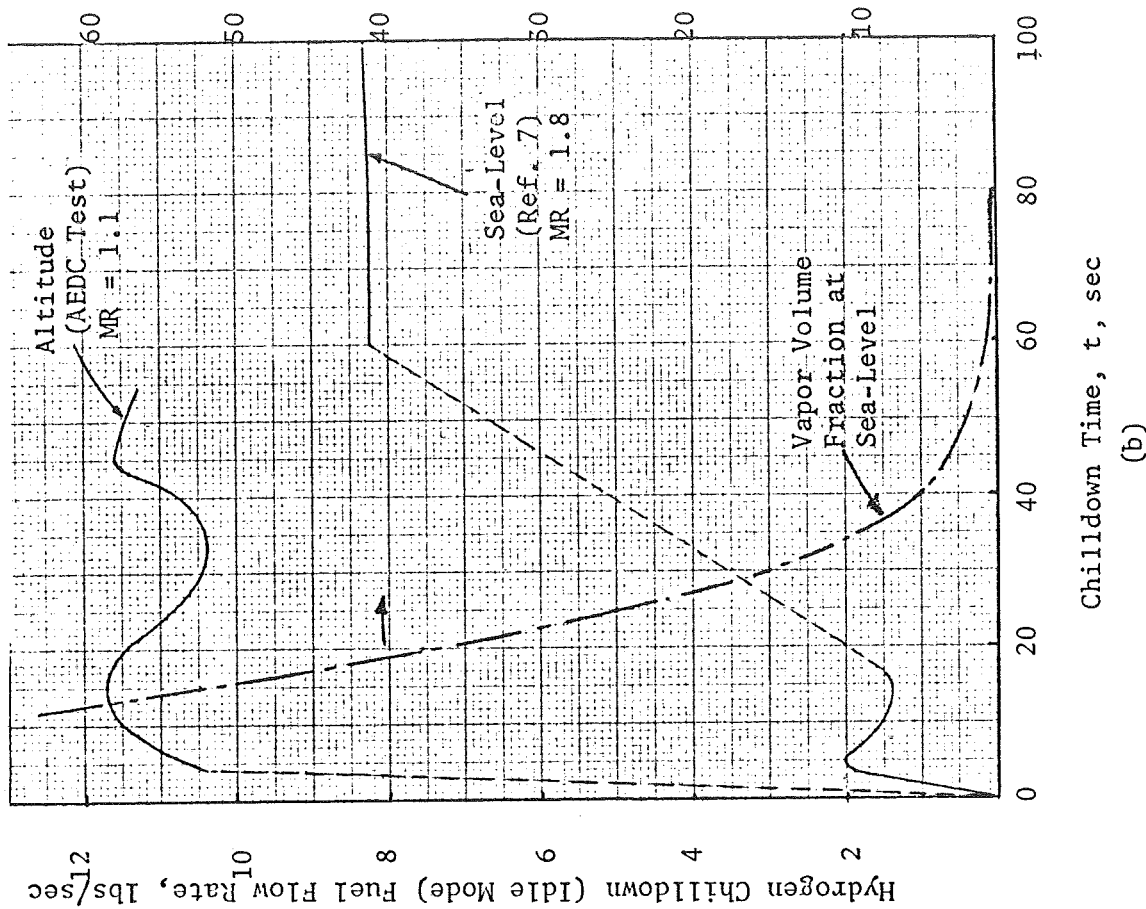
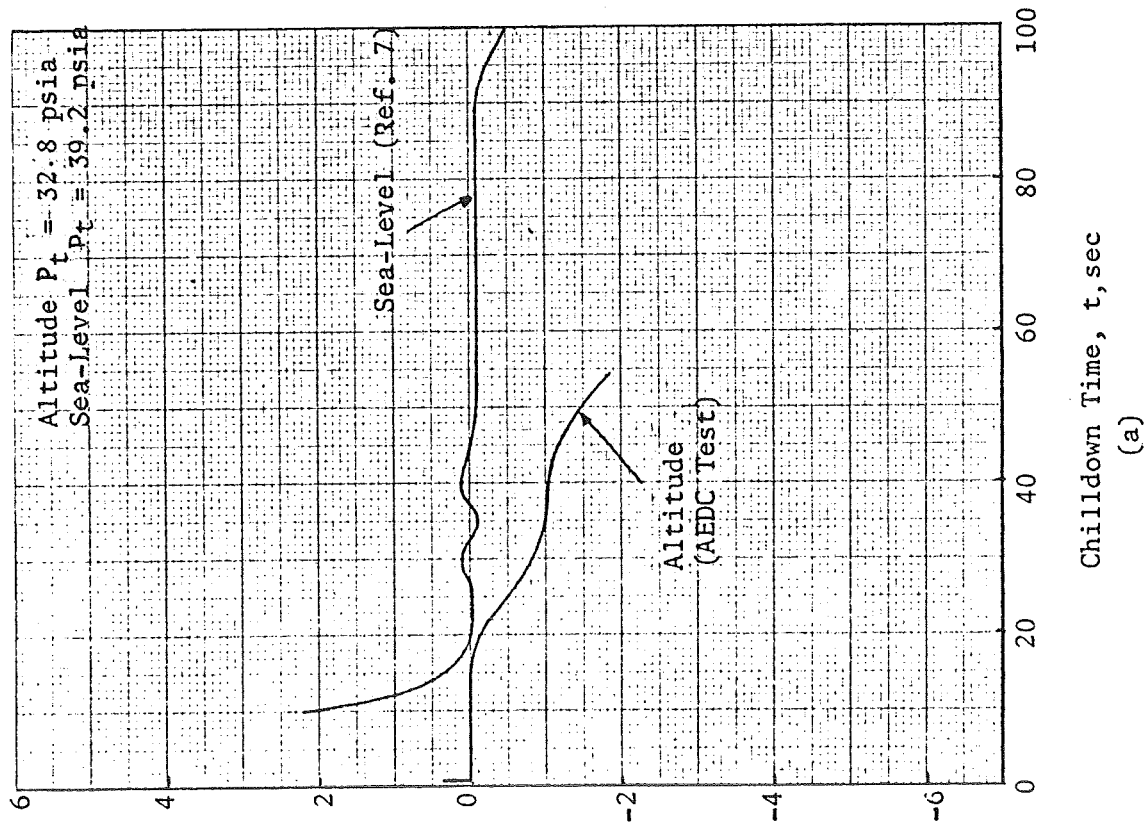


Figure 78. Typical Chilldown Transients for the J-2S Engine System (MK 29 LH_2 Pump) From Ambient Condition (Ref. 8)

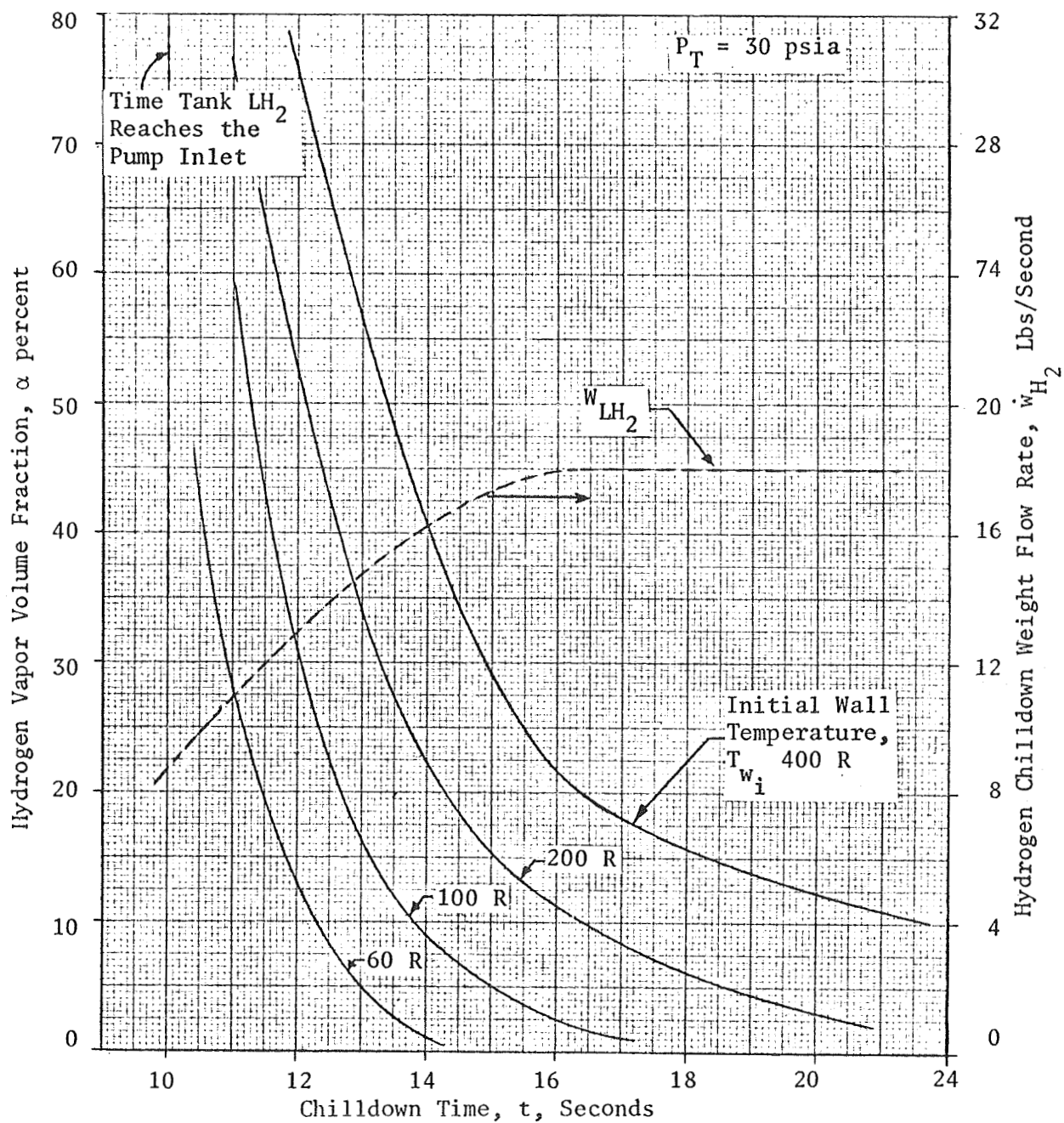


Figure 79. Flow Quality at the pump Inlet for the J-2 Hydrogen Engine

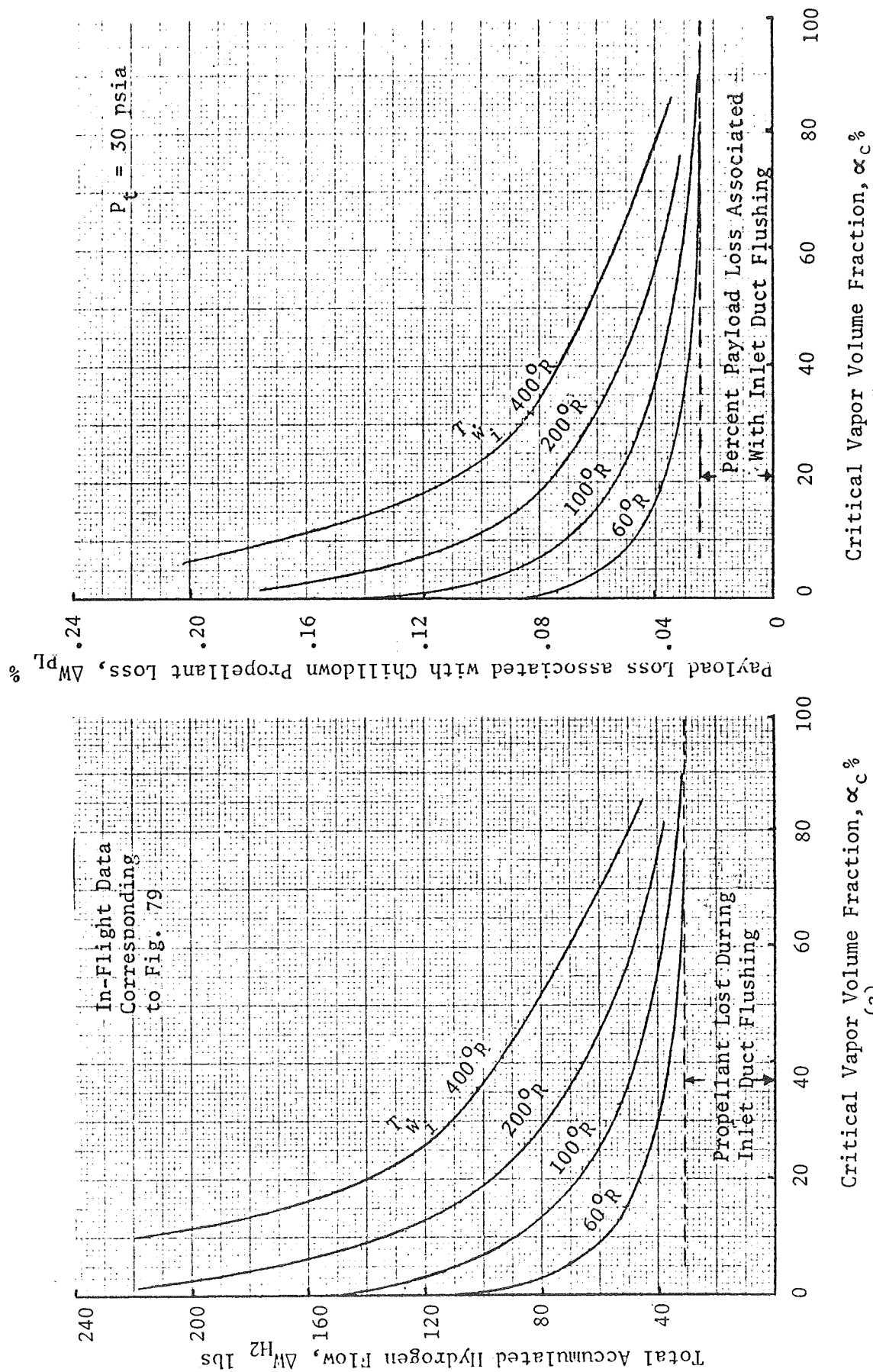


Figure 80. Fuel and Payload Losses for the J-2 Engine Inlet Line Chillown Transients in Figure 79 for Various Vapor Volume Fraction Pumping Capabilities

volume fraction above which pump operation cannot begin. Approximate percentage payload increments corresponding to these flow losses in Fig. 80a were estimated by means of the technique outlined in Appendix C and are presented in Fig. 80b. From this, it can be seen that for the particular mission of the S-IVB, increasing the inlet vapor pumping capability up to 50-percent volume fraction at engine start produces a 136-pound (0.15 percent) gain in payload for an initial duct temperature of 400 F. On advanced vehicles requiring multiple starts, payload gains will be more significant since 52 pounds of fuel would be saved for each start made.

Similar results were obtained using the J-2S engine chilldown data. In this case, inlet quality was measured directly (Fig. 78B) for the sea level test, and estimated from this and the temperature data in Fig. 78A for the altitude test as shown in Fig. 87. Total accumulated chilldown hydrogen flow is shown as a function of the limiting vapor volume fraction in Fig. 82A, and corresponding payload losses in Fig. 82B. While not particularly representative of a realistic situation, the sea level data are included in Fig. 82 to show that even though it takes longer to obtain pure liquid at the pump inlet at sea level (Fig. 87), the assumed flowrate trend in Fig. 78 is such that the composite result is a smaller payload loss for most representative vapor pumping limits.

Pump Chilldown. The preceding discussion applies primarily to cases where heat transfer to the flow within the pump is negligible. However, some additional flow may be vaporized if it is heated as it passes through the pump. A vapor pumping limit also exists in this case, but the mechanism may be different than before where choking in the inlet inducer blades was found to cause a severe drop in discharge pressure and result in a flow-limiting situation. If heat is transferred within the pump passages choking may occur anywhere within the pump depending on rotational speed, pump geometry, and heating rates. Not too much is known about the details of this process as yet, but it is an area deserving of attention in further studies. Pump design and insulation can be expected to influence flow properties significantly with a resultant influence on start characteristics. The magnitude of these effects will, of course, depend strongly on the system in question.

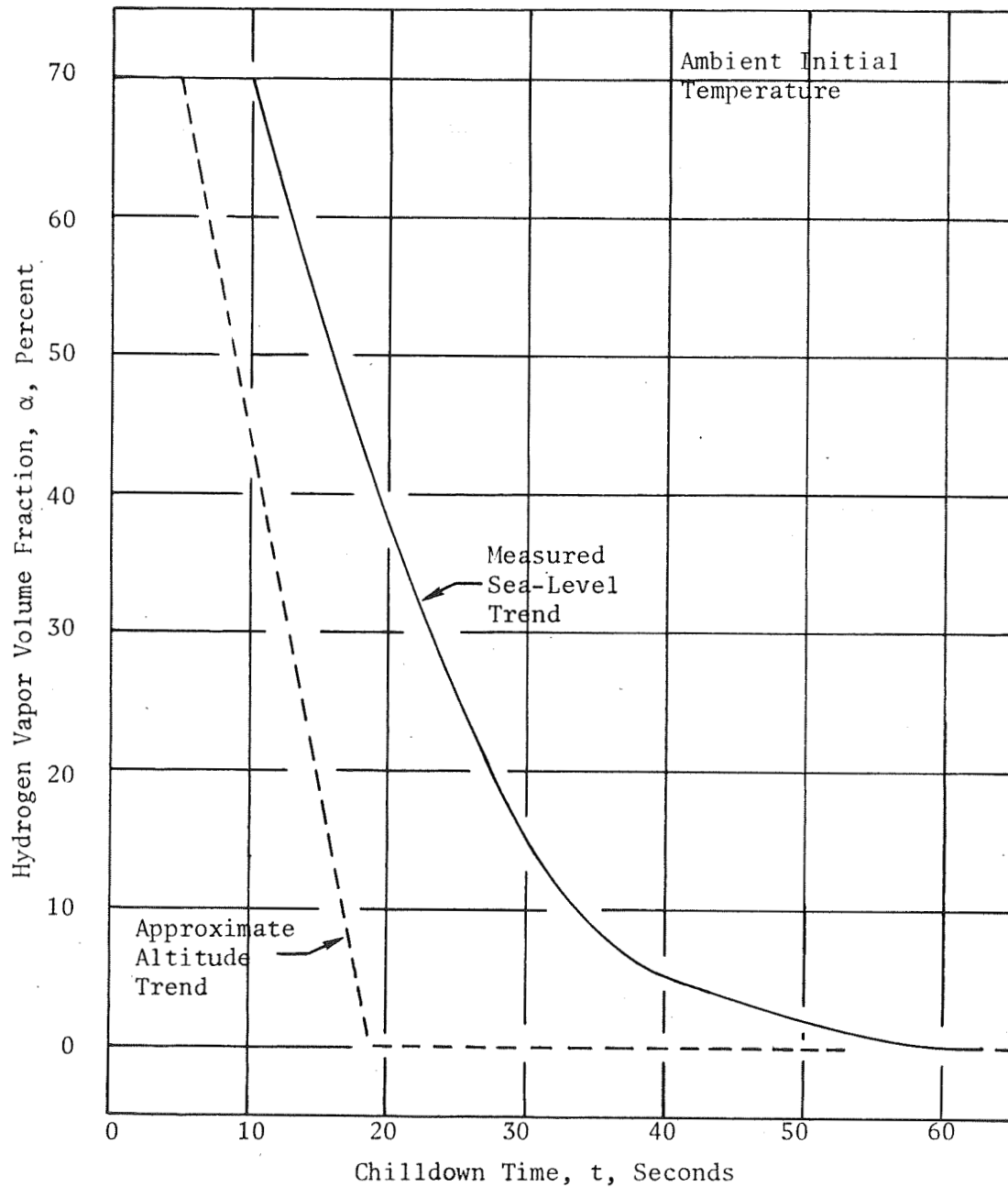


Figure 81. Flow Quality at the Pump Inlet for the J-2S Engine (Sea-Level Data From Ref 7 and Conservative Altitude Estimate Based on Temperature Data from Fig. 78)

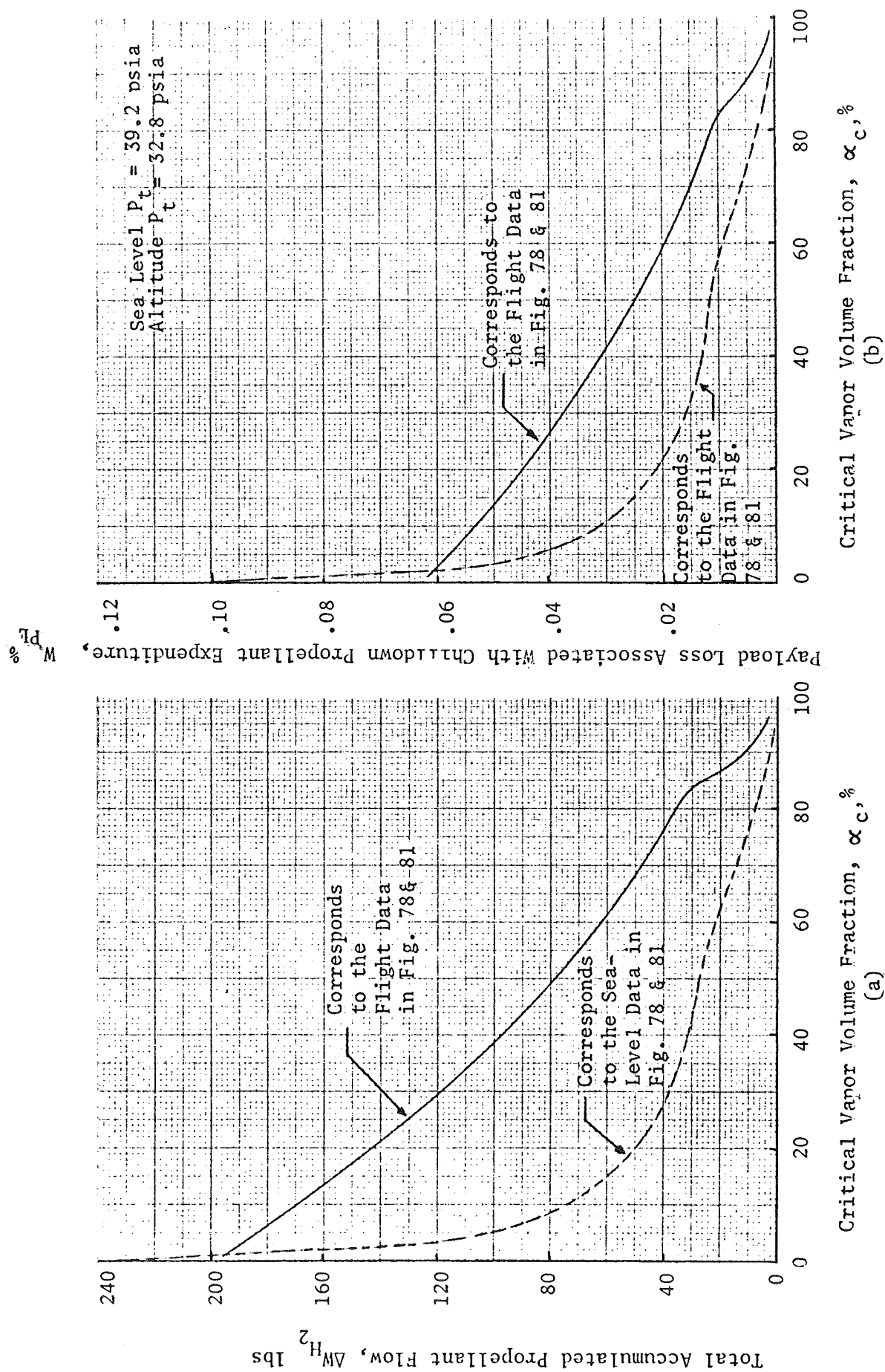


Figure 82. Estimated Typical Propellant Expenditure & Associated Payload Loss for J-2S Engine Chiddown Transients in Figs. 78 & 81 for Various Vapor Volume Pumping Capabilities

The manner in which heat transfer affects pump performance if flow is not vaporized within the pump is approximated by the data presented in Fig. 70. To determine the effect of this change in performance on a typical engine start, these data were superimposed on the $\psi - \phi$ curves in the start model and used in conjunction with assumed heating rates in a range representative of the S-IVB chilldown flows and initial temperature distribution. Since heating rates are also a function of flowrate, an iteration is required for precise results, but correct trends are reflected by simply using the chilldown data directly in conjunction with the performance data in Fig. 70. Results obtained using this procedure are presented in Fig. 83. As indicated, engine start time (Fig. 83B) is relatively unaffected. However, the increased resistance early in the transient causes a brief mixture ratio overshoot and an excursion into the unstable region for the pump. Because of their short duration and a normal time lag, these characteristics may not necessarily hinder engine operation, but since they are representative of the effects of pump heat input, methods of eliminating them were studied. Primary emphasis was placed on incorporation of a multiposition oxidizer valve, which earlier studies have shown to be the most effective means of mixture ratio control during start.

It was found that this control alone was sufficient to reduce these undesirable effects to a minimum as shown in Fig. 84C and 84D. The control valve positions corresponding to these transients are indicated in Fig. 84A. It can be seen in Fig. 84B that these added control requirements do, however, result in a small increase in start time. It was also found that, once an acceptable control sequence was established, the aforementioned undesirable effects of pump heat input are effectively eliminated by this sequence for the cases of prolonged heating periods examined in this study (Fig. 85).

Coating Effects. Insulation coatings on the surface of pump passages can also improve performance with heat transfer. A desirable coating would be one which resulted in a rapid surface chill and low heat flux to

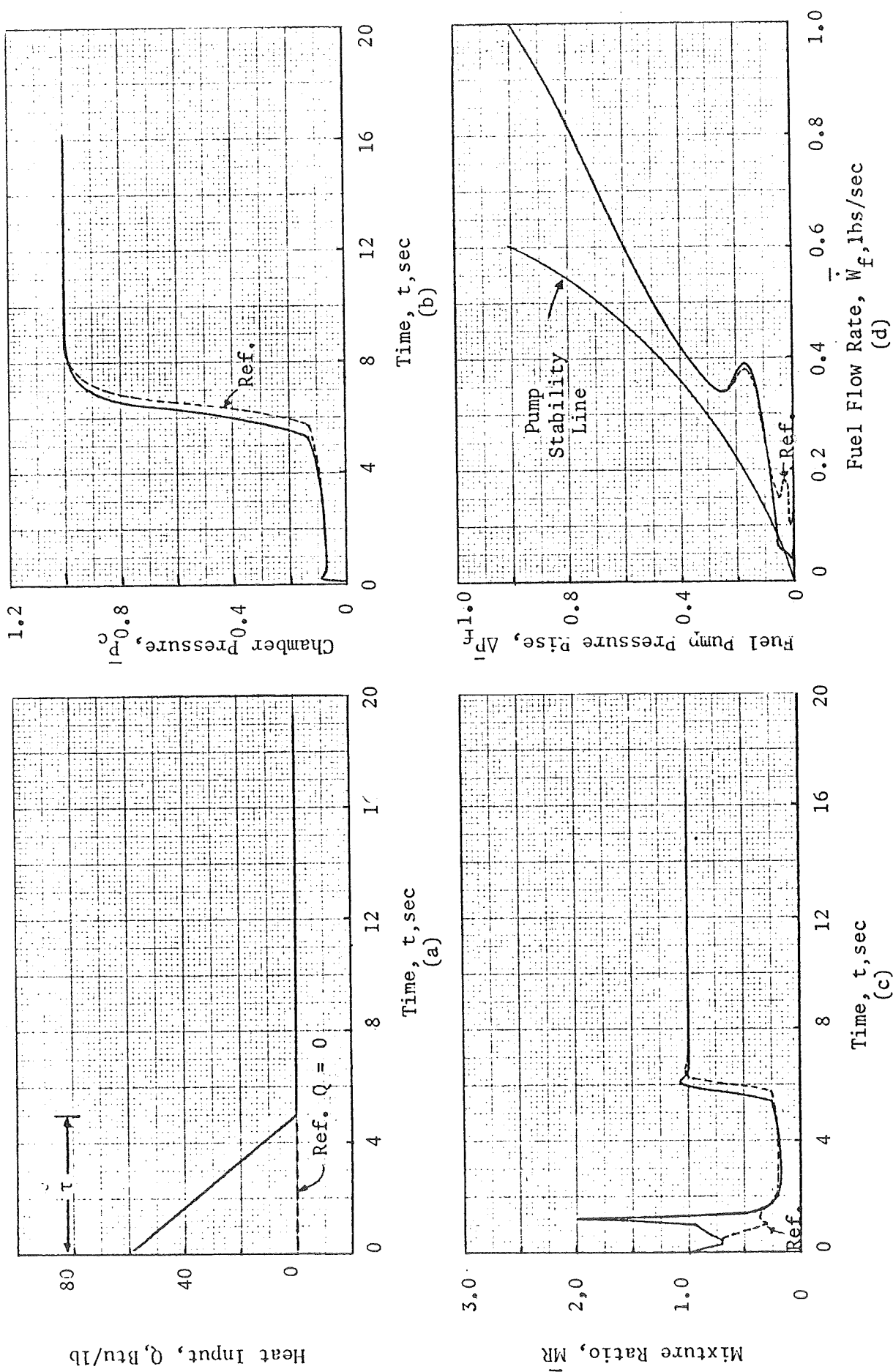


Figure. 83. Effect of Pump Heat Input on Engine Start Characteristics

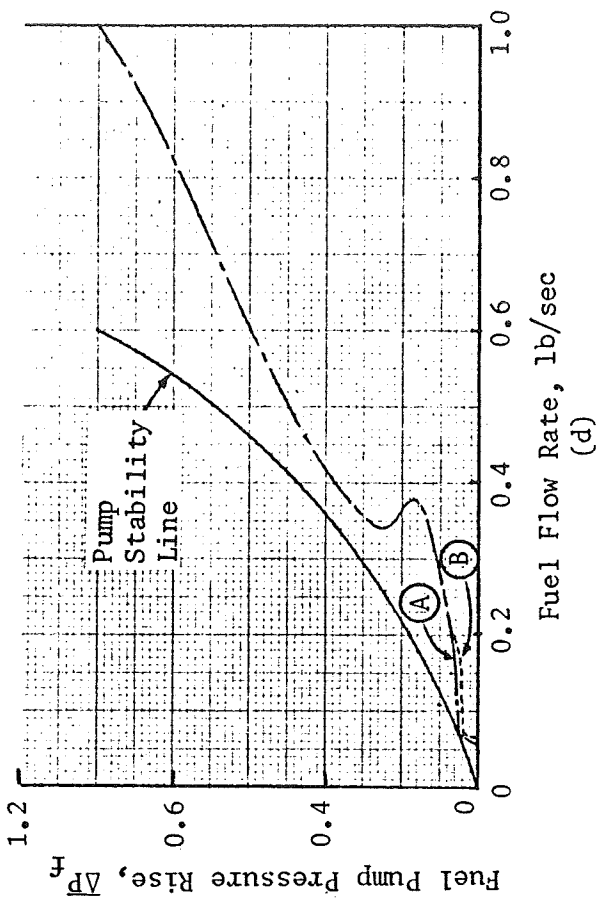
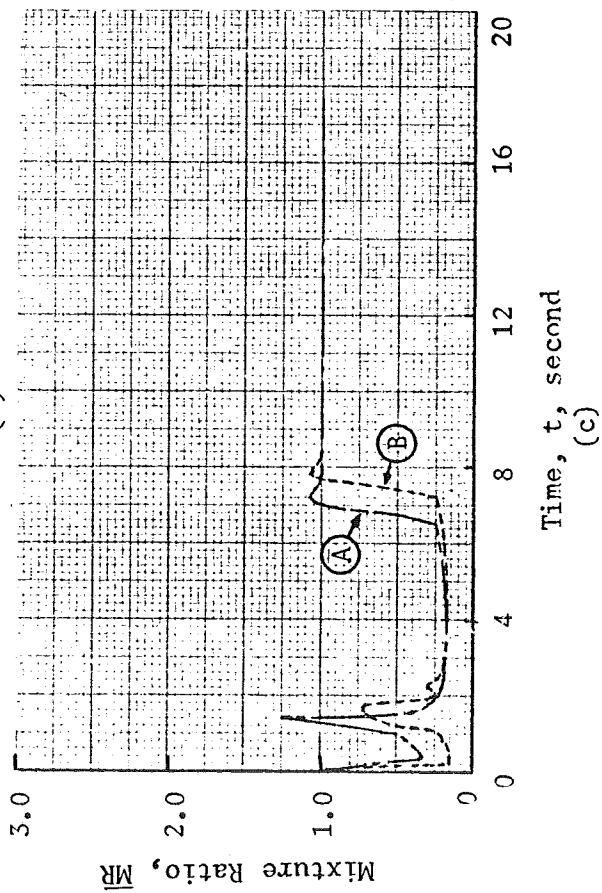
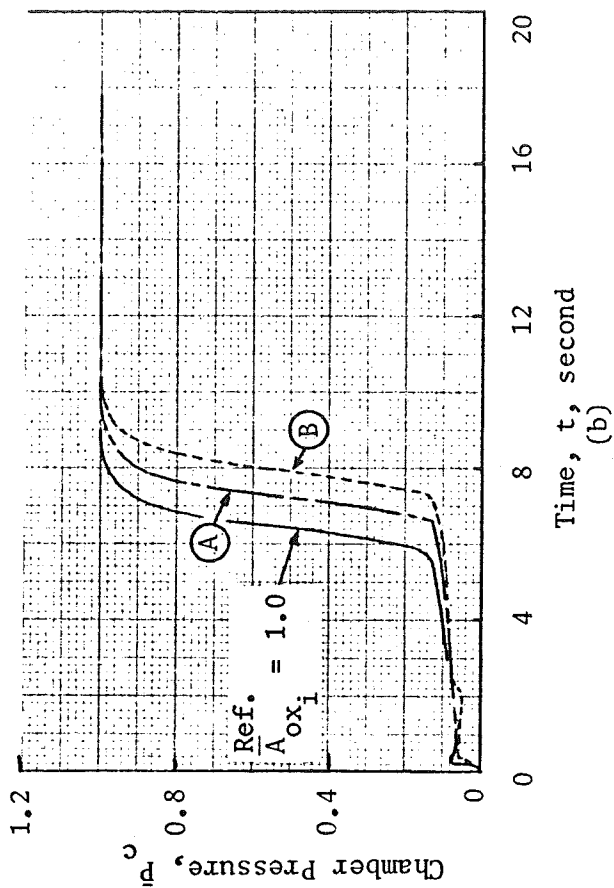
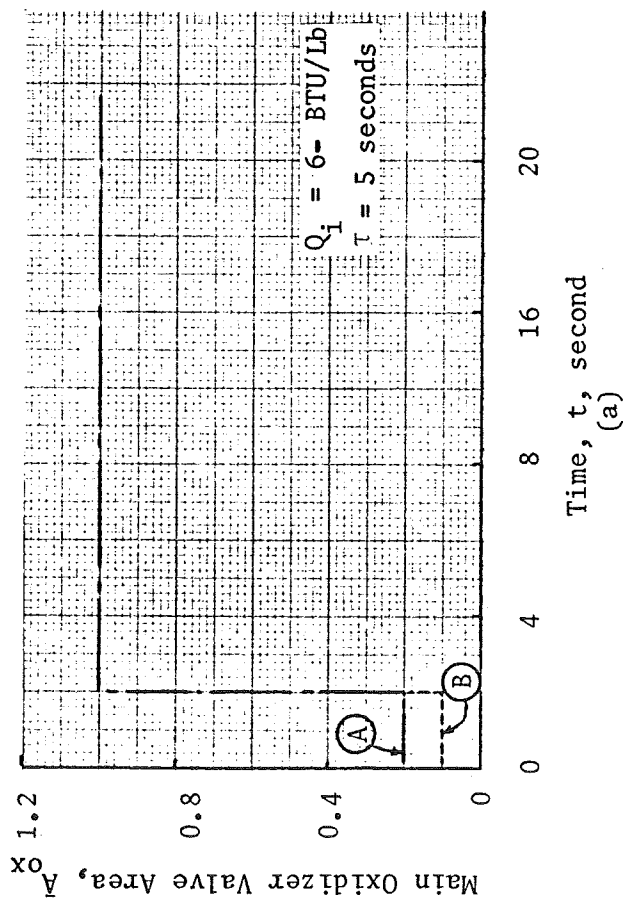


Figure 84. Effect of Stepped Main Oxidizer Valve Flow Control on Engine Start Characteristics With a Warm Pump ($Q_i = 60 \text{ BTU/Lb}$, $\tau = 5 \text{ seconds}$)

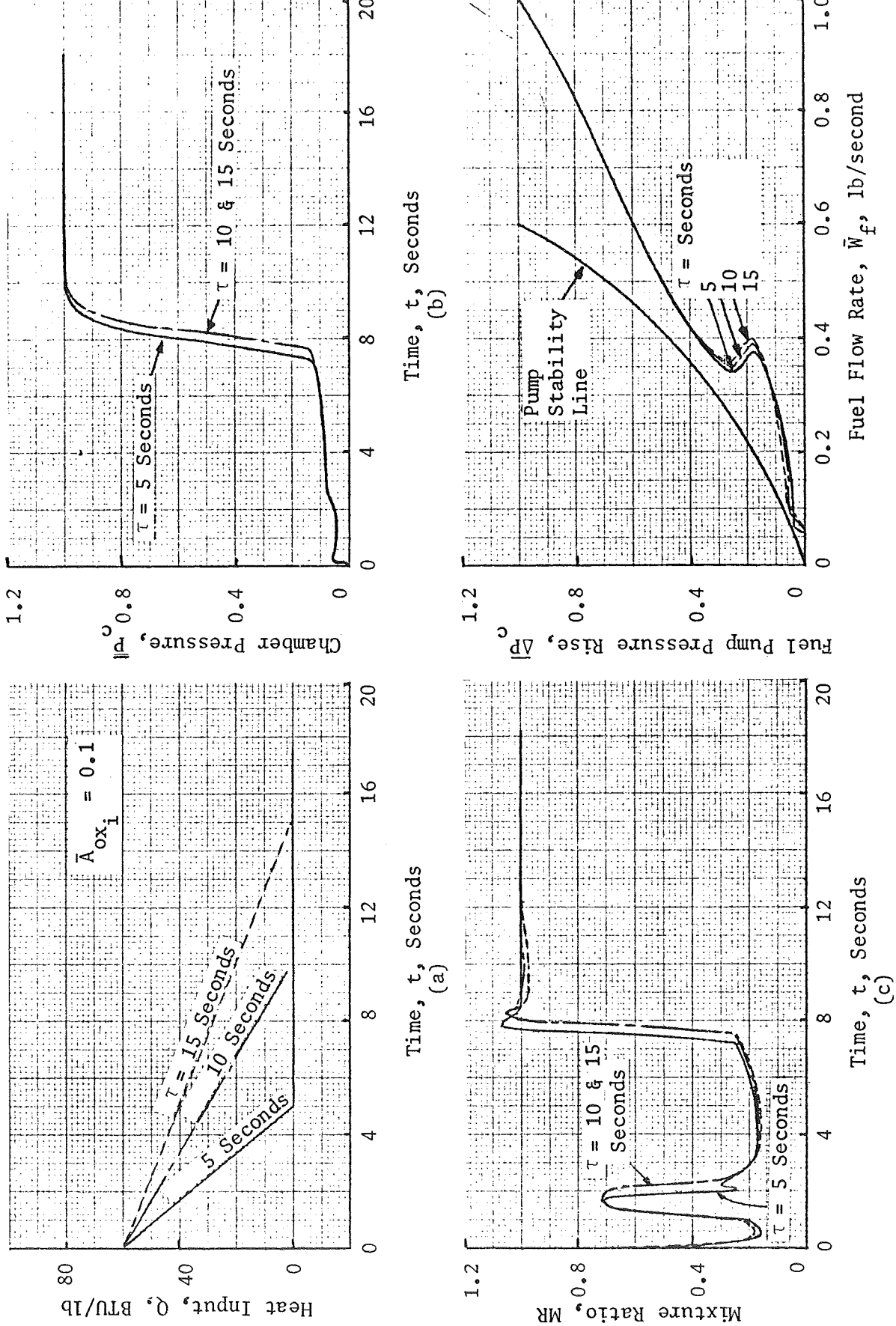


Figure 85. Effect of Prolonged Chilldown Period on Engine Start Characteristics With a Warm Pump and With Stepped Main Oxidizer Valve Flow Control ($\bar{A}_{ox_i} = 0.1$)

the propellant at the low flows corresponding to the beginning of the start sequence to provide minimum resistance during this critical period. Start transients generated as before showing the effects of this heating characteristic are presented in Fig. 86 . Start controls employed with the coated pump (case A in Fig. 86) are identical to those used for the reference case. The transient with high initial heat input and two-position oxidizer valve control is also shown for purposes of comparison. It must be mentioned that the differences in heating rates for the two cases in Fig. 86A are fictitious and may not be attainable in an actual system. The rate for case A is intended to serve only as an example to illustrate potential benefits of the coating if this heating characteristic can be achieved. Examination of Fig. 86B, C, and D indicates that for the assumed conditions these benefits may be significant in terms of reduced start time (due to the reduced control requirement) and improved pump stability and mixture ratio transients (due to the reduced initial heat input).

It should be noted in this regard that, since initial heat input to the flow from the walls of the thrust chamber is neglected in the start model, the effects of pump heat input and subsequent improvements provided by coatings may appear pronounced. This may or may not be the case, depending on the system. Data presented in Ref. 6 (reproduced in Fig. 87) indicate that pump heating effects strongly predominate over the influence of thrust chamber heat input for small systems. Later studies proved that pump coatings provided substantial start improvements for these systems, which supports the trends noted in Fig. 86 and 88. On the other hand, the J-2 system experiences much higher initial heat input to the flow from the thrust chamber than from the pump. In this case pump heating effects are less pronounced and improvements provided by pump coatings will be less. Of course, additional control requirements due to the pump heating effect will also be reduced, and the net effect will be a start transient very similar to the case without heat input.

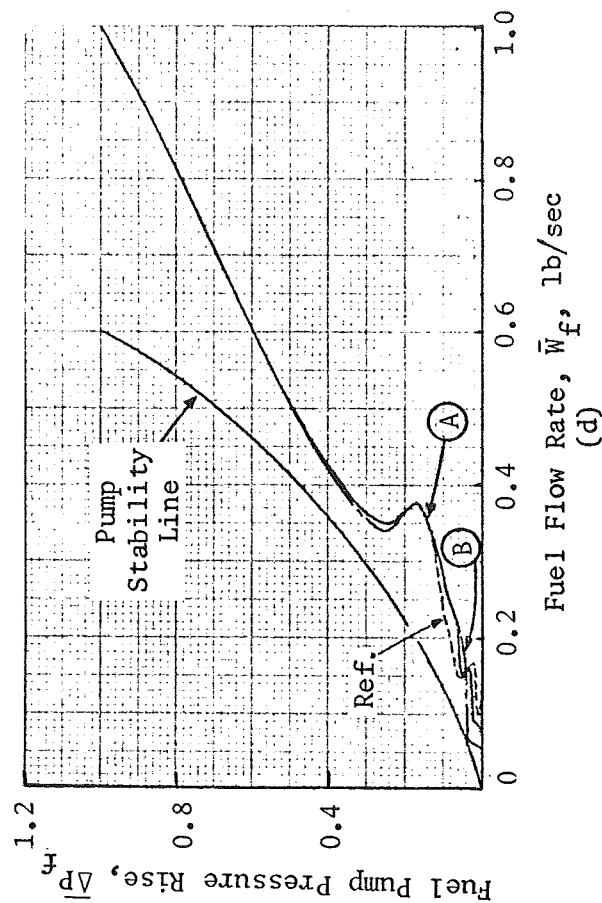
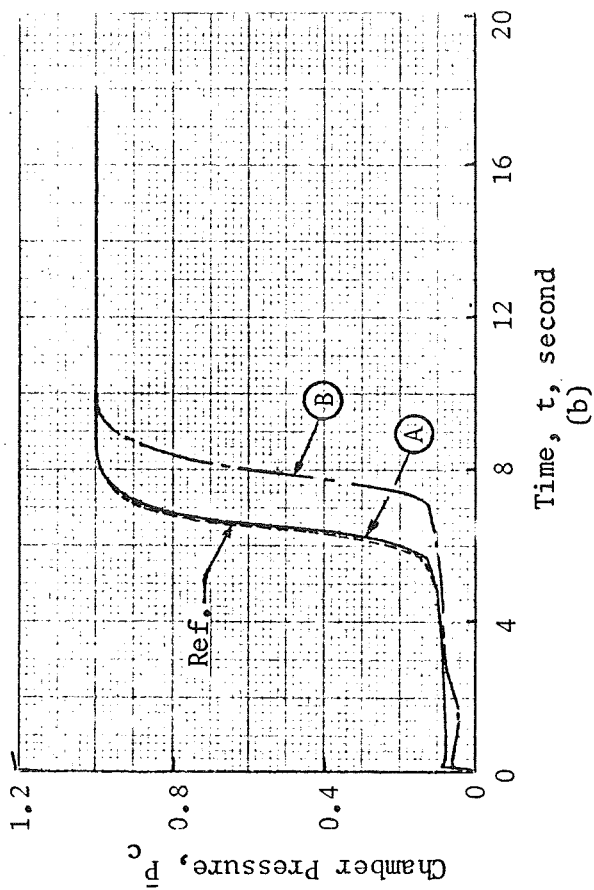
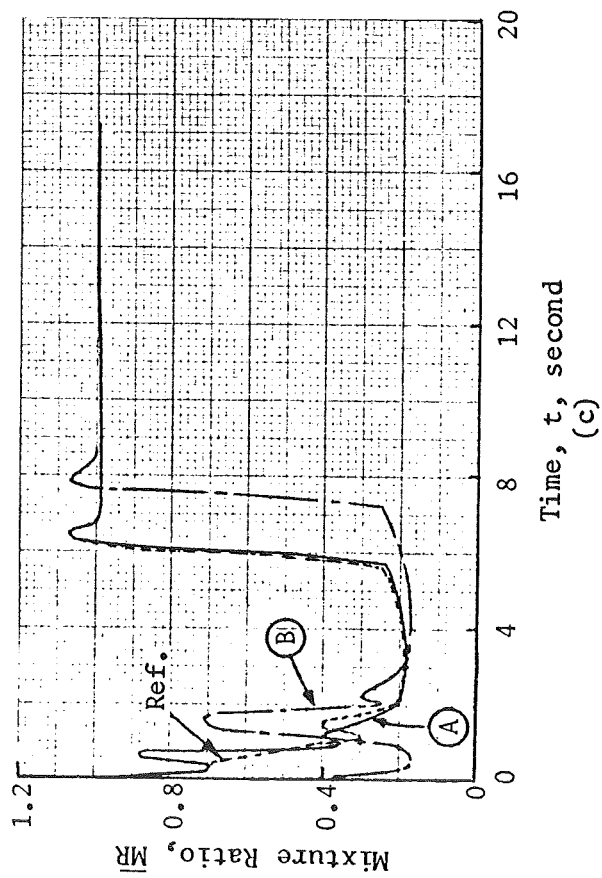
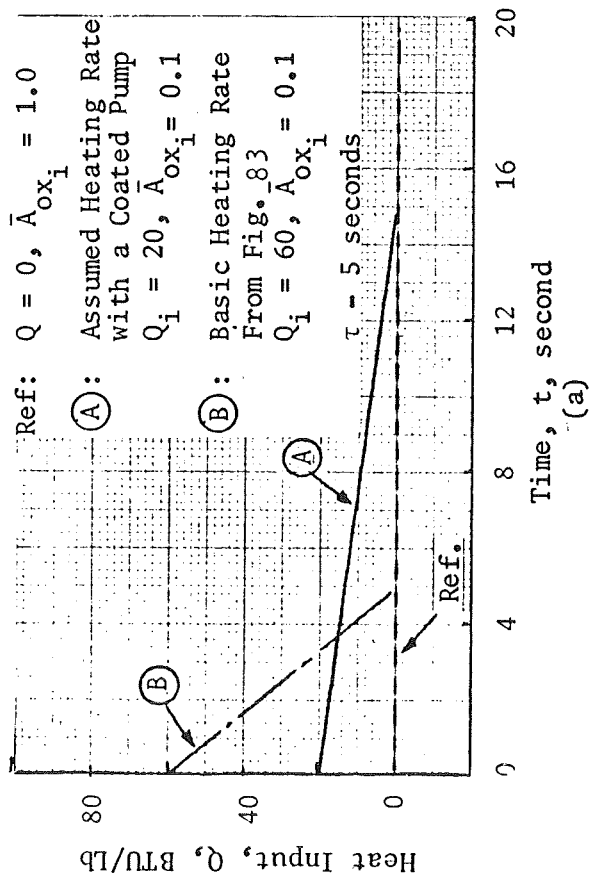


Figure 86. Projected Effects of Pump Coatings on Engine Start Characteristics With A Warm Pump

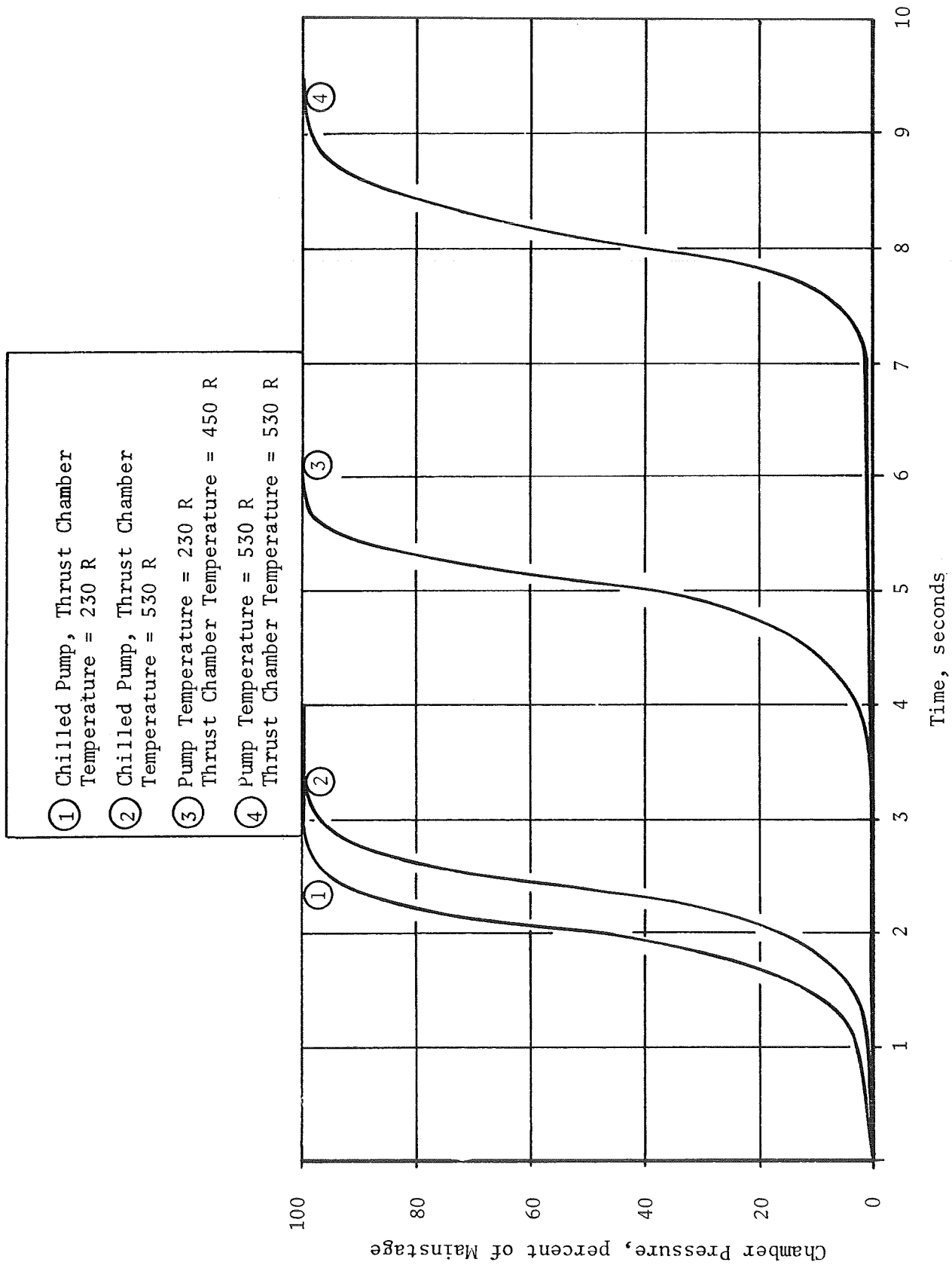


Figure 87. Engine Start Transient With Chill For a 30,000 Lb Thrust Engine (Ref. 7)

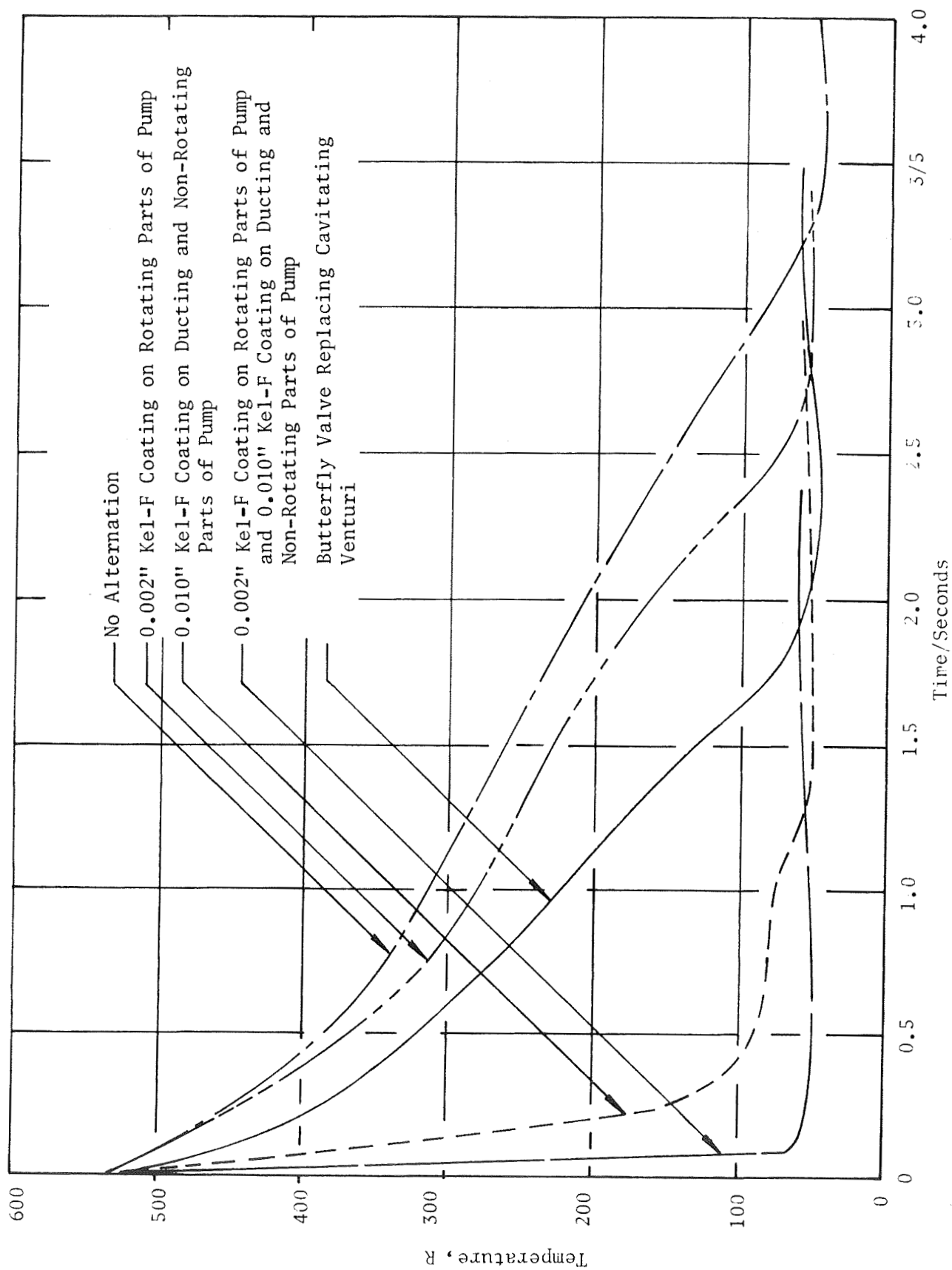


Figure 88. Fuel Temperature at Pump Discharge During Original Start Showing the Effects of Internally Coating the Pump and/or Ducting

Analysis of Saturn S-IVB Stage Fuel Lead Chillover

A start sequence with fuel lead thermal conditioning of the J-2 engine system in the Saturn S-IVB stage was analyzed to provide a backup start sequence in the event the normal pump recirculation preconditioning system (Fig 89) became inoperative. An analysis of fuel lead conditioning of the J-2 engine was conducted to determine the optimum fuel lead time to provide adequate chilling of the hydrogen turbopump, inlet duct, and thrust chamber cooling jacket without overchilling the injector.

Normally, the recirculation system pumps 120 gpm into the inlet duct below the fuel prevalue, through the pump and back to the fuel tank. Flow continues for approximately 8 minutes to chill the inlet duct and pump to ensure acceptable quality hydrogen at the pump inlet during the start transient. If the recirculation system malfunctions, the fuel lead chillover flow must flow through the pump, thrust chamber cooling jacket, and injector. If the chillover is too long, the injector is chilled beyond normal start experience. If the chillover is insufficient, the pump may choke with a subsequent shutdown of the engine signalled by an inadequate thrust buildup. A restart cannot be accomplished after an aborted start because of the inability to refill the spin bottles, which is normally accomplished during mainstage operation.

Thrust Chamber Chillover. The fuel injection temperature is an indicator of the tube bundle and injector chillover during fuel lead. Normal flight experience shows that LH_2 temperatures have been maintained at the main injector for no longer than approximately 3 seconds. Engine development experience has shown the main chamber combustion process may be unsatisfactory with an extended LH_2 flow condition (longer than 3 seconds) at the injector. Figure 90 shows the injection temperature for the third burn experiment of the S-IVB stage during flight AS-504. The fuel tank was not pressurized prior to chillover and the pump inlet pressure increased from 22.5 to 28.5 psia during the time period shown. The pump inlet pressure during the entire 52-second chillover is shown in Fig. 91. The fuel

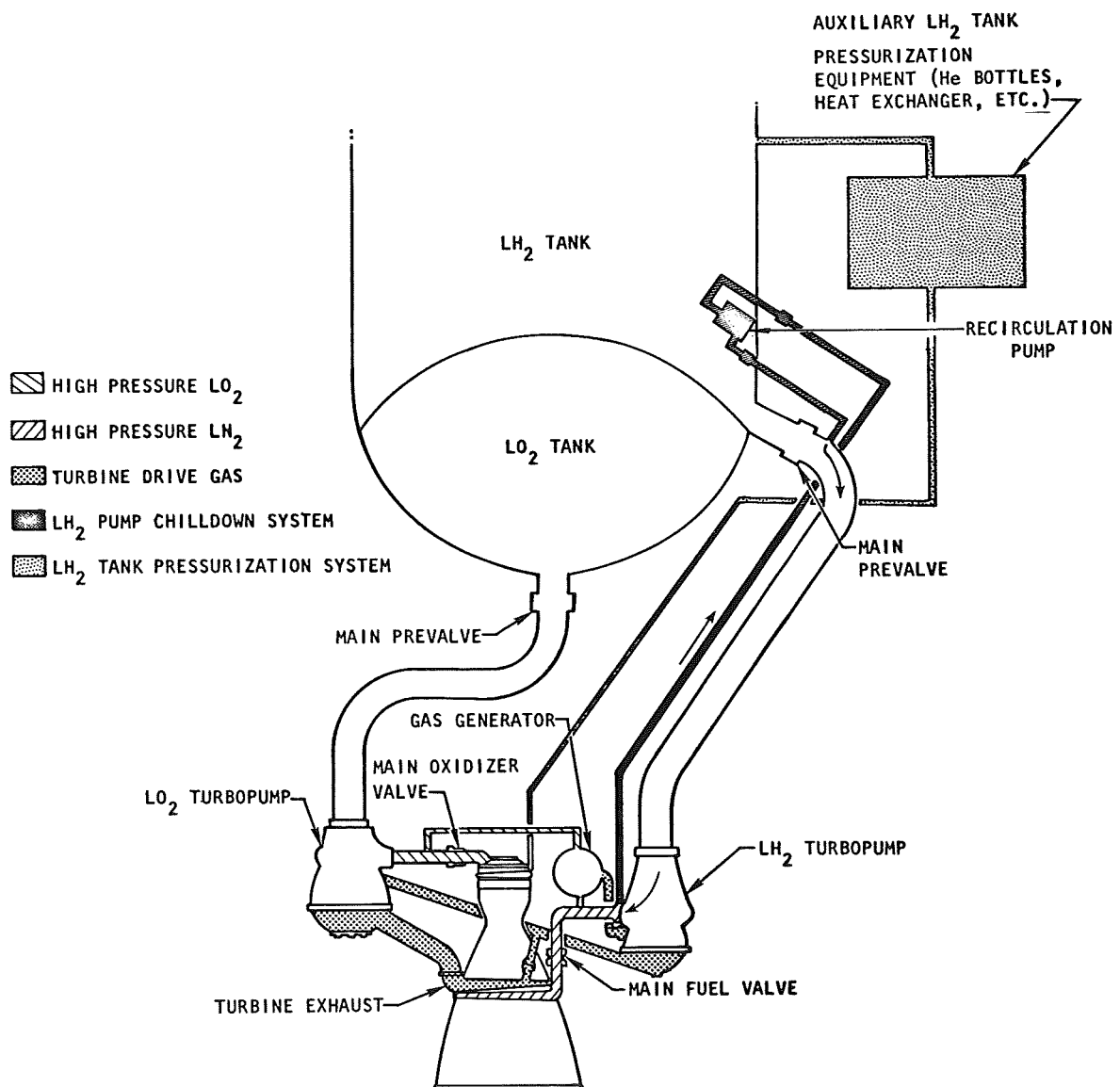


Figure 89A. Schematic of Saturn S-IVB Stage Engine Preconditioning and Tank Pressurization Systems

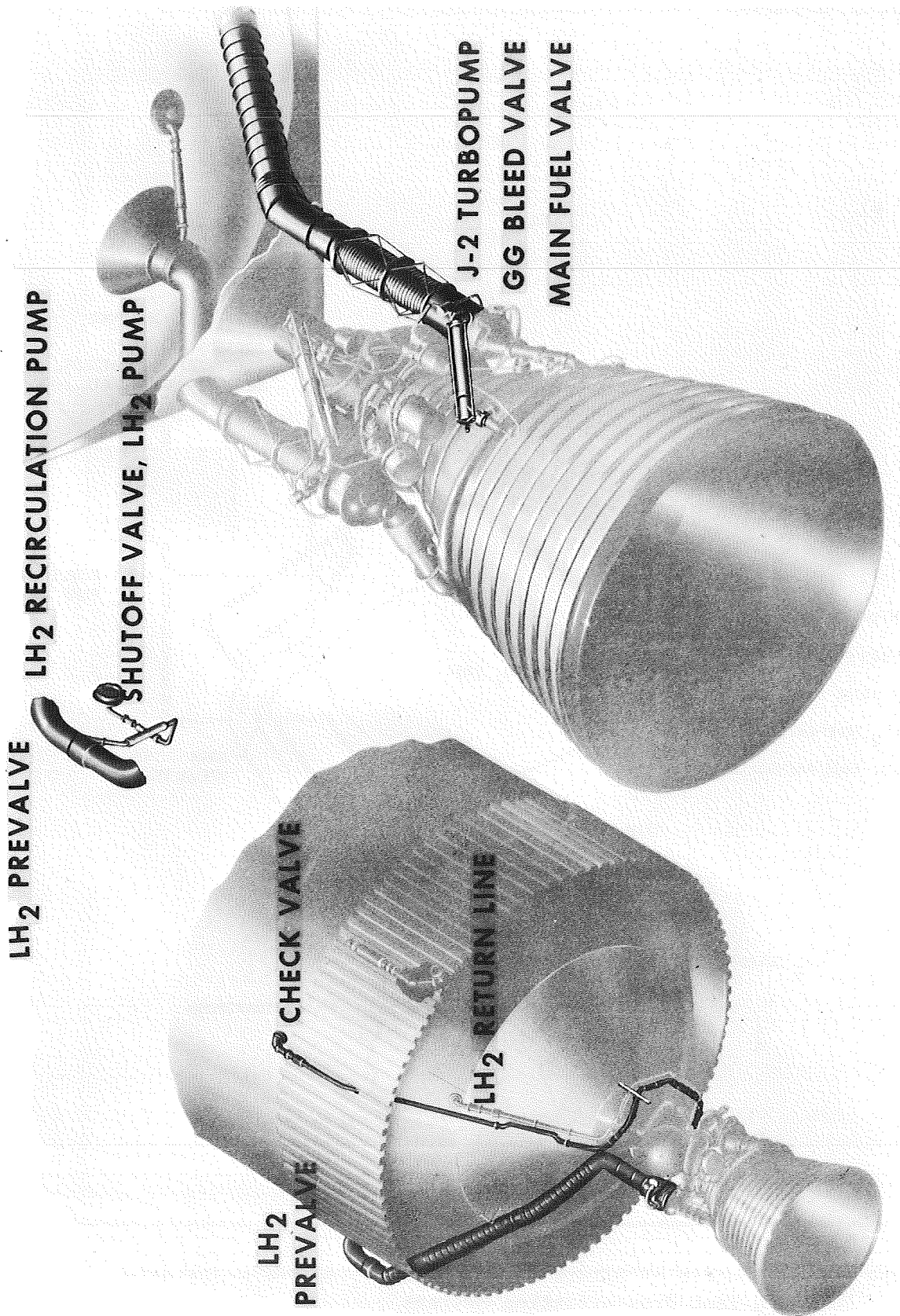


Figure 89B. S-IVB LH₂ Preconditioning System

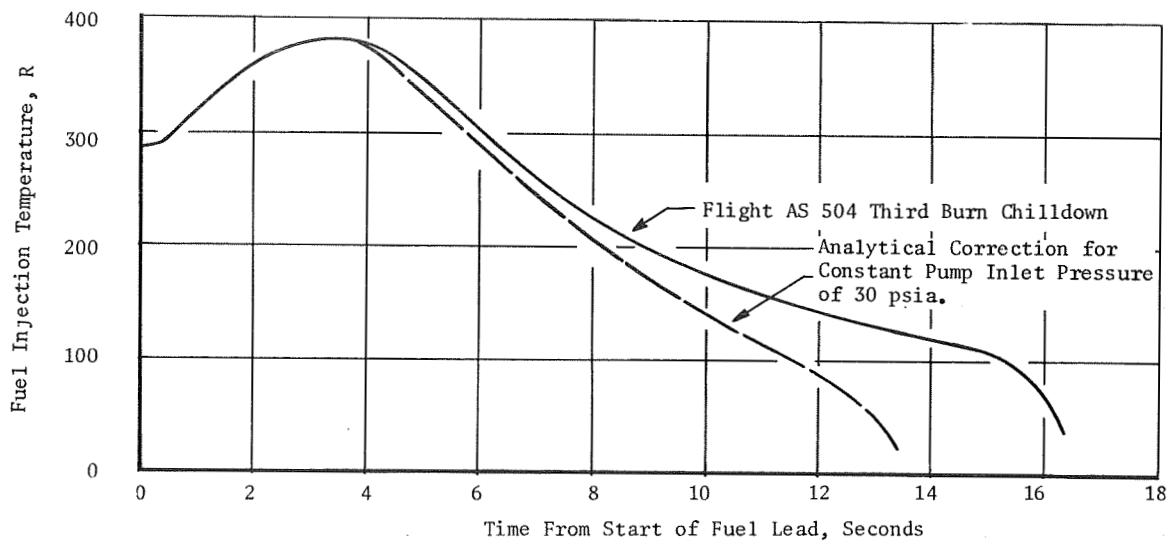


Figure 90. Thrust Chamber Chillover for S-IVB Stage

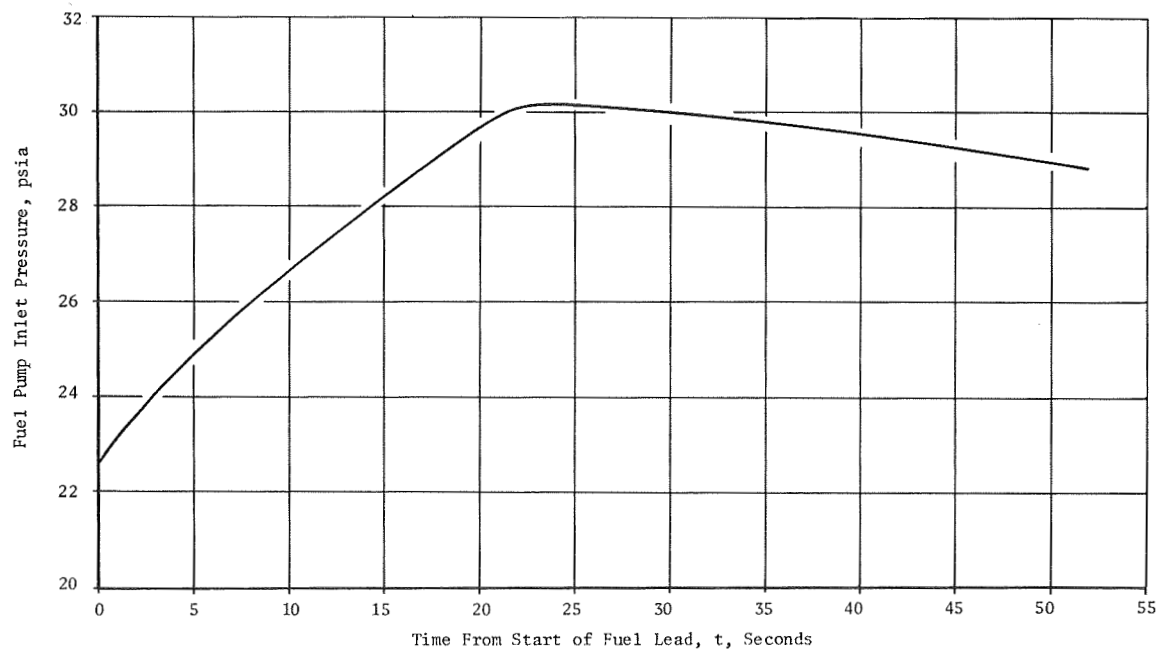


Figure 91. Fuel Pump Inlet Pressure for Third Burn of S-IVB Stage for Flight AS-504

injection temperature curve (Fig. 90) was corrected to a constant pump inlet pressure of 30 psia (normal flight condition) using the J-2 engine system start model. Allowing 3 seconds at LH_2 temperature dictates a maximum fuel lead of 16.5 seconds for a 30-psia pump inlet pressure and an initial thrust chamber temperature of approximately 44 R.

Pump Chillover. Previous studies of the soakback and chillover characteristics of the Mark 15 fuel pump (Fig. 130 of Ref. 6) were used to determine the soakback temperature in the pump and turbine as a function of the vehicle coast time. The transient chillover analysis presented in Ref. 6 was not applicable, however, since it was determined for a different start transient. Chillover analyses were conducted using the TAP II program geometry (Fig. 129 of Ref. 6). The program output was modified slightly to include the rotor blades and the region around the outlet manifold. Essentially no heat flows from the stator to the hydrogen. The main heat sources are the rotor and the rotor blades.

Several chillover transients were analyzed. These included (1) a variable tank pressure bleed (Fig. 91) typical of the third burn experiment on AS-504, and (2) a constant tank pressure bleed ($P = 30$ psia) and a spin bottle start after a fuel lead chillover typical of the backup start sequence for the S-IVB. The chillover analysis was conducted assuming prior 3- and 4-hour coast periods, as well as an ambient pump.

Predicted pump heat rejection rates for the AS-504 chillover flowrate are shown in Fig. 92. The chillover flowrate shown is the result of a simulation on the J-2 start model of the third burn fuel lead during flight AS-504. The flowrate monitored during the initial chillover transient was inaccurate because of overspinning of the flowmeter caused by the hydrogen vapor. As shown, the predicted heat rejection rates are about twice as large for a 3-hour coast as for a 1-hour coast. Similar results for a constant 30-psia tank pressure bleed are shown in Fig. 93. These results are more typical of the expected AS-505 flight profile. Pump heat rejection rates for AS-505 for a given coast time are higher due to the higher fuel flowrates obtained at the higher tank pressure.

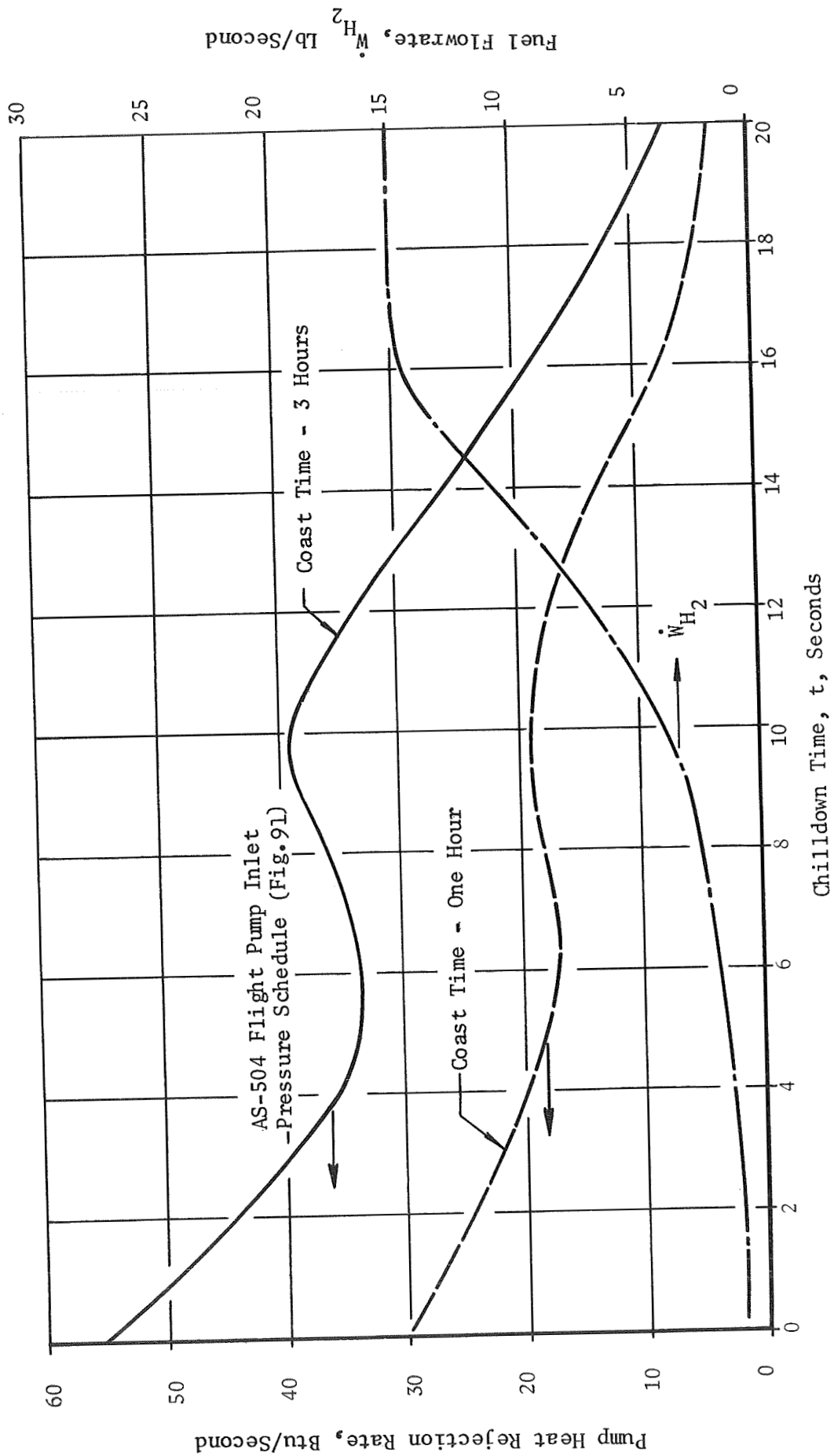


Figure 92. Mark 15 LH_2 -Pump Heat Rejection Rate and Chilldown Flowrate for Flight AS-504.

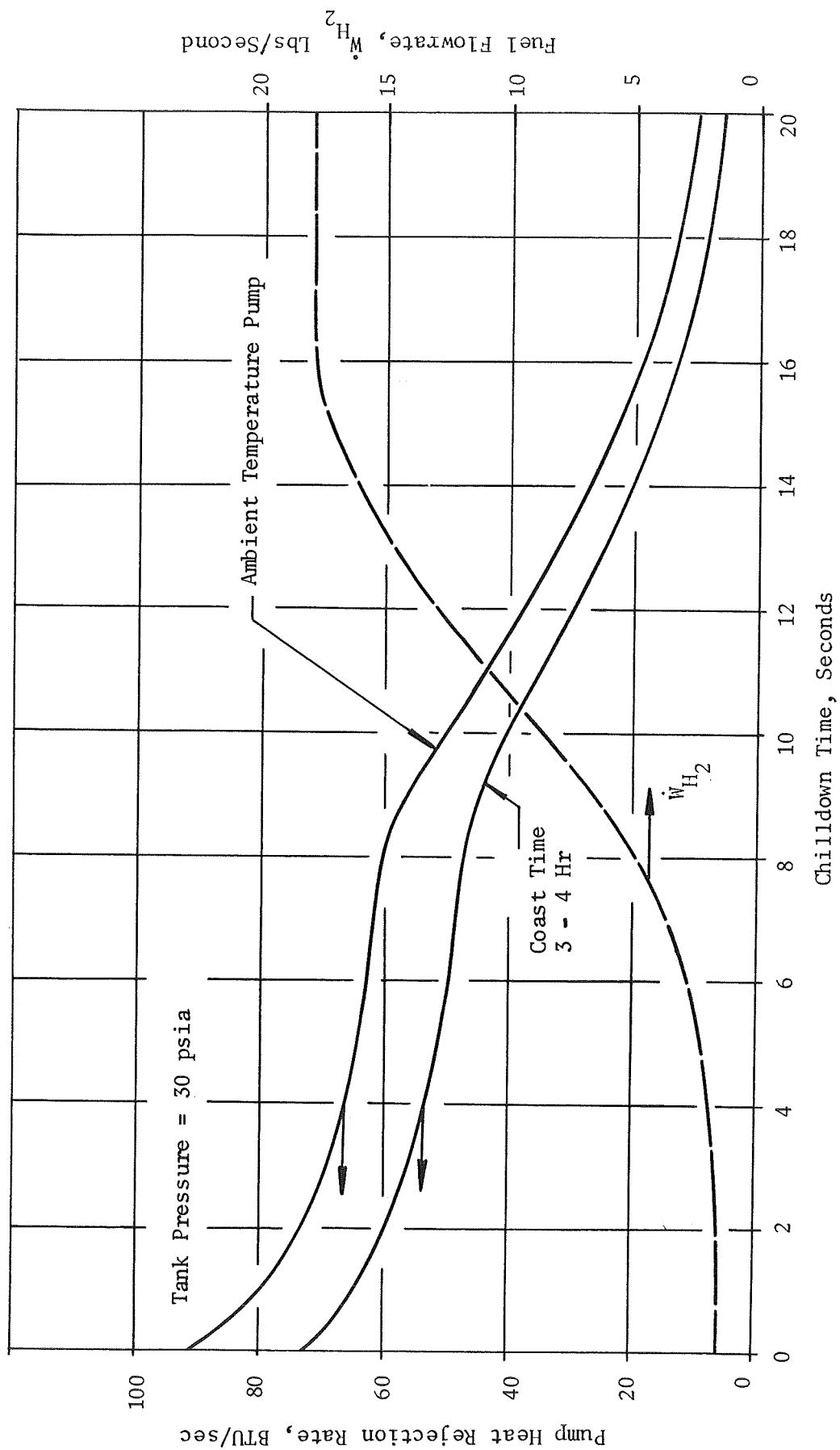


Figure 93. Expected Mark 15 Fuel Pump Heat Rejection Rate and Chillum Flowrate for Flight AS-505.

The third pump chilldown study was conducted for (3) a constant tank pressure of 30 psia and a spin-bottle start after 8 seconds of chilldown. Results are shown in Fig. 94. This is typical of the backup AS-505 S-IVB start sequence that will be used in the event of a recirculation system failure. Depending on the orbit in which the engine is restarted, coast periods of either 135 or 240 minutes (2.25 or 4.0 hours) are expected. The heat rejection rate at 8 seconds with the spin bottle start is approximately 2.5 times higher than without the spin start because the fuel flow-rate is much higher (45 lb/sec as compared to 5 lb/sec). Although the heat input is higher for a spin start, the enthalpy rise and consequently the quality of the propellant through the pump decreases considerably. The higher heat input results in a more rapid chilldown with the spin start.

Effects of Pump Heat Rejection. Throughout the chilldown transient following a 3-hour coast, the heat rejection rate for the pump is less than 2 percent of the rate for the thrust chamber and, therefore, has no effect on the chamber chilldown. Following a 3- to 4-hour coast, an engine start using the J-2 system model was conducted with a spin bottle start after 8 seconds of fuel lead (Fig. 94). The resulting fuel flowrate, fuel pump head and flow, and fuel injection temperature transients are shown in Fig. 95, 96, and 97, respectively. A comparison of these three figures with those for a cold pump engine start indicated the fuel pump heat addition rate shown in Fig. 94 has no effect on the engine start transient.

Hydrogen Quality With Cold Inlet Duct. Hydrogen quality within the pump is a function of the heat rejection from the pump and the quality of the hydrogen at the pump inlet. The latter is determined by the degree of subcooling in the fuel tank and by the heat rejection from the inlet duct. The inlet duct geometry is shown in Fig. 98.

For the first case examined, the wall temperature of the inlet duct was assumed to be equal to the hydrogen-saturation temperature. This implies that, as soon as tank hydrogen reaches the pump inlet, the inlet quality will be zero. This closely simulates the condition just prior to the third burn on AS-504, when it took approximately 2.5 seconds to obtain

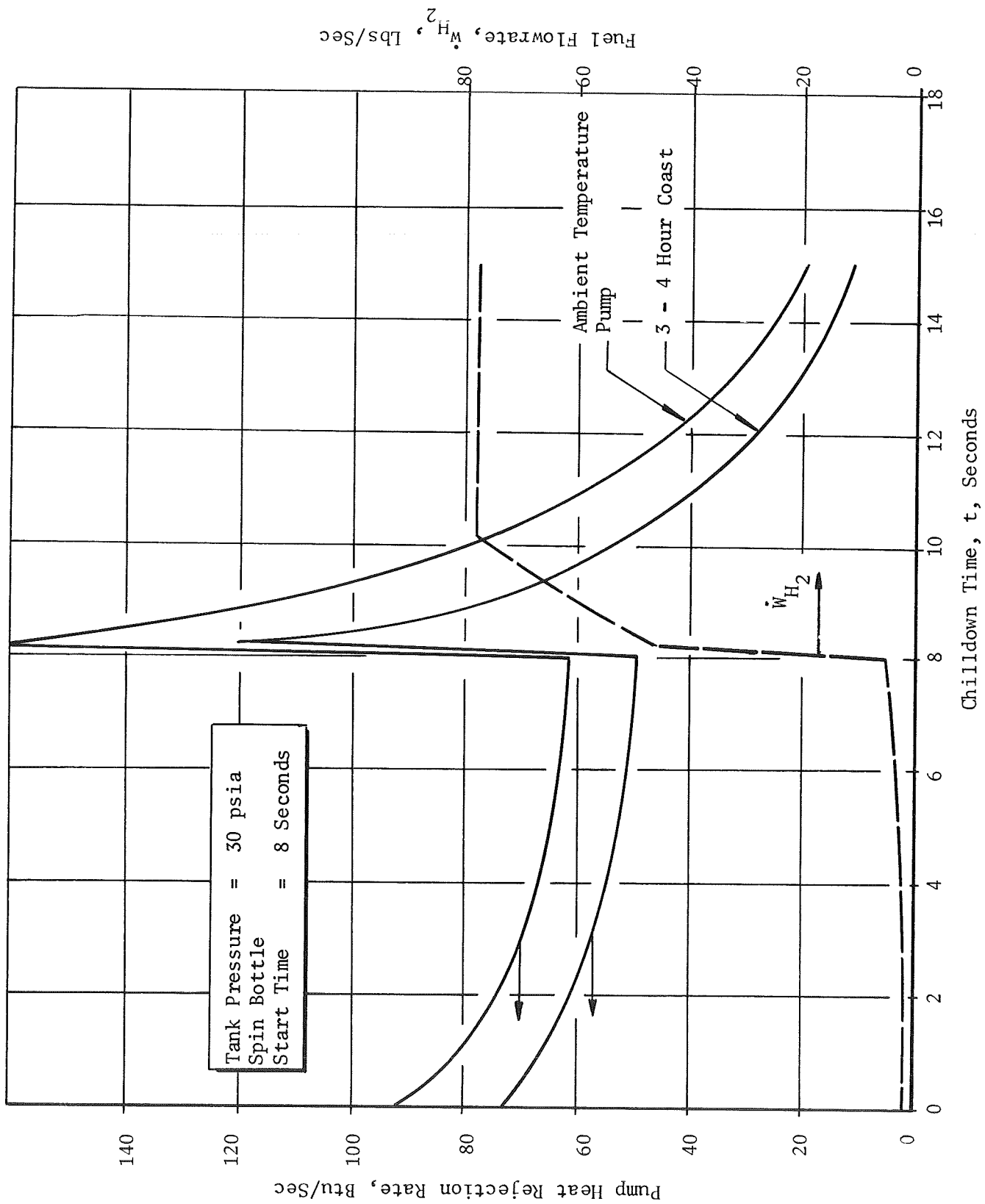


Figure 94. Expected Mark 15 LH₂ Pump Heat Rejection Rate for Backup AS-505 S-IVB Start Sequence

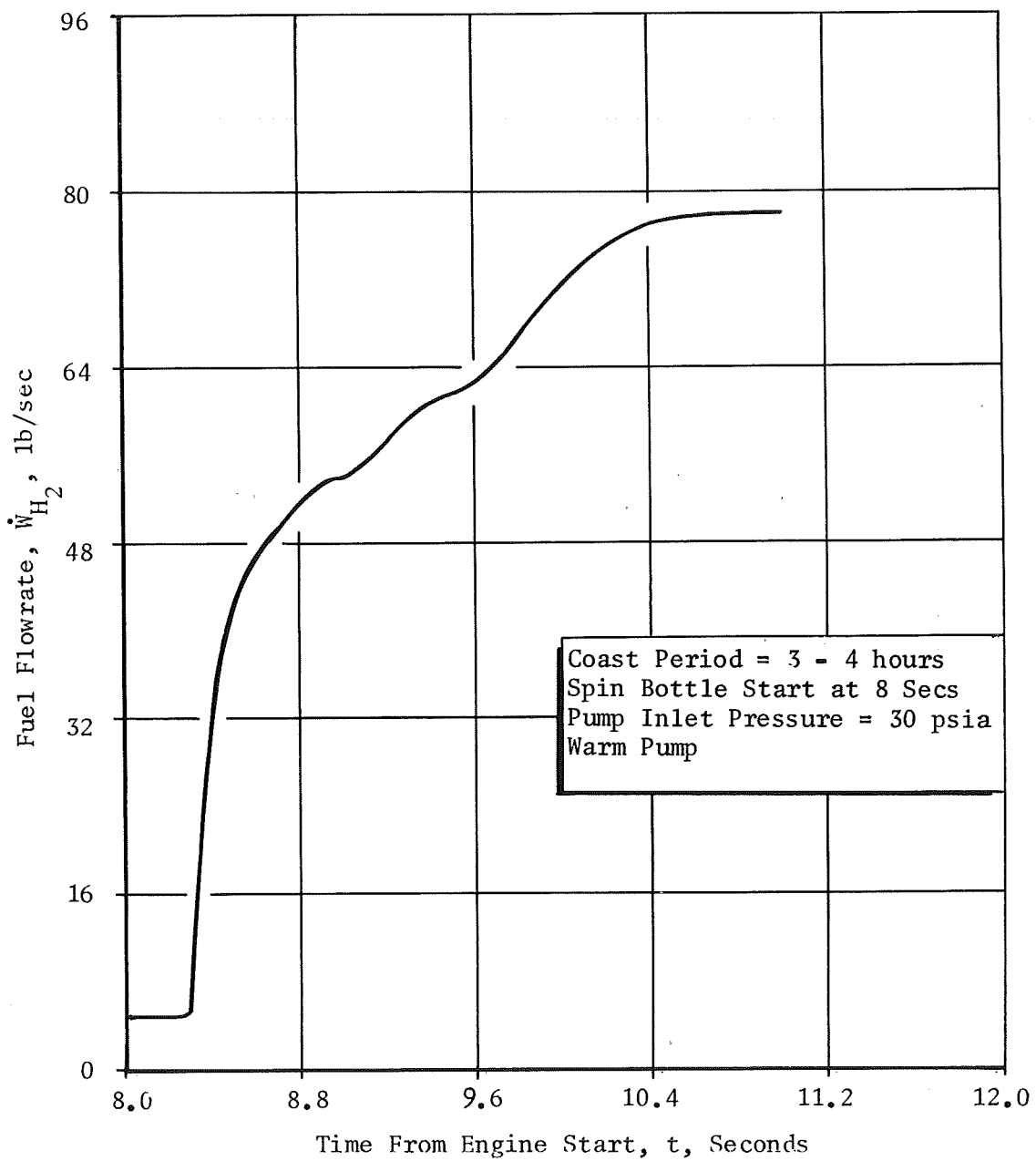


Figure 95. Fuel Flowrate Transient from J-2 System Start Model

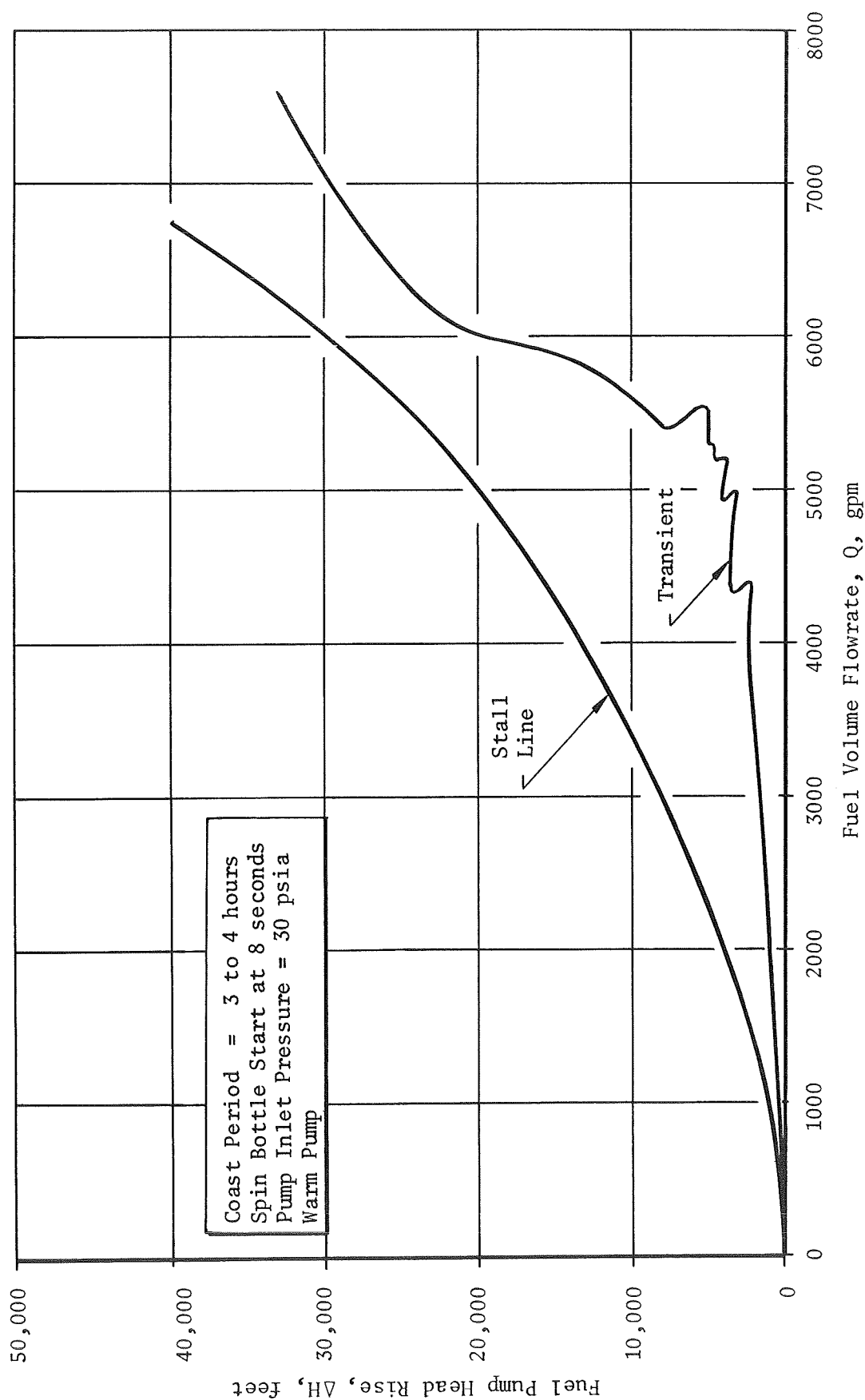


Figure 96. Fuel Pump Head vs Flow Start Transient From J-2 System Start Model

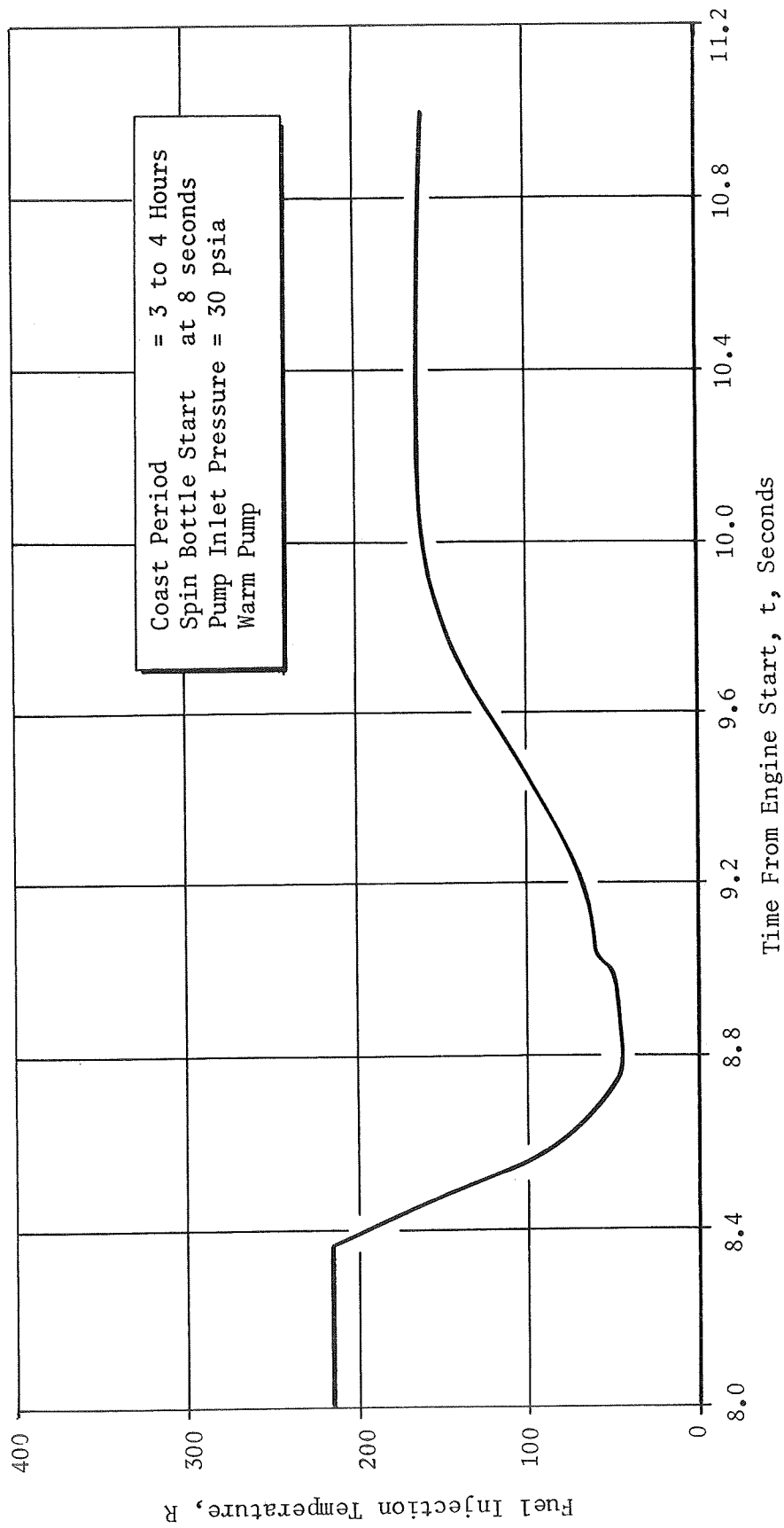


Figure 97. Thrust Chamber Chilldown Transient from J-2 System Start Model

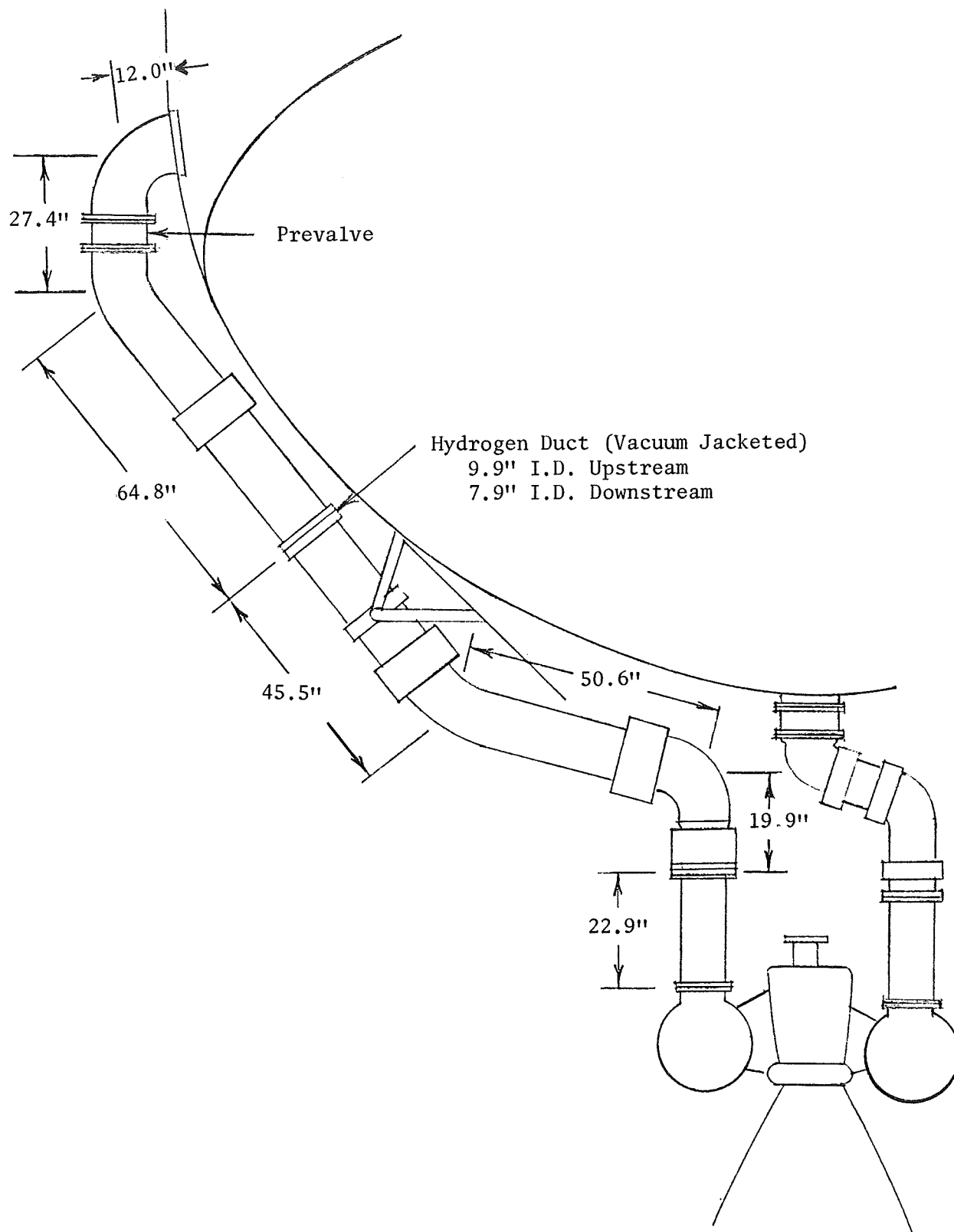


Figure 98. Saturn S-IVB Stage Propellant Feed System

saturation temperature at the pump inlet as shown in Fig. 99. The fact that the inlet duct is at saturation temperature does not imply that LH_2 will immediately enter the pump because the hydrogen quality at the pump inlet can be anywhere between 0 and 100 percent until the tank hydrogen enters the pump.

The time required for fuel to pass through the inlet duct can be determined from Fig. 100. These predictions are based on a line capacity of 31 pounds of LH_2 and the flowrate schedules for the corresponding start sequence. The time for a particle of fluid to pass through the duct at any given time is then determined by how long it takes to put 31 pounds into the duct. The analysis assumes a negligible gravity field, which is the case for a typical restart (10^{-3} to 10^{-4} g). For the ramped tank pressure case (Fig. 91), about 13 seconds are required for the tank hydrogen to reach the pump inlet, as compared to 10 seconds for the constant tank pressure case (30 psia). The constant tank pressure case with a spin bottle start at 8 seconds delivers tank hydrogen to the pump inlet in 8.35 seconds. Figure 101 shows the predicted hydrogen quality at the pump outlet for the ramped and constant tank pressure cases (without spin bottle start). The hydrogen quality at the pump inlet is unknown for the first 13 seconds (ramped tank pressure) or 10 seconds (constant tank pressure). After this period, the inlet duct is assumed to be at saturation temperature and, consequently, the hydrogen enters the pump as a liquid (zero quality). The pump outlet quality is determined by the heat input from the pump (Fig. 92 and 93).

Hydrogen Quality With Warm Inlet Duct. An estimate of the fuel inlet duct heat rejection into the hydrogen was made assuming various uniform initial duct wall temperatures (same for both 8- and 10-inch ducts) up to 400 R. The case shown in Fig. 102 is for a constant tank pressure of 30 psia with a spin bottle start at 8 seconds. Heat transfer coefficients for the low velocity hydrogen within the duct were determined from Ref. 7. Heat rejection rates to the hydrogen initially decreases with time as the wall temperature drops, then increase for a short duration due to the increased flowrate. There is a time lag between the increase in fuel and the increase in heat rejection rate to the hydrogen due to the time required for the hydrogen to pass through the inlet duct.

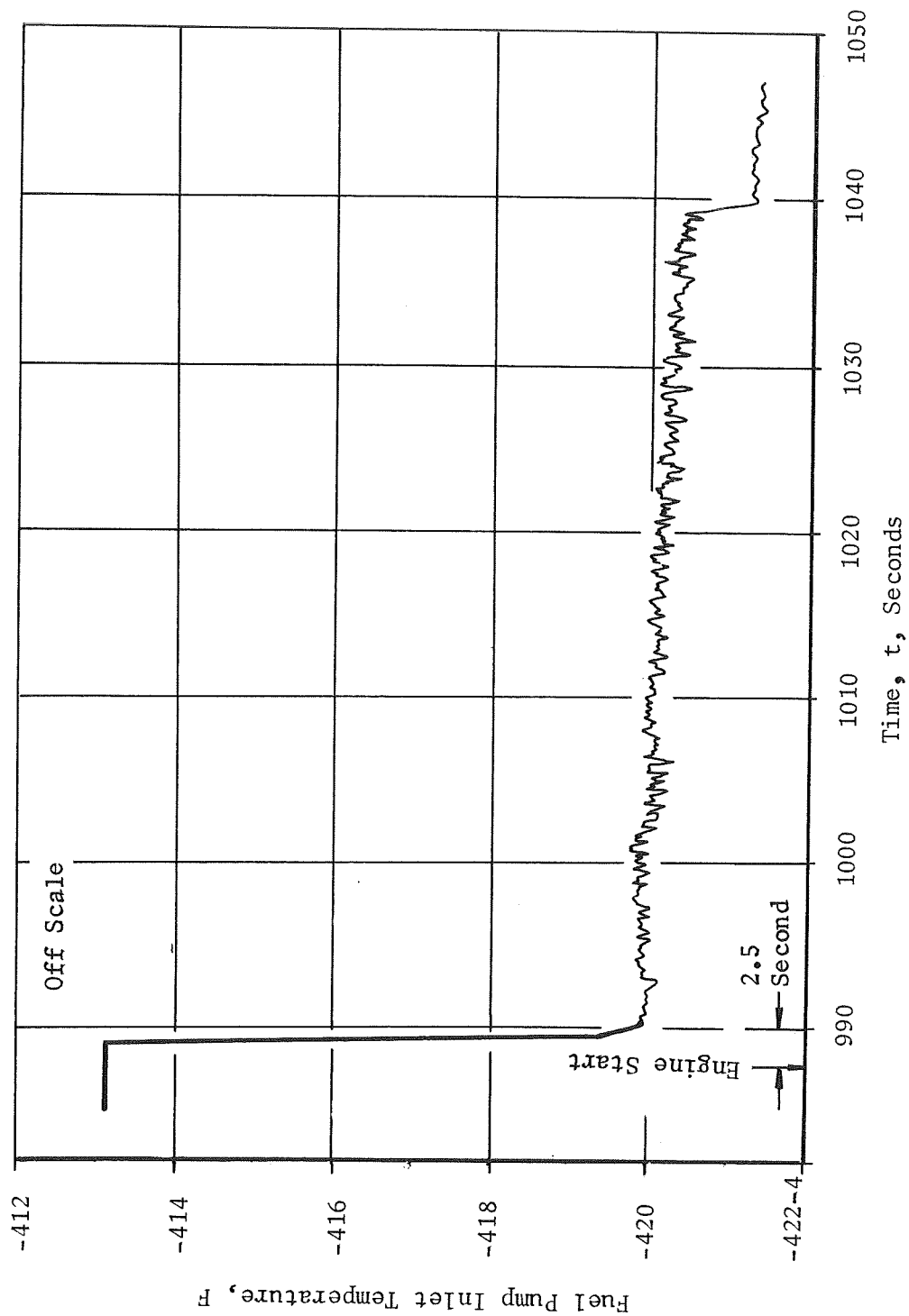


Figure 99. Fuel Pump Inlet Temperature Transient for Third Burn of S-IVB Stage for Flight AS-504

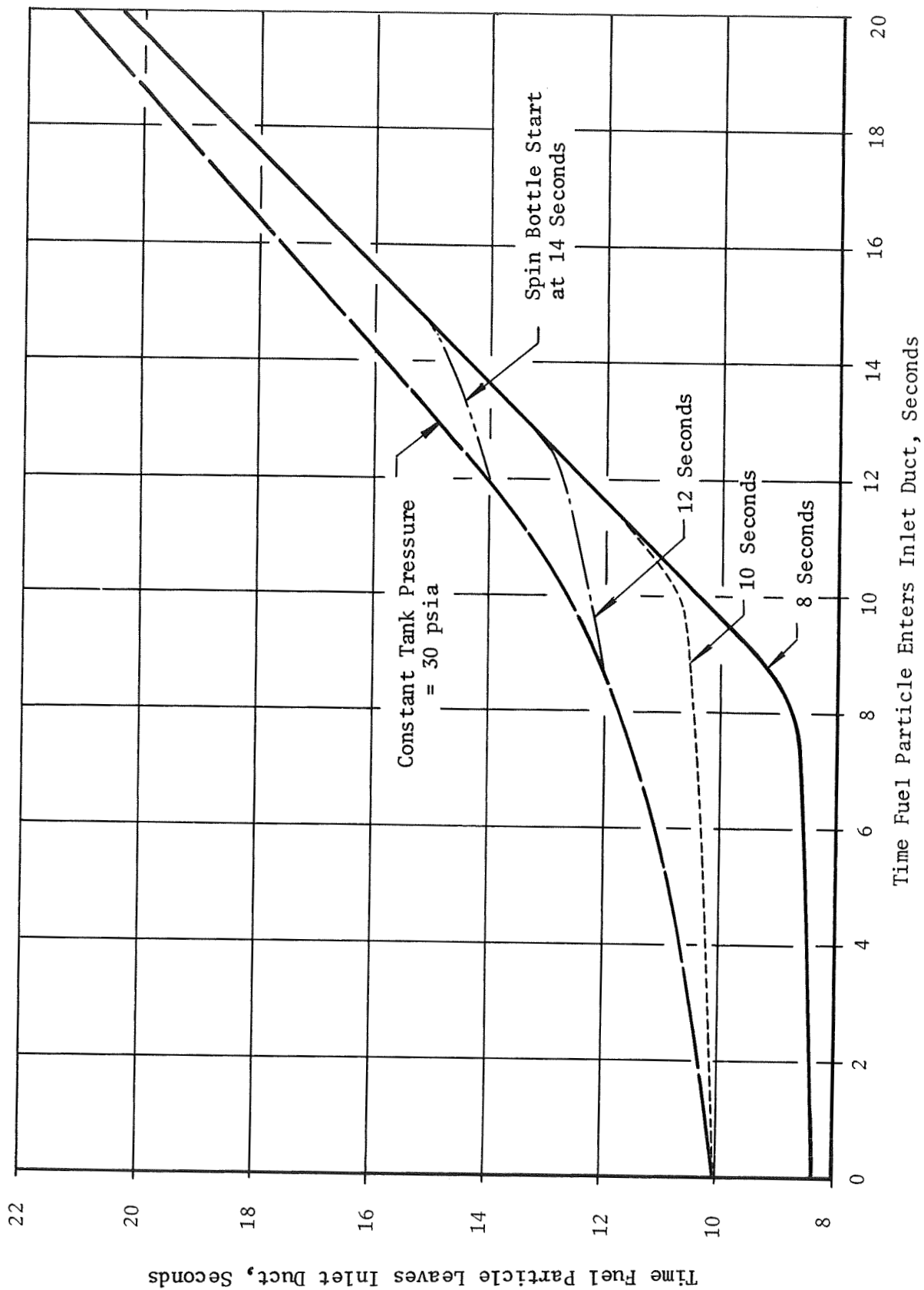


Figure 100. Flushing Time for S-IVB Stage Fuel Pump Inlet Duct

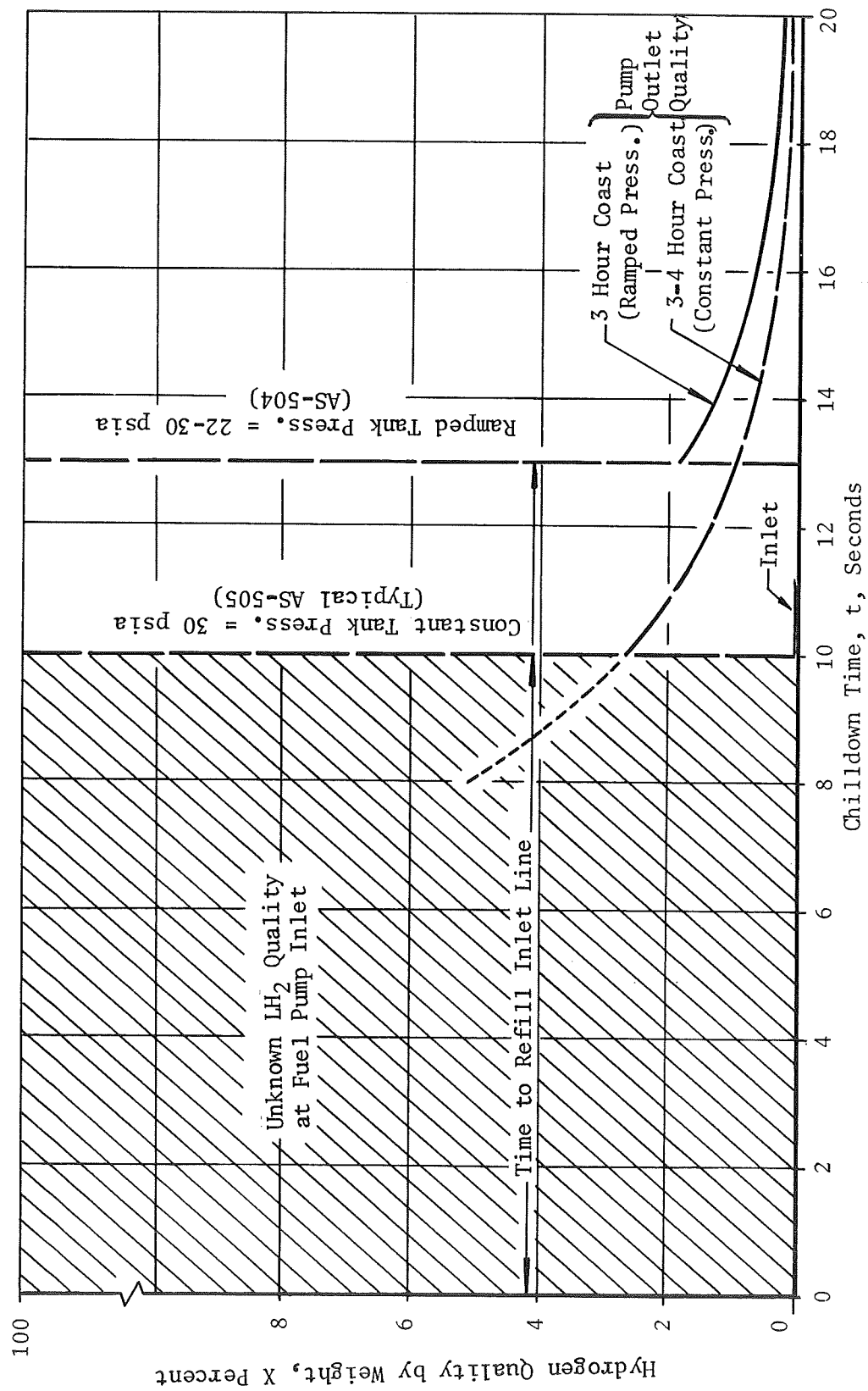


Figure 101. Mark 15 Fuel Pump Quality Predictions for AS-504 Flight and Typical AS-505 Flight

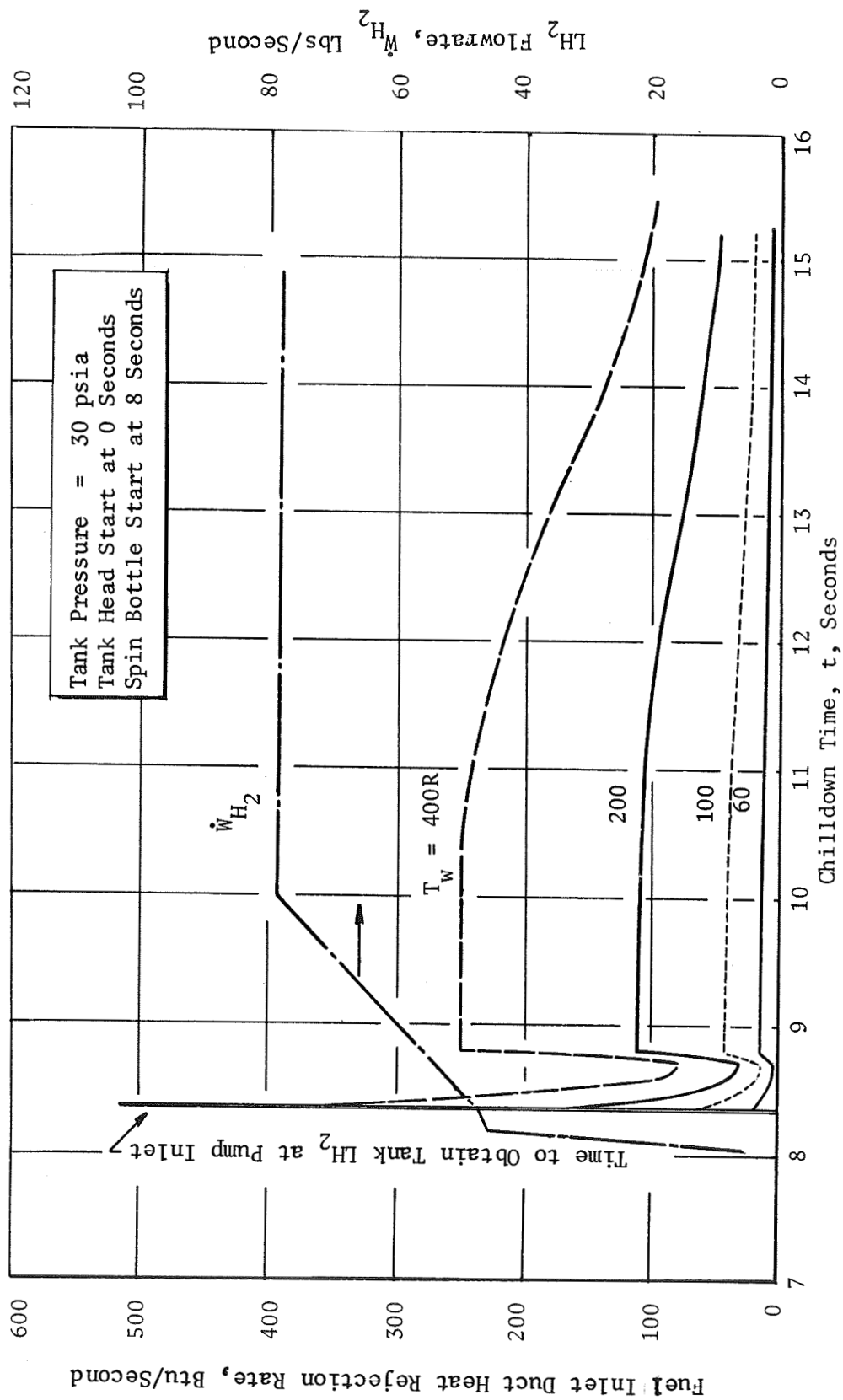


Figure 102. Effect of Fuel Inlet Duct Temperature on Duct Heat Rejection Rate for a Spin Bottle Start at 8 Seconds

Using Fig.102, the hydrogen quality at the pump inlet was estimated as a function of time and initial duct temperature, and is presented in Fig.103. Although the heat input increases with flowrate, the enthalpy and hence the quality decrease. A separate analysis (Fig.104) indicates that the Mark 15 LH_2 pump can operate with 13 to 25 percent vapor by volume (or 0.58 to 1.25 percent quality vapor by weight). These vapor fraction operating limits are at the pump design and the stall liquid flow coefficients, respectively. This indicates that, for a 100 R initial duct temperature, the pump would have excessive hydrogen quality for 0.7 second after spin bottle start. This increases to 0.9 second for a 200 R duct and to 2.3 seconds for a 400 R duct. Figures 105 and 106 are the corresponding curves for inlet duct chilldown without the spin bottle start.

Compared to the engine start sequence, all three duct chilldown times are excessive because gas generator (GG) ignition occurs in about 0.6 second after the spin bottle start. If full hydrogen flow is not obtained prior to this time, the GG and the turbine blades can overheat because of excessive GG mixture ratio. Also, the main oxidizer valve opens to its first position and with inadequate fuel flow, overheating of the combustor and nozzle can occur. As a third restraint (applicable to the 400 R initial duct temperature with a spin bottle start at 8 seconds), a reduced fuel flowrate will result in reduced chamber pressure. If the chamber pressure does not reach 500 psi within 3.5 seconds after the spin bottle start, the engine automatically shuts down.

Consequently, there are several factors to be considered aside from whether the fuel pump will choke initially and then recover as the pump inlet quality drops below the choking limit. It would appear desirable to use a spin bottle start sequence which would provide fuel qualities below 0.5 to 1.0 percent (by weight) prior to the GG ignition. Because of the time required to prime the inlet duct with tank LH_2 , this is difficult to achieve with an 8-second spin bottle start unless most of the inlet duct is already at the hydrogen saturation temperature.

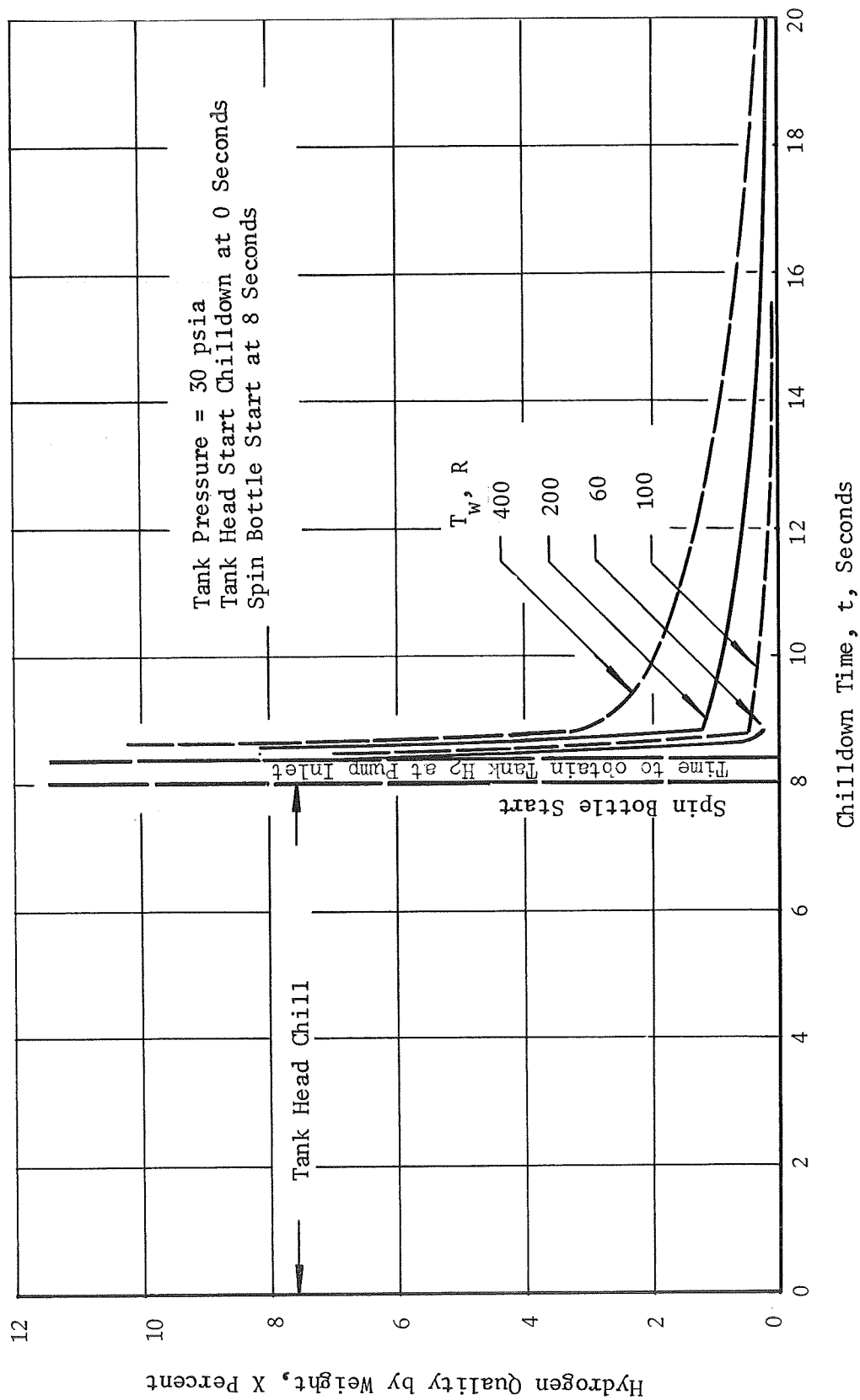


Figure 103. Effect of Fuel Inlet Duct Temperature on Fuel Pump Inlet Quality for a Spin Bottle Start at 8 Seconds

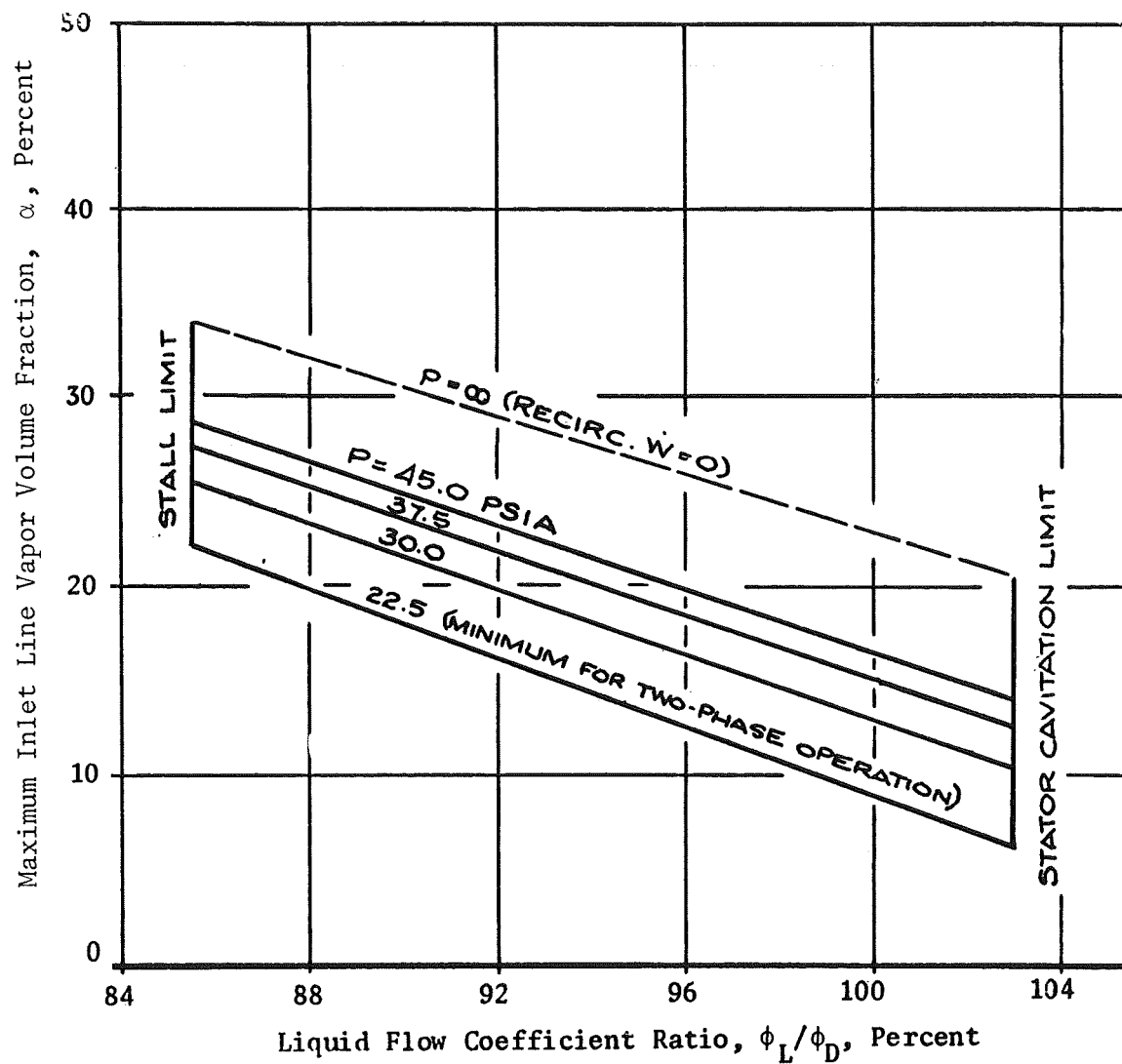


Figure 104. Vapor Pumping Capacities for MK 15 LH_2 Pump

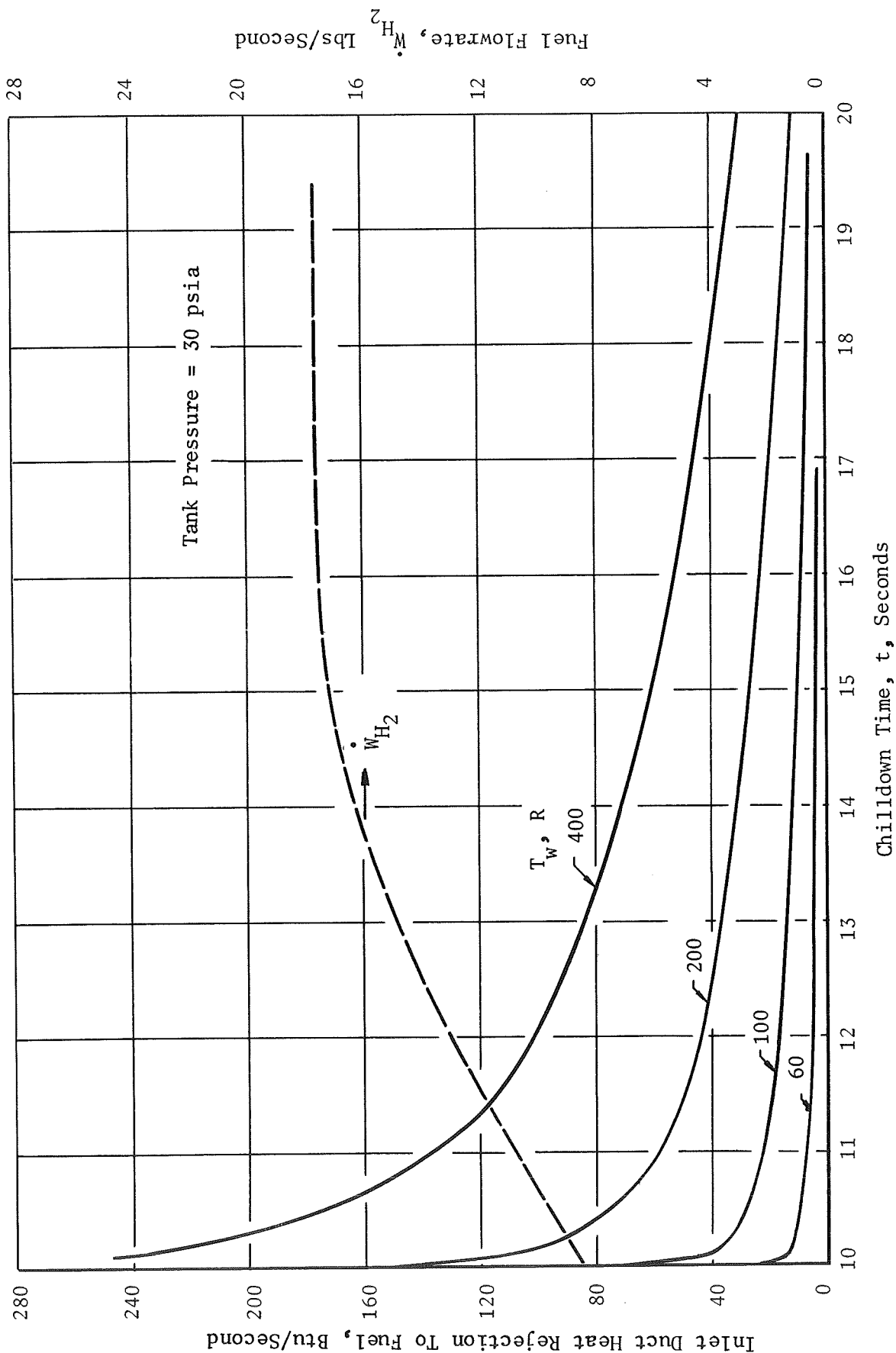


Figure 105. Effect of Fuel Inlet Duct Temperature on Duct Heat Rejection Rate for a Tank Head Chilldown

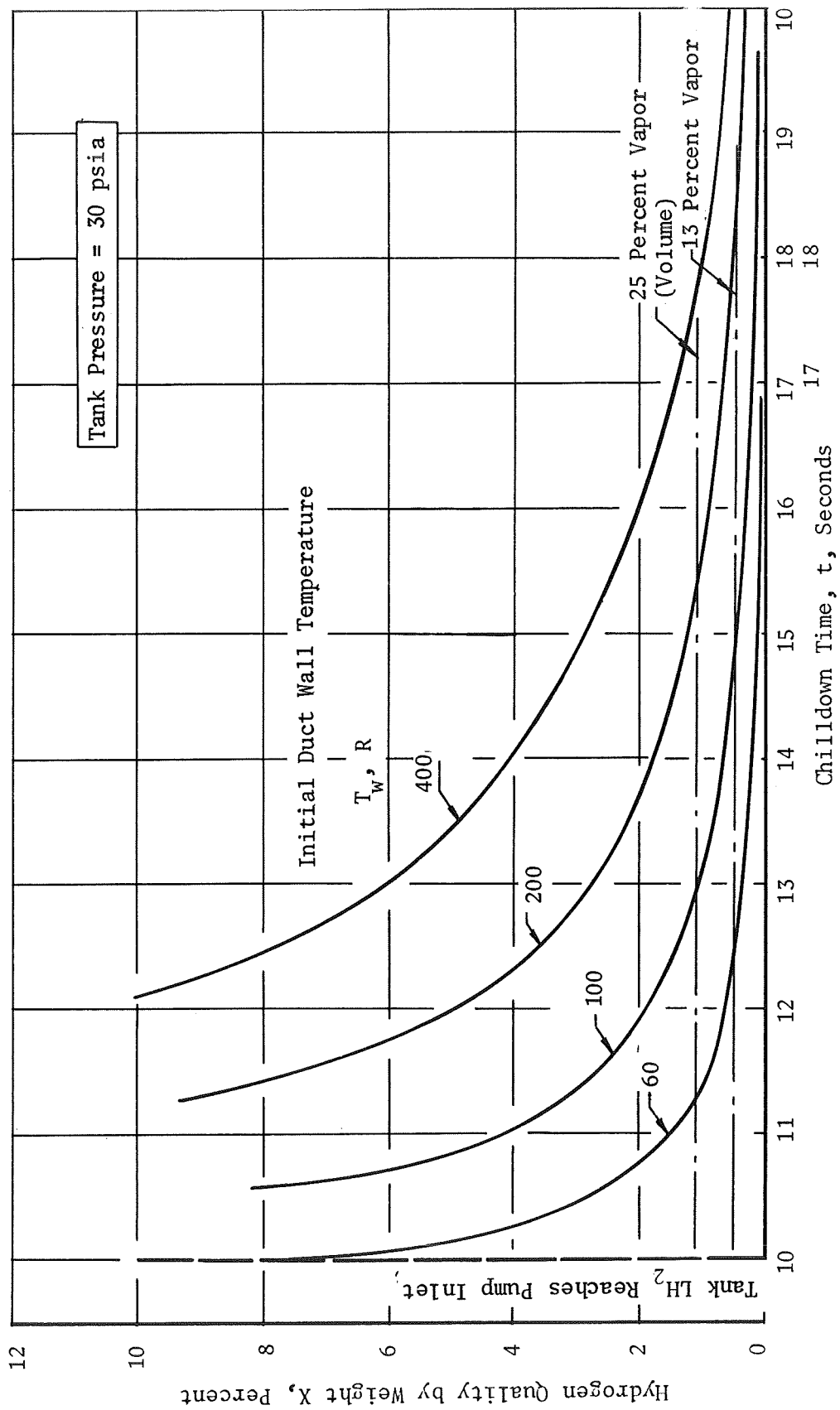


Figure 106. Effect of Fuel Inlet Duct Temperature on Fuel Pump Inlet Quality for a Tank Head Chilldown

By delaying the spin bottle start to 10 seconds, the inlet duct will be primed with tank hydrogen and the fuel quality should be low enough within 0.6 second (GG ignition) for initial duct wall temperatures below 100 R, as shown in Fig.107. For warmer ducts, a longer chilldown is required. Without benefit of a spin bottle start, about 17.5 seconds of fuel lead would be necessary to achieve the required fuel inlet with an initial duct temperature of 400 R.

As high as 4 degrees subcooling of the tank hydrogen has been observed just prior to chilldown as a result of tank pressurization. This subcooling has a large effect on the hydrogen quality at the pump inlet during fuel lead chilldown, especially for high initial duct wall temperatures. The time required to reduce the vapor at the pump inlet to 25 percent by volume is shown in Fig.109 as a function of subcooling.

Summary of Flight Data. The above analysis assumes that the inlet duct is initially at a uniform temperature over its full length. There is some possibility that the fuel geysers through a portion of the inlet duct when the pre valve is open, thereby maintaining LH_2 temperatures at that portion continuously. For this case, the predicted heat input into the fuel would be less than that previously predicted for the cases in which the full length was assumed to be at a uniform temperature.

An analysis of the chilldown for the AS-504 (S-IVB) third burn indicates that fuel saturation temperature was obtained at the pump inlet in 2 to 2.5 seconds (Fig. 99). For a flowrate of 120 gpm (about 1.1 lb/sec LH_2), the fluid travels about 2 feet in 2.5 seconds. Consequently, it may be concluded that, for this case, the remainder of the fuel duct must be at the hydrogen saturation temperature (approximately 42 R). This conclusion may be somewhat optimistic, however, since this chilldown followed a 60-second burn and an 1.33-hour coast compared to the more usual mission profile of a 120-second burn and a 2.5- to 4-hour coast period.

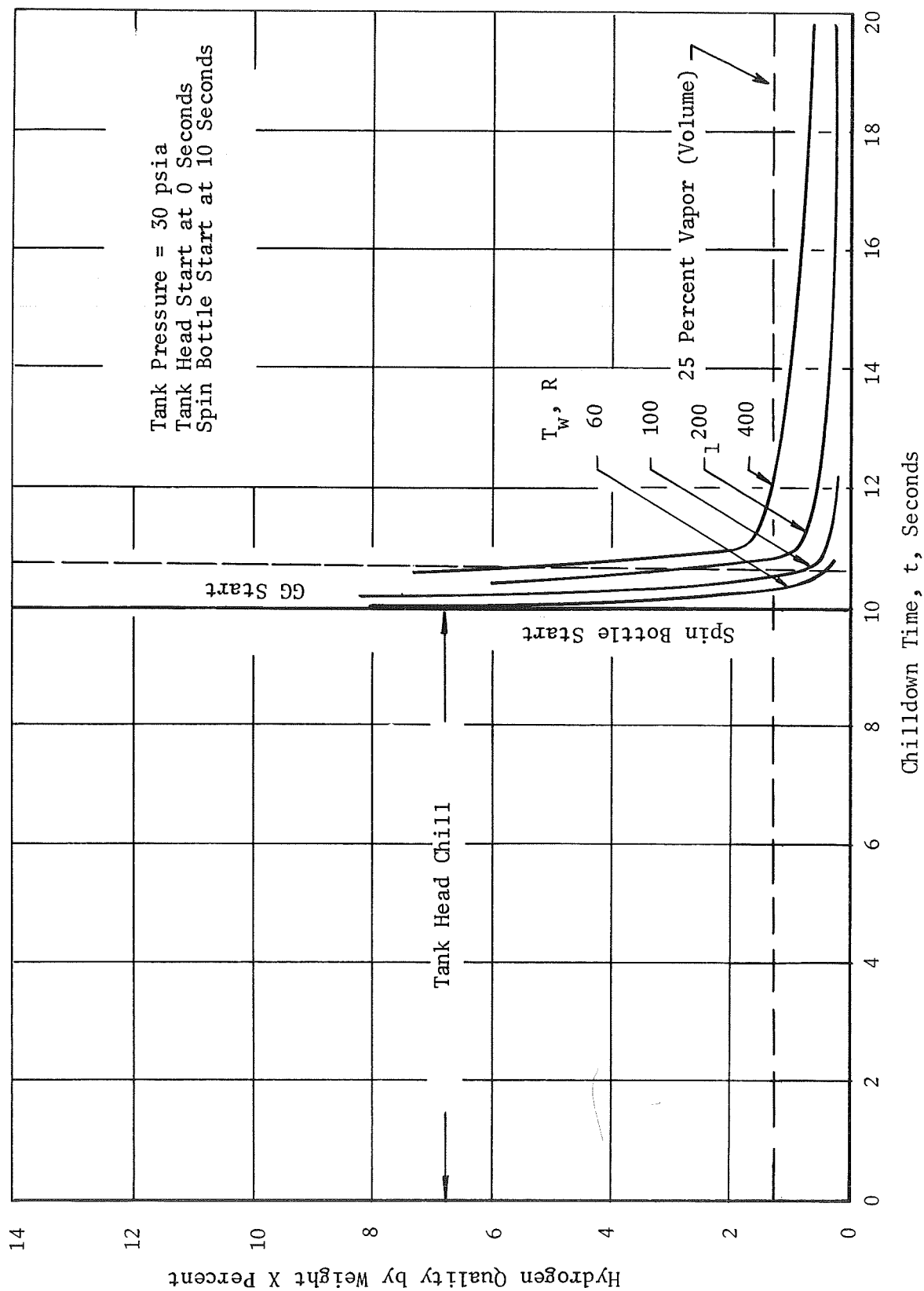


Figure 107. Effect of Fuel Inlet Duct Temperature on Fuel Pump Inlet Quality for a Spin Bottle Start at 10 Seconds

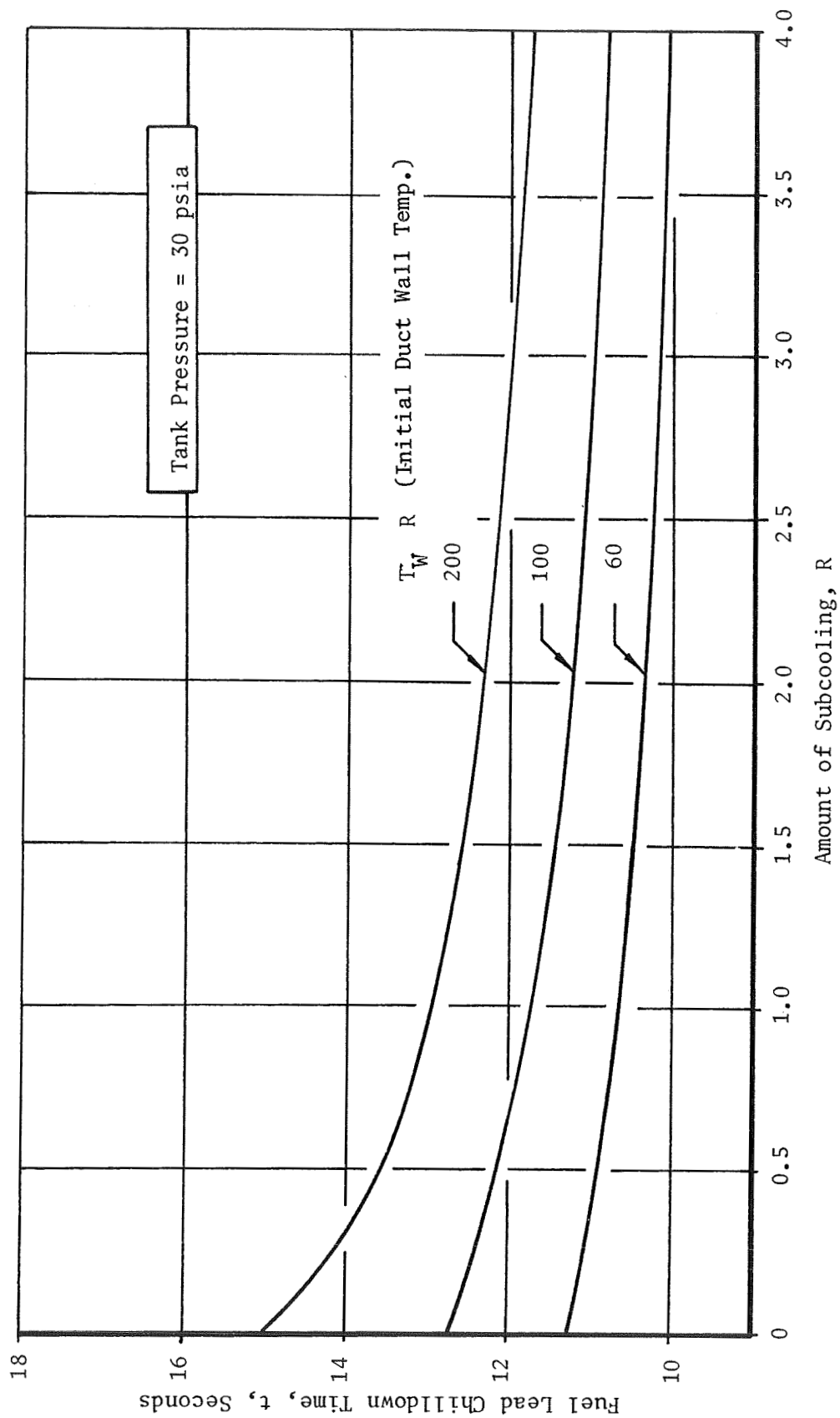


Figure 108. Effect of Tank Hydrogen Subcooling on Fuel Lead Chilldown Time Required to Reduce Pump Inlet Quality to 25 Percent Vapor

Figure 109 shows recirculation system chilldown for the AS-503 (2.5-hour coast) and AS-504 (4.5-hour coast) and indicates chilldown times of approximately 30 and 40 seconds, respectively, before the pump inlet temperature attained saturation temperature. It should be noted that the fuel system chilldown using the recirculation pump is slower than the chilldown using a 30-psia tank head blowdown because the flowrate is lower.

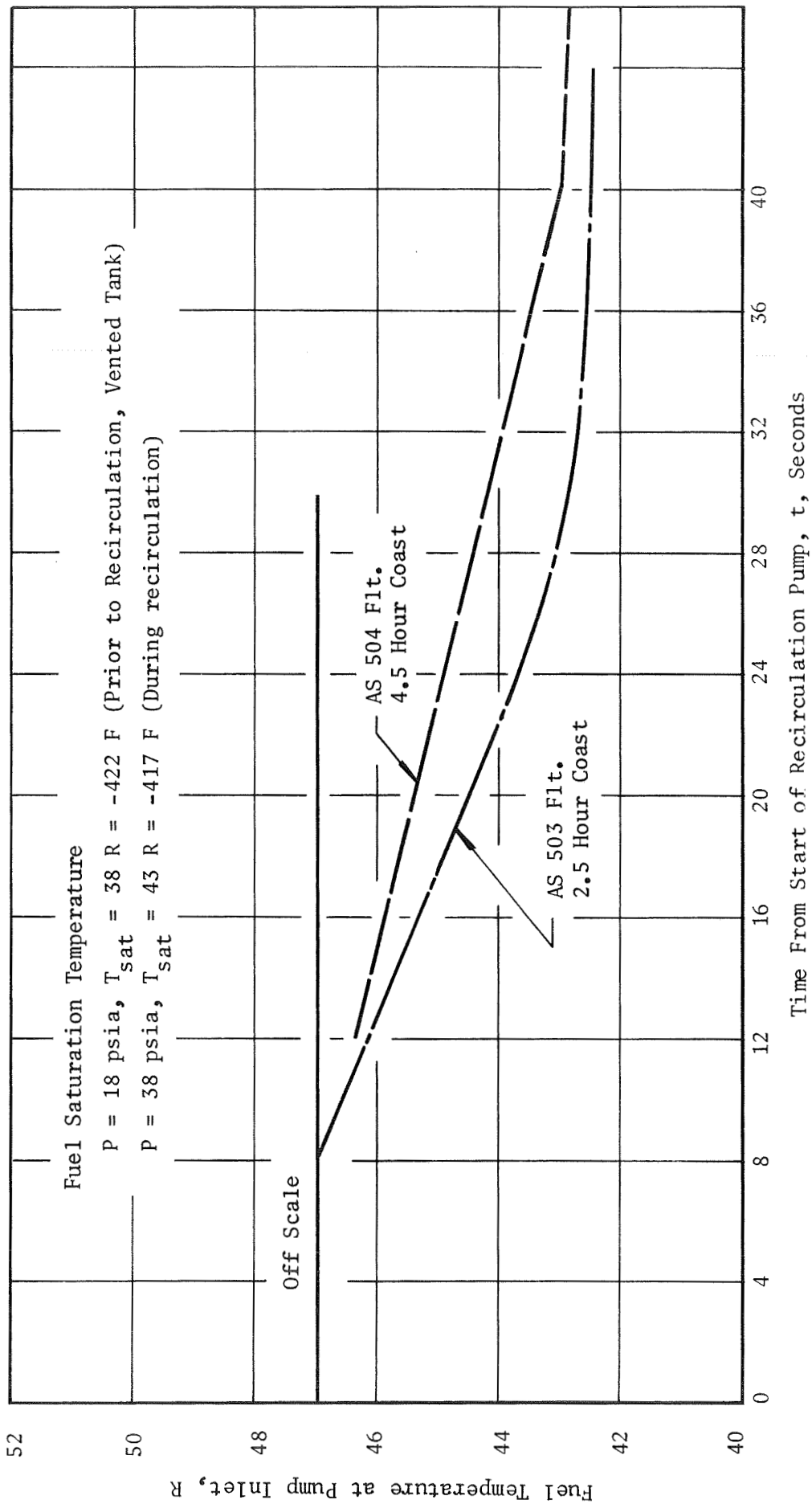


Figure 109 Fuel Temperature at Pump Inlet During Recirculation Chilldowns for AS-503 and AS-504 Flights

NOMENCLATURE

A	=	area
A	=	flow passage area normal to flow direction
B	=	constant
B	=	blockage fraction due to blade thickness and boundary layer
C_m	=	axial velocity at inducer inlet
C_p	=	specific heat
c^*	=	characteristic velocity
D	=	tip diameter at inducer inlet
F	=	gas flow factor
G	=	gravitational constant
G	=	mass velocity
g	=	gravitational constant
g_c	=	gravity field of heat transfer system being studied
g_e	=	earth gravity field (also used in some equations to designate the conversion between lbm and lbf)
H	=	pump head
H	=	heat of vaporization
h	=	inducer blade-to-blade spacing normal to flow direction
h	=	heat transfer coefficient
I	=	inertia
I_s	=	specific impulse
i	=	angle between blade and flow direction at inducer leading edge
k	=	thermal conductivity
L	=	characteristic length
l	=	length

M = Mach number
 MR = mixture ratio
 N = rotational speed
 NPSH = net positive suction head
 P = pressure
 Q = volume flowrate
 Q = heat transfer rate
 Q = heat input, Btu/lb
 Q/A = heat flux
 R = resistance, or mass fraction
 r_m = distance from the surface to the center of the metal being chilled
 T = temperature
 TSH = thermodynamic suppression head
 t = inducer blade thickness
 t = time
 t = thickness
 t_c = chamber time constant
 U = inducer blade tangential velocity
 V = volume
 V = velocity
 W = weight
 \dot{w} = weight flowrate
 X = length
 X = vapor fraction by weight
 α = vapor fraction by volume
 α = pressure ratio, P_d/P_u

β	= inducer inlet blade angle relative to tangential direction
β	= thermal factor for TSH
γ	= ratio of specific heats
δ	= wedge angle for supersonic flow
η	= efficiency
θ	= angular acceleration
λ	= hub-to-tip diameter ratio at inducer inlet
λ	= latent heat of vaporization
μ	= mixture ratio
μ	= absolute fluid viscosity
ρ	= density
σ	= oblique shock wave angle
σ	= surface tension
τ	= nondimensional NPSH ($2g \text{ NPSH}/U^2$)
τ	= torque, time period
ϕ	= flow coefficient at inducer inlet (C_m/U)
ψ	= pump head coefficient

Subscripts

1	= location 1
1	= inducer inlet
1	= upstream of shock wave
2	= location 2
2	= point of maximum blockage within inducer
2	= downstream of shock wave
a	= ambient

bo = burnout weight
b = bulk
C = coating, convective, cross section to the flow
c = chamber, critical
cold = cold pump surfaces
D = design, pump discharge
des = design
d = downstream
f = fuel
hot = warm pump surfaces
i = inverse
inj = injector
J-2 = J-2 engine value
L = line
L = liquid
max = maximum value
min = minimum value
m = metal
n = normal to shock wave
n = nominal
o = gross weight
ox = oxidizer
p = pump, propellant
PL = payload weight
S = heat transfer surface
sat = saturated condition

T = inducer blade tip
TB = tube bundle
t = turbine
t = parallel with shock wave
u = upstream
v = vapor phase
vf = vapor film

Superscripts

* = flow condition when choked
- = average

REFERENCES

1. Seader, J. D., W. S. Miller, and L. A. Kalvinskas: Boiling Heat Transfer for Cryogenics, R-5598, NAS8-5377, May 1964.
2. Siegel, R.: "Effects of Reduced Gravity on Heat Transfer," Advances in Heat Transfer, Vol. 4, Academic Press, New York, 1967.
3. Lewis, E. W., J. A. Clark, and H. Merte: Boiling of Liquid Nitrogen in Reduced Gravity Fields With Subcooling, Technical Report No. 2, 07461-20-T, University of Michigan, Ann Arbor, Michigan, May 1967.
4. Sherley, J. E.: "Nucleate Boiling Heat Transfer Data for Liquid Hydrogen at Standard and Zero Gravity," Advances in Cryogenic Engineering, Vol. 8, Plenum Press, New York, 1963.
5. Clark, J. A. and H. Merte: "Nucleate, Transition, and Film Boiling Heat Transfer at Zero Gravity," Advances in the Astronautical Sciences, Vol. 14, 1963.
6. R-7138, Thermodynamic Improvements in Liquid Hydrogen Turbopumps, Interim Report, Contract NAS8-20324, Rocketdyne, a division of North American Rockwell Corporation, Canoga Park, California, July 1967.
7. R-7585, Thermodynamic Improvements in Liquid Hydrogen Turbopumps, Second Interim Report, Contract No. NAS8-20324, Rocketdyne, September 1968.
8. Wright, C. C., and H. H. Walters: Single Tube Heat Transfer Tests, Gaseous and Liquid Hydrogen, TR59-423, WADC, August 1959.
9. Cowley, C. W., W. J. Timson, and J. A. Sawdye, "A Method for Improving Heat Transfer To A Cryogenic Fluid," Advances in Cryogenic Engineering, Vol. 7, Plenum Press, New York (1961), p. 385.
10. Maddox, P. J. and T. H. K. Frederking: "Cooldown of Insulated Metal Tubes to Cryogenic Temperatures," Advances in Cryogenic Engineering, Vol. 11, Plenum Press, New York (1965), p. 536.
11. Allen, D. L.: "A Method of Increasing Heat Transfer to Space Chamber Cryopanel," Advances in Cryogenic Engineering, Vol. 11, Plenum Press, New York (1965), p. 547.
12. Manson, L. and J. D. Seader: Study of Boiling Heat Transfer With LOX, LH₂ and LN₂, Report R-6259, Contract No. NAS8-11367, Rocketdyne, Canoga Park, California.

13. Manson, L. and W. S. Miller: A Study of Cooldown of Metals, Flow Instability, and Heat Transfer In Two-Phase Flow of Hydrogen, R. N. 68-4, Rocketdyne, Canoga Park, California, 1968.
14. Pron'ko, V. G., L. B. Bulanova, V. G. Baranov, and L. S. Akselrod: Some Problems of Heat Exchanger on Surfaces of Cylindrical Bodies, Moscow, 1969.
15. Vachon, I. R., G. H. Nix, G. E. Tanger, and R. O. Cobb: Pool Boiling Heat Transfer From Teflon-Coated Stainless Steel, Transaction of the ASME, August 1969.
16. Eddington, R. B.: Investigation of Shock Phenomena in a Supersonic Two-Phase Tunnel, AIAA Paper No. 66-87, Third Aerospace Sciences Meeting, New York, 24-26 January 1966.
17. Shapiro, A. H.: The Dynamics and Thermodynamics of Compressible Fluid Flow - Volume I, The Ronald Press Company, New York, 1953.
18. Connelly, R. E. and P. R. Meng: Inducer Performance With Hydrogen Liquid-Vapor Mixtures, 9th Liquid Propulsion Symposium, Vol. 2, presented 25-27 October, 1967 at St. Louis, Missouri, Chemical Propulsion Information Agency.
19. Bissell, W. R., G. S. Wong and T. W. Winstead: An Analysis of Two-Phase Flow in LH₂ Pumps for O₂/H₂ Rocket Engines, Presented at the AIAA 5th Propulsion Joint Specialist Conference, Colorado Springs, Colorado, 9-13 June 1969.
20. Pierce, S. E. and W. A. Kelley: "Techniques for Rocket Engine Simulation" November 1965.
21. Byron, R. A. and C. P. Morse: Advanced Pressurization System for Liquid Rockets, Rocketdyne, Presented at the AIAA 4th Propellant Joint Specialist Conference, Cleveland, Ohio, 10-14 June 1968.
22. GDC-DDB66-007, Liquid Hydrogen Suction Line Insulation Research and Development, Contract No. NAS 8-20167, General Dynamics, Convair Division, San Diego, California, July 1966.

APPENDIX A

LITERATURE SURVEY

This appendix describes pertinent literature on (1) conventionally applied and (2) plasma-sprayed materials and coating techniques.

CONVENTIONALLY APPLIED POLYMERIC MATERIALS

The evaluation of various classes of polymeric materials according to their generic classification is as follows: urethane, polyimide resin systems, and fluorocarbon. A summary of the pertinent literature survey reports and discussions are presented below.

Literature Survey Reports

Urethane Elastomers. "Structural Properties of Glass-Fiber Filament-Wound Cryogenic Pressure Vessels," Toth, J. M., Jr., and J. R. Barber.

Douglas Aircraft Company, Santa Monica, California, and NASA-Lewis Research Center, Cleveland, Ohio. Paper presented at Cryogenic Engineering Conference, August 18-21, 1964 at Philadelphia, Pennsylvania.

Mechanical properties of a standard polyurethane material in relation to its application in cryogenic service were included in this paper. Material tested was Seilon UR29E polyurethane. Thermal contraction and uniaxial tensile tests were performed including temperatures down to -423 F. Uniaxial tensile data of the polyurethane material is presented in Fig. A-1. The tests were performed at -423 F. Thermal contraction data of the polyurethane material tested at a temperature range of 77 to -423 F are presented in Fig. A-2. The contraction rate of the polymeric material is approximately four times as great as either of the proposed metallic substrate materials (Fig. A-2).

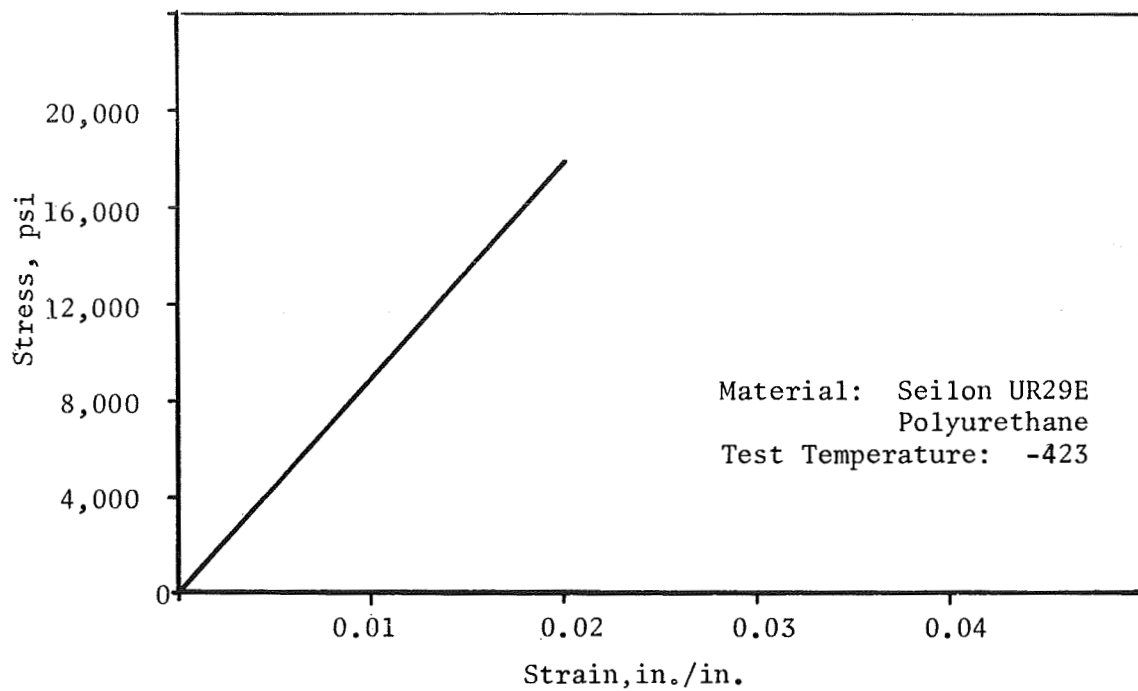


Figure A-1. Polyurethane Material Uniaxial Tensile Data

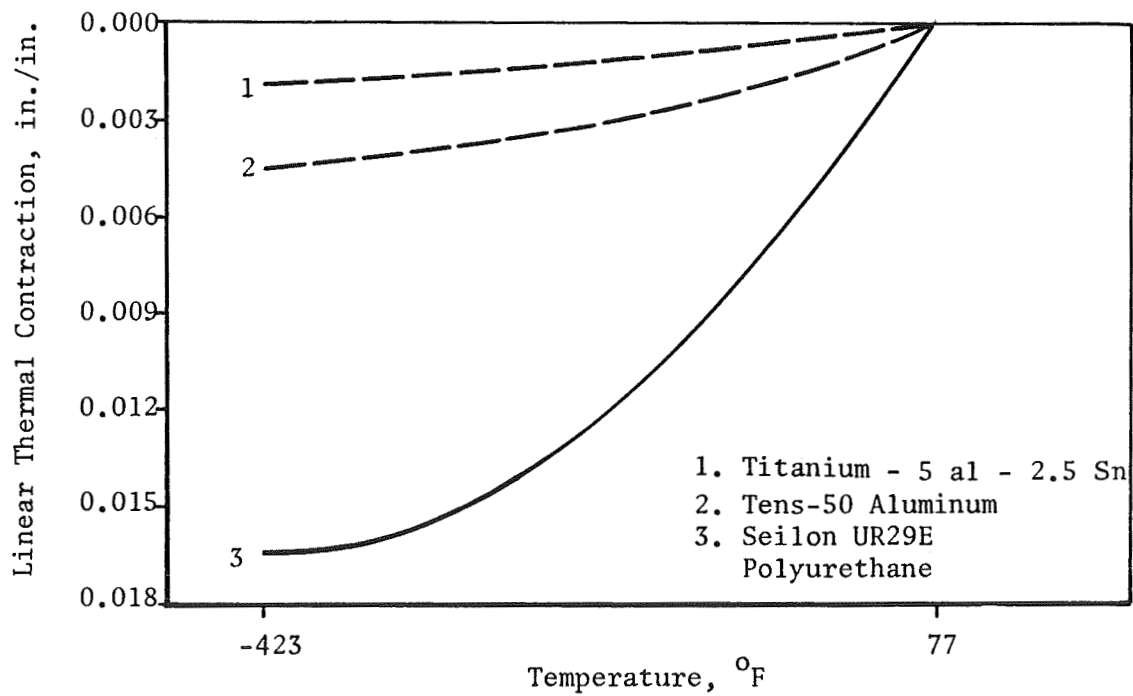


Figure A-2. Polyurethane Material Thermal Contraction Data

Based on the large differential in thermal contraction rates between the urethane material and the proposed metal substrates, coupled with its low residual uniaxial elongation at -423 F, the consideration of using this general classification of polymeric material for cryogenic insulation was abandoned.

Unfilled polyurethane elastomeric materials, as a general classification, maintain good ductility characteristics at low temperatures as compared with other organic materials. It was hypothesized that this property would allow the material to absorb the large strains caused by a differential coefficient of contraction inherent between polymeric materials bonded to metal substrates. Figure A-1 presents the results of uniaxial tensile tests performed on a typical polyurethane elastomer, Seilon UR29E. At liquid hydrogen temperature (-423 F), the ultimate strain of the material is approximately 2 percent (or 0.02 in./in. strain). Data presented in Fig. A-2 show that at -423 F, the thermal contraction of the material is approximately 0.16 in./in., and that of the titanium is 0.002 in./in. which would allow a net 0.006 in./in. of strain until the ultimate uniaxial tensile properties are reached. In actual application, the urethane material would be subjected to biaxial or possibly triaxial strains, which would further reduce the allowable 0.006 in./in. to a nonusable level.

Polyimide Resin Systems. "Structural Properties of Glass-Fiber Filament-Wound Cryogenic Pressure Vessels," Toth, J. M., Jr. and J. R. Barber, Douglas Aircraft Company, Santa Monica, California, and NASA-Lewis Research Center, Cleveland, Ohio. Paper presented at Cryogenic Engineering Conference, August 18-21, 1964 at Philadelphia, Pennsylvania.

The mechanical properties of a standard polyimide material in relation to its application in cryogenic service were presented. Material tested was Polyimide Film, H-Film (E. I. DuPont). Thermal contraction and uniaxial tensile tests were performed including temperatures down to -423 F. The ultimate strain on the polyimide film when tested at -423 F in a uniaxial direction was approximately 2 percent (or 0.02 in./in.). The thermal contraction of the material at liquid hydrogen temperatures is approximately 0.5 percent (or 0.005 in./in.).

The substantial residual uniaxial elongation of unfilled polyimide materials and similarity of thermal contraction rates between this generic classification of materials warranted a further investigation as to the feasibility of using a polyimide resin system for cryogenic insulation service.

"Final Report, Organic Materials to be Used as a Sealing Face for High Temperature, Pressure-Actuated Seals," Rocketdyne, A Division of North American Rockwell Corporation, Canoga Park, California (unpublished data).

Optimum cure cycles for the fusion of applied polyimide dispersions were developed along with process variations required to uniformly meet visual and coating thickness requirements. Material tested was RC5069 (polyimide varnish coating), E. I. DuPont, Wilmington, Delaware. The optimum cure cycle included a final fusion of the material for 8 hours at 475 F.

Based on the excessive time at a temperature considered detrimental to the properties of one of the proposed metal substrates (Tens-50 aluminum), the further consideration of polyimide material for cryogenic insulation application was no longer pursued.

The decision to evaluate the use of polyimide materials at cryogenic applications was based on the inherent mechanical and physical properties of the material. The material, as a general class, has good low-temperature ultimate uniaxial strain with approximately 25 percent of the allowable strain being utilized for thermal contraction. Furthermore, the differential contraction rates between the proposed metal substrate and the polyimide materials is of such a magnitude that there would be little concern as to loss of adhesion of the coating to the metal resulting from uneven contraction. In general, polyimide materials are tough, resilient materials and would be able to withstand the erosive effects of high-speed fluid flowing past the coating.

Certain limitations on the processing techniques of the coating were established. One consideration was the degradation of properties of Tens-50 cast aluminum alloy when exposed to a total maximum accumulated time of

1.75 hours at 470 F. The optimum cure cycle for the polyimide varnish was based on the fact that the combination of solvents used in polyimide varnishes are high-boiling and require enough dwell time above their boiling point to allow them to diffuse through the partially cured coatings. Therefore, 8 hours at 475 F was established as the optimum cure cycle for the polyimide coatings in the 0.003- to 0.005-inch-thickness range. This time at temperature is in excess of the acceptable processing range of the cast aluminum material proposed for pump components. An even longer schedule would be for thicker coatings.

Fluorcarbon Systems. "Final Report, Program of Testing Nonmetallic Materials at Cryogenic Temperatures" (AF04(611)-6354), Rocketdyne, A Division of North American Rockwell Corporation, Canoga Park, California.

The mechanical properties of various fluorcarbon materials were evaluated for application in cryogenic service. The effect of adding low coefficient of contraction materials on the rate of thermal contraction of the base resin was determined. Materials tested were: TFE* and FEP Teflon, Kel-F, filled TFE Teflon, and Kel-F materials. Thermal contraction data are presented in Fig. A-3 and A-4. Figure A-3 is a comparison of three types of fluorcarbons; TFE Teflon, FEP Teflon, and Kel-F. Figure A-4 shows the reduction in the contraction rates of a 60-percent filled TFE as compared to a 12-percent filled Kel-F. Tensile properties were evaluated at liquid hydrogen temperatures with the ultimate strain of the Kel-F and TFE materials being approximately 0.02 in./in. (or 2 percent) while the FEP is approximately twice that.

Based on information presented in the above report, it was concluded that fluorcarbon materials, including both TFE and FEP Teflon and Kel-F materials, are suitable for low-temperature applications. The feasibility of adding low-contraction fillers to the base resin and substantially reducing the relative rates of contraction of the filled material was demonstrated.

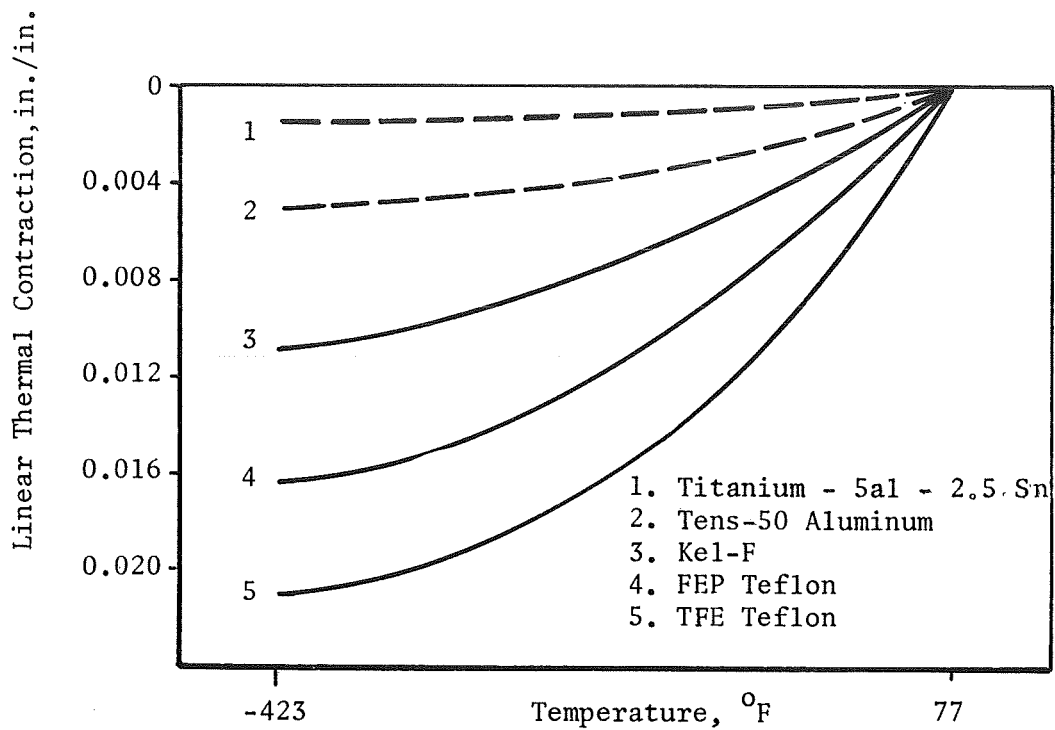


Figure A-3. Material Thermal Contraction Comparisons

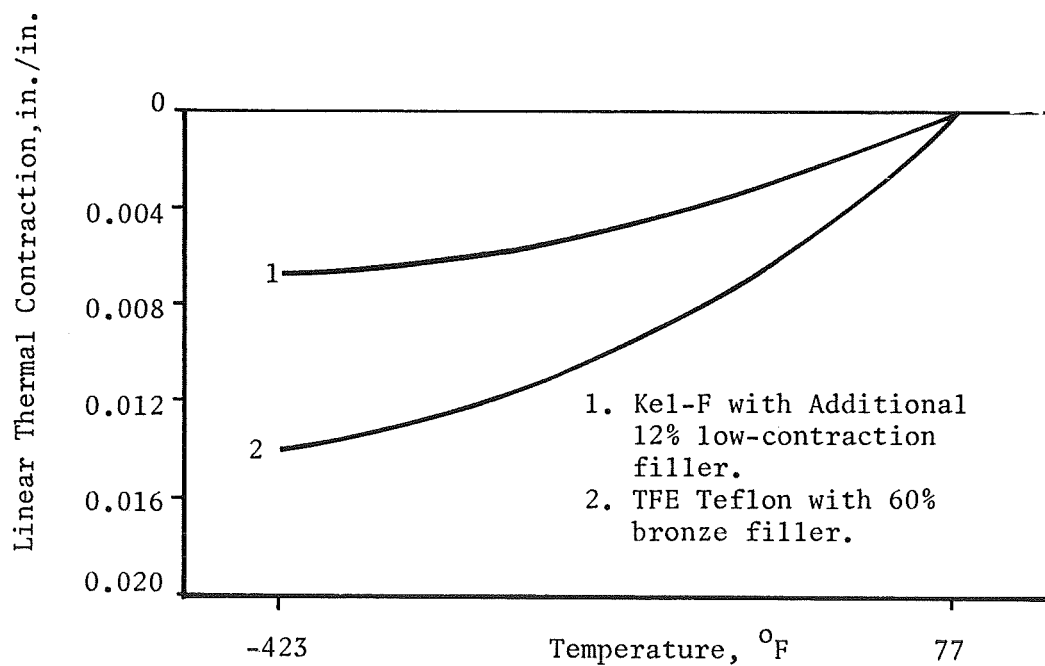


Figure A-4. Reduction in Thermal Contraction Using Fillers

The good ductility characteristics at low temperatures and adequate residual strain-absorbing capability indicated that further investigation of fluorcarbon materials for cryogenic usage was warranted.

"Summary Letter Report on RL 10A-3 Fuel Pump Cooldown Study," Pratt and Whitney Aircraft, Division of United Aircraft Corporation, West Palm Beach, Florida, 13 April 1962 (NAS8-2690).

The objective of this program was to develop an organic coating system that could be applied to internal surfaces of the liquid hydrogen fuel pump which would minimize chilldown preconditioning of the pump. Material tested was Ermalon-310 (TFE phenolic resin). Tests were performed with LH₂ at -423 F. All internal surfaces of the pump were coated. These included:

1. Inducer
2. First-stage inlet housing
3. First-stage impeller
4. Bearing support plate
5. Crossover tube between first-stage impeller and its exit
6. Second-stage impeller
7. Main gearbox housing

The material was applied to the surface and fused at 700 F, the temperature recommended by the manufacturer of the coating. During the first acceleration attempt, the internal insulation flaked off.

The limited success of the TFE-filled phenolic resin coating on the RL-10A-3 fuel pump and the excessive cure temperature required for TFE coating eliminated this type of coating from further consideration.

"Investigation of Potential Low Temperature Insulations," J. Hertz, General Dynamics/Convair, San Diego, California. Paper presented at Cryogenic Engineering Conference, 23-25 August 1965 at Houston, Texas.

The primary objective of this program was the evaluation of the thermal or mechanical properties of various organic materials with possible application as a low-temperature insulator. Materials tested were: Kel-F, polyethylene, epoxy, polystyrene, and various reinforced laminates. Linear thermal expansion, thermal conductivity, and linear tensile properties were determined at temperatures of 77 to -423 F. Thermal conductivity measurements showed that the Kel-F material had the lowest value at -423 F of all materials tested. Problems arose with certain classes of materials, specifically the polystyrene and reinforced epoxy, because of thermal shock caused by the rapid reduction in temperatures. Kel-F resulted in the lowest k-factor (thermal conductivity) over the temperature range investigated and is the most promising material for nonstructural applications.

"Physical and Mechanical Properties of KX 624 Insulative Coatings." Rocketdyne, A Division of North American Rockwell Corporation, Canoga Park, California.

The object of the report was to summarize various physical and mechanical properties of KX 635 Kel-F dispersion insulative coatings. Tests were performed at ambient and -423 F. The properties measured were the coefficient of contraction, thermal conductivity, and cryogenic (-320 F) fatigue life. Flexural fatigue life tests were conducted on coated Tens-50 aluminum samples (per ASTM DG71). All samples received 1×10^6 cycles at total deflections up to 0.20 inch. There was no evidence of coating separation from the metal after one-million cycles. The thickness of the coatings ranged from 0.020 to 0.150 inch. Thermal conductivity and linear coefficient of contraction data are presented in Fig. A-4 and A-5, respectively. The mechanical and thermal properties of the filled Kel-F materials were sufficient to warrant continuation of a development program for filled Kel-F materials for cryogenic service.

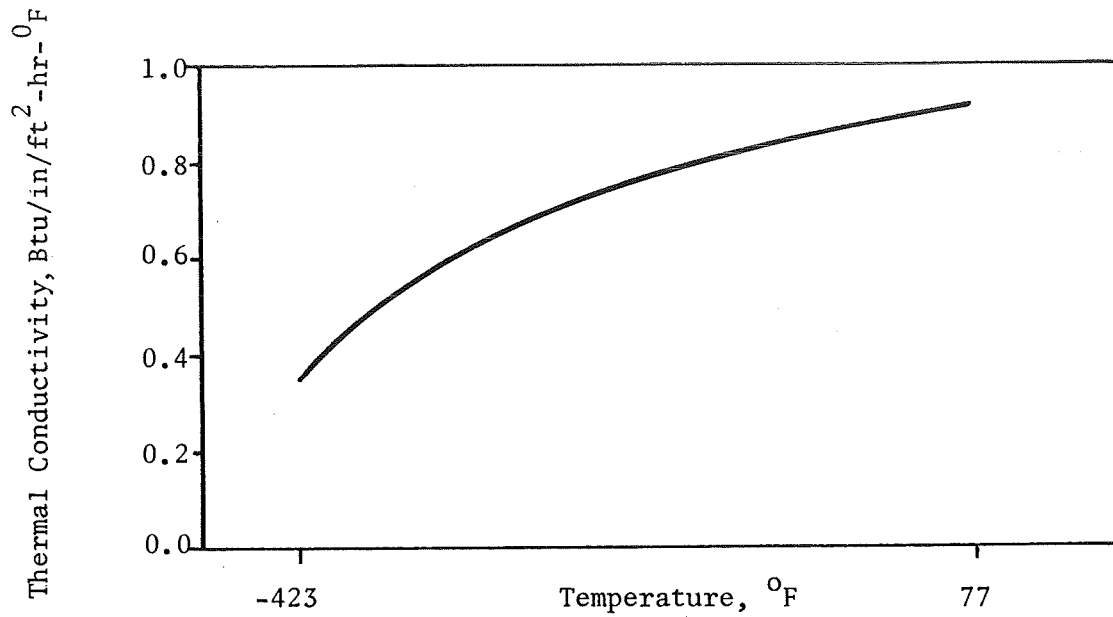


Figure. A-5. Thermal Conductivity of KX 635

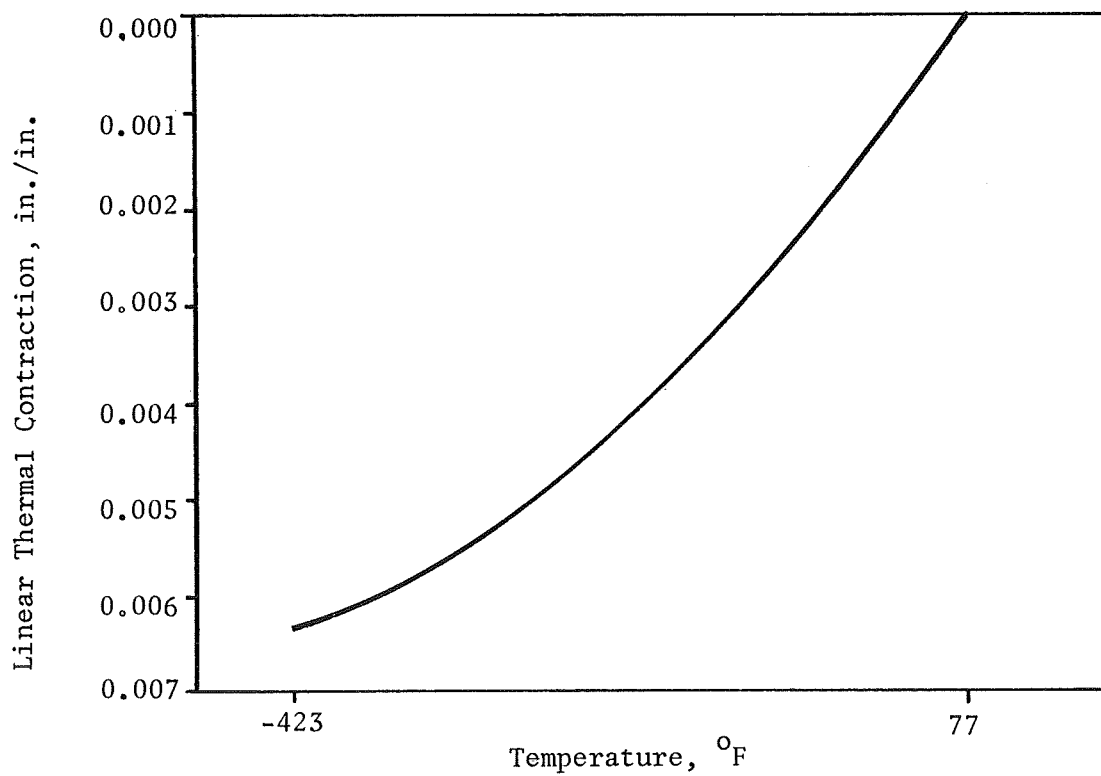


Figure A-6. Coefficient of Contraction of KX 635 Coating

"Evaluation of KX 635 for Turbomachinery Applications," Rocketdyne, A Division of North American Rockwell Corporation, Canoga Park, California.

The objectives were to determine if a filled fluorcarbon plastic (KX 635) might be developed for an insulating internal wearing service for cryogenic turbomachinery. Metallic substrate was Tens-50 aluminum casting alloy. Coating material was KX 635, a glass microballoon-filled Kel-F dispersion material. Bond strength between coating and substrate at ambient and cryogenic temperatures was determined by static tensile tests and flexural fatigue tests. Tests were performed at ambient and liquid nitrogen temperatures (-320 F). Tensile tests indicated that the coating adhered to the metallic substrate at all temperatures until metal failure occurred. Flexural fatigue tests at cryogenic temperatures showed that the coating adhered to the substrate at total deflections up to 0.200 inch without coating-to-metal separation. Erosion rates of the coating material caused by fluid flow were not determined.

The various data generated were promising enough that further efforts could be justified to evaluate this type of internal insulation wearing surface for cryogenic applications. The efforts at this time were terminated because of the fact that this Kel-F material was determined to be incompatible with LO_2 and the proposed use of this material was for LO_2 turbopumps.

"Investigation of the Instant Start Capabilities of the RL-10 Engine with Internally Insulated Fuel Pumps," Pratt and Whitney Aircraft, A Division of United Aircraft Corporation, West Palm Beach, Florida.

The object was to develop a coating system to insulate the internal passages of the RL-10 liquid hydrogen turbopump, to minimize the heat transfer into the propellants, and allow quick start of the turbopump. A Kel-F coating system which included KX 643 primer, KX 635 coating, and KX 633 top coat was investigated. Tests were performed in liquid hydrogen (-423 F).

Thirty-three actual engine hot firings were conducted utilizing insulated pumps. After 12 hot firings, small cracks were detected in the insulation but it was found in suitable condition for further testing. Six further test firings did not significantly degrade the coating adhesion to the substrate. Pump performance and engine acceleration in some cases was found to be acceptable using a zero chilldown start.

The limited test results demonstrated the feasibility of instant start with internally insulated pumps. However, continued experimental efforts would be needed to verify its applicability for engine systems. The further development and modifications of the existing insulation material and application techniques capable of satisfying the engine service life requirements with respect to durability and performance was warranted.

Fluorocarbons were the principal class of material considered for use as a cryogenic insulation. Besides having relatively low heat transfer coefficients and good low-temperature ductility, the techniques involved in the processing of these materials have been thoroughly investigated and successfully used. Of the fluorocarbon materials proposed, specific application requirements and experience gained through earlier programs indicated that the KX 635 glass microballoon modified Kel-F material system was the most promising of the materials evaluated.

Although the thermal and physical properties of the Teflons (TFE and FEP) were adequate for proposed applications, the processing times at temperature necessary to completely fuse the materials were considered in excess of the acceptable processing range of the cast aluminum material proposed for pump components. As an alternative to long-duration oven fusing, the use of a fluidized bed sintering operation* was considered. Although the fusing time could be reduced, the fusing temperature still remained in excess of the allowable safe limit.

The use of the KX 635 material for cryogenic insulation application will be discussed in further detail in the following sections.

*Sintering of 'Fluon' PTFE by Fluid Bed Techniques, Technical Report from I.C.I. Plastics Division, Welwyn Garden City, Herts.

Summary of Literature Search for Conventionally Applied Coatings

Of all material systems investigated in the literature search of conventionally applied organic coatings, the KX 635 material was the most promising. Although various other materials warranted further investigations, the decision was made to limit this developmental work to improvement by modifying the base material by the addition of various quantities of low-expansion fillers. The reasons for this decision were:

1. Superior mechanical and thermal properties of the Kel-F material to others mentioned in the literature
2. Past experience utilizing this type of material for similar application
3. Processing limitations imposed upon the evaluated metallic substrates

PLASMA COATINGS

Three articles were reviewed pertinent to plasma spraying of organic materials. They are described below.

"Plasma Spray Allocation of Plastic Materials," Kremith, D. and W. Rosenbery, Plasmadyne, Inc., Santa Ana, California, Presented at 12th National SAMPE Symposium.

Plasma spray parameters for applying organic materials to metal substrates were reported. Materials sprayed successfully include thermosetting epoxies and polyesters and thermoplastic polyethylene and polyamides. Attempts at spraying phenolics, polyimides, and silicones were unsuccessful. Coatings of over 0.008 inch in thickness, in general, had good flexibility, impact resistance, and dielectric strengths. Polyethylene and a polyamide exhibited best flexibility while an epoxy had the best impact resistance. All had dielectric strengths in excess of 5000 rms volts AC (tester limit).

Plasma-spray parameters were optimized for several organic materials and acceptable coatings were deposited. The information on spraying parameters is directly applicable to the thermal improvement study because Materials and Processes uses the same (Plasmadyne) equipment. Consequently, it was not necessary to undertake a development project to optimize equipment settings for several materials of interest. The report also provided valuable data on the necessity for preheating the substrate to obtain best adhesion. None of the data presented are directly applicable to cryogenic service.

"Flame and Plasma Sprayed Polymeric Protective Coatings," Janowiecke, R. J. and M. C. Willson, AFML-TR-66-152, Parts I, II and III.

Plasma-spray parameters for deposition of several organic materials were developed for the Plasmadyne SG-1 plasma gun. A silicone and polyimide prepolymer were successfully deposited by the plasma spraying technique. Crack-free coatings were produced by adding zinc oxide, titanium dioxide, and other pigments. The data included visual examination for cracks, pores, coalescence, and adhesion; pencil hardness tests for coatings deposited by various spray gun settings; substrate preheating temperature; and pigment/resin ratio.

Organic coatings can be deposited by plasma spraying by using optimum gun settings and substrate temperature. Coatings are improved by adding pigments. The report provided additional organic materials to choose from for the thermal improvement study, although the resins are not readily available in powder form. Moreover, no data at cryogenic temperatures were presented; however, the pigment/resin ratios given were useful in formulating mixtures of other materials for further Rocketdyne study.

"High Temperature Resistant Polymeric Coatings--Progress Report No. 6, October 1968," Monsanto Research Corporation, Dayton, Ohio, Contract F33-615-67-C1383 with Air Force Materials Laboratory, Wright-Pat AFB, Wright-Patterson, Ohio.

Polychlorotrifluoroethylene and fluorinated ethylene propylene copolymer, both with and without pigment, were successfully deposited by the plasma spray process. Coatings of Kel-F 6061 (3M Company) and FEP LC-1361 (Polymer Corporation) were evaluated. Pigments included titanium dioxide R-900 (DuPont Corporation) and zinc oxide SP-500 (New Jersey Zinc Company). Mixing proportions of pigment and resin powders and a special ball-milling technique to make the mixtures sprayable are described. As-sprayed coating integrity, adhesion, and hardness were generally good. Spraying parameters were presented for the Plasmadyne SG-1 plasma gun. Substrate temperatures on the order of 500 F were necessary to produce a good coating. Deposition of Kel-F and Teflon coatings by the plasma spray process are feasible and offer an advantage over some other deposition processes in that subsequent heat curing is not required.

Mixture ratios and the ball-milling preparation technique provided useful information for subsequent use in formulating and preparing other materials to obtain good coatings for the thermal improvement study. The applicability of either FEP or Kel-F to the study was considered questionable, because of the reported high substrate temperature requirement during coating deposition. A temperature of 500 F is too high for most aluminum alloys and would be difficult to control even on substrates which would not be affected by this temperature.

APPENDIX B

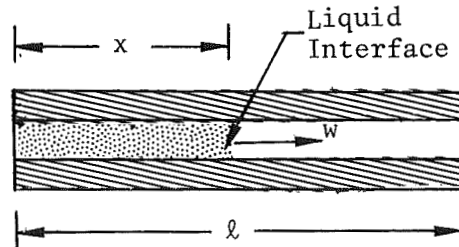
ENGINE START MODEL EQUATIONS

FEED SYSTEM

Liquid Line. Flow through liquid lines are represented by an incompressible dynamic form of Bernoulli's equation:

$$\Delta P = R_L \dot{W}^2 + \frac{\ell}{Ag} \frac{d\dot{W}}{dt} \quad (B-1)$$

The derivative of flowrate is omitted for flow-through valves. For the present analysis, the flow is assumed to be liquid throughout the oxidizer feed system, and up to the cooling jacket in the fuel feed system. Line length and resistance are allowed to vary with time according to the degree of line priming. Resistance is assumed to be proportional to line length, which is, in turn, proportional to the amount of flow in the line as illustrated below:



$$\frac{x}{\ell} = \frac{W}{(\rho V)_n} = \left(\frac{\dot{W}}{\rho V} \right)_n \int \bar{W} dt$$

Flowrate in downstream lines is taken to be zero in the model until the upstream line is fully primed. To date, all analyses have been conducted with the system primed up to the main valves (Fig. 72).

Tube Bundle. Compressible flow is assumed in the tube bundle. The form of the equation used to describe the flow process is the same as Eq.B-1 except that the line resistance is adjusted to reflect the change in gas density with operating conditions. The bulk temperature of the fluid rises as it passes through the jacket due to heat input from the combustion process and from the metal surfaces of the tubes. The latter effect has been neglected, which is valid for thrust chamber wall temperatures near that of the incoming hydrogen; also, it is indicated in Fig.87 that the initial temperature of the pump often has a much more significant effect than that of the thrust chamber. Heat input from the combustion process is assumed to be proportional to the eight-tenths power of chamber pressure. Thus, to a first approximation, the normalized bulk temperature rise through the jacket is given by:

$$\overline{\Delta T} = \frac{\overline{P}_c^{0.8}}{\dot{W}}$$

The normalized temperature at the injector is:

(B-2)

$$\overline{T}_{inj} = \overline{T}_{fp} \left(\frac{\overline{T}_{fp}}{\overline{T}_{inj}} \right)_n + \overline{\Delta T} \left(\frac{\overline{\Delta T}}{\overline{T}_{inj}} \right)_n$$

Flowrate through the injector is determined by assuming compressible low velocity orifice flow. That is:

$$\overline{\Delta P}_{inj} = \frac{1}{\overline{\rho}_{inj}} \dot{W}^2$$

where $\overline{\rho}_{inj}$ is determined from the perfect gas law and corresponds to \overline{T}_{inj} and \overline{P}_{inj} . The latter quantity (\overline{P}_{inj}) is determined from the following relationship:

$$\overline{P}_{inj} = \overline{P}_c \left(1/2 \frac{\overline{P}_c}{\overline{P}_{inj}} \right)_n + \sqrt{\overline{P}_c^2 \left(1/2 \frac{\overline{P}_c}{\overline{P}_{inj}} \right)_n^2 + \dot{W}^2 \overline{T}_{inj} \left(1 - \frac{\overline{P}_c}{\overline{P}_{inj}} \right)_n}$$

Likewise, flowrate through the tube bundle is obtained from Eq.B-1 with:

$$R_L = R/\rho_{TB}$$

In this case, the flow density is computed from the perfect gas law at a point in the jacket where the bulk temperature is an average between inlet and outlet (injector) temperatures. The pressure at this point is approximated by Eq. B-3 which neglects the line inductance for the pressure calculation in order to maintain simplicity while representing correct trends. The above approach yields qualitative results, but it is felt that the flow characteristics with heat transfer due to combustion are adequately represented.

This procedure also assumes that the flow through the tube bundle is steady (i.e., the inlet flow is equal to the exit flow). Actually, mass is accumulated in the tube bundle during the start transient because of compressibility. Density should be determined by:

$$\rho = \frac{1}{V} \int (\dot{W}_{in} - \dot{W}_{out}) dt \quad (B-4)$$

Temperature should be governed by Eq.B-2, and pressure obtained from the perfect gas law. The pressure drop through the tube bundle should be used in conjunction with Eq. 39 to determine the flow leaving the downstream portion of the tube bundle. This technique, which is described in more detail in Ref.B-1*, was briefly examined during the study. It was found that introducing the added degree of freedom significantly increased solution time on the computer. Reducing the accuracy of the problem integrations decreased this time, but seriously compromised the stability of the solution. Thus, in the interest of expediency, this approach was abandoned once it was established that the trends predicted were similar to those obtained using the simplified treatment outlined in the preceding paragraph.

*Ref. B-1

Hot-Gas Section. Flowrate to the turbines depends on the pressure available at the combustion chamber tapoff ports and the pressure distribution and geometry through the gas flow path, in addition to the control valve areas. The compressible flow equation employed in this analysis is:

$$\dot{W} = P A F g/c^* \quad (B-5)$$

where F is a modifying factor to the choked flow function, and c^* is the gas characteristic velocity which can be normalized to give $c^* = \sqrt{\dot{T}}$. This equation states that the gas flowrate through a particular area, A, is a fraction, F, of the flowrate that would exist if the flow were sonic with upstream pressure, P. If it is assumed that upstream velocity can be neglected, the factor, F, is unity for downstream-to-upstream pressure ratio less than the critical value, which is found from:

$$\alpha_c = \left(\frac{P_d}{P_u} \right)_c = \left(\frac{2}{\gamma + 1} \right)^{\frac{\gamma}{\gamma - 1}}$$

For larger values of α , the gas flow function is given by:

$$\bar{F} = \frac{1}{\bar{\alpha}^{\frac{\gamma}{\gamma - 1}}} \left[\left(\frac{\gamma + 1}{\gamma - 1} \right) - \left(\frac{2}{\gamma - 1} \right) \bar{\alpha}^{\frac{\gamma - 1}{\gamma}} \right]^{1/2}$$

In this study it was found convenient to deal with downstream pressure and define an inverse gas flow function as follows:

$$\bar{F}_i = \frac{\bar{\alpha}}{\bar{F}} \frac{\bar{P}_D \bar{A}}{\bar{W} \sqrt{\dot{T}}} \quad (B-6)$$

pressure ratio is then found from:

$$\bar{\alpha} = \left\{ \bar{F}_i \left[\left(x^2 + a \bar{\alpha}_c^{-2/\gamma} \right)^{1/2} - x \right] \right\}^{\frac{\gamma}{\gamma - 1}} ; \quad \bar{\alpha}_c < \bar{\alpha} < \frac{1}{\bar{\alpha}_n} ; \quad \left. \begin{array}{l} \bar{\alpha}_c > \bar{\alpha} > 0 \end{array} \right\} \quad (B-7)$$

$$\bar{\alpha} = \bar{F}_i \quad \bar{\alpha}_c > \bar{\alpha} > 0$$

where

$$x = \bar{F}_i \left(\frac{b}{2} \right) \bar{\alpha}_c^{-\left(\frac{1+\gamma}{\gamma} \right)} ; b = \frac{2}{\gamma-1} ; a = \frac{\gamma+1}{\gamma-1}$$

Flowrates and pressures in the turbines and bypass circuit in Fig. 72 are obtained by an iterative solution of a set of equations like Eq. B-5, B-6 and B-7, which is made possible by knowing chamber pressure downstream ambient pressure.

Turbines. The torque delivered by a gas turbine is a function of mass flowrate, ideal drop in enthalpy through the turbine, efficiency, and speed. In this study, the relationship between these quantities is determined by means of parametric torque maps. These maps were curve-fitted by means of a relation of the form:

$$\frac{\bar{\tau}}{\bar{P}_{in}} = A - B \left(\frac{\bar{N}}{\sqrt{\bar{T}}} \right) - C \bar{\alpha} \quad (B-8)$$

for constant $\alpha < \alpha_o$. Values of A, B, and C used for the oxidizer and fuel turbines are indicated below.

	A	B	C	α_o	α_m	D	E
Oxidizer Turbine	2.202	0.512	0.690	1.402	2.639	0.999	0.414
Fuel Turbine	1.674	0.412	0.262	4.654	8.757	0.111	0.100

For $\alpha > \alpha_o$, the form of the curve fit is:

(B-9)

$$\frac{\bar{\tau}}{\bar{P}_{in}} = \left[D - E \left(\frac{\bar{N}}{\sqrt{\bar{T}}} \right) \right] (\alpha_m - \alpha)$$

The constants D, E, and α_m are also listed in the above tabulation. Temperature at the fuel turbine inlet is determined on the basis of the J-2X chamber tapoff test data shown in Fig.B-2. The indicated dependence on chamber pressure and mixture ratio closely follows the expression below:

$$\bar{T}_f = (0.23) + (0.19) \bar{P}_c + (0.58) \overline{MR} \quad (B-10)$$

Temperature decrease through the fuel turbine is given by:

$$\overline{\Delta T} = \bar{N} \bar{\tau} / \bar{W}_t$$

The gas temperature at the oxidizer turbine inlet is determined by:

$$\bar{T}_{ox} = \left(\frac{T_f}{T_{ox}} \right)_n \bar{T}_f - \left[\left(\frac{T_f}{T_{ox}} \right)_N - 1 \right] \overline{\Delta T} \quad (B-11)$$

A similar relation is used to determine the gas temperature at the exit orifice.

The start model does not have the capability for analytical representation of an auxiliary turbine power source, which is often used to decrease start time by providing additional high-energy flow to the turbines during the start transient. The rapid starts achievable by means of this component are currently simulated by initially providing larger-than-nominal tapoff valve areas (of Eq.B-5) and high tank pressures.

Turbopumps. Pump operation is characterized by relationships between head, flow, speed, efficiency, and power. These are usually expressed by means of curves of normalized head coefficient versus normalized flow coefficient, which for the Mark 29 pumps used in the start model can be fitted as follows:

$$\begin{aligned} \bar{\psi} &= -0.51 \bar{\phi}^2 + 0.536 \bar{\phi} + 0.974 \text{ (fuel)} \\ \bar{\psi} &= -0.408 \bar{\phi}^2 + 0.244 \bar{\phi} + 1.164 \text{ (oxidizer)} \end{aligned} \quad (B-12)$$

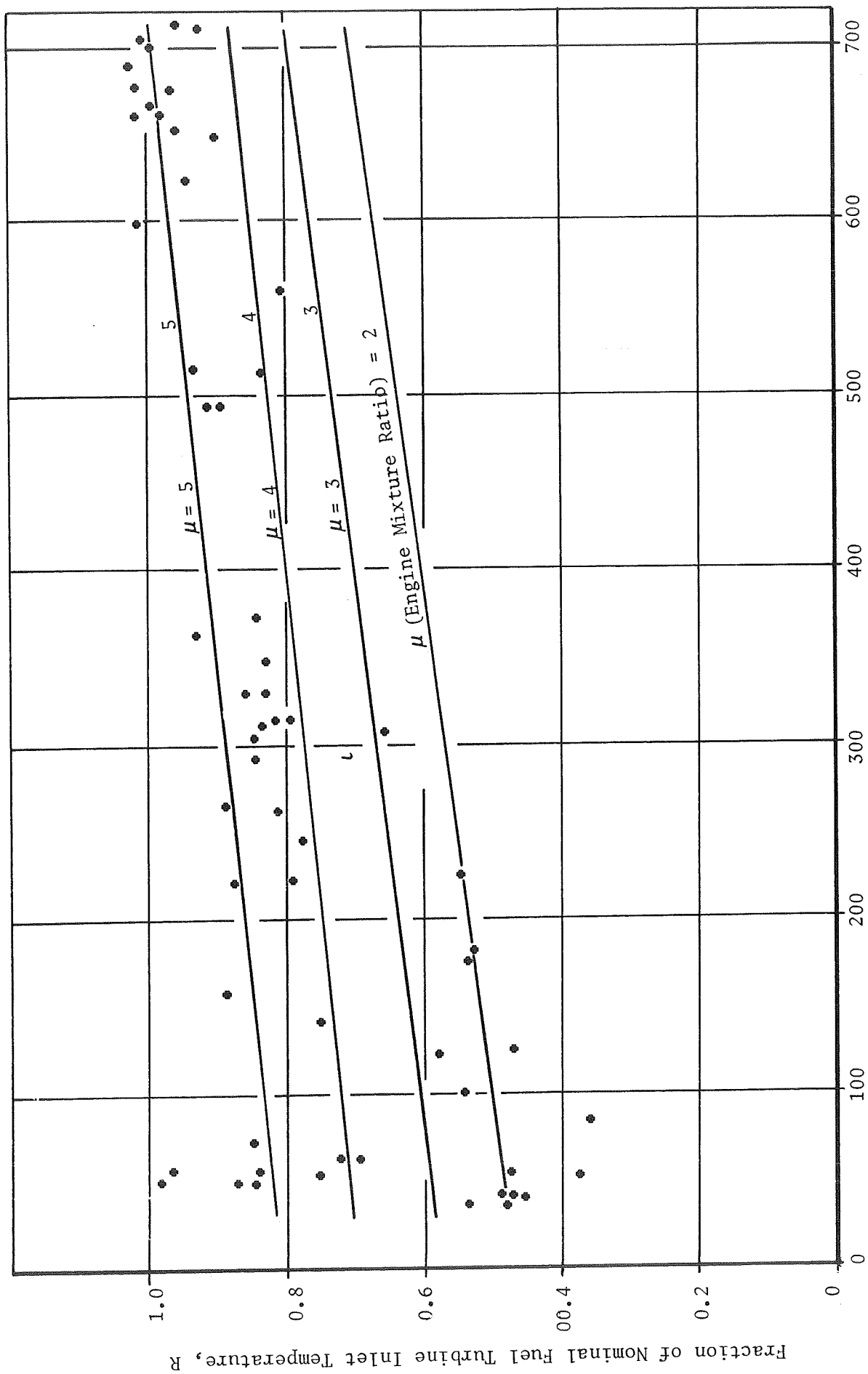


Figure B-1. Normalized Turbine Inlet Temperature Data Obtained in a J-2X Chamber Tapoff Test

where

$$\bar{\psi} = \frac{\overline{\Delta P}}{2 \bar{N}}$$

and

$$\bar{\phi} = \frac{\bar{Q}}{\bar{N}} = \frac{\dot{\bar{W}}}{\bar{N}} \quad (\text{constant } \rho)$$

Pump head loss or instability because of positive slope of the $\bar{\psi}$ - $\bar{\phi}$ curve is not reflected by the model and therefore is checked manually for each run. Efficiency for these pumps is given by:

$$\eta_p = \frac{\dot{\bar{W}}}{\bar{\tau}_p} \frac{\overline{\Delta P}}{\bar{N}} \approx 2.667 \bar{\phi} - 1.667 \bar{\phi}^2$$

which provides an expression for $\bar{\tau}_p$. Since each pump operates on a common shaft with its turbine, pump and turbine speeds are equal. Acceleration depends on the difference between turbine-produced and pump-required torque as indicated below:

$$\ddot{\theta I} = (\bar{\tau}_t - \bar{\tau}_p) \bar{\tau}_n$$

This equation can be integrated to give shaft speed as a function of time:

$$\bar{N} = \left(\frac{30 \tau_n}{\pi I \bar{N}_n} \right) \int (\bar{\tau}_t - \bar{\tau}_p) dt \quad (B-13)$$

The coefficient preceding the integral in Eq. B-13 is the inverse of the turbopump time constant. It is usually the one of the largest^r in the system and, therefore, strongly influences the system low-frequency response characteristics.

Thrust Chamber. In the chamber, ignition is assumed to occur as soon as the LO₂ dome is primed. The normalized flowrate through the injector is determined from:

$$\dot{\bar{W}} = \left(\frac{\mu}{1 + \mu} \right)_n \dot{\bar{W}}_{ox} + \left(\frac{1}{1 + \mu} \right)_n \dot{\bar{W}}_f \quad (B-14)$$

Mixture ratio is given by:

$$\bar{\mu} = \frac{\dot{\bar{W}}_{\text{ox}}}{\dot{\bar{W}}_{\text{f}}}$$

and is used to determine characteristic velocity by means of the functional relationship shown for LO_2/H_2 in Fig. B-2. A first-order lag is assumed for chamber pressure such that:

$$t_c \frac{d\bar{P}_c}{dt} + \bar{P}_c = \dot{\bar{W}} \bar{c}^*$$

A relatively low value is used for the thrust chamber time constant, t_c , in the start model.

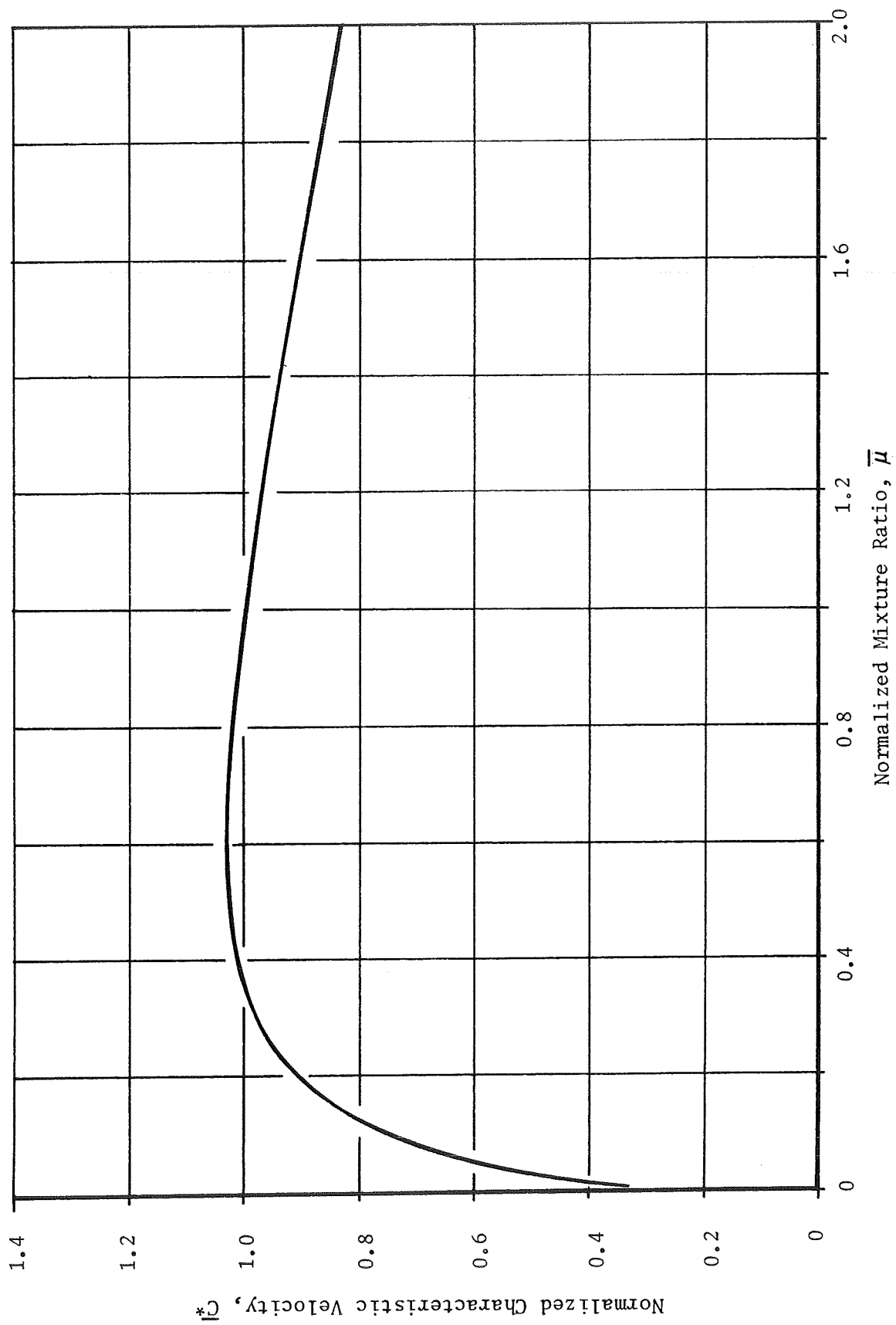


Figure B-2. Thrust Chamber Characteristic Velocity vs. Mixture Ratio

APPENDIX C

PAYLOAD ESTIMATES

FUEL LEAD (DUMP) CHILLDOWN

This case typifies the backup chilldown operation utilized with the current S-IVB system after coasting in earth orbit. For a given mission requirement, ΔV , and performance during the second burn, the change in burnout weight for propellant dump prior to the second burn can be determined by noting that:

$$\Delta V = I_s g \ln R = \text{const}$$

or

$$R = \text{const} = \frac{W_{BO1} + \dot{W}_{P1}}{W_{BO1}} = \frac{W_{BO2} + \dot{W}_{P2}}{W_{BO2}}$$

which reduces to

$$\frac{\Delta W_{BO}}{W_{BO1}} = \frac{\Delta W_P}{W_{P1}} = \frac{\Delta W_{PL}}{W_{BO1}}$$

or

$$\frac{\Delta W_{PL}}{W_{PL1}} = \left(\frac{W_{BO1}}{W_{PL1}} \right) \frac{\Delta W_P}{W_{P1}}$$

For a typical S-IVB mission: $W_{BO_1} = 148.3K$, $W_{PL_1} = 113.6K$, $W_{P_1} = 163.7K$, so:

$$\% \frac{\Delta W_{PL}}{W_{PL_1}} = (0.798 \times 10^{-3}) \Delta W_P$$

IDLE-MODE CHILLDOWN

In this case, payload loss associated with chilldown can be estimated from the performance loss during idle-mode operation. The technique is outlined in Ref. B-1*. The propellant required to make up the ΔV loss at the end of the flight due to the performance loss is assumed to be equal to the loss in payload. For small increments of propellant burned, the propellant weight required for a given ΔV can be closely approximated by the following relationship:

$$\Delta V_1 = W_{P_1} I_s g/W_o$$

and at the end of the flight:

$$W_P = \Delta V_2 W_{BO}/I_s g$$

These can be combined to give:

$$\Delta W_{PL} = W_{BO} \left(\frac{\Delta I_s}{I_s} \right) \left(\frac{\Delta V_1}{I_s g} \right) = W_{BO} \left(\frac{\Delta I_s}{I_s} \right) \left(\frac{W_P}{W_o} \right) = \frac{W_P}{R} \frac{\Delta I_s}{I_s}$$

For the S-IVB idle mode: $\Delta I_s/I_s = 0.355$, $R = 2.1$, $W_{P_1} = 113.6K$

$$\% \frac{\Delta W_{PL}}{W_{PL_1}} = (0.150 \times 10^{-3}) \Delta W_P$$

In this case, W_P includes both oxidizer and fuel so idle-mode mixture ratio must be known.

*Ref. B-1. Byron, R. A. and C. P. Morse: Advanced Pressurization System for Liquid Rockets, Rocketdyne, Presented at the AIAA 4th Propellant Joint Specialist Conference, Cleveland, Ohio, 10-14 June 1968.

APPENDIX D

DISTRIBUTION LIST

<u>COPIES</u>	<u>RECIPIENT</u>	<u>DESIGNEE</u>
	NASA Marshall Space Flight Center	
	Huntsville, Alabama 35812	
2	Office of Technical Information , MS-IP	(X)
1	Technical Library	(X)
1	Purchasing Office, PR-SC	(X)
1	Patent Office, CCP	(X)
1	Keith Chandler, R-P&VE-PA	(X)
1	Technology Utilization Office, MS-T	(X)
2	T. W. Winstead (R-P&VE-P) (Technical Monitor)	(X)
4	Chief, Liquid Propulsion Technology, RPL	(X)
	Office of Advanced Research and Technology	
	NASA Headquarters	
	Washington, D. C. 20546	
25	NASA Scientific and Technical Information	(X)
	Facility	
	P.O. Box 38	
	College Park, Maryland 20740	
1	Mr. Vincent L. Johnson	(X)
	Director, Launch Vehicles and Propulsion, SV	
	Office of Space Science and Applications	
	NASA Headquarters, Washington, D. C. 20546	
1	Mr. Doug Lord	(X)
	Director, Advanced Manned Missions, MT	
	Office of Manned Space Flight	
	NASA Headquarters, Washington, D. C. 20546	
1	Leonard Roberts	(X)
	Mission Analysis Division	
	NASA Ames Research Center	
	Moffett Field, California 24035	

NASA FIELD CENTERS

<u>COPIES</u>	<u>RECIPIENT</u>	<u>DESIGNEE</u>
2	Ames Research Center Moffett Field, California 94035	H. J. Allen Mission Analysis Div.
2	Goddard Space Flight Center Greenbelt, Maryland 20771	Merland L. Moseson Code 620
2	Jet Propulsion Laboratory California Institute of Technology 4800 Oak Grove Drive Pasadena, California 91103	Henry Burlage, Jr. Propulsion Div., 38
2	Langley Research Center Langley Station Hampton, Virginia 23365	Dr. Floyd L. Thompson Director
2	Lewis Research Center 21000 Brookpark Road Cleveland, Ohio 44135	Dr. Abe Silverstein Director
2	Marshall Space Flight Center Huntsville, Alabama 35812	Hans G. Paul Code R-P&VE-P
2	Manned Spacecraft Center Houston, Texas 77001	Dr. Robert R. Gilruth Director
2	John F. Kennedy Space Center, NASA Cocoa Beach, Florida 32931	Dr. Kurt H. Debus

GOVERNMENT INSTALLATIONS

<u>COPIES</u>	<u>RECIPIENT</u>	<u>DESIGNEE</u>
1	Aeronautical Systems Division Air Force Systems Command Wright-Patterson Air Force Base Dayton, Ohio 45433	Dr. L. Schmidt Code ASRCNC-2
1	Air Force Missile Development Center Holloman Air Force Base, New Mexico	Maj. R. E. Bracken Code MDGRT
1	Air Force Missile Test Center Patrick Air Force Base, Florida	L. J. Ullian
1	Air Force Systems Division Air Force Unit Post Office Los Angeles 45, California	Col. Clark Tech. Data Center

<u>COPIES</u>	<u>RECIPIENT</u>	<u>DESIGNEE</u>
1	Arnold Engineering Development Center Arnold Air Force Station Tullahoma, Tennessee	Dr. H. K. Doetsch
1	Bureau of Naval Weapons Department of the Navy Washington 25, D. C.	J. Kay, Code RTMS-41
1	Defense Documentation Center Headquarters Cameron Station, Building 5 5010 Duke Street Alexandria, Virginia 22314 Attn: TISIA	
1	Headquarters, U. S. Air Force Washington 25, D. C.	Col. C. K. Stambaugh Code AFRST
1	Picatinny Arsenal Dover, New Jersey 07801	I. Forsten, Chief Liquid Propulsion Lab.
1	Air Force Rocket Propulsion Laboratory Research and Technology Division Air Force Systems Command Edwards, California 93523	RPRR
1	U. S. Atomic Energy Commission Technical Information Services Box 62 Oak Ridge, Tennessee	A. P. Huber Oak Ridge Gaseous Diffusion Plant (ORGDP) P. O. Box P
1	U. S. Army Missile Command Redstone Arsenal Alabama 35809	Dr. Walter Wharton
1	U. S. Naval Ordnance Test Station China Lake California 93557	Code 4562 Chief, Missile Propulsion Div.

INDUSTRY CONTRACTORS

1	Chemical Propulsion Information Agency Applied Physics Laboratory 8621 Georgia Avenue Silver Spring, Maryland 20910	Tom Reedy
1	Aerojet-General Corporation P. O. Box 296 Azusa, California	L. F. Kohrs

<u>COPIES</u>	<u>RECIPIENT</u>	<u>DESIGNEE</u>
1	Aerojet-General Corporation P. O. Box 1947 Technical Library, Bldg. 2015, Dept 2410 Sacramento, California 95809	R. Stiff
1	Aeronutronic Philco Corporation Ford Road Newport Beach, California	D. A. Carrison
1	Aerospace Corporation 2400 East El Segundo Boulevard P. O. Box 9508 Los Angeles, California 90045	Owen Dykma MS-2293 Propulsion Dept.
1	Arthur D. Little, Inc. 20 Acorn Park Cambridge 40, Massachusetts	E. Karl Bastress
1	Astropower Laboratory Douglas Aircraft Company 2121 Paularino Newport Beach, California 92663	Dr. Goerge Moc Director, Research
1	Astrosystems International, Inc. 1275 Bloomfield Avenue Caldwell Township, New Jersey	
1	Atlantic Research Corporation Edsall Road and Shirley Highway Alexandria, Virginia 22314	R. Friedman
1	Beech Aircraft Corporation Boulder Facility Box 631 Boulder, Colorado	J. H. Rodgers
1	Bell Aerosystems Company P. O. Box 1 Buffalo 5, New York	Dr. Kurt Berman
1	Bendix Systems Division Bendix Corporation, 3300 Plymouth Rd. Ann Arbor, Michigan	John M. Brueger
1	Boeing Company P. O. Box 3707 Seattle 24, Washington	J. D. Alexander

<u>COPIES</u>	<u>RECIPIENT</u>	<u>DESIGNEE</u>
1	Missile Division Chrysler Corporation P. O. Box 2628 Detroit, Michigan 48231	John Gates
1	Wright Aeronautical Division Curtiss-Wright Corporation Wood-ridge, New Jersey 07075	G. Kelley
1	Missile and Space Systems Division Douglas Aircraft Company, Inc. 3000 Ocean Park Boulevard Santa Monica, California 90406	R. W. Hallet Chief Engineer Advanced Space Tech.
1	Aircraft Missiles Division Fairchild Hiller Corporation Hagerstown, Maryland 10	J. S. Kerr
1	General Dynamics/Astronautics Library & Information Services (128-00) P. O. Box 1128 San Diego, California 92112	Frank Dore
1	Re-Entry Systems Department General Electric Company 3198 Chestnut St. Philadelphia, Pennsylvania 19101	F. E. Schultz
1	Advanced Engine & Technology Dept. General Electric Company Cincinnati, Ohio 45215	D. Suichu
1	Grumman Aircraft Engineering Corp. Bethpage Long Island, New York	Joseph Gavin
1	Aerospace Operations Walter Kidde and Company, Inc. 567 Main Street Belleville, New Jersey 07109	R. J. Hanville Director of Research Engineering
1	Ling-Temco-Vought Corp. Astronautics P. O. Box 5907 Dallas, Texas 75222	Warren C. Trent

<u>COPIES</u>	<u>RECIPIENT</u>	<u>DESIGNEE</u>
1	Lockheed California Company 2555 N. Hollywood Way Burbank, California 91503	G. D. Brewer
1	Lockheed Missiles and Space Company Attn: Technical Information Center P. O. Box 504 Sunnyvale, California	Y. C. Lee
1	Lockheed Propulsion Company P. O. Box 111 Redlands, California 92374	H. L. Thackwell
1	The Marquardt Corporation 16555 Saticoy Street Van Nuys, California 91409	Warren P. Boardman, Jr.
1	Baltimore Division Martin Marietta Corporation Baltimore, Maryland 21203	John Calathes (3214)
1	Denver Division Martin Marietta Corporation P. O. Box 179 Denver, Colorado 80201	J. D. Goodlette (A-241)
1	McDonnell Aircraft Corporation P. O. Box 516/Municipal Airport St. Louis, Missouri 63166	R. A. Herzmark
1	Space & Information Sytems Division North American Rockwell Corp. 12214 Lakewood Blvd. Downey, California 90241	D. Simkin
1	Northrop Space Laboratories 3401 West Broadway Hawthorne, California	Dr. William Howard
1	Florida Research and Development Center Pratt & Whitney Aircraft United Aircraft Corporation P. O. Box 2691 West Palm Beach, Florida 33402	R. J. Coar
1	Astro-Electronics Division Radio Corporation of America Princeton, New Jersey 08540	S. Fairweather

<u>COPIES</u>	<u>RECIPIENT</u>	<u>DESIGNEE</u>
1	Rocket Research Corporation 520 South Portland Street Seattle, Washington 98108	Foy McCullough, Jr.
1	Reaction Motors Division Thiokol Chemical Corporation Denville, New Jersey 07832	Arthur Sherman
1	Republic Aviation Corporation Farmingdale Long Island, New York	Dr. William O'Donnell
1	Rocketdyne (Library, Dept. 586-306) Division of North American Rockwell Corp. 6655 Canoga Avenue Canoga Park, California 91304	E. B. Monteath
1	Space General Corporation 9200 Flair Avenue El Monte, California 91734	C. E. Roth
1	TRW Systems Group TRW Incorporated One Space Park Redondo Beach, California 90278	G. W. Elverum
1	Stanford Research Institute 355 Ravenswood Avenue Menlo Park, California 94025	G. Marxman
1	TAPCO Division TRW, Incorporated 23555 Euclid Avenue Cleveland, Ohio 44117	P. T. Angell
1	Thiokol Chemical Corporation Huntsville Division Huntsville, Alabama	John Goodloe
1	Research Laboratories United Aircraft Corporation 400 Main Street East Hartford, Connecticut 06108	Erle Martin
1	United Technology Center 587 Methilda Avenue P. O. Box 358 Sunnyvale, California 94088	B. Abelman

UNCLASSIFIED

Security Classification

DOCUMENT CONTROL DATA - R & D

(Security classification of title, body of abstract and indexing annotation must be entered when the overall report is classified)

1. ORIGINATING ACTIVITY (Corporate author)

Rocketdyne, a Division of North American Rockwell Corporation, 6633 Canoga Avenue, Canoga Park, California 91304

2a. REPORT SECURITY CLASSIFICATION

UNCLASSIFIED

2b. GROUP

3. REPORT TITLE

THERMODYNAMIC IMPROVEMENTS IN LIQUID HYDROGEN TURBOPUMPS

4. DESCRIPTIVE NOTES (Type of report and inclusive dates)

Final

5. AUTHOR(S) (First name, middle initial, last name)

Rocketdyne Engineering

6. REPORT DATE

May 1970

7a. TOTAL NO. OF PAGES

244 & xiv

7b. NO. OF REFS

22

8a. CONTRACT OR GRANT NO.

NAS8-20324

b. PROJECT NO.

c.

d.

9a. ORIGINATOR'S REPORT NUMBER(S)

R-8083

9b. OTHER REPORT NO(S) (Any other numbers that may be assigned this report)

10. DISTRIBUTION STATEMENT

11. SUPPLEMENTARY NOTES

12. SPONSORING MILITARY ACTIVITY

National Aeronautics and Space Administration
Propulsion and Vehicle Engineering Division
George C. Marshall Space Flight Center

13. ABSTRACT

This report describes the completed effort in the evaluation of thermal conditioning problems of liquid hydrogen turbo-pumps to enhance mixed-phase operation and to minimize engine system constraints on starts and restarts. The program consists of the following three interrelated tasks: I: Reduced Gravity Effects on Heat Transfer, II: Coated Feed Systems, and III: Engine System Analyses.

14. KEY WORDS	LINK A		LINK B		LINK C	
	ROLE	WT	ROLE	WT	ROLE	WT
Two-Phase Flow						
Engine Start Transients						
Insulation and Coatings						
Boiling Heat Transfer						
Engine Feed System						
Hydrogen Rocket Engine						
Hydrogen Pumps						
Reduced Gravity						
Saturn V, S-IVB Stage						
Forced Convection Heat Transfer						
Inducer Cavitation						
Pump Chillover						